A Holistic Evaluation Concept
for Long-Term Structural Health Monitoring

Von der Fakultät für Bauingenieurwesen und Geodäsie
der Gottfried Wilhelm Leibniz Universität Hannover
zur Erlangung des Grades

DOKTOR-INGENIEUR

genehmigte Dissertation

von

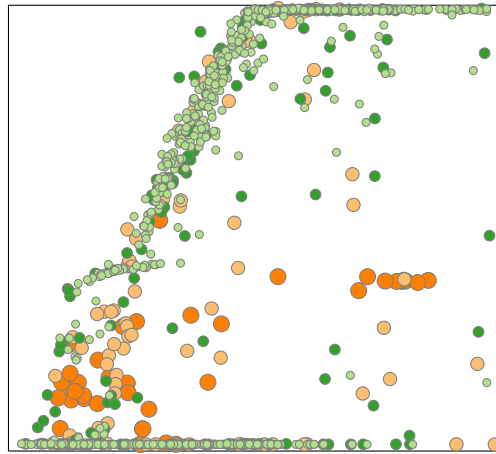Dipl.-Ing. MORITZ WERTHER HÄCKELL

geboren am 10.02.1985, in Bremen

2015

A Holistic Evaluation Concept
for Long-Term Structural Health Monitoring

Dissertation

Dipl.-Ing. MORITZ WERTHER HÄCKELL

Abstract

The monitoring of the integrity of large scale civil structures, also known as structural health monitoring (SHM), was brought into the focus of research and industry by an ever increasing amount of aging infrastructure and new designs and materials that display an unknown long-term behaviour. An increasing proportion of the world's population lives in hazardous regions, e.g. with the danger of seismic events, storms, or flooding, requires SHM, too. Wind turbines (WTs) form systems with a distinct dynamic loading and response. Many identical turbines are erected within remote wind farms, aiding the application of vibration based SHM.

In recent decades, SHM was applied to a variety of structures around the globe, mainly in terms of tracking modal properties as frequencies or mode shapes with respect to fixed reference values. Recently, more complex residual condition parameters (CPs) between system states have been formulated. These provide higher sensitivity in terms of structural changes but also less robustness to environmental and operational conditions (EOCs), raising the question of proper machine learning (ML) and hypothesis testing (HT) as compensation.

This work focuses on the application of a new SHM framework that can also be used for the evaluation of long term SHM of civil infrastructure. To pioneer the way for the suggested evaluation of variability in SHM, different SHM components, such as machine learning, condition parameters, and hypothesis testing (ML-CP-HT), are investigated. On this basis, a holistic approach for damage detection and performance evaluation is introduced and formulated theoretically. Furthermore, different technical novelties such as accumulated energies such as CPs or the triangulation-based extraction of modal parameters (TEMP) are presented.

Modal parameter extraction and extensive SHM performance evaluation is carried out for a laboratory benchmark structure with different damage scenarios, a small-scale wind turbine with reversible damage and a 5 MW offshore wind turbine. For all examples, it is shown that the proposed concept is capable of providing a common basis for the performance evaluation and comparison for a variety of different SHM realizations. Influences of different ML-instances, a variety of different CPs and HT settings on SHM performance are analyzed and guidelines for optimal settings are given. Damage detection and partial localization were achieved for the given methods. Changes in dynamics of a 5 MW offshore wind turbine due to EOCs forms another focus, which is discussed in detail.

Keywords: Structural Health Monitoring, Offshore Wind Turbines, Modal Analysis, Statistical Analysis, Machine Learning Algorithms, Condition Parameter, Hypothesis Testing.

Zusammenfassung

Die Überwachung der strukturellen Integrität von Bauwerken (engl. structural health monitoring, SHM) wurde in der Vergangenheit durch eine immer größer werdende Zahl von alternden und in von Naturkatastrophen bedrohten Regionen gelegenen Bauwerken sowie der Einführung von neuen Entwürfen und Materialien mit unbekanntem Langzeitverhalten in den Fokus von Forschung und Entwicklung gerückt. Durch ein ausgeprägtes dynamisches Verhalten und eine Vielzahl an sehr ähnlichen Bauwerken innerhalb abgelegener Windparks, begünstigen Windenergieanlagen (WEAs) die Herangehensweise zur Überwachung von dynamischen Strukturantworten.

Innerhalb der vergangenen Jahrzehnte wurde SHM an einer Vielzahl von Strukturen angewendet, meist realisiert durch das Betrachten modaler Größen wie Frequenzen und Eigenformen. In der jüngeren Vergangenheit wurden vermehrt Zustandsparameter (engl. condition parameter, CP) formuliert, welche auf Residuen zwischen Zeitreihen unterschiedlicher Systemzustände basieren. Diese bieten eine größere Sensitivität bezüglich struktureller Änderungen jedoch auch weniger Robustheit gegenüber Betriebs- und Umgebungsbedingungen. Maschinelles Lernen (ML) und Hypothesentests (HT) werden genutzt um diese unerwünschten Einflüsse zu kompensieren.

Die vorliegende Arbeit beschäftigt sich mit der Anwendung eines SHM-Konzepts, welches auch zur Bewertung von Langzeit-SHM für Bauwerke geeignet ist. Als Grundlage für die Bewertung der Variablen innerhalb des Konzepts werden mit maschinellem Lernen, Zustandsparametern und Hypothesen Tests unterschiedliche SHM Komponenten definiert. Auf dieser Basis wird ein allgemeingültiger Ansatz zur Schadensdetektion und Bewertung der Leistungsfähigkeit formuliert und theoretisch hergeleitet. Zusätzlich werden technische Neuheiten wie akkumulierte Energien als Zustandsparameter oder eine auf Triangulation basierende automatische Extraktion modaler Parameter (TEMP) eingeführt.

Die Extraktion modaler Parameter sowie die Bewertung der Leistungsfähigkeit von SHM werden anhand einer Laborstruktur, einer Klein-WEA sowie einer 5 MW offshore WEA dargestellt. Für alle Beispiele wird gezeigt, dass das vorgeschlagene Konzept eine einheitliche Basis für den Vergleich unterschiedlichster SHM Ansätze bzw. Implementierungen schafft. Es werden der Einfluss unterschiedlicher ML Realisierungen, verschiedener CPs sowie HT Einstellungen auf die SHM Performance betrachtet, auSSerden werden Anhaltswerte für die Bestimmung der unterschiedlichen Parameter dargelegt. Eine Schadensdetektion, für die Laborstruktur auch eine Lokalisierung, ist mittels der beschriebenen Methoden erfolgreich umgesetzt. Zusätzlich werden Änderungen des dynamischen Verhaltens der offshore Windenergieanlage identifiziert und diskutiert.

Schlagwörter: Zustandsüberwachung, Offshore Windenergieanlagen, Modalanalyse, Statistische Analyse, Maschinelles Lernen, Zustandsparameter, Hypothesen Tests.

Acknowledgements

Contents

List of Figures

List of Tables

Symbols and Acronyms

Acronyms

Acronym	Description
CP	**Condition parameter**
HT	**Hypothesis testing**
ML	**Machine learning**
SHM	**Structural Health Monitoring**
AANN	Auto associative neural networks
AASD	Automatic assesment of stabilization diagrams
AE	Accumulated energy
AP	Affinity propagation
AR	Auto–regressive
AUC	Area under the curve
CDF	Cumulative distribution function
CF	Cover factor
CMI(F)	Complex mode indicator (function)
CL	Center Line
DFT	Discrete Fourier transformation
DoF	Degrees of freedom
EMA	Experimental modal analysis
EOC	Environmental and operational condition
ERA	Eigensystem realization algorithm
FA	Fore-aft (mode direction)
FCM	Fuzzy c–means clustering
FEM	Finite element method
(E)FDD	(Enhanced) Frequency domain decomposition
FN	False negative
FP	False positive
FPE	Final prediction error
FT, FFT, IFFT	Fourier transformation, Fast-, Inverse-
FRF	Frequency response function
HC	Hierarchical clustering
IPR	Inter percentile range
KM	K-means (clustering)

Acronyms

Acronym	Description
LAT	Lowest astronomical tide
LCL	Lower control limits
LMS	Least mean squares
LSCF	Least-squares complex frequency-domain
LSCE	Least-squares complex exponential
MAC	Modal assurance criterion
MEP	Multi-parameter eigenvalue problem
MLE	Maximum likelihood estimator
MPC	Mode phase co-linearity
MPD	Mean phase deviation
MSD	Mahalanobis square distance
NCB	New Carquinez bridge
(AA)NN	(Auto associative) Neural Networks
OMA	Operational modal analysis
PCA	Principal component analysis
PDF	Probability density function
PSD	Power spectral density
RMS	Root mean square
ROC	Receiver operating characteristic
SK	Spectral kurtosis
SS	Side-side (mode direction)
SBC	Schwartz's Bayesian criterion
SSI (Cov/Data)	Stochastic subspace identification (covariance /data driven)
S-ML	Supervised machine learning
SVD	Singular value decomposition
SVM/SVR	Support vectors machines / regression
TEMP	Triangulation based extraction of modal parameters
TLP	Tension leg platform
UCL	Upper control limits
U-ML	Unsupervised machine learning
(V)AR	(Vector) Auto regressive
(O)WT	(Offshore) Wind turbine

Symbols

Symbol	Description
$\mathbf{A}_c, \mathbf{A}_d$	State Space System Matrix in continuous and discrete time
$\mathbf{A}_k$	VAR Coefficient matrix
$\mathbf{B}_c, \mathbf{B}_d$	State Space Input Matrix in continuous and discrete time

Symbols

Symbol	Description
$\mathbf{B}, \mathbf{B}_g$	Damping matrix and generalized damping matrix
$\mathbf{C}_c, \mathbf{C}_d$	State Space Output Matrix in continuous and discrete time
$\mathbf{D}_c, \mathbf{D}_d$	State Space Direct Throughput Matrix in continuous and discrete time
$\mathcal{D}_i$	Data set i with $\mathcal{D}_i^{\mathbf{EOC}}$ and $\mathcal{D}_i^{\mathbf{Y}}$ as EOCs and output data
$\mathcal{H}_i$	Block Hankel Matrix
$\mathbf{K}, \mathbf{K}_g$	Stiffness matrix and generalized stiffness matrix
$\mathbf{L}$	Selection matrix
$\mathbf{M}, \mathbf{M}_g$	Mass matrix and generalized mass matrix
N	Number of degrees of Freedom
$\mathbf{O}$	Extended observability matrix
I	Unity matrix
$\mathbf{R}_i$	Output covariance matrix for time shift i
$\mathbf{S}$	Singular value Matrix (PSD)
$S_{yy}(\omega), S_{xy}(\omega)$	Power spectral density
$\mathcal{S}$	Set of solution from parametric system identification procedure
$\mathcal{S}_i^p, \mathcal{S}_i^f, \mathcal{S}_i^\zeta$ and $\mathcal{S}_i^\psi$	Model order, frequency, damping and Eigenvector if i-th solution
$\mathbf{U}$	Left matrix of Singular value decomposition
$\mathbf{V}$	Right matrix of Singular value decomposition
$\mathbf{Y}$	Data matrix
$\mathbf{Y}_{(,)}$	Block-Hankel matrix
$a(i,k)$	Availability in Affinity Propagation
b_g	Generalized damping coefficient of i-th mode
$d_{f_{i,j}}$	Frequency difference between two system identification solutions
$d_{\zeta_{i,j}}$	Damping difference between two system identification solutions
$\mathbf{f}$	Force vector
f_i	i-th natural frequency
j	Complex number
k_g	Generalized stiffness coefficient of i-th mode
m	number of data channels
m_g	Generalized mass coefficient of i-th mode
n	State space model order
$\bar{n}$	Dimension of data point for clustering

Symbols

Symbol	Description
n_b, N_b	Number of data blocks for and samples in blocks for CP^γ
n_Δ	Number of triangles in triangulation
n_e	Number of frequencies in accumulated energy range
n_ω	Number of discrete frequencies in spectrum
n_{sig}	Number of significant columns
n_{is}	Number of insignificant columns
n_X	Number of entries in CP vector $n_{mathsf}X$
n_{rs}	Number of samples in rational subgroup
n_t	Number of samples in time series
$n_\mathcal{S}$	Number of solutions in $\mathcal{S}$
$\mathbf{q},\dot{\mathbf{q}},\ddot{\mathbf{q}}$	Vector of displacement, velocity and acceleration in modal coordinates
p	VAR-Model order or number of shifts in SSI block Hankel Matrix
$r(i,k)$	Responsibility in Affinity Propagation
$s(i,k)$	Similarity in Affinity Propagation
$\mathbf{u},\dot{\mathbf{u}},\ddot{\mathbf{u}}$	Vector of displacement, velocity and acceleration
$\mathbf{v}$	Measurement noise (state space model)
$\mathbf{w}$	Process noise (state space model)
$\mathbf{x}$	State vector
x	Variable vector
$\mathbf{y}$	State space output vector
$\mathbf{y}_{(i)}$	Data channel
λ	Eigenvalue
Λ	Spectral matrix, diagonal matrix holding the eigenvalues
Φ	Mass-normalized modal matrix
$\Phi_{yy}(\tau),\Phi_{xy}(\tau)$	Autocorrelation, Cross correlation
$\beta_{i,j}$	Angle in complex plane between Eigenvector i and entry j of Eigenvetor i
χ^2	Chi-square test statistic
δ	Logarithmic decrement
ε	Gaussian noise term (VAR-model)
$\varkappa_j$	Machine learning output vector
ω_{0i}	Circular frequency
ω_{Di}	Damped circular frequency
$\psi, |\psi|$	Eigenvector, mode shape
Ψ	Modal matrix, holding the eigenvectors
Γ	Kalmann state matrix

Symbols

Symbol	Description
ζ	Residual damage vector
ζ_i	Damping ratio of i-th mode

Operators

Operator	Description
$E\left[\bullet\right]$	Expectation Value
$E\left(\bullet\vert\bullet\right)$	Orthogonal projection
$F\{\bullet\}$	Fourier Transformation
$Im\left(\bullet\right)$	Imaginary part of a complex number
$Re\left(\bullet\right)$	Real part of a complex number
$\vert\bullet\vert$	Absolute value
$\bullet^T$	Transpose
$\bullet_i$	Variable for i-th mode or time shift for $\mathbf{R}$
$\bullet_k$	Variable at discrete time instance k
$\hat{\bullet}$	Estimate
$\bullet^{-1}$	Inverse
$\bullet^*$	Complex conjugate
$\bullet^\dagger$	Moore-Penrose pseudo-inverse
$\hat{\bullet}$	Variable estimate from a finite number of values

1 Introduction

1.1 Motivation

Since potential risks for human lives and major economic impacts can result from failure, health monitoring of distinct civil and industrial infrastructure has been a significant task over the course of the last few decades. Conventional approaches based on visual inspection of cracks and corrosion, or the monitoring of long-term static displacements are frequently applied. Non-destructive testing procedures such as ultrasonic measurements have also become important tools for observations. Structural health monitoring (SHM) was brought into the focus of research and industry by an ever increasing amount of aging structures, a large number of buildings in seismic active regions, and the introduction of high performance materials with unknown long term behavior. Originating from aerospace and military, where very expensive structures or large numbers of units are analyzed, SHM focuses on the continuous monitoring of dynamic structural responses and linking them to structural changes. This goal can be achieved through various monitoring approaches that track different physical quantities such as accelerations, displacements, guided waves or acoustic emission, to name only a few.

This work focuses on the application of a new SHM framework for long term observation of civil infrastructure. Since, alongside solar- and hydro-power, wind energy plays an important role in the renewable energy sector, on- and offshore wind turbines (WTs) have drawn major attention during the last decade. Additionally, an increase of 'green' energy is a declared goal of a variety of countries. Together with skyscrapers or bridges, WTs form systems with a distinct dynamic behavior due to their slender structures and a large mass concentration at the nacelle. Further, many identical turbines are erected within wind farms, which is rather atypical for conventional civil engineering structures and an advantage for SHM where concepts can be copied and result extrapolated. Since a large part of the overall costs for WTs lies in operation and maintenance, optimizing service intervals through SHM can help reduce energy prices. With a large number of onshore plants and a rapidly increasing number of offshore installations with weather dependent accessibility, the need for (remote) monitoring of these structures is evident.

The following sections will provide an introduction to SHM for civil engineering structures as well as a state of the art review on literature for the applied procedures and methods originating from diverse scientific fields. While Section 1.2 gives a general overview of the topic, Section 1.3 investigates different SHM components. This section's organization goes along the author's framework which divides all SHM procedures into main blocks: Data acquisition, machine learning (ML), condition parameters (CPs), and hypothesis testing (HT). The outline and organization of this thesis will be given at the end of this chapter in Section 1.7.

1.2 Monitoring Civil Engineering Structures

In the field of monitoring, the notation condition monitoring (CM) exists alongside SHM. Generally, CM refers to the monitoring of electrical systems and (rotating) machinery while SHM considers approaches for load-bearing parts of aerospace and civil structures. Hence, both (CM and SHM) might be applied to different components of the same overall structure. This applies especially for WTs as power generation units where electrical components and rotating machinery form an important part. CM solutions for rotating machinery, gears, bearings, and electrical components are taken from 'conventional' fields of industry, where different systems have already been introduced to the market. In contrast, SHM for WT blades and the support structure below the nacelle forms a rather new scientific field. This is also valid for large scale engineering structures such as bridges or skyscrapers. Even though many of the procedures presented are applicable to both fields, CM and SHM, this work will focus on SHM and hence use this acronym subsequently.

Originating from the field of modal analysis, SHM has developed quickly during the last two decades and many fields of application have been introduced. Most approaches target the main *SHM-levels* which can be understood in a successive manner: detection, localization, quantification and forecast of damage (see Rytter [166]). Within these four general steps, damage detection and localization can be purely based on measurements while quantification and prediction necessitate a numerical model. While this is a typical description of SHM-goals, their implementation is subject to research and can be realized in different ways.

Further, fundamental axioms of SHM were contributed by Worden Worden et al. [211], condensing knowledge gained over many years into general statements. This work tries to underline and extend axiom II, which states that "the assessment of damage requires a comparison between two system states" [209]. The suggested extension leads to "'the assessment (...) requires a comparison of' *relevant* 'system states'" and accordingly necessitates machine learning procedures to group states with the given data instances by environmental and operational conditions (EOCs).

This becomes important for commercial SHM applications on large scale structures and especially for WTs, since there is not only one certain healthy state but many different ones under varying EOCs. Hence, for offshore wind turbines (OWTs) a learning phase is necessitated to cover the differing behavior over typical operation and yearly seasons. Next, type, location, and extent of damage can vary strongly which leads to the conclusion that a single CP might not be sufficient for a good SHM performance. A CP can be any metric or value extracted from the measured time series with the goal of indicating a change in the structures dynamic behaviour. Last but not least, to be of use for owners and operators, the parameters monitored must be put into a probabilistic context and a clear layout. All of these steps are targeted within this work.

It is intuitive that EOC-influences may vary strongly depending on the analyzed structure. Early work focused on the changes in modal parameters of bridges, before more abstract CPs were introduced. Extensive reviews on SHM techniques have been carried out [45, 48, 49, 54–56, 184] and dependencies of CPs and dynamic behavior on EOCs were investigated [46, 118, 146]. Especially temperatures below freezing show strong influence on some bridges [142]. Fassois summarizes

many approaches in SHM with a strongly statistical orientation, pointing out dependencies and theoretical distribution characteristics [58]. A good overview on machine learning techniques and influencing EOCs can be found in [176]. Worden and Manson [209] provide a state of the art review that is based on Rytters SHM-steps, stating many examples for different objectives. One focus is put on support vector machines. Another current paper that summarizes SHM techniques with a focus on control charts and sensor validation was written by Kullaa [99]. Linear and non-linear models for EOC consideration are distinguished, giving several real world examples. Figueiredo [60] uses one CP and four machine learning techniques as a comparison. Discussion of SHM on bridges is collected by Ko and Ni [96]. Recently Farrar and Worden published a book that states the machine learning aspects of SHM, covering extensive examples and many aspects of SHM in a detailed manner [57]. The focus on machine learning or data normalization reflects a large number of conference contributions to the International- and European Workshop on Structural Health Monitoring in these fields.

Furthermore, a differentiation between local and global monitoring approaches exists. Even though there is no clear differentiation between these two fields, local monitoring refers mostly to the observation of substructures. It usually goes along with higher sampling frequencies since local, high-frequency modes of structures and possibly artificial excitation are used. For WTs, local attempts address specific parts of the structure such as bolted joints, the wave impact zone, or grouted connections. In some cases even special sensing devices are applied. Global approaches consider large parts or the whole structure and use naturally occurring excitation sources or a forced excitation. These techniques are mostly vibration based, generally focusing on changes in the dynamic behavior, which might be influenced by local mechanisms.

Another distinction can be made between active and passive approaches. Active-sensing approaches use actuators to excite a structure and work predominantly on a local scale. Passive monitoring uses natural excitation under operational conditions. Hence, most global approaches are passive, as the presented work in this thesis. Nevertheless, most extracted condition parameters, as well as machine learning techniques and hypothesis testing, are applicable to local and global SHM.

1.3 State of the Art for SHM-Components

Putting the problem of monitoring large scale structures into a general context, the next sections will discuss the present literature along the introduced framework, which is introduced in detail in Chapter 3.4. The sections will follow this framework, displaying existing techniques for the single proposed steps: starting with machine learning (which might be included passively or unintentionally) followed by condition parameters (these will always explicitly be present in a SHM scheme) and closing with hypothesis testing, which is utilized to draw a decision about the structure's state. The framework could be understood as a menu, where one can choose between different option in each step (ML-CP-HT). Automated extraction of modal parameters, as a specific group of CPs, is handled separately in Chapter 1.5. Accordingly, references might appear in several sections under different points of view.

1.3.1 Machine Learning

Machine learning (ML) as a term for retrieving coherence and relations within data is widely used in computer science, engineering, mathematics, and statistics. Whenever data is collected and stored and underlying patterns within the data need to be revealed, ML provides tools to address these tasks. In SHM, it is desired to reveal the dependency of condition parameters on EOCs as formulated in Equation (3.5) or more generally in Equation (3.6). In general, machine learning is understood as a technique to train or learn the structure's behavior.

On the one hand, the problem is addressed through directly modeling the relationship $f(\bullet)$, using in- and output variables to perform regression or classification analysis (supervised machine learning, S-ML). On the other hand, only input data is used for clustering (unsupervised machine learning, U-ML). In this case input variables are attributes of the data instances as EOCs, output variables are usually CPs. The former results in predictive models, while the latter groups the data points. In SHM, single data records (data instances) are understood as data points, which can be clustered by their attributes. Commonly, the attributes are additionally recorded averaged EOCs such as wind speed, temperature, or rotor speed, but could also be values derived from the time series. In U-ML clustering can be used to decompose the training sets into several clusters. Evaluation of the goal variables is then carried out within these clusters. A selection of examples for different ML techniques can be found in Worden and Manson [209] and Farrar and Worden [57]. The following section will give an overview of some machine learning techniques present in the literature.

Distance Measures

A very direct approach to machine learning can be achieved through distance measures as Euclidean distance or the Mahalanobis square distance (MSD) in a multidimensional (CP or EOC) space. The reference space is built using CPs from training data instances ($\mathcal{Y}$) in healthy conditions. In the testing-phase, where the structure's state is unknown, the distance between the mean of $\mathcal{Y}$ and the new CPs is calculated. These distance measures could also be interpreted as relative CPs. For later hypothesis testing, distances between mean and all training sets are usually calculated and a percentile value of this parameter distribution is chosen as a threshold. Theoretically, the distance to CPs from a damaged state or states under new EOCs is larger than the observed values. Distance measures can also be used subsequently to clustering.

Figueiredo et al. [60] stack ten AR-coefficients from four acceleration sensors as CPs from measurements on a three story laboratory structure with base excitation to detect damage through MSD without EOC measurements. Hu [88, 89] uses the MSD in combination with a residual from the linear mapping of natural frequencies from footbridges to calculate CPs. Again, no EOCs are considered. The minimum Euclidean distance between transmissibility-functions with a foregoing negative selection approach is used in [188] to detect damage on a simulated offshore structure and a numerical aircraft wing, also without EOC measurements. In [177] MSD is used with AR/ARX coefficients from strain signals to perform SHM on a patrol boat. Further, the MSD is used with AR-coefficients from a concrete beam under differing temperature loading in [35].

Regression

Regression analysis forms a large field including linear-, polynomial- and AR-models, support vector machines (SVM) and neural networks. In general, the relation between input and output is iteratively modeled by minimizing an objective function (e.g. through least mean squares (LMS)). Applications range across many research fields and technical areas, hence only a few applications, with a focus on SHM, are given here. AR-models for response time series were already mentioned in the condition parameter section (1.3.2). Regression methods can be used to model the dependency between different CPs or between EOCs (input) and CP.

A linear filter model is used to predict the first two modal frequencies by Sohn [178]. Using input and output data, Cross et al. [40] utilize response surface models with six EOCs as input to model the first and second modal frequency of a suspension bridge. Non-linear polynomial models are used to approximate the dependencies of up to ten temperature measurements on the modal frequencies of a footbridge in [129]. Variations in modal frequencies from the long-span New Carquinez bridge due to traffic load and daily variations are captured by linear and polynomial models in [221]. In [108] linear regression is used to model the frequency-temperature dependency of a curved concrete highway bridge.

Support vectors machines or regression (SVM/SVR) form a rather new and powerful field in SHM. Parameters in a given parameter space can be separated or fitted through the so-called *kernel trick*: data points or distances are projected into a high dimensional space where separation can be done through a plane. It results in non-parametric estimates for output variables in a continuous parameter space. The projection functional is called the kernel-function and many different types exist (e.g. Gaussian or radial basis kernel). The choice of the kernel parameters is subject to regression and neither clear rules for the choice of kernel functions nor their parameters exist. A brief introduction to the topic, including the application with inspection panels of an aircraft wing is given in [209]. Least-squares (LS-)SVM is an extension of SVM where a cost function is introduced to iteratively weight the input data points by means of distances to the estimate [189]. Byon et al. use LS-SVM to detect abnormalities in WT power production [212].

Another popular and well-developed group of regression techniques are artificial neural networks (NN) [18, 82]. The basic idea of neural networks is to express an unknown relationship between input and output variables as in (3.5) through several linear (or nonlinear) relations between different hidden layers (e.g. mapping-, bottleneck- and de-mapping layer)[113]. In the context of SHM, neural networks can be used with or without EOC measures as inputs. If the neglection of EOCs is desired, the goal CP vector is simply used as input and output to train the model. All CPs can potentially be used to feed this procedure. Condition measures can either be certain inner parameters of the neural network, if the network is newly trained and in the testing-phase, or a residue between input and output CPs, if parameters from the testing-phase are used to simulate new CPs based on a trained network.

In [181–183], AR-coefficients (AR(50),ARX(5,5)) are used as CPs are estimated by NN for every measurement node of a mass-spring-chain. ARX models are used by Peeters et al. to model temperature dependent modal frequencies [142, 143]. Auto-associative neural networks (AANN)

are used to train a model of the AR-coefficients with respect to themselves and evaluate the bottle-neck layer coefficients to detect changes in spring stiffness [181, 182]; no EOC measure is taken. An AANN is also used in [60] in combination with AR-coefficients, here the difference between input and estimate is investigated in the testing-phase. Ko et al. use linear and non-linear regression techniques as neural networks and SVM [96] to link the temperature and modal frequencies of a suspension bridge.

Clustering

The automatic partition of a point set into a number of groups by certain attributes is a central task in many scientific fields. In the case of SHM, the point cloud is defined by meta data (EOCs and/or CPs) for each data instance in the training phase. In general, clustering procedures can be divided into hierarchical and non-hierarchical approaches. The former procedure results in tree-like structures, while the latter forms separated clusters. A manual classification is also possible in many cases.

Hierarchical clustering (HC) approaches can be considered as one of the most straight forward approaches to clustering. Depending on the chosen approach, each data point forms its own initial cluster and these clusters are merged successively (*agglomerative*) or a single cluster exists at the initial step and is then divided (*divisive*). Division or merging of clusters is defined by similarities between all data points. One linkage is added (or erased) during each step. Depending on the similarity definition, different procedures for data point assignment exist: single linkage, complete linkage, average linkage, Ward's method and centroid method [78]. Two major drawbacks for HC exist: a high computational cost and a user defined threshold for the resulting trees (dendrograms), which defines a cutting level and hence the number of resulting, separate clusters.

A standard approach for non-hierarchical methods is k-centers-clustering, where k points are chosen at random from the data instance to be exemplars (centers) for k sub sets [18, 114]. The remaining points are assigned to the centers so as to reduce the summed square error, usually Euclidean distance, between exemplars and points. Another commonly used procedure is k-means-clustering (KM) [18, 51, 131]. Here, the distance between the cluster centroids and corresponding points is minimized. Both procedures are quite sensitive to the initial set of exemplars/centroids and are therefore usually repeated many times with varying sets of exemplars to increase the chance of finding the global minimum. One of the major drawbacks of these methods is the fixed number of centers/centroids that has to be chosen initially by the user.

Another group of approaches which assign each data point to all centers with a certain membership rate rather than to a single cluster, can be seen in fuzzy clustering. The most common approach is the fuzzy c-means clustering (FCM) [17]. It works as c-means clustering but every data instance is assigned to every cluster with a weight, defined by the distance to the cluster center. Two major drawbacks are that FCM can only deal with hyper spherical partitions and due to its Euclidean distance metric, FCM leads to equally important clusters with similar point densities [168]. Extensions such as FCM Gustafson-Kessel (FCM GK) [74] and FCM Gath-Geva (FCM GG) [69] try to overcome these with the usage of MSD and the assumption that data points

originate from different Gaussian normal distributions, respectively [168].

The generic algorithm [86] is an evolution based approach that simulates evolution using a *survival of the fittest* technique. A population is evolved over time and mutations are possible for a random set of members. It can be used as a classification algorithm or initiation for FCM as presented in [168]. The procedure has a high level of computational effort and complex functionality must be defined for an application.

In the presented work, a rather new non-hierarchical method is used. It was created by Frey and Dueck [63] and Dueck [52], called affinity propagation (AP). It solves the clustering problem by passing information (or messages) between data points without the need for a predefined number of centers. The number of resulting clusters is instead influenced by preferences, which are set for the input data points. It is faster than standard clustering approaches. Examples for a variety of fields are given in [63] and it was introduced to the field of SHM in [77]. One run of AP is able to provide better results than several thousand runs of standard classification procedures as shown in [52, 63, 77]. First, similarities between points are calculated. In the standard case these are negative Euclidean distances but may be potentially any measure between two points, even allowing for $\overline{AB} \neq \overline{BA}$. With these similarities, indicating "how well the data point with index k is suited to be the exemplar for point i" [63], the iterative procedure is run. During the iterations, two different messages are passed between the data points. One is the responsibility $r(i, k)$, sent from point i to candidate exemplar k. It "reflects the accumulated evidence for how well-suited point k is to serve as the exemplar for point i, taking into account other potential exemplars for point i" [63]. In contrast, the availability, $a(i, k)$ "from candidate exemplar k to point i, reflects the accumulated evidence for how appropriate it would be for point i to choose point k as exemplar, taking into account the support from other points that point k should be an exemplar". Hence, there is one measure $r(i, k)$ from point to candidate giving support and one from candidate to point $a(i, k)$ collecting support. The iterative procedure is updated and stops after a certain number of iterations without changes in clusters. It provides excellent results, proving to perform faster and leading to better classifications than k-means [52, 63, 77].

Conclusion

Many recent publications utilize ML techniques that omit EOC measurements and hence indirectly use a single cluster for the entire training-phase. In [60] MSD proves to have the best overall performance compared to neural networks, factor analysis and SVD for an experimental structure under unmeasured EOC changes and damage. Simple implementation and cheap calculations support this statement. It is emphasized that there is no guarantee for CP changes as a result of actual damage not being masked or mimicked by EOC variations, which is implicitly assumed in SHM approaches that omit EOCs. It is stated by Farrar and Worden that "if the damage produces changes in the system's dynamic response characteristics that are similar to those produced by the source of variability, it is not at all guaranteed that these algorithms (algorithms omitting EOC inputs, author's note) will be able to separate changes in the features caused by damage from changes caused by EOVs" (environmental and operational variations) ([57], p.428).

Furthermore, if residues are used as CPs, their quality strongly depends on the reference data instances. If no information about the system state is used to calculate these residues, the monitoring performance will decrease. SVR analysis, with its kernel-functions, provides a powerful tool if input and output data is available. If the input-parameter space has gaps, the performance suffers. If residues should also be included in the SHM framework, an unsupervised ML technique is desired, since references for the residual CPs need to be defined. AP typically shows superior clustering performance compared to KM and its fast implementation serves an optimal algorithm for the given tasks [52, 63, 77]. Hence, it will be used next to a references classification with a single cluster in the training phase along with manual classifications. The different ML types are also briefly summarized in Table 1.1.

1.3.2 Condition Parameters

As sensors "cannot measure damage" [209], damage sensitive features or condition parameters have to be extracted from the time signals through signal processing. In addition, no extracted parameter at a certain time will measure damage directly until it is compared to at least a single similar parameter from an earlier instant of time.

In general, two kinds of condition parameters must be distinguished: Parameters that can be derived from a single data instance directly (dubbed *absolute* CPs), such as modal parameters, statistical values or AR-coefficients, and parameters that need by definition (at least) a second data instance for their estimation (dubbed *relative* CPs) – usually referred to as residues. This does not contradict the above stated axiom since both need a reference to act as condition parameters later on. The following paragraphs will state some condition parameters, starting from basic statistical values to more sophisticated residues; theoretical insight of applied parameters will be given in section 2. Finding and applying a parameter that is sensitive to damage and preferably insensitive to EOCs is one of the core tasks in SHM. The field of condition parameters is vital and the utilized parameters originate from a broad field of scientific areas.

Table 1.1: Overview of ML types

ML type	Pros	Cons	References
Distance measures	No input variables; Fast computation; Can be used to fuse different CPs	Only applicable to absolute CPs; Might mask damaged states	[35, 60, 88, 89, 177, 188]
Regression	Possibly fast computation; Might reveal physical insight	Difficult handling of realtive CPs; Definition of Kernel function; Def. of NN architecture; Def. of model order	[18, 40, 60, 82, 96, 108, 113, 129, 142, 143, 178, 181–183, 189, 209, 212, 221]
Clustering	Fast computation; Handling of relative and absolute CPs; Physical traceability	Definition of cluster number (or preference for AP)	[17, 18, 51, 52, 63, 69, 74, 77, 78, 86, 114, 131, 168, 168]

Statistical Values

Two well known statistical values for time series are the mean value and standard deviation (the first and second statistical moment). Both can be used to describe signal characteristics of dynamic outputs. The former is usually zero for acceleration signals but can be of use for strain or displacement. The third moment is called skewness and represents the asymmetry of the probability density function (PDF) for a given variable. The fourth statistical moment, the kurtosis, reflects the peakness of a given signal. Assuming that structural damage might result in impulse loading or non-linearity, the kurtosis can be used as damage indicator, "providing a measure of distance to gaussianity." [203]. Values larger than three indicate a peaked distribution with more values far from the mean. Further, a time series can be divided into non-overlapping blocks and from the different frequency-domain representations, a spectral kurtosis (SK) can be calculated for each frequency bin. Different fractions of kurtosis can be identified with the following goal values: random signal ($SK = 0$), stationary harmonic ($SK = -1$), and non-stationary ($SK > 0$) [97] . Another statistical value, originating from the significant wave height used in oceanography, is the mean of the highest third of values [87]. Further, condition parameters, which are of more graphical/visual nature, can be drawn from the PDF functions of recorded time series. Most processes can be assumed to be normally distributed and hence, PDFs of recorded acceleration values can be plotted against normal distributions to detect deviations [59]. Another approach is the fitting of distributions for a later comparison using a kernel density estimator [20, 59, 171]. In general, extreme value statistics play a major role in SHM to detect outliers and, Depending on the investigated CP, the analysis of a generalized extreme values distribution might become necessary.

These statistical approaches can be applied to structural responses such as accelerations or strain measurements, and represent well traceable approaches. Yet often they might not be able to capture structural changes.

Matrix Decompositions

To make use of matrix decompositions, a matrix is built from measured time series or CPs derived from those. After the decomposition, resulting values can be chosen to build a probabilistic model and hence, to feed hypothesis testing. One of the most famous matrix decompositions is the singular value decomposition (SVD). It can also be used to calculate the matrices needed for principal component analysis (PCA). In the context of SHM, the state matrix $\mathcal{Y}$ in Equation (2.1) is subject to SVD and its rank is used as an index of structural changes [165]. When a new column from a possibly damaged state is added to the state matrix, the rank of this new matrix is supposed to be similar to the rank of the state matrix for a healthy structure. In practice, noise and unknown influences complicate a clear estimation of the matrix's ranks.

Ruolto et al. [165] apply the rank analysis from SVD to a simulated and an experimental cantilever beam, using frequency response functions as CPs. In [60] SVD is also used for SHM in the example stated above. In [46] PCA is used on CP vectors built from modal parameters and peak indicators from modal filters to distinguish between temperature gradient changes and

stiffness reduction on a numerical bridge model. PCA as a clustering technique based on modal frequencies as CPs derived from a numerical and physical model and the well-known Z24-bridge is applied in [213, 214]. Worden et al. [210] use PCA for coefficients of auto-regressive models after manual clustering data instances by temperature as a numerical example. Kullaa [100] uses estimator ratios from single sensors, each modeled as a Gaussian process, as CPs for simulated data and a physical wooden bridge model. These are further analyzed by PCA and control charts; no EOCs are included in the procedure.

Modal Parameters

The estimation of modal parameters, e.g. modal-frequency, -damping and mode shape, originates from mechanical engineering and has been a well established field for many decades. Small scale structures or parts of complex (aerospace) structures were initially investigated. In experimental modal analysis (EMA), modal parameters are calculated through the measurement of dynamic structural responses occurring due to one or several measured inputs. A broad review of methods and theory is collected in Ewins [53] and Maia et al. [119]. When considering large scale structures such as dams, bridges, sky scrapers or wind turbines, a forced excitation necessitates heavy equipment and a measurement of the exact loading is very difficult or mostly impossible. To combat this, operational modal analysis (OMA), also called output-only modal analysis, in which only structural responses are used, has been gaining popularity during the past decade [27]. This was strongly supported by the introduction of subspace-based methods. Since modal properties such as the modal-frequency, are directly linked to physical values like mass and stiffness, it is self-evident to use these values for the identification of structural changes.

The estimation of modal parameters is a large field with many different approaches in the time and frequency domain. An early, straight forward approach is *peak-picking*, where peaks in a frequency spectrum are simply visually identified as modes. Damping can be approximated by the width of the peaks and mode shapes result from amplitudes of, and phase angles between, sensors. A sort of extension to this approach is the frequency domain decomposition (FDD), where the singular value decomposition (SVD) of a tensor with auto and cross spectra from different sensors is computed for each frequency bin. When the singular values are plotted over frequency, again peaks can be identified and the left singular matrix holds according mode shapes [25, 26]. Application can be found in [185] and [136]. Automation attempts for this method have also been published [28].

Hu uses modal frequencies from footbridges as CPs [88], Lui investigates a curved highway bridge [108] and in Sohn [178] the first two modal frequencies from the Alamosa Canyon Bridge is used to show a temperature dependency. The dynamic behavior of the Z24 highway bridge is investigated among others in [142, 143]. In [118] modal frequencies of a suspension bridge are linked to wind speed and hence vibration amplitudes. Further studies on modal frequency changes of large scale suspension bridges were carried out in [96, 220, 221]. Kraemer [98] investigates this aspect for an onshore WT.

Originating from the field of economics, auto-regressive (AR) models and their extensions have

been applied to a wide field of applications during the last few decades. OMA is one of these fields where AR-models have proven to be of great value. Time series of structural responses (e.g. accelerations) are used as the basis for modeling. In general, AR-models describe a certain datum using weighted predecessors of at least one channel. All different derivations of this model class have this basic idea in common. A detailed insight into the different approaches can be found in [112, 132]. If a certain time series is described by an AR-model, it is possible to perform a prognosis of future time steps and to extract the system's (modal) properties [8, 19, 23, 133]. When several data channels are used, the models are called Vector-Auto-Regressive (VAR). For example, Kraemer [97] applied VAR-Models for the identification of modal parameters for a prototype of an offshore WT (installed onshore) successfully. If desired, the use of Auto-Regressive-Moving-Average(ARMA)-Models could improve the quality of prediction for a certain model order. Furthermore Time Variant-ARMA-Models (TARMA) with time-varying coefficients modeled by sine and cosine can be used to cover time-varying system properties [10, 58, 151, 186]. However, the involved computations are rather expensive and equally good results can be achieved with AR-models of a higher order [146].

Alongside an estimation of modal parameters, VAR-coefficients can also be used directly as condition parameters if compared between different data instances, resulting in residues [8, 59, 60, 177]. For this purpose, AR residues of separate channels can be combined or the VAR-coefficient matrix is stacked into a vector. In [183] AR-coefficients are used to train a neural-network for an EOC independent SHM procedure and in [35] AR coefficients are used with Mahalanobis square distances on a concrete beam. Wang and Ong [205] analyse AR-coefficients, derived for single sensors, to detect damage in a reinforced concrete beam. In [179], AR-coefficients are extracted from data relating to concrete columns.

Stochastic subspace identification (SSI) is a data driven time domain system identification method using output-only data to estimate a stochastic state space model. It was introduced by van Overschee and de Moor [197, 198] and is based on the Eigensystem Realization Algorithm (ERA) by Juang [92][1]. It is considered to be a very powerful tool in system identification [24]. During the last two decades the method has widely been used in the field of civil and mechanical engineering and has been able to provide excellent results (see e.g. [40, 77, 97, 123, 124]). In general, two different schemes of the SSI exist. One is the covariance driven SSI (SSI-COV), the other a data driven SSI (SSI-Data) formulation [142, 144, 146]. Both methods are derived from a state space system with random white noise inputs. For high model orders, SSI performs faster than VAR procedures. Another distinct advantage is the fact that many different model orders can be derived from a single block matrix without the need for further matrix decompositions, resulting in very fast computation. Application of SSI can be found also in [46] and [40] where SSI-Data is used to calculate the modal properties of a long span suspension bridge. SSI-COV [88] and SSI-Data [129] were also utilized to extract modal frequencies from footbridges. Peeters and De Roeck [142] apply a reference-based formulation of SSI-COV to identify the modal parameters

---

1   The original code, performing excellent after correction of a few Matlab expressions, can be found on floppy disk in [198].

of a steel mast.

For both, SSI and VAR models, it holds that if the assumption of white noise excitation is violated, frequency parts of the colored noise will occur in the VAR/SSI solutions. In practice, this will always be the case since excitation such as wind and waves will have colored spectra. For WTs, also excitations from blades, resulting from each blade passing the main column, and from blade-imbalances, have a distinct frequency that depends on the rotor speed. Due to its fast computation and possible automation, SSI-Data is used for (automated) system identification in this work (see 2.3).

Due to their direct connection to the structure's stiffness and mass, the usage of modal parameters as damage indicators can be counted among the fist approaches in SHM. The variation of modal frequencies over time is one of the most common schemes. Also mode shapes were used to identify damage [95] and their derivatives have been used for damage localization [137, 204]. A distinct drawback of the usage of mode shapes is their more erroneous estimation compared to frequencies and the large number of sensors needed for a good solution.

Nevertheless, even though many other condition parameters are available today, modal parameters still play a key role in SHM and are also justified by their usage in the updating, validation and fitting of numerical models [75, 163], which play a key role in modern engineering. These updated models can also potentially be used in higher SHM-levels such as localization and quantification. The problem of the automated extraction of modal parameters, which forms a vital field in current research, is addressed in 3.2.

Residuals

A very instinctive way of calculating a residual is the comparison of two frequency spectra from the same location and structure. Fassois normalizes time series by mean and standard deviation to calculate different response spectra [58]. These can be compared and their residual follows a Gaussian distribution. Hence, hypothesis testing for each frequency bin can be directly applied.

The minimum Euclidean distance between transmissibility-functions with a foregoing negative selection approach is used in [188] to detect damage to a simulated offshore structure and a numerical aircraft wing, without EOC measurements. Ruotolo uses frequency response functions from a cantilevered beam [165] to detect damage.

For more advanced condition parameters from VAR-models, a new time series is modelled by AR-coefficients gathered at one (or several) past time series[1] and the difference between measurement and estimate is calculated, resulting in a residue. Two condition indicators are derived from this residue: One is the (fitted) coefficient of determination according to Neter [132], basically summing the error, taking the number of channels and samples into account. The second condition parameter is based on the *M-Test* according to Box [21, 187]. The residue co-variance matrix is built and an M-Test compares the consistency of distributions of the co-variance matrix with the distributions of one (or several) reference co-variance matrice(s) [97]. Both parameters

---

1   Reference data instances can be defined through machine learning.

are potential candidates for a long term SHM procedure but are also strongly dependent on EOCs. Hence, they have to be combined with machine learning as presented later (see Chapter 3).

The block-Hankel matrix of SSI-COV can be used for the estimation of residues. Similarly to the AR based residue, the residue derived from SSI compares system dynamics from an earlier time instance to the ones from the current data instance. The residue was introduced by Basseville et al. [13] and Zhang and Basseville [219] and can be directly derived from a co-variance block-Hankel matrix built from measured output signals. To calculate the desired parameter, the *nullspace* of one Hankel matrix of a current measurement is compared to one (or several averaged) from reference data instance(s). The *nullspace* indirectly represents the underlying dynamic (state space) system, a change in the structure's dynamics will result in a differing *nullspace* and hence a residue other than zero. Again, reference data instances are dependent on the machine learning in use. First a *left nullspace* is calculated for the reference data instance, if several data instances are used, the *nullspaces* are averaged. For the actual data instance, the co-variance block Hankel matrix is calculated and multiplied with the reference *nullspace*, the resulting matrix is stacked to a vector and a multidimensional statistical test is performed on this variable to see if its means differ from zero [13, 84, 97]. Kraemer applies this parameter in combination with a manual classification to an onshore wind turbine [97]. The parameter is sensitive to EOCs and hence data classification is very important in its application. A potentially more robust version of this attempt was presented recently in [50].

Accumulated Energy

Accumulated energy (AE) describes the normalized integral of power spectral densities over the measured frequency range. Accordingly energy distributions over the inspected frequency range can be visualized by AE. The parameter was used for shape analysis [41] and to characterize earthquakes [192]. Accumulated energy from frequency spectra of accelerometers (not power spectral densities) was used within the IRIS - Industrial Safety and life cycle engineering project. Wenzel [208] uses AE over time to identify changes in bridge dynamics visually and to track the AE centroid's position over time. Different demolitions were artificially introduced to the "S101 Overpass" close to Reibersdorf in Austria and the spectral distribution between 0 and 250 Hz was analyzed. Certain energy levels for AE from PSDs are linked to frequencies as CPs in [77]. Obviously, all CPs based on spectra strongly depend on the given measurement set-up, that is, the sampling frequency, recording time and measuring chain characteristics.

Conclusion

It is the author's belief that, similar to health checks for human beings, not a single indicator will resolve all problems in SHM. In other words, no parameter will be sensitive to all damage cases while being robust against all EOC variations and ultimately fulfill all needs of the owners and operators of WTs or large scale structures.

In presenting a link to numerical models and being of distinct physical meaning, modal parameters must be understood as standard parameters. Residues play an important role and

have the intrinsic advantage of analyzing the whole (measured) frequency spectrum rather than single maxima (modal parameters) and hence do not imply that abnormalities will manifest them-selves in a certain frequency range of the response spectrum. Accumulated energies have this advantage in common. Consequently, statistical values and modal parameters will be used along with residues and AE for an SHM system in the presented work. The different CPs are also briefly summarized in Table 1.2. As mentioned above, CPs must be supported by machine learning techniques and hypothesis testing to complete the SHM-scheme. Some available technique will be presented in the following section.

1.3.3 Hypothesis Testing

Setting up a hypothesis about a phenomenon is essential to all fields of science. The process of evaluating these hypotheses is generally dubbed hypothesis testing (HT). A philosophical question arising from these tests is: can a hypothesis ever be *accepted*, or in contrast, only be *rejected* by a contrary observation? In test set-ups it will never be possible to investigate the complete set of realizations or exemplars and hence accept the stated hypothesis. This is often illustrated by the black swan theory: One can watch white swans for a lifetime but never be sure that there are only white swans, while by seeing one black swan, the hypothesis of there being only white swans is rejected [193]. Recently, Bayesian theory, where one can gain knowledge about the entity of events through prior observations, opened a new, contrasting field to the existing points of view [73].

In SHM, the term hypothesis testing is used to indicate that a decision about the current

Table 1.2: Overview of CP types

CP type	Pros	Cons	References
Time series statistics	Fast computation; (mostly) no input variables; useful for sensor fault detection	Insensitive to (smal) structural damage	[20, 59, 87, 97, 171, 203]
Matrix decompositions	Fast computation; (mostly) no input variables	Insensitive to (smal) structural damage	[46, 60, 100, 165, 210, 213, 214]
Modal parameters	Physical meaning; Useful for model updating	Difficult to automate extraction; Insensitive to (small) damage	[27, 53, 88, 96, 98, 108, 118, 119, 142, 143, 178, 220, 221]
SSI residuals	Very sensitive to damage	Abstract physical interpretation; very sensitive to EOCs; difficult to determine input variables	[13, 13, 84, 97, 219]
VAR residuals	Very sensitive to damage	Abstract physical interpretation; very sensitive to EOCs	[21, 58, 97, 132, 165, 187, 188]
Accumulated energy	Physical interpretation; Sensitive to damage; fast computation	Sensitive to EOCs; Dependent on sampling frequency and record time	[41, 77, 192, 208]

system state is extracted from data. Namely, if the system is in a normal or abnormal state, $\mathcal{H}_0$- and $\mathcal{H}_1$-hypothesis respectively, where abnormal might mean damaged or unobserved till the given point of time. Through the implementation of machine learning, the boundaries for testing depend on EOCs. If a single cluster is used, all data instances are evaluated by the same boundaries.

Coming to a decision about the structure's current state should be the final goal of any SHM-system or framework. The previously described approaches and methods provide the tools to divide a database into homogeneous groups and further to extract condition parameters from each data instance. Accordingly, the final step is a comparison of condition parameters from a new data instance with the condition parameters of an according group of data instances during training. As stated in Figure 3.10, hypothesis tests for each combination of ML and CP can be performed for a new data instance. Major characteristics of the HT step are the used probabilistic model and the according thresholds. Further, results can be displayed and evaluated through different control charts.

Probabilistic model and control limits

Within the probabilistic environment in which an SHM framework is applied, each extracted variable x (CP, nomenclature as in 2.7) will take on different values for different samples taken. This applies to all possible CPs, even if derived under the same EOCs, where EOCs are represented by average values of random processes for a certain period of time. Providing a mathematical formulation for the expected values of x is the core purpose of probabilistic models or PDFs. These functions link parameter values to probabilities of occurrence for those values. A variety of different functions exist, such as the Normal, Gamma or Weibull distribution. Each of these has certain parameters which can be fitted to collected data as an approximation to the true, underlying PDF. Most commonly a normal distribution is assumed, based on the central limit theorem [158, 164]. For example in [57] the probabilistic framework for SHM is outlined in detail.

From the assumption of a PDF, or directly from percentiles, one can draw boundaries within which x will lie with a certain probability. For the Normal-distribution these boundaries are usually defined using a multiple of the standard deviation σ, e.g. 3σ for a 99.7% confidence interval. If x exceeds those boundaries $\mathcal{H}_0$ is rejected. Many of the examples given in 1.3.2 state a fixed percentage to make the decision between $\mathcal{H}_0$- and $\mathcal{H}_1$-hypothesis.

Control Charts and ROCs

If many data instances of a testing period are evaluated, they can be displayed chronologically in so-called control charts. The confidence intervals become upper and lower control limits (UCL/LCL), between which the healthy parameter ranges. A detailed description of many different control charts, including their theoretical background and application can be found in [128]. Univariate control charts analyze one data instance after the other while multivariate charts group data instances or multiple variables of a similar kind for evaluation. In the multivariate case, control limits must be adjusted according to the group size. Kullaa [99] provides an extensive overview

paper of control charts applied in SHM. A multivariate Shewhart T-control chart with subgroups of four is applied to principal components in [46]. Extreme value control charts with constant control limits for CP from PCA are used with experimental data from a wooden bridge model in [100]. Fugate et al. [66], Sohn et al. [179] investigate Shewhart $\bar{X}$ and multivariate S-control charts to identify damage on highway bridge concrete columns in a laboratory setting through AR-coefficients. Both sources use a fixed confidence interval of 99%. Based on simulated data of a reinforced concrete frame, Wang and Ong [205] analyze AR-coefficients through the multivariate Hotelling's T^2 control chart at a 99.73% confidence interval, combining several sensors. Results are compared to the univariate Shewhart $\bar{X}$ control chart, favoring the multivariate version.

When the actual system state during the testing phase is known, which is the case for the majority of present literature, SHM performance can be evaluated through the count of false positive (FP) and false negative (FN) alarms or describing an alarm under healthy conditions and no alarm under damaged conditions, respectively. It is crucial to state that both values and hence performance, might strongly depend on the chosen confidence interval.

Accordingly, for a test of an observed continuous variable, variation of decision boundaries (UCL/LCL) and hence confidence intervals, will result in different FP and FN values for the same test data. The overall performance of a test with varying decision boundaries can be evaluated using receiver operating characteristic curves (ROCs) displaying (1-FN) (detection rate) over FP values for differing confidence intervals [44, 80, 121].

Zweig [224] provides a review on ROCs, citing early medical applications in the 1950s as well as underlining the usefulness of this tool in "the face of the lack of a standardized approach to performance" [224]. Furthermore, "the ROC plot provides a comprehensive picture of the ability of a test to make the distinction being examined *over all decision thresholds.*" ROCs are linked to other visualization procedures and different examples are given.

Akobeng [2] gives two different metrics for ROC evaluation: The area under the curve (AUC) and the Youden index for a non-visual comparison of different ROC-curves. Further parameter ranges for evaluations of the AUC are given. These curves provide a visual insight into how strongly the parameter distribution (PDF) overlaps under healthy conditions with the one under damaged conditions.

A first application of ROCs in SHM was presented by Mujica et al. [130]. PCA is used to calculate CPs during the training phase and a normal distribution is fitted to those CPs. ML is implemented using basic clustering into four base lines for damage detection in a steel plate through piezoelectric transducers. An χ^2-test determines if CPs from new sets in the testing phase differ from the healthy structure. ROCs are used to evaluate different CP settings (number of scores).

Conclusion

Even though multivariate control charts provide a promising tool for SHM, the uni-variate case is applied within this work to limit the sources of variability (group size). Further, multivariate charts have an averaging characteristic which might reduce FP alarms but also potentially mask

phenomena occurring from changing EOCs. Here, the use of uni-variate Shewhart $\bar{X}$ control charts is investigated. A crucial tool, which has only been applied to SHM for a single CP without distinct ML techniques, can be seen in ROCs which form an essential part of the presented framework. Further, the AUC analyzed in this work serves as a global parameter for performance evaluation, which is new to the field of SHM.

Table 1.3: Overview of HT

HT component	Info	References
Probabilistic models	Normal distribution most common, many others exist; Generalized extreme value distribution is important tool; Percentiles are useful, no distribution type is presumed	[57, 158, 164]
Control charts	Overview of HT results over time; Uni-variate control charts for mean; Multivariate for Standard deviation but might mask single events	[46, 66, 99, 100, 128, 179, 205]
Receiver operating characteristic curves	Combine FP and 1-FN results for several confidence intervals; Very important for general performance estimation; Provide global performance metric; Distribution of points along ROC gives important insight.	[2, 44, 80, 121, 130, 224]

1.4 State of the Art for SHM at Wind Turbine Support Structures

The following section will detail the existing approaches for SHM of WT support structures. On- and offshore wind turbines have in common that they cover a large variety of engineering professions: Beginning with the footing of piles or gravity foundations in soil, over large steel constructions, turbines, and generators to the aerodynamic design and high performance materials of blades in a complex environment. As a result, a variety of different monitoring fields exist. Recently, basic literature has been released covering all fields of wind turbines from historical evolution to design and operation. An early work considering offshore wind turbines and a financial viewpoint of different wind turbine designs is presented by Harrison et al. [81]. Tong et al. [194] cover a wide range of WT engineering including dynamics and acoustics. Component design, aerodynamics, controller design, evolution of design rules and principal innovations in technology with a focus on offshore turbines can be found in [30]. Gasch et al. [68] provide a general overview of design, historical development as well as covering planning, operation, and economics.

Large variations in EOCs[1] and their influence on the dynamic behavior make EOC-monitoring an essential part of every SHM system. For offshore turbines, each labor-based monitoring task becomes even more critical since transitions between turbines have to be undertaken by ship and weather windows with acceptable wind and wave conditions can be a very limiting factor. Hence, one overall goal in WT monitoring is the performance of condition-based maintenance rather than

---

1 Typical EOCs are: wind speed and direction, wave direction, height and spectra, temperature, nacelle position, rotor speed, pitch angle and electrical output.

preventive or corrective maintenance to omit unforeseen damage and down times. Even though the current major focus of monitoring of WTs is on CM, SHM approaches play an important role for ageing towers and remote plants with limited accessibility. Inspection of support structures is mandatory, but its realization remains unspecified. Instead of a visual inspection of kilometers of welded seams or local monitoring with hundreds of sensors, permanent monitoring of the global structure's behavior during operation provides a promising alternative. In the case of WTs, SHM can be divided into global (vibration based) monitoring and local monitoring of specific parts such as scour monitoring or monitoring of grouted joint connections.

During the last decade, a lot of effort has been directed towards CM for electric systems, rotating machinery and the pitch system within the wind turbine's nacelle and rotor. Hameed et al. [79] provide an extensive review on methodology and algorithms. García Márquez et al. [67] provide a broad range of literature reviews on CM giving a compact overview of available CM types and signal processing methods. The vast majority of reviewed literature concentrates on the blades, rotor, gearbox, generator and bearings, not on the support structure. Nevertheless, this review marks a good starting point for a broad overview of the topic. Growth of wind energy and discussion of SHM/CM costs are found in [31], major challenges and demands are also pointed out. Liu et al. [109] analyses SHM for (offshore) wind energy systems from the Chinese point of view, also providing a status of wind energy in China - the 2nd largest market after Europe by installed wind power capacity. A survey of available condition monitoring systems on the market was prepared within the SUPERGEN initiative by Crabtree et al. (see Crabtree et al. [39] and Crabtree [38]), pointing out "a clear trend towards vibration monitoring". Discussion of the companies in question is included as well. The company information and product details provide an especially good overview. A further review on available CM-methods was carried out by Yang et al. [215]. In both cases, the support structure is only addressed marginally. Concluding these reviews it becomes clear that SHM systems for support structures are in pre- commercial development due to the lack of specific requirements in guidelines or codes. Some approaches will be reviewed in the following section.

In [1] a Micon 65/13 turbine is investigated. Acceleration power-spectral-densities at different blade harmonics, modal frequencies and MAC values are used as CPs. To simulate output data, the numerical model was validated by the first 14 measured modal frequencies up to 16 Hz. Simulated damage locations are: the blade root, the low speed shaft and the yaw joint. The procedure is linked to the approach in Sohn et al. [180]. For ML, a single cluster is used and 3-σ boundaries are constructed for HT. Global modal frequencies only shows small changes due to relatively large damage in the blade root (about 4% for a stiffness reduction of 25%). Modal contribution shows higher sensitivities with a 100% change at 50% damage.

In Lachmann et al. [103], acceleration data from an onshore WT monitored for 17 years is used for system identification. Wind loads, inertia forces at the rotor and dynamic loading in the support structure are identified as fatigue relevant loads. As CPs, modal parameters are extracted using SSI and EFDD. Based on the modal parameters, model validation is undertaken using MOPAC [134], a java based software package. Artificial damage is applied within the numerical model at four spring elements, representing tower section connections. Damage detection

is then performed with wavelet transformation [33, 110]. Further investigations on ultrasonic measurements for fatigue analysis are given in [85]. Numerical simulations for blade and tower including multi-criteria optimization can be found in [106].

In [172–174] monitoring is carried out in a similar manner: A monitoring system for a 500 kW ENERCON E-40 onshore WT in Dortmund, Germany, is presented. The sensor system is composed of a displacement, strain and acceleration sensor and combined with a self managing software-system that continuously collects data and runs analysis. Faulty signals (such as a damaged temperature sensor) can be detected and users are automatically notified by mail. In [175] a system extension, including automated system identification through ARTeMIS (EFDD, SSI) and automated model updating with MOPAC [134], is presented. Hence, modal parameters are used as CPs with a base line classification of a single cluster. Based on the bending stiffness at four points in the FE-model, a damage catalog is created for future monitoring. Wind turbine power output and efficiency are monitored additionally. In [141] Gaussian mixture models are used in the ML step to train 20 min mean values of wind speed and its standard deviation to quartiles of displacements at the 42 m level. As a first step for HT, it is checked if the right load class was predicted and no HT about the structures state is carried out through control limits.

A SHM procedure dubbed wavelet auto regressive diagnostic energy network (WARDEN) based on AR-parameters and wavelet decomposition was carried out by Bassett [12]. The approach focuses on different operational states such as ambient excitation, static yaw, start up, operation and shut down of an onshore 2.3 MW WT, identified using a manual classification in the ML step. Accelerometers at three different tower levels plus EOCs (wind speed, rotor speed and generator speed) serve as input. AR parameters are used as CPs comparing the Euclidean distance of these parameters from an actual data instance to the mean of a database and the data instance stored in the database closest to the actual conditions. Healthy data is stored in a database and no HT step is included. Potential damage localization is carried out through wavelet decomposition. Further, different stopping events are analyzed in [11].

Benedetti et al. [15] monitor an onshore WT with a 13 m rotor diameter and 18 m hub height with strain sensors. Measurements are taken with fiber brag gratings (FBGs), a relatively new optical method for strain measurement, at the tower root right above the foundation to estimate the strain field perturbation and root moments as CPs. Numerical simulation of the WT tower provides Eigenfrequencies and tower base strain. ML is realized by investigating strain abnormalities for reference simulations of different crack lengths, HT is not included in the analysis. It is pointed out that "the axial strain gradient along the circumferential direction (...) can be regarded as an indication of the structural integrity." The number of required sensors and their placement for damage detection is discussed as well. Influences on the fatigue life and structural integrity after crack detection are investigated in [16]

Molinari et al. [127] use acceleration measures from an 18 m high wind turbine with 13 m rotor diameter and an output of 11 kW for monitoring purposes. The signals are captured on seven different levels in two planar directions each. Monitoring is motivated by fatigue problems at the WT's base. Dynamic characteristics as modal frequencies and mode shapes as CPs are investigated. It is found that the first two modes are close to the vortex shedding frequency.

These modes also have the largest torsional components on the base and cause fatigue problems. ML and HT are not carried out.

A complete SHM-approach is applied to the onshore support structure of a 5 MW offshore turbine in [65, 97]. Even if boundary conditions and loading differ from the actual offshore structures, all of the important SHM steps have been realized. System identification through VAR-Models and vibration based damage detection through damage residues (from SSI- and AR-models) as CPs and numerical model updating are derived from acceleration data. Machine learning is realized using fuzzy data classification and HT is included by setting a constant one-sided upper limit at 95% confidence interval, based on the training phase [64, 65, 97]. The possibility of sensor fault detection is also included in the scheme. The approach was part of the IMOWIND project which comprised all major parts of a monitoring system, applied to the above mentioned onshore structure [159]. The study comprises data acquisition and management, load analysis, examination of dynamic properties, damage identification and model updating.

In [207] an SHM concept based on modal parameters as CPs is presented. Acceleration data from an offshore monopile foundation is used to track modal frequencies over a period of two years. Modal parameter extraction is based on the poly-reference least squares complex frequency-domain estimator (pLSCF). Alongside the dynamic responses, tidal levels, wind speed, rotor speed, wave height, temperature, and jaw angle are collected as EOCs for each ten minute data instance. Machine learning is implemented via a two step approach: First, data instances are manually clustered by major EOCs. Within each cluster a low-order non-linear regression is applied to fit the dependency between modal frequencies and EOCs. Finally, in the HT step, the residual errors between measured and predicted frequencies are monitored in a control chart based on a normal distribution. Control limits are set to $\mu \pm 3\sigma$. Significant dependency of modal parameters to tidal levels as well as seasonal variations are identified. In addition, the so-called J-tube reveals a strong influence on the structure's bending modes. An overall stiffening of the structure is accounted to soil stiffening under cyclic loading.

In [47], data from the same turbine in parked or idling position is analyzed with PolyMAX, and SSI-COV, and mode shapes frequencies and damping ratios as CPs are tracked over a period of two weeks. A single cluster is used in ML for this period. Frequency and damping are shown to be dependent on EOCs. HT is not applied since only the base line phase is analyzed.

Rolfes et al. present an SHM approach which addresses damage identification, quantification and localization [160–162]. Damage identification is realized by monitoring the proportionality between accelerations below the nacelle and strain at the tower root also including wireless sensing [161]. Data was acquired from a fourteen year old NEG-Micon 250 (250 kW), and a six year old Vestas V-80 (2 MW) turbine. Numerical model validation is performed as well.

An array of wireless sensors is used on a NEG Micon and Vestas with a 40 and 78 m hub height respectively [191]. Modal frequencies were identified with ERA. A detailed overview and introduction for all technical components of wireless-sensing for civil infrastructure, as one of the key features for an cost efficient SHM approach, can be found in [113]. For damage localization, the multiparameter eigenvalue problem (MEP) [36, 37], is applied to physical models. This method uses frequency changes in combination with the decomposed stiffness matrix of a numerical model

of the structure to locate and quantify structural changes. This method was also applied to two onshore wind turbines with artificial damage [162]. One is a Südwind S70 (1.5 MW) with a 144 m lattice tower where bolts were loosened at the highest section, the other a guyed Südwind S1200 where tension was reduced in one suspension cable. In both cases the MEP is able to localize and quantify structural damage correctly.

Current research shows many traditional applications based on modal parameters and fatigue monitoring. A first step towards investigating variations under different EOCs has been made during the past years. A fully automated investigation including advanced ML and HT (self adapting) and more sophisticated CP, other than modal frequencies, is missing so far.

1.5 State of the Art for Automated Operational Modal Analysis

As an extension of the CP estimation, the automated extraction of modal parameters will be analyzed in this section in detail. In the field of operational modal analysis, the automation of modal parameter extraction has been a goal for over four decades, reaching back to the 1960s where modal analysis was performed with analog equipment. All strategies, independent on whether they rely on frequency or time domain approaches, have this goal in common. Today, many procedures and computer programs still necessitate human interaction for this task. If this is the case for each analyzed data instance, it prohibits the desired analysis of large databases for SHM. Accordingly, a lot effort has been made in the recent years to automate this procedure. A broad review of different approaches dealing with the (semi-) automated identification of modal parameters was recently published by Reynders, Allemang, Lau and Magalhães (see [3, 105, 116, 157]). Many of these approaches, including the latest one by Reynders, rely on clustering points in a stabilization diagram. Due to the calculation of distances between, or the comparison of, all points, clustering might become computationally rather expensive.

The most rudimentary approach in automated system identification is to choose a single conservative model order, performing a fit, and using the results as system poles e.g. modal parameters. In general, these solutions might contain spurious or not all of the desired modes. Today, it is possible to calculate solutions for a large number of different model orders for parametric system identification procedures[1] within a sufficiently short period. This avoids the iterative estimation of an alleged optimal model order but raises the problem of a growing number of spurious solutions. The key problem is the separation between non-physical or spurious solutions and those of physical relevance which correlates with the grouping of poles belonging to one mode.

In most cases, this problem is addressed with stabilization (or consistency) diagrams. Typically the frequency of each solution from a parametric system identification method (system poles) is plotted over the model order. Stable paths (straight vertical lines), with a fairly constant frequency (and damping, plus optional further parameters) over several model orders, are assumed to belong to physical solutions and thus representing the modal properties of the system. When frequencies

---

1 System identification procedures are considered to be *parametric* when they extract a finite number of solutions (system poles, and, if applicable, zeros) when run for a certain model order.

of all solutions are plotted versus their according damping ratios (frequency-damping-plane), dense, elliptic clusters occur for stable modes. It is also possible to plot solutions of different model orders in the complex s-plane. Further, pole surface consistency and density are considered a helpful addition to stabilization diagrams [149]. The next section will describe parameters used in the automated procedures followed by a review of proposed approaches.

1.5.1 Parameters used for Automation

Each solution (or pole) from parametric system identification comprises a complex eigenvalue (frequency and damping) and a complex eigenvector. To eliminate spurious and group physical solutions, parameters for evaluation are necessary. Again, it is important to differentiate between absolute and relative parameters: While the former can be interpreted directly for a single solution (as damping ratio or mean phase deviation) the latter necessitates (at least) two solutions (as frequency differences or the modal assurance criterion (MAC)) for an evaluation. Further, *soft* and *hard* criteria can be distinguished. *Hard* criteria indicate direct, absolute thresholds (as damping ratios above e.g. 20%) while *soft* criteria range from potentially spurious to physical (usually normalized to $[0-1]$).

A general, initial criterion originating from basic theory is the appearance of solutions in complex conjugate pairs [53, 119]. Each solution without a complex conjugate counterpart can be erased. The two major (and most commonly displayed) pole parameters are frequency and damping. No pair of solutions far apart from each other in one of the two dimensions in the stabilization diagram, especially frequency, can be considered to belong to the same mode. While the (modal) frequency is an relative parameter between poles[1], modal damping can serve as absolute and relative parameter since very large or negative values can be suspended (hard criteria) in many cases.

In addition, several different parameters can be derived from an eigenvector. The complexity of the modal vector is measured by the mode phase colliniarity (MPC), values range from 0 to 1 where 1 indicates perfect co-linearity [156, 201] indicating a purely real eigenvector. Alternatively, the mean phase deviation (MPD) can be calculated for each mode shape. Ranging from 0° to 45°, it indicates how much the mode shape's DoFs differ from a straight line through origin in the complex plane, providing a better applicable parameter than MPC since real-valued modes cannot be postulated in general. Both can serve as *hard* or *soft* absolute criteria.

One of the most popular vector criteria is the modal assurance criterion (MAC) [5, 6] which indicates the linear dependency between two (complex) vectors. It is used as a relative criterion, indicating if two solutions belong to the same mode (MAC value close to 1). High root-mean-square values of unscaled mode shape magnitudes indicate the importance of a mode. A similar parameter is the modal contribution, denoting how much a single mode contributes to the total response. In addition, pole weighted/scaled modal vectors provide a concept that is supposed to

---

1 In general, no frequency value can be excluded initially. Hence, frequency differences between solutions are defined.

give the modal vector more sensitivity [3].

Besides these general parameters, parameters for specific system identification methods have been derived. For the frequency domain decomposition (FDD), the modal coherence, a comparison of mode shape at a spectral peak with neighboring mode shapes is used as a criterion [28]. For automated system identification, the complex mode indicator function (CMIF) [150] is used as parameter by Lanslots [104]. Being the primary accuracy indicator in the ERA, the consistent mode indicator (CMI) is used as identification parameter by Pappa ([139, 140]). Values range from 0 to 100%, "modes with CMI values greater than approximately 80% are identified with high confidence." Modal transfer norms, based on SSI, give a measure of the reduction error when one mode is removed from the model [155]. Scionti uses modal norms between two different stochastic subspace balanced realization model instances to compare estimates [169]. Pole-zero cancellations of a stochastic state space system are investigated in [71]. Another set of parameters is based on the frequency-domain maximum likelihood estimation (MLE) where uncertainties in pole estimates, the number of close zeros to a pole and pole-zero correlations are investigated [199, 201].

All of these parameters are used in different combinations to aid the task of automated modal parameter extraction from measured time series. Some of the existing attempts are outlined in the next sub chapter.

1.5.2 Existing Procedures

The following section will give an overview of the existing investigations and procedures that focus on automated extraction of modal parameters making use of the parameters mentioned in the previous paragraph. In automated OMA basically two groups of approaches exist: One is based on dividing (PSD) frequency spectra into several modes; the other is to cluster solutions in stabilization diagrams. These diagrams might be built from various system identification procedures working in the time or frequency domain. The approaches utilize ML techniques previously outlined in Chapter 1.3.1, a focus is laid on the usage within the different approaches here.

Frequency Domain

The above mentioned FDD proved to be one of the most popular modal identification techniques. An automation of this technique was recently presented and dubbed enhanced frequency domain decomposition (EFDD) [28, 91]. First, peak identification for the power spectral density is performed. Subsequently, the peak is identified as physical or noise by collecting surrounding points by MAC values larger than a threshold (0.8 suggested). The identified domain over several frequencies, which must contain more points than a user defined threshold, is then deleted from the frequency spectrum and the search is repeated. An IFFT of the selected frequency domain, the pole, is used for the determination of damping in the time domain. The procedure was tested on a highway bridge [9] and was also applied to a long span arch bridge by Magalhães [117].

A drawback is the dependency on the frequency resolution, where peak identification might fail due to noise levels or for poorly excited modes. Further, SVD for each frequency bin is needed

and many MAC values are calculated around each peak to define the modal domain. This results in large numerical efforts. The modal coherence assumes noise mode shapes to be of random character, which is not necessarily the case. Finally, estimated damping ratios strongly depend on width of the identified modal domains around the peak.

An extension of the EFDD was presented by Rainieri [152–154]. Based on the power spectral density, as in (E)FDD, MAC values are calculated at each frequency bin between different measurements (minimum of 10 suggested). Mean and standard deviation of MAC values are subsequently investigated over the frequency range and for several measurements. The so called MAC sequence must have an average above 0.95 and a standard deviation smaller than 0.01. The derivatives of the sequence are investigated as well. Finally, a band width is defined by investigation of a sufficient MAC sequence which is used for peak identification within these bands for modal frequencies and an IFFT of the corresponding power spectral density band to determine damping ratios. The procedure was applied to a concrete tower, a star vault and bell towers.

This approach can potentially overcome the problem of peak picking within the whole frequency band but the number of frequency bins can be very large, hence, again computational effort is rather high. Furthermore, many measurements are necessary, which might be undesirable or may see EOCs change and influence the modal parameter between measurements.

Stabilization Diagrams

To create a stabilization diagram, many different parametric system identification procedures are available. Along with SSI and VAR-models, the PolyMAX is a popular approach for achieving a clear stabilization diagram [145, 147]. It is a "polyreference version of the least squares complex frequency-domain (LSCF) estimator method" [145]. Attempts for mode extraction through identification of stable paths include pure path estimation [46, 138, 140, 155], one-dimensional attempts using analysis of frequency bands/histograms [104, 105, 122, 125, 126, 169, 223] over hierarchical clustering [47, 115, 116, 156], singular value decomposition [3, 4, 29, 149], neural-networks Lim et al. [107] over fuzzy c-means or k-means clustering [32, 47, 156, 168, 199–202] to support vector machines [71]. The next sections will outline some of the more advanced procedures.

Singular Value Decomposition   The common statistical subspace autonomous mode identification (CSSAMI) is presented in [3, 4, 29, 149]. Pole weighted modal vectors from a stabilization diagram are used to build a MAC matrix. This matrix is cleared with a fix threshold and decomposed with SVD to determine the number of clusters of significant singular values. The grouped, pole-weighted eigenvectors are decomposed again to estimate modal vectors, damping and frequency of each single cluster. Solutions from the unified matrix polynomial algorithm (UMPA) for a laboratory test and bridge field data are used to demonstrate the CSSAMI approach in [29]. Statistical evaluation of pole cluster standard deviations for frequency and damping as well as different modal vector residues are investigated for these examples in [4].

Histograms and Frequency Bands   Mevel et al. introduce the SSI-COV based COSMAD (covariance subspace modal analysis and diagnosis) approach that is based on pole counting in frequency bands [122, 125, 223]. The method is an initial step to later histogram based methods and comprises several hand set parameters. User interaction is required to select modal frequencies. The procedure was applied to in flight data from the Eureka file project.

The automatic assessment of stabilization diagrams (AASD), which was "modeled on the knowledge of a human engineer" is presented in [169]. First, a histogram with user-defined bin-width[1] is derived along the frequency axis of the stability diagram and solutions per frequency-bin are counted. Bins are shifted by half a bin and the procedure is repeated. The bins are also investigated according to: Summed Euclidean distance between each frequency in a bin and its *center* frequency, resulting in a bin weight. Stable poles (meaning small differences in frequency, damping and high MAC-values) are counted within the bins. A value of less than three stable poles is punished. Bins are locally compared to their (shifted) neighbors based on the number of solutions, Euclidean distance, and stable poles. Bins without stable poles are erased, poles within bins are clustered. Beyond this, "the best cluster is picked, and from that cluster, the best pole is determined." A feature to capture double poles is implemented as well.

Application of AASD, carried out in an automated manner in combination with Cada-X, LMS Test.Lab^{TM} software dubbed "The Modal Analysis Chain", is applied to in-flight data of an air plane in [104]. The poly-reference LSCE and LSCF method (PolyMAX) were used to generate stabilization diagrams which were investigated by eight probands (4 novices, 4 experts) and AASD. Application of an commercial implementation of the AASD, the automatic modal parameter selection (AMPS), is presented in [105] by using car vibration data.

Hierarchical Clustering   An approach based on hierarchical clustering of poles was presented by Magalhães [115, 116]. The hierarchical tree is based on numerically expensive similarities (distances) between all pairs of solutions computed as a combination of frequency difference and MAC values. A single linkage procedure is used to connect the poles. To predict the number of tree-branches (resulting number of clusters), the cut off criterion "consists of imposing a maximum limit for the distance between any point and its closest point of the same cluster." [116]. Frequency, damping and mode shape result as cluster means, outlier analysis is suggested as a means to eliminate scattering solutions. The method is applied to field data from a concrete arch bridge [115, 116], as well as a stadium roof [115].

Fuzzy C-/K-Means Clustering   The frequency-domain maximum likelihood estimator (MLE) is used for the calculation of poles (and zeros) in [200–202]. In [200] an iterative fuzzy c-means algorithm groups solutions of a single model order into two clusters. Classification criteria are standard deviation of the poles, the "ratio of the number of zeros within the 99% uncertainty circle and the total number of transfer functions", the correlation between pole and nearest zero and the inverse of MPC and RMS of mode shape magnitude. With a membership rate larger

---

1   As width 1 to 5% of the maximum frequency is suggested.

than 50% a solution belongs to one of the two classes. In [201], an agglomerative hierarchical approach (iterative applied k-means algorithm, where the number of poles within a cluster is preset automatically) divides the solutions into several clusters. Further, small frequency variations need to hold true and more than 50% of the solutions in a cluster need to be stable, also MAC and MPC must exceed certain thresholds to indicate a physical solution. Both procedures were applied to a slat track (part of an air plane wing).

In a combined approach Devriendt et al. [47] apply robust agglomerative hierarchical clustering and fuzzy C-means clustering to extract modal parameters for a monopile WT support structure. A relative distance for frequency and damping and minimum or maximum path length must be set for hierarchical clustering. Again, all solutions of the stability diagram are compared to each other with possibly large numerical effort. In the spirit of Vanlanduit et al. [199], Verboven et al. [201, 202] clusters from hierarchical clustering are divided into physical and spurious ones by frequency, damping, a newly defined success rate, MPC, and MPD.

Scionti also introduced a hybrid FCM procedure in the frequency-damping domain [168]. The set and number of initial seeds is selected by a generic algorithm and clustered by an extended FCM algorithm, leading to better results than standard FCM clustering. Finally, resulting clusters are rejected by a user defined threshold of *contribution ratio* and *compactness*. The procedure is applied to the results of the balanced realization parameter estimation method [144] from air plane in-flight test data. Both generic algorithms and clustering are time consuming and consist of many iteration steps.

FCM clustering was also applied in [32]. It is stated that FCM naturally forms spherical clusters. Hence, attempting to cluster almost aligned point clusters in the real-valued frequency-damping plane does not fit with the FCM approach. Hence, clustering of poles in the complex z-plane is performed, where less ellipsoidal clusters result but no further automation is undertaken. Demonstration is done on bridge and sky scraper data.

Reynders et al. propose a technique where several soft and hard criteria are used in combination with k-means and hierarchical clustering [156]. The criteria used are frequency and damping ratio distance, MAC value, MPD, MPC and relative difference of modal transfer norms between modes. The hard criteria are damping between 0 and 20% and the appearance in complex conjugate pairs. To clear the stabilization diagram, a k-means clustering algorithm divides all solutions using soft criteria into two clusters of spurious and possibly physical modes. Hard criteria are applied to the cluster of possibly physical solutions. Remaining modes form a cleared stabilization diagram. Subsequently, the remaining solutions are grouped by hierarchical clustering; the cut off value to determine the number of clusters is calculated from the previous clustering. Afterwards, k-means clustering again divides the cluster into two groups (physical/spurious) by the numbers of contained solutions. A representative solution of each cluster yields the final results. Demonstration is done at a post-tensioned concrete two-cell box-girder bridge. Again, the number of clustering stages and comparison of all solutions results in expensive computations.

Conclusions

As presented thus far, many different attempts for the automated extraction of modal parameters exist using various combinations of parameters and clustering techniques. One group of methods focuses on the automated interpretation of stabilization diagrams, the other on the automated interpretation of spectra.

Within the stabilization diagrams, a significant drawback is the comparison of every possible solution pair. This leads to unnecessarily long calculation times. Some attempts overcome this through a hand set fragmentation into frequency bands. For analysis using histograms and hence frequency bands, window-size or band width have to be defined. Implicitly this limits the number of possible modes resulting from these procedures. In hierarchical clustering this is implied in the cut-off distance for branches. Also (fuzzy) c-/k-means clustering necessitates an *a priori* definition of cluster numbers.

So far, none of the presented approaches provides a general description or intuition of the solution's distribution in a stability diagram - which is essentially what is needed to understand and optimize classification. In a stability diagram, physical damping values will follow a log-normal distribution along the damping axis, corrupted by mathematical solutions. The distribution in frequency direction depends on the investigated structure, sampling rate, noise, input forces, and the included model orders as well as the system identification technique. Therefore, the frequency distribution cannot be generalize. The newly introduced triangulation-based approach uses the most common and robust parameters for automation and gives a general solution by only comparing neighboring solutions (see Chapter 3.2).

1.6 Goals and Objectives

The outline of different SHM applications provides an insight into the diversity of existing procedures. Yet, a holistic metric for performance comparison is lacking. In most cases, damage detection is dealt with on a phenomenological level where a certain selection of training data combined with a specific condition parameter and specific thresholds leads to a (more or less) clear identification of instances of damage. Some reviews compare different condition parameters and machine learning techniques but a holistic comparison is missing. Further, only an onshore installation of an offshore wind turbine structure has been subject to a more complex monitoring concept outrunning the investigation of modal parameters or strains. Additionally, modal parameters under changing operational conditions for WTs have only recently been in focus and only a few case-studies can be cited for mono-pile foundations. From these findings, the following main goals and objectives are formulated for this thesis:

Goals

- Deeper understanding of main SHM components and parameters which influence results and performance.

- Investigation of such parameter.

- A better comprehension of the dynamic behaviour of (offshore) wind turbines under EOC influences.

- An improvement of automated modal parameter extraction.

Objectives and Questions

- A conceptual derivation and numerical implementation of an SHM framework which will be able to address different types of variables present in SHM frameworks in an automated manner.

- Validation of such framework on a comprehensible, public database.

- Consecutive to the implementation and validation, recommendations should be given for feasible machine learning techniques, well-performing condition parameters and hypothesis testing set-ups. Along with this, first performance values for the benchmark example shall be provided for a reference comparison to alternative applications and implementations.

- Different sources claim to omit the need for EOCs , and inherently ML, in their analysis, e.g. through the usage of Mahalanobis square distances. This poses the question of whether sophisticated ML with more than a single cluster in training improves SHM performance?

- To aid the goal of modal parameter extraction for large databases, an automated procedure for OMA is desired.

- The analysis of an offshore wind turbine's dynamic behavior under changing environmental and operational conditions (EOCs) over a long time span.

- Codes for offshore WTs imply an analysis of the first bending mode to be separated from rotor harmonics. Further, certain constant values for system damping are given. The question is whether, for those highly dynamic systems, these assumptions meet the requirements of OWT operation in situ?

The author intends to contribute to the community on three levels: To provide a starting point, a short overview, and a selection of valuable literature and tools. Further, to add to the field of SHM and CM on a conceptual level by defining four blocks in any SHM concept, that should be accounted for, and to provide a general metric for performance comparison. Finally, the aim is to introduce novelties on a technical level through new methods/parameters, providing a benchmark for future parameters and methods, and the analysis of a unique database for an offshore wind turbine.

1.7 Organization of Presented Work

Ageing infrastructure, a large number of structures in highly active seismic areas, and new structures with unknown long-term dynamic behavior provide the basis for the need of long-term remote monitoring. The core task of the presented work is to provide a holistic framework to

evaluate SHM performance for industrial scale wind turbines and other large-scale civil engineering structures under changing environmental and operational conditions. An essential point is the evaluation of SHM on known benchmark examples addressed through a discussion of four main variables to gain knowledge about performance and robustness.

From the given literature review, several decisions regarding applied methods are drawn for the presented analysis. ML is implemented in a supervised manner through classification. Even though continuous EOCs might call for regression analysis, it raises the problem of reference definition for relative CPs. Further, affinity propagation is used for clustering due to its superior performance compared to conventional clustering techniques such as k-means-clustering. A reference clustering with a single cluster in the training phase is included, since an omission of machine learning is often claimed through the use of a single cluster. From the variety of CPs present in literature, statistical values for time-series are chosen due to their simplicity and possible ability for sensor fault detection. Modal parameters are included since they provide the link to numerical models and assumptions in fatigue analysis (modal damping). Finally, AE and residues from SSI- and VAR-model are state of the art parameters which showed excellent performance in recent studies. For HT, the normal distribution assumption is justified by the central limit theorem and percentile values allow a confidence interval definition without the need for a probabilistic model. For control charts a simple x-bar chart is used to avoid the introduction of further variables, such as group sizes for multivariate charts. This also avoids averaging effects within groups. Finally, ROCs represent a unique tool to cover a test's performance in entirety and to provide metrics for a global comparison.

Based on the introduction to SHM, its constituents, and application examples in this chapter, the relevant theoretical background will be outlined in Chapter 2. It holds the core equations to provide the basis for the subsequent analysis. Nevertheless, it represents only a small fraction of theoretical background in the wide range of scientific fields included in the SHM framework. Further references are provided at respective locations.

Chapter 3 outlines novelties and example studies. Accumulated energy as a condition parameter is extended to cross-correlations and the monitoring of certain energy levels. Further, a new automated procedure for the extraction of modal parameters based on a Delaunay-triangulation is presented with the TEMP method. An example for a real-life application of TEMP is given by means of a long span suspension bridge. Subsequently, the modular SHM framework is presented. Affinity propagation, as a recently developed type of data classification, is adapted to the field of SHM. Also, the evaluation of receiver operating characteristics through the area under the curve, as a universal performance measure, is a novelty. All four main points of variability are discussed and additional theory is provided if necessary. A benchmark example for the framework is provided through an application to a laboratory test structure originating from a publicly available database.

Subsequent to the benchmark example, a small scale onshore wind turbine with artificially introduced damage states is investigated in Chapter 4. In contrast to the laboratory structure noise, complex dynamic behavior and environmental and operational conditions come into play. Hence, machine learning plays an important role. Due to the known damage scenarios, the overall

SHM performance and robustness for different machine learning realizations, condition parameters, hypothesis testing assumptions, and training data instances can be evaluated.

Finally, the SHM framework is applied to an industrial-scale offshore wind turbine with a rated power production of 5 MW in Chapter 5. An important part of the analysis is the investigation of modal parameters of this complex structure. Subsequently, the analysis of influences from environmental and operational conditions on the structure's dynamics serve as background for long-term SHM.

The work closes with summary, conclusions and an outlook over future work in Chapter 6. Possible starting points are given to deepen the level of knowledge for specific methods but also on a general level. Further, figures on certain aspects of chapters 3, 4, and 5 can be found in the appendix sections.

2 Theoretical Background

Within this chapter the theoretical background required for the analysis presented is outlined in a compact manner. Starting from time series, basic descriptions of dynamic systems are derived. These are necessary for the subsequent theory of system identification as a basis for the extraction of modal parameters in 2.4. Subsequently, sub-chapters 2.5, 2.6, and 2.7 go through the main SHM components as stated in chapter 1.3 and describe the theory of applied methods and parameters.

2.1 Data Instances and Time Series

The SHM-scheme and its sub-components rely strongly on measured data from a physical structure. Even though this work is based on acceleration signals, in general there is no limitation of the sensor types and measurement set-ups for this procedure, as long as they serve the desired goals. A data instance $\mathcal{D}_i$ is always composed of the measured response data, sampled with the sampling frequency f_s, and additional information about the current set, dubbed environmental and operational conditions (EOCs), defined as $\mathcal{D}_i^{\mathbf{Y}} := \mathbf{Y}$ and $\mathcal{D}_i^{\mathbf{EOC}} = \mathbf{EOC} \in \mathbb{R}^{\bar{n}}$, respectively. Usually $\mathcal{D}_i^{\mathbf{EOC}}$ will have a lower sampling rate than $\mathcal{D}_i^{\mathbf{Y}}$, e.g. only one value per EOC-parameter and data instance. The data matrix is composed of different channels as follows

$$\mathbf{Y} = [\mathbf{y}_1, \mathbf{y}_2, ..., \mathbf{y}_{n_t}] = \begin{bmatrix} \mathbf{y}_{(1)} \\ \mathbf{y}_{(2)} \\ \vdots \\ \mathbf{y}_{(m)} \end{bmatrix} \in \mathbb{R}^{m \times n_t}. \tag{2.1}$$

This matrix holds one output or measurement channel per row, where m is the number of measured channels and n_t the number of data samples. A single channel is referenced to as $\mathbf{y}_{(i)} \in \mathbb{R}^{1 \times n_t}$, a single entry is denoted by $\mathbf{y}_{(i),j}$. The measurement period T results from $T = n_t * 1/f_s = n_t * \delta t$.

To gain insight into the frequency content of a time domain signal, the Fourier transformation (FT) provides an important tool. This transformation splits the time signal into an infinite sum of harmonic functions with infinitely close frequencies. The continuous time signal $y(t)$ is linked to its FT spectrum $Y(j\omega)$ through

$$Y(j\omega) = \int_{-\infty}^{\infty} y(t)e^{-j\omega t}dt. \tag{2.2}$$

The continuous formulation is only of limited use for discrete time signals and approximated using

the discrete Fourier transformation (DFT) with

$$F\{\mathbf{y}\} = \mathbf{Y}(j\omega_q) = \sum_{k=1}^{n_t} \mathbf{y}_{(i),k} e^{\frac{-j2\pi kq}{n_t}}, (q = 0,1,...,n_t - 1), \tag{2.3}$$

with the discrete frequencies being $\omega_q = q2\pi/T$. Through the DFT, the time signal is implicitly assumed to be periodic within the recorded interval. Hence, $\mathbf{y}_{(i),1} \neq \mathbf{y}_{(i),n_t}$ will introduce a jump and subsequent distortions in the frequency domain (spectral leakage). This problem can be addressed through the application of window-functions (see e.g. [216]). Due to the time discrete sampling rate, aliasing effects can become a problem for signal analysis. To avoid these effects, f_s should be at least twice as high as the highest frequency of interest. In most cases a fast Fourier transformation (FFT), an efficient implementation of the DFT, is used. It applies a repeated division into two equally long parts to the time signal and hence postulates a time series with $n_t = 2^n, n \in \mathbb{N}$. If this assumption is violated, the signal is padded with zeros (until n_t equals the next power of two) which alters the frequency content as well.

In the context of signal analysis, the (power) spectral density PSD provides another helpful tool. It represents a measure of the power per frequency bin within a given signal. To derive the PSD, the autocorrelation of a signal from channel i, $\Phi_{ii}(\tau)$, is calculated using

$$\Phi_{ii}(\tau) = \sum_{n=1}^{n_t-\tau} \mathbf{y}_{(i),n}\mathbf{y}_{(i),n+\tau}, \tau = 1,2,...,n_t - 1. \tag{2.4}$$

The FT of $\Phi_{ii}(\tau)$

$$S_{ii}(\omega) = F\{\Phi_{ii}(\tau)\} \tag{2.5}$$

is then called the PSD of $\mathbf{y}_{(i)}$. Through the auto-correlation, harmonic and periodic signal contents are amplified and will occur more distinct in the spectrum. Both values also exist for the cross-correlation between channel i and j. The PSD is often used to underline and/or validate results from system identification procedures visually.

2.2 Representations of Dynamic Systems

A mathematical description of a certain mechanical system is essential in engineering science. Good knowledge of the systems helps to improve performance and to predict the material behavior. The linear physical model can be represented by the following linear equation of motion

$$\mathbf{M\ddot{u}}(t) + \mathbf{B\dot{u}}(t) + \mathbf{Ku}(t) = \mathbf{f}(t), \tag{2.6}$$

with $\mathbf{M}$, $\mathbf{B}$ and $\mathbf{K} \in \mathbb{R}^{N \times N}$ as mass-, damping- and stiffness matrix. Where N is the number of discrete degrees of freedom (DoF). $\mathbf{f} \in \mathbb{R}^{N \times 1}$ is the force vector and $\mathbf{u},\dot{\mathbf{u}},\ddot{\mathbf{u}} \in \mathbb{R}^{N \times 1}$ the displacement, velocity and acceleration vector, respectively. In many cases the damping matrix is

simplified to a linear combination of mass and stiffness matrix with

$$\mathbf{B} = \alpha\mathbf{M} + \beta\mathbf{K} \tag{2.7}$$

[53, 148]. In doing so, the system is *proportionally damped*, the so called *Rayleigh-damping*, which ensures a symmetric matrix $\mathbf{B}$ and orthogonality with respect to the Eigenvectors. For undamped and proportional damped systems the Eigenvalue problem is given as

$$\left(\mathbf{K} - \lambda_i^2\mathbf{M}\right)\psi_i = 0 \tag{2.8}$$

and solved for the Eigenvalues λ_i with the corresponding Eigenvectors ψ_i. The word *Eigenvectors* will be used to refer to the (complex) solution of the Eigenvalue problem (holding amplitude and phase information), while a *mode shape* will hold only the amplitudes of these Eigenvectors. In this case the λ_i equal the circular natural frequencies ω_{0i}. The solutions for all DoFs are assembled in the spectral matrix $\Lambda = diag(\lambda_i^2) \in \mathbb{R}^{N \times N}$ and the modal matrix $\Psi = [\psi_1,...,\psi_N] \in \mathbb{R}^{N \times N}$. For a system with proportional damping, a transformation to modal coordinates with $u(t) = \Psi q(t)$ and multiplication of (2.6) with Ψ^T from left, leads to n discoupled equations, due to the orthogonality proportions of the Eigenvectors. Each has modal properties such as generalized mass, damping and stiffness:

$$\mathbf{M}_g\ddot{\mathbf{q}}\left(t\right) + \mathbf{B}_g\dot{\mathbf{q}}\left(t\right) + \mathbf{K}_g\mathbf{q}\left(t\right) = \Psi^T\mathbf{f}, \tag{2.9}$$

with $\mathbf{M}_g = diag(m_{gi}), \mathbf{B}_g = diag(b_{gi}), \mathbf{K}_g = diag(k_{gi})$. For damped systems, in general the Eigenvalues depend on both circular natural frequency (hence mass and stiffness) and damping as follows

$$\lambda_i = -\delta_i \pm j\omega_{Di} = -\omega_{0i}\zeta_i \pm j\omega_{0i}\sqrt{1 - \zeta_i^2}. \tag{2.10}$$

Here, j denotes the complex number, ω_{Di} the damped circular natural frequency and ζ the damping ratio. The Eigenvalue now comprises two parts: an imaginary or oscillating one and a real part that indicates the decay with a damping rate of $\zeta_i\omega_{0i}$. Further one might extract natural frequency and damping from Equation 2.10 with

$$\omega_{0i} = |\lambda_i| = 2\pi f_i = \sqrt{k_{gi}/m_{gi}}; \qquad \zeta_i = -\frac{Re\left(\lambda_i\right)}{|\lambda_i|}. \tag{2.11}$$

One of the goals of the latter analysis will be the (system) identification of natural frequencies and damping ratios along with the corresponding Eigenvectors. The dependency of natural frequencies on mass and stiffness in (2.11) is obvious. This fact can be used to localize and quantify damage within a numerical model through model updating procedures. For this purpose, and for generally damped systems it is more convenient to rewrite the equation of motion in state space.

2.2.1 State Space in Continuous Time

The state of a system is given by its displacements and velocities. Holding information about its complied potential and kinetic energy for a given state, the state vector is defined as

$$\mathbf{x}(t) = \begin{bmatrix} \mathbf{u}(t) \\ \dot{\mathbf{u}}(t) \end{bmatrix} \in \mathbb{R}^{n \times 1} \tag{2.12}$$

where $n = 2N$. Multiplication of (2.6) with the inverse mass matrix and solving for $\ddot{\mathbf{u}}$ leads to:

$$\ddot{\mathbf{u}}(t) = -\mathbf{M}^{-1}\mathbf{B}\dot{\mathbf{u}}(t) - \mathbf{M}^{-1}\mathbf{K}\mathbf{u}(t) - \mathbf{M}^{-1}\mathbf{f}(t). \tag{2.13}$$

Equation (2.13) in combination with the equality $\dot{\mathbf{u}} = \dot{\mathbf{u}}$ can be re-written in state space using Equation (2.12). The continuous $([...]_c)$ time state space equation thus becomes

$$\dot{\mathbf{x}}(t) = \underbrace{\begin{bmatrix} \mathbf{0} & \mathbf{I} \\ -\mathbf{M}^{-1}\mathbf{K} & -\mathbf{M}^{-1}\mathbf{B} \end{bmatrix}}_{\mathbf{A}_c} \mathbf{x}(t) + \underbrace{\begin{bmatrix} \mathbf{0} \\ -\mathbf{M}^{-1}\mathbf{L} \end{bmatrix}}_{\mathbf{B}_c} \mathbf{f}(t), \tag{2.14}$$

where $\mathbf{A}_c \in \mathbb{R}^{n \times n}$ and $\mathbf{B}_c \in \mathbb{R}^{n \times l}$ denote the system matrix and input matrix, respectively. Further, the corresponding measurement equation is

$$\mathbf{y}(t) = \underbrace{\begin{bmatrix} \mathbf{L} & \mathbf{0} \end{bmatrix}}_{\mathbf{C}_c} \mathbf{x}(t) + \underbrace{\begin{bmatrix} \mathbf{0} \end{bmatrix}}_{\mathbf{D}_c} \mathbf{f}(t), \tag{2.15}$$

with $\mathbf{C}_c \in \mathbb{R}^{m \times n}$ and $\mathbf{D}_c \in \mathbb{R}^{m \times l}$ as *output matrix* and *direct throughput matrix*. $\mathbf{y}(t) \in \mathbb{R}^{m \times 1}$ is the m-variant output or measurement vector. Matrix $\mathbf{L}$ is introduced if sensor locations on given DoFs need to be selected from all DoFs. For non-proportional damping the Eigenvalue problem from Equation (2.6) becomes

$$\left(\lambda_i^2 \mathbf{M} + \lambda_i \mathbf{B} + \mathbf{K} \right) \phi_i = 0. \tag{2.16}$$

For the state space formulation the Eigenvalue problem can be simplified to

$$\left(\mathbf{A}_c - \lambda_i \mathbf{I} \right) \phi_i' = 0. \tag{2.17}$$

It should be noted that this equation leads directly to the Eigenvalues λ_i which appear in complex conjugate pairs. The Eigenvectors ϕ_i' now consist of $n = 2N$ entries for displacement and velocities.

2.2.2 State Space in Discrete Time

Data collection is one of the central topics in monitoring. To store, process or analyze any continuous physical phenomenon, it is necessary to sample the given quantity digitally. Hence, the analyzed data is present at discrete times $\mathbf{y}(\mathbf{t}_k) = \mathbf{y}(k\Delta t) = \mathbf{y}_k$ as in (2.1) with intervals of

Δt, leading to a time series of n_t samples. This has a major influence on the state space matrices. A detailed discussion of sampling theorems and important assumptions can be found in [14, 62]. The continuous time state space equations are formulated in discrete time ($[...]_d$) through

$$\mathbf{x}_{k+1} = \mathbf{A}_d\mathbf{x}_k + \mathbf{B}_d\mathbf{f}_k$$
$$\mathbf{y}_k = \mathbf{C}_d\mathbf{x}_k + \mathbf{D}_d\mathbf{f}_k \tag{2.18}$$

with the discrete time state space matrices linked to their continuous counterparts with:

$$\mathbf{A}_d = e^{\mathbf{A}_c\Delta t}; \qquad \mathbf{B}_d = \int_0^{\Delta t} e^{\mathbf{A}_c\tau} d\tau \mathbf{B}_c; \qquad \mathbf{C}_d = \mathbf{C}_c; \qquad \mathbf{D}_d = \mathbf{D}_c. \tag{2.19}$$

Where $e^{\mathbf{A}_c\Delta t}$ denotes the matrix exponential. The Eigenvalue problem can be solved in the same way as Equation (2.17). It should be noted that the resulting discrete, complex Eigenvalues λ_{di} correspond to the continuous ones with $\lambda_{ci} = |\lambda_{di}|/\Delta t$. The system in 2.18 has no noise terms, either in the input nor output term. If a system is randomly excited, unknown input- and measuring errors must be covered. The force vector is neglected and both equations are extended by noise terms:

$$\mathbf{x}_{k+1} = \mathbf{A}_d\mathbf{x}_k + \mathbf{w}_k$$
$$\mathbf{y}_k = \mathbf{C}_d\mathbf{y}_k + \mathbf{v}_k. \tag{2.20}$$

Here $\mathbf{w}_k$ and $\mathbf{v}_k$ are zero mean white gaussian noise terms called *process noise* (covering discretization errors and excitation) and *measurement noise*, respectively. Hence, $E[\mathbf{w}] = 0$ and $E[\mathbf{v}] = 0$. Further, for random excitation, the following expectation values can be given:

$$E[\mathbf{x}_k\mathbf{w}_k^T] = 0, \qquad E[\mathbf{x}_k\mathbf{v}_k^T] = 0, \qquad E[\mathbf{w}_{k+1}\mathbf{y}_k^T] = 0, \qquad E[\mathbf{v}_{k+1}\mathbf{y}_k^T] = 0. \tag{2.21}$$

These system descriptions and matrices will provide the basis for the system identification methods discussed within the following chapter. For detailed theoretical insights to modal analysis it is referred to [14, 53, 119] .

2.3 System Identification

The following section will provide a short introduction to a few *output-only* system identification techniques and what is done to extract modal parameters from their results[1]. Two time-domain based methods will be outlined: *Auto-Regressive* models and the *Stochastic Subspace Identification*.

---

1   In many cases the term *System Identification* is used synonymously for the identification of modal parameters. But, for more complex methods such as AR-models or SSI the general system identification will lead to a number of solutions, while only a subset of these solutions will represent modal parameters describing the analyzed physical structure. Many solutions will occur due to excitation, noise and mathematical reasons. Hence, the extraction of modal parameters is herein understood as a further step following the system identification.

In the studied case *output-only* means only the system responses, such as measured accelerations or strain, are used to perform identification. Forces acting on the structure being investigated remain unknown. This is due to the fact that, in general, it is impossible to accurately measure the input forces on complex large-scale structures such as wind turbines, bridges or skyscrapers. This fact reduces the number of available identification methods for the presented application. In any case, there are many solutions and approaches left to be applied in the studied case. An overview of *output-only* system identification methods is given in [27].

2.3.1 (Vector-) Auto-Regressive-Models

Originating from the field of economics, auto-regressive (AR) models have been applied in a wide field of applications over the last few decades [22]. Operational modal analysis (OMA) is one of the fields where AR-Models, used for modal parmeter estimation, proved to be of great value. Time series of structural responses are used as a basis for the modeling. In general, AR-Models describe a certain datum by weighted predecessors of one or more channels. All different derivations of this model class have this basic idea in common. A detailed insight into the various types can be found in [111]. If a certain time series is described by an AR-Model, it is possible to perform a prognosis of future time steps and to extract the system's (modal) properties [7, 8, 19, 23] . When several data channels are used, the models are called vector auto-regressive (VAR)-Models.

In this work, VAR-Models are used to calculate condition parameters. Through the use of auto-regressive moving average (ARMA)-Models the quality of prediction at a certain model order was able to be improved. Further, time-variant ARMA-models (TARMA) with varying coefficients modeled by sine and cosine, can be used to cover varying system properties [151]. However, the involved computations are rather expensive and equally good results can be achieved with AR-models of higher order [146]. Hence, only non-varying VAR-Coefficients serve as basis for system identification and condition parameters. The principal construction of a VAR(p)-model of order p is

$$\mathbf{y}_k = \boldsymbol{w} + \sum_{l=1}^{p} \mathbf{A}_l \mathbf{y}_{k-l} + \boldsymbol{\varepsilon}_k. \tag{2.22}$$

Where $\mathbf{y}_k$ is a m-variant time series at time instant k (see Equation (2.1)). The constant weighting coefficients in matrices $\mathbf{A}_1,...,\mathbf{A}_p$ are multiplied with previous time steps of $\mathbf{y}$. Each predicted data point for a certain channel depends on $\boldsymbol{p}$ previous values of its own time series and all other channels. Since this sum is only an estimate, differences between estimate and original time series occur. These are covered by the independent, zero-mean, Gaussian distributed noise terms $\boldsymbol{\varepsilon}_k$. Constant offsets can be captured by $\boldsymbol{w}$. A detailed procedure for estimating the coefficient matrices $\mathbf{A}_l$ from the given time series $\mathbf{y}$, with the goal of minimizing $\boldsymbol{\varepsilon}$ through least squares, can be found in [133].

2.3.2 Stochastic Subspace Identification

The stochastic subspace identification (SSI) - method is a data driven time domain identification method using output-only data to estimate a stochastic state space system as in (2.20). It was introduced by van Van Overschee and De Moor [197, 198] and is based on the eigensystem realization algorithm (ERA) by Juang [92]. The original code, performing excellently after correction of a few Matlab expressions, can be found on floppy disk in [198]. Over the last two decades, the method has been widely used in the field of civil and mechanical engineering and has provided very good results (see e.g. [123, 124]).

In general, two different schemes of SSI exist. One is the co-variance driven SSI (SSI-Cov), the other a data driven SSI (SSI-Data) formulation [142, 144, 146]. Both methods are derived from a state space system with random white noise inputs as given in (2.20). If the assumption of white noise excitation is violated, frequency parts of the colored noise will occur in the SSI solutions. In practice, this will always be the case, since excitation such as wind and waves will have colored spectra. For OWTs also the blade excitation, resulting from each blade passing the tower dam and unbalances, have a distinct frequency that depends on the rotor speed Ω and also occurs in higher harmonics (see Chapter 5). SSI-Data and the first step of SSI-COV will be used for system identification and the estimation of condition parameters respectively.

Covariance driven SSI

For the covariance driven identification, an output covariance matrix for a certain time shift i is calculated from the given output signals defined as

$$\mathbf{R}_i = E[\mathbf{y}_{k+i}\mathbf{y}_k^T] = \lim_{n_t \to \infty} \frac{1}{n_t} \sum_{k=0}^{n_t-1} \mathbf{y}_{k+i}\mathbf{y}_k^T. \tag{2.23}$$

For application, the number of data samples n_t will not tend to infinity. Hence the sum is calculated for a finite number of samples. It can be shown that $\mathbf{R}_i \in \mathbb{R}^{m \times m}$ can be decomposed into the (*system* and *output*) state space matrices of (2.20) with

$$\mathbf{R}_i = E[\mathbf{y}_{k+i}\mathbf{y}_k^T] = \mathbf{C}_d \mathbf{A}_d^{i-1} \mathbf{G}. \tag{2.24}$$

and $\mathbf{G} = E[\mathbf{x}_{k+1}\mathbf{y}^T]$ being the state-output covariance matrix. To estimate the state space matrices, a block matrix with a Hankel structure is built from a set of output covariances with different offsets i as shown in (2.25).

$$\mathcal{H}_{p+1,q} = \begin{bmatrix} \mathbf{R}_0 & \mathbf{R}_1 & ... & \mathbf{R}_{q-1} \\ \mathbf{R}_1 & \mathbf{R}_2 & ... & \mathbf{R}_q \\ ... & ... & ... & ... \\ \mathbf{R}_p & ... & ... & \mathbf{R}_{p+q-1} \end{bmatrix} \in \mathbb{R}^{m \cdot p \times m \cdot q} \tag{2.25}$$

Where $p=q$ in most applications. Hence, $\mathcal{H}_p := \mathcal{H}_{p+1,q}$ for $p = q$ is defined. This matrix can be decomposed into the *extended observability matrix* $\boldsymbol{\Gamma}_i \in \mathbb{R}^{m \cdot i \times n}$ and the *reversed extended stochastic controllability matrix* $\mathbf{O}_i \in \mathbb{R}^{n \times m \cdot i}$ by introducing (2.24) into (2.25) with:

$$
\mathcal{H}_p = \begin{bmatrix} \mathbf{C}_d \\ \mathbf{C}_d \mathbf{A}_d \\ ... \\ \mathbf{C}_d \mathbf{A}_d^{p-1} \end{bmatrix} \begin{bmatrix} \mathbf{G}_d & ... & \mathbf{A}_d^{i-2}\mathbf{G}_d & \mathbf{A}_d^{p-1}\mathbf{G}_d \end{bmatrix} = \boldsymbol{\Gamma}_i \mathbf{O}_i. \tag{2.26}
$$

From theory, each column of $\mathcal{H}_p$ is a free decay to as yet unknown initial conditions and $\boldsymbol{\Gamma}_i$ contains the Kalman states at time lag zero [24]. It is obvious that the desired system matrices can be calculated directly from the observability matrix. To do so, $\mathcal{H}_p$ is decomposed through singular value decomposition:

$$
\mathcal{H}_p = \mathbf{U}\mathbf{S}\mathbf{V}^T. \tag{2.27}
$$

Here, $\mathbf{U}$ and $\mathbf{V}$ are full matrices holding the singular vectors and $\mathbf{S}$ is of diagonal structure holding the singular values. Further, the SVD is truncated to the model order n. Looking at the singular values of $\mathbf{S}$ to estimate the accurate model order is often suggested. Theoretically, there is a maximal "gap" between two singular values, indicating the optimal model order. In practice, several or any of these gaps will be present in $\mathbf{S}$. To avoid this problem, solutions for several orders are calculated and *stabilization diagrams* can lead to a subset of solutions with physical relevance (see 2.4.2). Estimates of the observability and controllability matrix from measured outputs, indicated by $\hat{\boldsymbol{\Gamma}}$ and $\hat{\mathbf{O}}$, are calculated from the decomposed block Hankel matrix through

$$
\hat{\boldsymbol{\Gamma}}_i = \mathbf{U}\mathbf{S}^{1/2}; \qquad\qquad \hat{\mathbf{O}}_i = \mathbf{S}^{1/2}\mathbf{V}^T. \tag{2.28}
$$

Since $\mathbf{S}$ is a diagonal matrix, it is easy to calculate the roots of the diagonal entries. The discrete output matrix $\mathbf{C}_d$ can be found directly from the first block of $\hat{\boldsymbol{\Gamma}}_i$, the system matrix $\mathbf{A}_d$ from the lower blocks. Eigenvalues and Eigenvectors can be calculated as indicated in (2.10) and (2.16).

Data driven SSI

The data driven stochastic subspace identification avoids the computation of correlations between the outputs. Blocks of the output signals are stacked into a matrix and the so-called *future* row spaces ($\mathbf{Y}_{hf}$) are projected into the *past* row spaces ($\mathbf{Y}_{hp}$) [197, 198]. To do so, an output block Hankel matrix $Y_h \in \mathbb{R}^{2 \cdot m \cdot i \times n_t - 2i}$ can be built by stacking $2i$ data blocks with $n_t - 2i$ samples

from the complete set of measured outputs $\mathbf{Y}$ given in (2.1):

$$
Y_{(0,2i-1)} = \left[\begin{array}{ccccc}
\mathbf{y}_0 & \mathbf{y}_1 & \mathbf{y}_2 & \cdots & \mathbf{y}_{j-1} \\
\mathbf{y}_1 & \mathbf{y}_2 & \mathbf{y}_3 & \cdots & \mathbf{y}_j \\
\cdots & \cdots & \cdots & \cdots & \cdots \\
\mathbf{y}_{i-1} & \mathbf{y}_i & \mathbf{y}_{i+1} & \cdots & \mathbf{y}_{i+j-2} \\
\hline
\mathbf{y}_i & \mathbf{y}_{i+1} & \mathbf{y}_{i+2} & \cdots & \mathbf{y}_{i+j-1} \\
\cdots & \cdots & \cdots & \cdots & \cdots \\
\mathbf{y}_{2i-2} & \mathbf{y}_{2i} & \mathbf{y}_{2i+1} & \cdots & \mathbf{y}_{2i+j-3} \\
\mathbf{y}_{2i-1} & \mathbf{y}_{2i+1} & \mathbf{y}_{2i+2} & \cdots & \mathbf{y}_{2i+j-2}
\end{array}\right] = \left[\begin{array}{c} \mathbf{Y}_{(0,i-1)} \\ \hline \mathbf{Y}_{(i,2i-1)} \end{array}\right] = \left[\begin{array}{c} \mathbf{Y}_{hp} \\ \hline \mathbf{Y}_{hf} \end{array}\right].
\tag{2.29}
$$

The first subscript in $\mathbf{Y}_{(\bullet,\bullet)}$ denotes the upper left, the second the lower left entry of the block Hankel matrix, respectively. To underline the direction of time shifts, the upper block of this matrix ($\mathbf{Y}_{hp}$) is called the *past*, the lower block ($\mathbf{Y}_{hf}$) the *future*. Directly from the $2i$ block rows and the number of time samples n_t, a maximum block length follows with $n_t - 2i$. The orthogonal projection of row spaces for the future matrix $\mathbf{Y}_{hf}$ onto the past $\mathbf{Y}_{hp}$ is defined as

$$
E(\mathbf{Y}_{hf}|\mathbf{Y}_{hp}) = \mathbf{Y}_{hf}\mathbf{Y}_{hp}^T \left(\mathbf{Y}_{hp}\mathbf{Y}_{hp}^T\right)^{\dagger} \mathbf{Y}_{hp},
\tag{2.30}
$$

$\bullet^{\dagger}$ denotes the Moore-Penrose pseudo-inverse of $\bullet$ [198]. This projection can be decomposed in the same way as (2.26) and (2.27) to estimate the state space matrices. Van Overschee and De Moor use quotient-singular value decomposition (QSVD, [196]) of the data block Hankel matrix to calculate the state space matrices through observability and controllability matrices. A detailed derivation of the procedure that results in a similar formulation as in (2.26) to (2.28), can be found in [197].

Using this method, it is very convenient and fast to calculate a large number of different model orders, since from a system of maximum model order the lower orders can be calculated directly without the need for further matrix decompositions. The largest extractable model order can be estimated from the number of block rows $2i$ times the number of data channels m. The calculation of several orders leads to a set of solutions $\mathcal{S}_{SSI}$. Each solution $\mathcal{S}_{SSI,i}$ holds model order p, complex Eigenvalue λ and complex Eigenvector ψ as attributes. Each denoted with $\mathcal{S}_{SSI,i}^p$, $\mathcal{S}_{SSI,i}^{\lambda}$ and $\mathcal{S}_{SSI,i}^{\psi}$, respectively. These attributes will be used in 2.4.2 to distinguish between mathematical and physical solutions.

2.4 Automated Extraction of Modal Parameters

The boost in computing capacity and the possibility of performing parametric system identification for a large number of different model orders within a short time avoids the iterative estimation of an optimal model order but raises the problem of separation between a growing number of spurious solutions and the desired extraction of modal parameters. This problem is addressed using stabilization diagrams. Typically the frequency of each solution is plotted over the model order.

Stable paths, with a fairly constant frequency (and damping, plus optional further parameters) over several model orders, are assumed to belong to physical solutions and thus represent the modal properties of the underlying system. Scattering points, in contrast, represent spurious solutions which need to be sorted out. Based on the above mentioned initial set of solutions $\mathcal{S}_{SSI}$, different parameters can be defined to separate between physical an erroneous solutions in a stability diagram. Some are explained in the following sub-chapters.

2.4.1 Modal Validation Parameters

As mentioned previously, each solution or mode $\mathcal{S}_i$ from any parametric system identification method has the same attributes, namely, the Eigenvalue λ_i (from this also frequency f_i and damping ζ_i), the complex Eigenvector ψ_i and the model order p. The solution's components are addressed with $\mathcal{S}_i^p$, $\mathcal{S}_i^f$, $\mathcal{S}_i^\zeta$ and $\mathcal{S}_i^\psi$. Using (2.31), (2.32) and (2.33) relative differences between two modes can be calculated from frequencies, damping ratios and Eigenvectors. The frequency difference between two modes $\mathcal{S}_i$ and $\mathcal{S}_j$ is defined as

$$d_{f_{i,j}} = d(\mathcal{S}_i^f, \mathcal{S}_j^f) = |\mathcal{S}_i^f - \mathcal{S}_j^f| \tag{2.31}$$

and the difference in damping as

$$d_{\zeta_{i,j}} = d(\mathcal{S}_i^\zeta, \mathcal{S}_j^\zeta) = |\mathcal{S}_i^\zeta - \mathcal{S}_j^\zeta|. \tag{2.32}$$

For both, small values indicate close modes. The similarity between two Eigenvectors is calculated via the modal assurance criterion (MAC)[5, 6].

$$\text{MAC}(\mathcal{S}_i^\psi, \mathcal{S}_j^\psi) = \frac{|\mathcal{S}_i^{\psi*}\mathcal{S}_j^\psi|^2}{|\mathcal{S}_i^{\psi*}\mathcal{S}_i^\psi||\mathcal{S}_j^{\psi*}\mathcal{S}_j^\psi|} \in [0,1], \tag{2.33}$$

two vectors are linear dependent for $MAC(\psi_i, \psi_j) = 1$, usually a threshold of 0.9 to 0.99 is set to indicate similarity of modes. It should be noted that these three distance measures can only be applied to pairs of modes.

The fourth applied criterion is the mean phase deviation (MPD) of a single mode shape [157]. This intuitive variable illustrates how severe the entries of a certain complex Eigenvector diverge from a straight line in the complex plane. For linear, proportionally damped systems, the phase angle between different DoFs should either be 0 or 180° resulting in a MPD of 0°. For OMA, this will never be exactly the case but for lightly damped systems, small phase diversions still indicate physical modes. Large phase divergences indicate modes resulting from noise or external excitation. First, for an Eigenvector a line through the origin in the complex plane with best fit for all DoFs, is calculated. To do so, its real and imaginary components are separated and combined in $\mathbf{X} = [Re(\psi_i), Im(\psi_i)] \in \mathbb{R}^{m \times 2}$. Using a singular value decomposition, $\mathbf{X}$ is decomposed into

$$\mathbf{X} = \mathbf{U}\mathbf{S}\mathbf{V}^T. \tag{2.34}$$

For the two-dimensional case given, the mean phase (MP) (the rotation angle for the optimally fitted line), can be calculated directly from $\mathbf{V} \in \mathbb{R}^{2 \times 2}$ using (2.35).

$$\text{MP}(\mathcal{S}_j^\psi) = \arctan\left(\frac{-\mathbf{V}_{11}}{\mathbf{V}_{22}}\right) \in [0, 180] \tag{2.35}$$

Further, for each DoF $\mathcal{S}_{i,j}^\psi$ of the Eigenvector $\mathcal{S}_i^\psi$, a line through origin in the complex plane can be drawn and the angle $\beta_{i,j}$ between that line and the line with $\text{MP}(\mathcal{S}_i^\psi)$ rotation is calculated. The weighted MPD is then defined as

$$MPD(\mathcal{S}_i^\psi) = \frac{\sum\limits_{j=1}^{m} |\mathcal{S}_{i,j}^\psi| \beta_{i,j}}{\sum\limits_{j=1}^{m} |\mathcal{S}_{i,j}^\psi|} \in [0, 45[. \tag{2.36}$$

The weighting is proportional to the inverse of the DoFs amplitude. Accordingly, for DoFs with large amplitudes larger deviations are allowed. Further, modal transfer norms [72] and uncertainty bounds [155], for modes from SSI, can be calculated. However, in this study only (2.32) - (2.36) are used.

2.4.2 Stabilization Diagrams

SSI- and AR-Models, or indeed any other parametric system identification procedures, lead to a growing number of solutions with increasing model order. In the beginning of OMA and EMA, an optimal model order was selected and all solutions of the model were taken as modes. Estimating an optimum model order might be very time consuming and the optimal order might be subject to changes due to loading scenarios. Further, the estimation of models with a high order became very affordable in a computational sense. Accordingly, it is a common practice to estimate models for many different model orders and to track similar solutions. As a drawback, models with a high order will contain purely mathematical solutions and those resulting from external forces and noise, dubbed *spurious*. Accordingly, spurious solutions need to be eliminated. As already stated by Peeters and De Roeck (for reference based SSI-models), it is better to over-specify the model order and eliminate mathematical solutions afterwards than to choose a (too) low order [142]. To perform this separation, stabilization diagrams are a popular visual tool. Today the idea of stabilization diagrams is the basis for a variety of procedures for the extraction of modal parameters (see 2.4).

To derive a stabilization diagram, all solutions of $\mathcal{S}$ are plotted over their model order (y-axis) and frequency (x-axis). Damping can be included along the z-axis in a three-dimensional plot. If the analyzed data contains physical modes, "paths" at certain frequencies, that run over many different model orders will become clearly visible (see 3.5 on page 65). A second important hint for a stability is a fairly constant (and reasonable) damping value along the path. This can be used as a second indicator in combination with constant frequencies. For structures within civil engineering in general the modal damping will be quite low around $1 - 5\%$, especially for steel

structures. If artificial damping is added, for example using dampers, this value might rise up to 10%. A third indicator for multi degree of freedom systems is the Eigenvector. Typically vectors are compared using MAC-values (see Equation 2.33). The MAC value is calculated between two modes, typically between a single mode and the Eigenvectors of all other modes of an adjacent model order p or even all other Eigenvectors. For these three indicators (frequency, damping and Eigenvector) Peeters and De Roeck [142] suggest a maximal variation of 1%, 5% and 1%, respectively, to indicate stable paths. However, these values postulate optimal conditions and a sufficiently excited structure.

Generally speaking, the extraction of modal parameters is a clustering problem where a set of solutions $\mathcal{S}$ has to be divided into several clusters in a multi-dimensional space. Spurious solutions need to be eliminated using thresholds and paths within proper clusters need to be identified. Utilizing the validation parameters in 2.31, 2.32, 2.33 and 2.36 along with a *Delaunay*-Triangulation, a new procedure for modal parameter extraction will be presented in 3.2, other clustering methods are outlined in the next sub-chapter.

2.5 Machine Learning

Machine learning (ML), often also dubbed data normalization, as a group of methods to learn patterns in data, is a critical component of SHM, particularly when structures with changing dynamic characteristics are being investigated. As stated in Chapter 1.3.1, many different procedures exist to realize the ML-step in SHM-analysis and only two applied unsupervised ML-approaches will be outlined here.

In general, the relationship between an input and an output parameter is "learned" from training data dubbed $\tilde{\mathcal{D}} := \mathcal{D}_i; i \in [1,...,n_{nt}]$ by their EOC-components $\mathcal{D}_i^{\textbf{EOC}1}$. Each later ML setting or type will result in a division of $\tilde{\mathcal{D}}$ into several clusters with $\tilde{\mathcal{D}} = D_1, D_2, ... D_k$ and hence an allocation of each data instance into a certain cluster. If actual points from the set are taken as centers, they are called *exemplars*. The following sub-chapters give a brief introduction to the underlying theory of both methods.

2.5.1 K-centers and K-means

A standard approach for clustering is *k-centers*-clustering [2], where k points $\in \mathbb{R}^{\bar{n}}$ are randomly chosen from the data instances $\tilde{\mathcal{D}}$ to be *exemplars* for k sub sets [114]. The remaining points are assigned to the centers as to reduce the summed squared error J, usually Euclidean distance (see Equation 2.49), between *exemplars* and points. Another commonly used procedure is *k-means*-clustering. Here, the distance between the cluster centroids, not a single exemplar (point), and its

---

1   It should be noted that for large numbers of available training data instances n_{nt} sets can be selected (randomly).
2   E.g. implementations are available in Matlab.

corresponding points is minimized. Both procedures are realized through minimizing

$$J = \sum_{j=1}^{k} \sum_{i \in P_j} ||P_i - \mu_{c_j}||. \tag{2.37}$$

P_j contains all points assigned to cluster j with exemplar or center μ_{P_j} during a single iteration. Both procedures are quite sensitive to the initial set of exemplars/centroids and therefore usually repeated many times with varying sets of exemplars to increase the chance of finding the global minimum. One of the major drawbacks of these methods is the fixed number of centers/centroids that has to be chosen initially by the user. Here, *k-means*-clustering will serve as a reference for assessing the performance of *Affinity Propagation*, which will be introduced in the next sub-chapter.

2.5.2 Affinity Propagation

In the presented work, a rather new method introduced in Dueck [52], Frey and Dueck [63], dubbed *Affinity Propagation* (AP) is used. It solves the problem of clustering by passing information or *messages* between data points without the need for a pre-defined number of cluster. It is proven to be very fast compared to standard clustering approaches, examples for a variety of fields are given in [63].

Rather than taking the actual positions $\in \mathbb{R}^{\bar{n}1}$ of all points into account, so called *similarities* $s(i,k)$ between point i and k are calculated. In the standard case these are negative Euclidean distances but potentially may be any (distance) measure between two points. The possibility of setting $s(i,k) \neq s(k,i)$ is a unique feature in clustering. Self-similarities $s(k,k)$ are dubbed *preferences*, indication how well suited point k is to be an exemplar (cluster center). The number of resulting centers partly depends on these *preferences*[2].

With these similarities, indicating "how well the data point with index k is suited to be the exemplar for point i" [63], the iterative procedure is started. During the iterations, two different messages are passed between the data points. One is the responsibility $r(i,k)$, sent from point i to candidate exemplar k. It "reflects the accumulated evidence for how well-suited point k is to serve as the exemplar for point i, taking into account other potential exemplars for point i" [63]. The updating rule is

$$r(i,k) \leftarrow s(i,k) - max\{a(i,k') + s(i,k')\}, k' \neq k. \tag{2.38}$$

In contrast, the *availability* $a(k,i)$ "from candidate exemplar k to point i, reflects the accumulated evidence for how appropriate it would be for point i to choose point k as exemplar, taking into

---

1   For SHM the position in the EOC space.
2   Frey and Dueck recommend setting all *preferences* to the median of $s(i,k); i,k \in [1,...,n_{nt}]$ for a moderate number of centers.

account the support from other points that point k should be an exemplar". Updated through

$$a(i,k) \leftarrow min\{0, r(k,k) + \sum_{i' \neq \{i,k\}} max\{0, r(i',k)\}\}. \tag{2.39}$$

Hence, there is one measure $r(i,k)$ from point to candidate giving support and one from candidate to point $a(k,i)$ collecting support. The self-availability is updated with

$$a(k,k) \leftarrow \sum_{i' \neq k} max\{0, r(i',k)\}\}. \tag{2.40}$$

At different stages of computation, availabilities and responsibilities can be compared to extract exemplars from the data points. "For point i, the value of k that maximizes $a(i,k) + r(i,k)$ either identifies point i as an exemplar if $k = i$," Frey and Dueck [63] or another point for $k \neq i$. The procedure can be stopped after a fixed number of runs, when the passed messages fall below a threshold or if no changes in the decisions can be observed for several iterations. Detailed insights into the algorithm can be found in Dueck [52], Frey and Dueck [63] and a complete Matlab code is provided on-line as well. For the presented SHM framework, different realizations of AP, by selected EOCs or different preference values, will be indicated by ML^{AP_i}.

2.6 Condition Parameters

In the context of SHM, condition parameters (CPs) are values derived from measured time series that serve as a basis for decision-making regarding the systems state. *Absolute* CPs can be directly calculated from a single time series of dynamic response data, if *relative* CPs, or residues, are used then a reference data instance is needed. In this case, the CP-value depends on machine learning since it defines the reference data instances. This distinction is necessary in the view of the author, since *relative* CPs require an extra step within the SHM framework: Those values have to be re-calculated for every ML realization, since references might change. Based on a sample of similar CPs, e.g. taken from a cluster, decision boundaries can be drawn and statements about the current condition can be given in the hypothesis testing step described in 2.7. The following sections will derive the mathematical formulations for several CPs used within this work. In this context, the different condition parameters are indicated by $CP^{\bullet}_{\bullet}$. The superscript holds the CP name or symbol, while the subscript holds additional, CP-dependent parameters. An overview of the different CPs can be found in Table 3.3.

2.6.1 Absolute Condition Parameters

The following CPs can be calculated from single data instances (and channels) and are therefore dubbed *absolute* CPs.

Statistics

Some very basic parameters for SHM can be directly calculated from the time series of a single sensor. Even though these are not the most sophisticated CPs, their estimation can reveal important (and fast) insight into the validity of data instances next to abnormality detection for dynamic behavior. Starting from the collected time series $\mathbf{Y}$ in Equation 2.1, the n-th statistical moment of channel i is defined as

$$\mu_{(i),n} = E[(E[\mathbf{y}_{(i)}] - \mathbf{y}_{(i)})^n]. \tag{2.41}$$

For the discrete case it is approximated with

$$\mu_{(i),n} = \frac{1}{n_t - 1} \sum_{k=1}^{n_t} (\bar{y}_{(i)} - y_{(i),k})^n. \tag{2.42}$$

With $\bar{y}_{(i)}$ as the mean of channel i. Accordingly, the CPs for standard deviation, skewness, and kurtosis are defined as

$$CP_{(i)}^{\sigma} = \sigma_{(i)} = \sqrt{\mu_{(i),2}} = \sqrt{\frac{1}{n-1} \sum_{j=1}^{n} \left(\bar{y}_{(i)} - y_{(i),j} \right)^2} \tag{2.43}$$

$$CP_{(i)}^{\gamma_1} = \frac{\mu_{(i),3}}{\sigma_{(i)}^3} = \frac{1}{n} \sum_{j=1}^{n} \left(\frac{\bar{y}_{(i)} - y_{(i),j}}{\sigma_{(i)}} \right)^3 \tag{2.44}$$

$$CP_{(i)}^{\gamma_2} = \frac{\mu_{(i),4}}{\sigma_{(i)}^4} = \frac{1}{n} \sum_{j=1}^{n} \left(\frac{\bar{y}_{(i)} - y_{(i),j}}{\sigma_{(i)}} \right)^4, \tag{2.45}$$

respectively. While CP^{σ} represents the width of the distribution's density function, CP^{γ_1} indicates the asymmetry and CP^{γ_2} the peakness. If CP^{γ_1} becomes negative, the data is located more below the mean, if $CP^{\gamma_1} > 0$ the data is more located above. $CP^{\gamma_2} = 0$ indicates a mesokurtic distribution (normally peaked), $CP^{\gamma_2} < 0$ a leptokurtic (more strongly peaked) distribution, and $CP^{\gamma_2} > 0$ a platykurtic (flattened) distribution.

Accumulated Energy

Accumulated energy (AE) is defined as the integral of a power spectral density (see Equation 2.5) and serves as an indicator for energy distribution within a certain frequency range of a given signal. In the context of the SHM framework, the AE is calculated for each channel and data instance. It is defined as

$$E_{ii}(\omega_k) = \frac{100 * \hat{E}_{ii}(\omega_k)}{\hat{E}_{ii}(\omega = \frac{f_s}{2})} \in [0,100] \, \% \tag{2.46}$$

where

$$\hat{E}_{ii}(\omega_k) = \sum_{n=1}^{k} |S_{ii}(\omega_n)|. \tag{2.47}$$

Following 2.46 and 2.47 $E_{ii}(\omega_k)$ relates each frequency between 0 and $\frac{f_s}{2}$ Hz (Nyquist frequency) to an energy level between 0 and 100%. The value for $E_{ii}(\omega_k)$ denotes the percentage of energy that is present in the signal up to ω_k, summing up all k values at discrete frequencies. Vice versa, once $E_{ii}(\omega)$ is calculated, the frequency ω_{e_j} at which a given energy level e_j is reached, can be derived. Following these derivations, a new CP is defined in Chapter 3.1.

Modal Parameters

Another well known group of CPs are modal parameters. Commonly, modal frequencies as in Equation 2.11 are extracted from each data instance and monitored over time. In this work, the condition parameter is simply defined as the i-th modal frequency with

$$CP^{f_i} = f_i, i \in [1,...,n_f]. \tag{2.48}$$

A problem arising from an automated extraction of modal parameters is the varying number of resulting frequencies per data instance, n_f. For an analysis, one has to be careful when comparing CPs over many data instances since only frequencies belonging to the same mode have to be included. Here, the newly introduced TEMP-procedure (see 3.2) can be of great value: Results from the training phase can be processed as in a stabilization diagram and frequencies are grouped automatically. Sometimes modal damping is investigated as well, but it suffers from larger errors and estimation quality is generally lower.

2.6.2 Relative Condition Parameters

The following sub-chapters will outline the theory necessary for the estimation of relative CPs. In general, every absolute CP can also be formulated as residue, directly comparing two data instances or a new data instance with a reference. Reference definition is achieved through machine learning. This reference must not be confused with the reference that is taken for the derivation of control charts in which boundaries are calculated for every CP from a distribution taken from the training phase for both, absolute and relative CPs. References are initially needed to calculate the parameter and hence, have to be re-calculated for every ML instance. As a consequence, a single data instance will have different CP-values for each ML instance, in contrast to absolute CPs, for which the values stay constant for a single data instance, independent of the ML instance.

Distance Measures

Distance measures are the simplest example of a relative CP. Two commonly used measures are Euclidean and *Mahalanobis* squared distance (ESD, MSD), defined as

$$\mathsf{D}_{ES} = \sqrt{\sum_i (\bar{\mathsf{X}}_i - \mathsf{x}_i)^2} \tag{2.49}$$

$$\mathsf{D}_{MS} = (\bar{\mathsf{X}} - \mathsf{x})^T \mathbf{R}_0(\mathsf{X})^{-1} (\bar{\mathsf{X}} - \mathsf{x}), \tag{2.50}$$

respectively. Here, x is an arbitrary data vector and $\bar{\mathsf{X}}$ indicates the row wise mean of matrix X. X is composed of one or several reference vectors with the same dimension as x. $\mathbf{R}_0(\mathsf{X})$ is the covariance matrix of X with zero shift (see Equation 2.23).

These two measures can be used to compare two frequency spectra or vectorized AR-matrices from two different data instances to form a single, relative CP. This procedure is a handy way to reduce a CP's dimensionality but holds the drawback of transforming a multi-dimensional absolute CP into a scalar relative CP. MSD is often used in the context of data normalization and outlier analysis.

Residues from Stochastic Subspace Identification

Two different CPs can be derived from the block Hankel matrix used in SSI-Cov (see Equation 2.25). Both avoid the extraction of modal parameters and are based on a comparison of the Hankel matrix of a reference data instance, $\mathcal{H}_{p,ref}$, with one from a new measurement, $\mathcal{H}_{p,new}$. First, a singular value decomposition of the reference Hankel matrix $\mathcal{H}_{p,ref}$, with

$$\hat{\mathcal{H}}_{p,ref} = \hat{\mathbf{U}}\hat{\mathbf{S}}\hat{\mathbf{V}}^T \tag{2.51}$$

is performed. To assure a unique solution, all columns of $\hat{\mathbf{U}}$ and $\hat{\mathbf{V}}$ are multiplied by -1 if the corresponding column of $\hat{\mathbf{U}}$ has a negative first entry. Further, the three resulting matrices can be divided into blocks, resulting in

$$\hat{\mathcal{H}}_{p,ref} = \begin{bmatrix} \hat{\mathbf{U}}_1 & \hat{\mathbf{U}}_0 \end{bmatrix} \begin{bmatrix} \hat{\mathbf{S}}_1 & \mathbf{0} \\ \mathbf{0} & \hat{\mathbf{S}}_0 \end{bmatrix} \begin{bmatrix} \hat{\mathbf{V}}_1^T \\ \hat{\mathbf{V}}_0^T \end{bmatrix} \tag{2.52}$$

where $\hat{\mathbf{U}}_1, \hat{\mathbf{V}}_1, \hat{\mathbf{S}}_1 \in \mathbb{R}^{m*N_{shift} \times n_{sig}}$ and $\hat{\mathbf{U}}_0, \hat{\mathbf{V}}_0, \hat{\mathbf{S}}_0 \in \mathbb{R}^{m*n_{shift} \times n_{is}}$. Here, N_{shift} denotes the number of block rows in 2.29. n_{sig} and n_{is} denote the number of significant and insignificant columns, respectively. Obviously, $n_{sig} + n_{is} = m * n_{shift}$ must hold true. From this decomposition, two damage parameters can be derived.

The first relative CP from SSI used in this work is based on the interpretation of $\hat{\mathbf{U}}_0$ as a Nullspace of $\hat{\mathcal{H}}_p$, as proposed by Basseville et al. [13]. If n_{is} is properly chosen and Equation 2.52

is truncated to only $\hat{\mathbf{U}}_0$, $\hat{\mathbf{S}}_0$, and $\hat{\mathbf{V}}_0$, it can be re-written as

$$\hat{\mathbf{U}}_0^T \hat{\mathcal{H}}_p = \hat{\mathbf{S}}_0 \hat{\mathbf{V}}_0^T \approx \mathbf{0}. \tag{2.53}$$

This equation holds true if both $\hat{\mathbf{U}}_0^T$ and $\hat{\mathcal{H}}_{p,ref}$ are calculated from the same data instance and $n_{is} = m * n_{shift}$. Equation 2.53 will result in a matrix with small values for $n_{is} \leqq m * n_{shift}$. To compare two different states, the Hankel matrix of the current data instance $\mathcal{H}_{p,new}$ is multiplied by the Nullspace from a reference $\hat{\mathbf{U}}_{0,ref}$. The residual vector ζ is then defined as

$$\hat{\zeta} = \sqrt{N} * vec(\hat{\mathbf{U}}_{0,ref}^T \hat{\mathcal{H}}_{p,new}) \tag{2.54}$$

and the CP as its mean:

$$CP^\varepsilon(n_{shift}, n_{is}) = \bar{\zeta}. \tag{2.55}$$

The CP depends on the number of shifts in the Hankel matrix (n_{shift}) and the amount of insignificant columns chosen (n_{is}). If several data instances are used as reference, e.g. all data instances of a cluster, $\hat{\mathbf{U}}_0$ is calculated for each data instance in the reference and $\hat{\mathbf{U}}_{0,ref}$ is an average of the matrices $\hat{\mathbf{U}}_{0,ref_i}$. It should be noted that in the stated literature, the Nullspace-based CP is calculated from a Chi-square test statistic which results from

$$\chi^2 = \hat{\zeta}^T \mathbf{R}_0^{-1} \hat{\zeta}. \tag{2.56}$$

Recently, Döhler et al. [50] published a new version of the test parameter in Equation 2.56, which is claimed to display more robust behavior than previous formulations. It is also based on a Chi-square test statistic and built from the block Hankel matrix $\mathcal{H}_p$. In contrast to CP^ε, the residual vector is defined as

$$\hat{\zeta} = \sqrt{N} * vec(\hat{\mathbf{U}}_0^T * \hat{\mathbf{U}}_1) \tag{2.57}$$

where $\hat{\mathcal{H}}_p$ is replaced by $\hat{\mathbf{U}}_1$. Further, $\hat{\mathbf{R}}_0^{-1}$ in Equation 2.56 is divided into

$$\hat{\mathbf{R}}_0^{-1} = \hat{\mathbf{R}}_0^{-\frac{1}{2}T} \hat{\mathbf{R}}_0^{-\frac{1}{2}} = (\mathcal{A}\mathcal{K})^{\dagger T} (\mathcal{A}\mathcal{K})^\dagger. \tag{2.58}$$

To calculate the CP, $\hat{\mathbf{U}}_0$ and $\hat{\mathbf{R}}_0^{-\frac{1}{2}}$, or rather $\mathcal{A}$ and $\mathcal{K}$, are taken from the reference data instance(s)[1] and $\hat{\mathbf{U}}_1$ is calculated from the current data instance.

For an estimation of $\mathcal{A}$ and $\mathcal{K}$, the recorded data matrix $\hat{\mathbf{Y}}$ is divided into n_B blocks with $N_B = N/n_B \in \mathbb{Z}$ samples each. Each block "may be long enough to assume statistical independence between blocks"[50]. Now, sub Hankel matrices $\hat{\mathcal{H}}_p^{(j)}, j = 1, 2, ..., n_b$ are calculated for each data

---

1 In the same manner as for CP^ε, these matrices are averaged if several reference data instances exist.

block. Then, the matrix $\mathcal{K}$ is defined as

$$\mathcal{K} := \sqrt{\frac{N_B}{n_B - 1}} \begin{bmatrix} h_1 & h_2 & ... & h_j \end{bmatrix} \text{ with } h_j = vec(\hat{\mathcal{H}}_p - \hat{\mathcal{H}}_p^{(j)}), j = 1,2,...,n_b. \tag{2.59}$$

Matrix $\mathcal{A}$ is built from the sensitivities of the left singular vectors $\mathcal{J}_{\hat{\mathbf{U}}_1}$ of $\hat{\mathcal{H}}_p$ multiplied by the Nullspace with

$$\mathcal{A} = \left(\mathbf{I} \otimes \hat{\mathbf{U}}_0 \right) \mathcal{J}_{\hat{\mathbf{U}}_1} \tag{2.60}$$

in which

$$\mathcal{J}_{\hat{\mathbf{U}}_1} := \begin{bmatrix} \mathbf{E}_1 \mathbf{F}_1 \\ \vdots \\ \mathbf{E}_{n_B} \mathbf{F}_{n_B} \end{bmatrix} \tag{2.61}$$

and

$$\mathbf{F}_j := \frac{1}{\lambda_i} \begin{bmatrix} v_j^T \otimes \left(\mathbf{I} - u_j u_j^T \right) \\ \left(\mathbf{I} - v_j v_j^T \right) \otimes u_j^T \end{bmatrix} \qquad \mathbf{E}_j := \begin{bmatrix} \mathbf{I} + \mathbf{K}_j \left(\frac{\hat{\mathcal{H}}_p}{\lambda_j} - \begin{bmatrix} \mathbf{0} \\ u_j^T \end{bmatrix} \right) & \mathbf{K}_j \end{bmatrix}. \tag{2.62}$$

The vector u_j and v_j are taken from $\hat{\mathbf{U}}_1$ and $\hat{\mathbf{V}}_1$, respectively. Finally, $\mathbf{K}_j$ is defined as

$$\mathbf{K}_j := \frac{\hat{\mathcal{H}}_p}{\lambda_j} \left(\mathbf{I} + \begin{bmatrix} \mathbf{0} \\ 2v_j^T \end{bmatrix} - \frac{\hat{\mathcal{H}}_p^T \hat{\mathcal{H}}_p}{\lambda_j^2} \right)^{-1}. \tag{2.63}$$

For any data instance, the robust CP is calculated by

$$CP^\gamma(n_{shift}, n_{sig}, n_b) := \hat{\zeta}^T \hat{\Sigma}_{ref}^{-\frac{1}{2}T} \hat{\Sigma}_{ref}^{-\frac{1}{2}} \hat{\zeta} \tag{2.64}$$

with

$$\hat{\zeta} = \sqrt{N} * vec(\hat{\mathbf{U}}_{0,ref}^T * \hat{\mathbf{U}}_{1,new}) \tag{2.65}$$

and

$$\hat{\Sigma}^{-1/2} = (\mathcal{A}\mathcal{K})^\dagger. \tag{2.66}$$

Accordingly, both condition parameters, CP^γ and CP^ε, depend on the number of blocks in the Hankel matrix and the division of the SVD matrices into a significant and insignificant part. Furthermore, the second parameter also depends on the number of blocks the data instance is divided into. Both can handle a single or several reference data instances to calculate values for the current set.

Residues from Vector-Autoregressive-Models

For the derivation of relative CPs from VAR(p)-models, the difference between a measured time series $\mathbf{Y}$ and a time series estimate $\hat{\mathbf{Y}}$ modeled by AR-coefficients, is investigated. Through this comparison the $m \times n_t$-dimensional residual is reduced to a scalar as the MSD does in a different manner. In Equation (2.67) the time series Y_{new} of a new data instance is approximated through coefficients $\mathbf{A}_{ref}$ from a reference data instance, resulting in an estimate $\hat{\mathbf{Y}}_{new}(\mathbf{A}_{ref})$:

$$
\begin{aligned}
(\boldsymbol{\varepsilon}_k) &:= (\mathbf{y}_k)_{new} - \sum_{l=1}^{p} (\mathbf{A}_l)_{ref} (\mathbf{y}_{k-l})_{new} \\
\boldsymbol{\varepsilon} &:= \mathbf{Y}_{new} - \hat{\boldsymbol{Y}}_{new}(\mathbf{A}_{ref}).
\end{aligned}
\tag{2.67}
$$

If the coefficients $(\mathbf{A}_l)_{new}$ from the same data instance are used, $\boldsymbol{\varepsilon}$ is a measure of how well a certain data instance can be approximated by a VAR-model of order p. Recalling that $\mathbf{Y}$ has n_t samples, $\boldsymbol{\varepsilon}$ is $\in \mathbb{R}^{m \times n_t - p - 1}$. Two condition parameters are derived from the residue $\boldsymbol{\varepsilon}$: One is the coefficient of determination according to Neter et al. [132], with

$$
R^2 = \frac{1}{m} \sum_{s=1}^{m} \left(1 - \sqrt{\frac{\sum_{i=p+1}^{n_t} (\mathbf{y}_{(s),i} - \hat{\mathbf{y}}_{(s),i})^2}{\sum_{i=p+1}^{n_t} (\mathbf{y}_{(s),i} - \overline{\mathbf{y}}_{(s)})^2}} \right).
\tag{2.68}
$$

Here, $\overline{\boldsymbol{y}}_{(s)}$ is the mean value of the measured channel s. The fitted coefficient of determination, which takes the model order and number of samples into account, is the first AR-condition parameter with

$$
\tilde{C}P^{R^2} = \overline{R}^2 = 1 - (1 - R^2)\frac{n_t - 1}{n_t - p - 1}.
\tag{2.69}
$$

From theory, the boundaries for $\overline{R}^2$ can be given as in Table 2.1. Nevertheless, these boundaries will not be used directly since the validity for large scale structures under unknown EOCs is not granted and a similar processing of all CPs was desired in the presented scheme.

Since this parameter has an upper border of one and tends towards negative values for bad agreement between data instances, the suggestions is to transform $\tilde{C}P^{R^2}$ to behave as do the other monitored parameters according to

$$
CP^{R^2}(p) = -1 * (\tilde{C}P^{R^2} - 1).
\tag{2.70}
$$

This formulation is used in the presented SHM framework, CP^{R^2} has a lower border of zero and

Table 2.1: Theoretical boundaries for $\overline{R}^2$

$\overline{R}^2 = 1$	Perfect linear correlation between measurement and approximation, no damage.
$0.8 < \overline{R}^2 < 1$	Statistical deviation, no damage.
$\overline{R}^2 \ll 0.8$	No linear correlation, damage possible.

tends towards higher values for bad agreement. Table 2.1 translates to $CP^{R^2} = 0, 0 < CP^{R^2} < 0.2$, and $CP^{R^2} > 0.2$, respectively.

The second CP is based on the *M-Test* according to Box [21], Stevens [187]. For a derivation, the residue covariance matrix of a data instance is defined as

$$\hat{\boldsymbol{\Sigma}}_{AR} = \frac{1}{n_t - mp - 1} \sum_{k=1}^{n_t - mp - 1} \boldsymbol{\varepsilon_k \varepsilon_k}^T \in \mathbb{R}^{m \times m}. \tag{2.71}$$

The M-Test compares the consistency of distributions of a new covariance matrix $\hat{\boldsymbol{\Sigma}}_{AR,new}$ to the distributions of one (or several) reference covariance matrices $\hat{\boldsymbol{\Sigma}}_{AR,ref}$. The test statistic value is M with

$$M = (\tilde{n} - g)log|\boldsymbol{\Sigma}| - \sum_{i=1}^{g}(\tilde{n}_i - 1)log|\boldsymbol{\Sigma}_i| \text{ and} \tag{2.72}$$

$$\boldsymbol{\Sigma} = \frac{1}{\tilde{n} - g} \sum_{i=1}^{g}(m_i - 1)\boldsymbol{\Sigma}_i; \; \tilde{n} = \sum_{i=1}^{g}\tilde{n}_i. \tag{2.73}$$

m is the number of vectors in ε. Hence, it correlates with the number of input channels of the m-variant model. $\tilde{n}_i$ is the number of data points in $\boldsymbol{\varepsilon}$, depending on the number of samples n_t, the model order p and number of input channels m with $\tilde{n}_i = n_t - mp - 1$. Further, g is the number of covariance matrices combined in *the pooled covariance matrix $\boldsymbol{\Sigma}$*. If two data instances are compared, covariance matrices $\hat{\boldsymbol{\Sigma}}_{AR,new}$ and $\hat{\boldsymbol{\Sigma}}_{AR,ref}$ are used. For sufficiently large $\tilde{n}_i$ (e.g. $\tilde{n}_i > 20$ see [187], which is assumed here) M approximately has a χ^2 distribution with f_{χ^2} degrees of freedom. For smaller values, M is F-distributed and further values have to be calculated, see [21]. M is fitted in a manner that the confidence interval can directly be calculated from the inverse χ^2-distribution. The level of significance P, which displays the probability for a certain value of M, is then calculated by

$$P = 1 - \chi^2(M(1 - \gamma), f_{\chi^2}) \tag{2.74}$$

with

$$f_{\chi^2} = \frac{m(m+1)(g-1)}{2} \text{ and } \gamma = \frac{2m^2 + 3m - 1}{6(m+1)(g-1)}\left(\sum_{i=1}^{g}\frac{1}{\tilde{n}_i - 1}\frac{1}{\tilde{n} - g}\right). \tag{2.75}$$

The desired condition parameter is defined as

$$CP^{\mathcal{M}}(p) = M(1 - \gamma) < \left[\chi^2_{(1-\alpha), f_{\chi^2}}\right]^{-1}. \tag{2.76}$$

$CP^{\mathcal{M}}$ is zero if two similar data instances are compared and tends to large values for differing sets.

Estimation of an Optimal Model Order

In contrast to the extraction of modal parameters (using stability diagrams), a single model order p is used for both VAR-based CPs. Hence, it is important to choose this order carefully. An a priori estimation of model orders for AR-models is a wide field that provides many different approaches and possible parameters. It is beyond the scope of this work to discuss these values in detail. Two different approaches are introduced to indicate an optimal model order for m-variant time series. Namely, the *Schwarz's Bayesian Criterion*(SBC) and the *Akaikes's Final Prediction Error*(FPE), derivations for these and further iterative criteria can be found in [111, 133]. A third, straight forward criterion, the *Cover-Factor*(CF) according to Haake [75], Rolfes et al. [163] which is estimated empirically, is also taken into account.

$$SBC(p) = \frac{log(det(\hat{\boldsymbol{\Sigma}}_{AR}\tilde{n}_t))}{m} - (1 - \frac{mp+1}{n_t})log(N) \tag{2.77}$$

$$FPE(p) = \frac{log(det(\hat{\boldsymbol{\Sigma}}_{AR}\tilde{n}_t))}{m} - log\frac{n_t\tilde{n}_t}{n_t + mp + 1} \tag{2.78}$$

$$CF = \frac{k_{AR,f_u} \cdot f_s}{f_u}. \tag{2.79}$$

With $\tilde{n}_t = n_t - (mp+1)$. In (2.79), f_u is the lowest frequency that needs to be described by the AR-Model and k_{AR,f_u} is the *Cover Factor* that describes what percentage of the f_u-oscillation is covered by the AR-coefficients. A value of $k_{AR,f_u} = 0.7$ provided good results for different offshore structures with a mono-pile foundation [75]. Due to their slender structure, this value can also be assumed to be sufficient for tripod and jacket based OWTs. Furthermore, this *Cover Factor* is also applicable to SSI-models. The number of offsets e.g. from (2.25) or (2.29) times inverse sampling frequency f_s gives a certain time span. This time span compared to the period of the lowest modal frequency of interest can also be interpreted as a *Cover Factor*.

2.7 Hypothesis Testing

Hypothesis testing (HT) defines the process of evaluating a postulated hypothesis, in this case the healthy state of a structure. Up to this point, different procedures for machine learning (ML), along with the definition of several condition parameters (CPs), have been introduced. Independent of what ML-CP combination is used, a set of CP values from training data instances, in combination with a similar CP from a new, incoming data instance, forms the basis for the targeted decision making process, in which the $\mathcal{H}_0$-hypothesis of a healthy structure is evaluated. Hence, a necessary first step lies in the definition of decision boundaries.

2.7.1 Decision Boundaries

Let X be a vector of CPs with length n_{X}, each entry holds a CP-value for a single data instance $\tilde{\mathcal{D}}$ (from the training phase). Further, the probability density function (PDF) of a continuous variable x is defined as $p(\mathsf{x})$. In general, $p(\mathsf{x})$ is continuous and unknown *a priori*. Often, $p(\mathsf{x})$ is

assumed to be normally distributed with a PDF defined as

$$p(\mathsf{x}) = \frac{1}{\sigma_{\mathsf{x}}\sqrt{2\pi}}e^{-(\mathsf{x}-\bar{\mathsf{x}})^2/2\sigma_{\mathsf{x}}^2} = \mathcal{N}(\bar{\mathsf{x}},\sigma_{\mathsf{x}}), \tag{2.80}$$

with $\bar{\mathsf{x}}$ and σ_{x} as mean and standard deviation. Many other PDFs exist to define the distribution of a (random) variable such as the gamma or Weibull-distribution with

$$p(\mathsf{x}) = \frac{x^{k-1}e^{-x/\theta}}{\theta^x \Gamma(k)}; \Gamma(k) = (k-1)!; x > 0, \tag{2.81}$$

and

$$p(\mathsf{x}) = \frac{x}{\lambda}\left(\frac{x}{\lambda}\right)^{k-1}e^{(-\lambda/k)^k}; x > 0, \tag{2.82}$$

respectively. See [57] for an example of a detailed discussion of statistical derivations in the context of SHM. The probability of a single variable X_i taking a value between certain boundaries a and b, $p(\mathsf{X}_i = \mathsf{x}; a < \mathsf{x} < b)$, is defined as the integral from a to b over $p(x)$ as in 2.83.

$$p(\mathsf{X}_i = \mathsf{x}; a < \mathsf{x} < b) = \int_a^b p(\mathsf{x})d\mathsf{x}. \tag{2.83}$$

A general property is $p(\mathsf{X}_i = \mathsf{x}; a < \mathsf{x} < b) = 1$ for $a = -\infty$ and $b = \infty$. The integration of $p(\mathsf{x})$ is called cumulative distribution function (CDF) with

$$P(\mathsf{x}) = \int p(\mathsf{x})d\mathsf{x}. \tag{2.84}$$

Since $p(\mathsf{x}) \geqq 0$ for all x, the CDF increases monotonically, expressing the cumulative probability that x takes on a value up to b with

$$P(\mathsf{x} \leqq b) = \int_{-\infty}^b p(x)dx. \tag{2.85}$$

The value $P(\mathsf{x} \leqq b)$ is also called percentile, linking a parameter value b with a percentage of values from x lying in an interval $[-\infty, b]$. The percentile is formally written as $\mathsf{X}_{\mathsf{p}\%}$, describing the value below which $\mathsf{p}\%$ of X resides. E.g. $\mathsf{X}_{50\%} = \bar{\mathsf{x}}$ for normally distributed variables. Through solving $P(\mathsf{x} \leqq b) = \mathsf{p}/100, \mathsf{p} \in [0,100]$ for b, percentiles $\mathsf{X}_{\mathsf{p}\%}$ can be directly calculated from the CDF function.

$\mathsf{X}_{\mathsf{p}\%}$ can also be calculated if no distribution is fitted to the data. To do so, the CDF is represented in a discrete manner: First the data vector X is sorted in ascending order, written $\acute{\mathsf{X}}$. Afterwards, the i-th entry is taken as the $100((i-0.5)/n_X)\%$-percentile:

$$\acute{\mathsf{X}}_i = \mathsf{X}_{\mathsf{p}_i\%}, \quad \mathsf{p}_i\% = 100((i-0.5)/n_X). \tag{2.86}$$

Values are interpolated linearly to estimate percentiles which do not fit into the raster. Figure 2.1 shows the procedure for a vector X with ten entries. In the left plot, counts of X are given along with the analytical and fitted PDF functions of a normal distribution. The fitted function shows a small shift to the right with a slight differing standard deviation. On the right side, CDFs are plotted for the fitted and analytical PDF. The blue line denotes the percentiles calculated with Equation 2.86.

The boundaries which X_i lies in between with a certain probability $\mathcal{W} \in [0,1]$ are called the confidence or tolerance interval, written $P(\mathcal{W}) = [a,b] = P(a < \mathsf{X}_i < b) = 1 - \alpha$. Where α is the percentage of values outside the interval. E.g. in the case of a normal distribution 68.269% of the values lie within 1σ-boundaries around the mean. Hence, $P(0.68269) = [\bar{\mathsf{x}} - \sigma_{\mathsf{x}}, \bar{\mathsf{x}} + \sigma_{\mathsf{x}}]$. For a known, PDF function $P(\mathcal{W})$ can be calculated for a given interval, or a given interval can be calculated for a given $P(\mathcal{W})$. For normally distributed variables, the error function

$$erf(x) = \frac{1}{\sqrt{\pi}} \int\limits_{-x}^{x} e^{t^2} dt, \tag{2.87}$$

is used to calculate those boundaries. For symmetric and asymmetric distributions, the interval starts from the median (= mean for a normal distribution) assuring equal areas to both sides of the median. If the PDF of a variable is unknown a common PDF can be fitted to the sample of the variable or alternatively one can work with percentiles. Accordingly, $P(\mathcal{W})$ can be expressed through a lower boundary $\mathsf{X}_{(1-\mathcal{W})/2\%}$ and an upper boundary $\mathsf{X}_{1-(1-\mathcal{W})/2\%}$ in between which $\mathcal{W}\%$ of the variables will lie. Typically $\mathcal{W}$ is replaced by $1 - \alpha$ and $\mathsf{X}_{\alpha/2\%}$, $\mathsf{X}_{(1-\alpha/2)\%}$ become the desired decision boundaries.

2.7.2 Control Charts and Hypothesis Testing Results

Monitoring a certain variable over time is a common task in industry, usually implemented using control charts [128]. In general, the control variable (X) is compared to upper and lower control
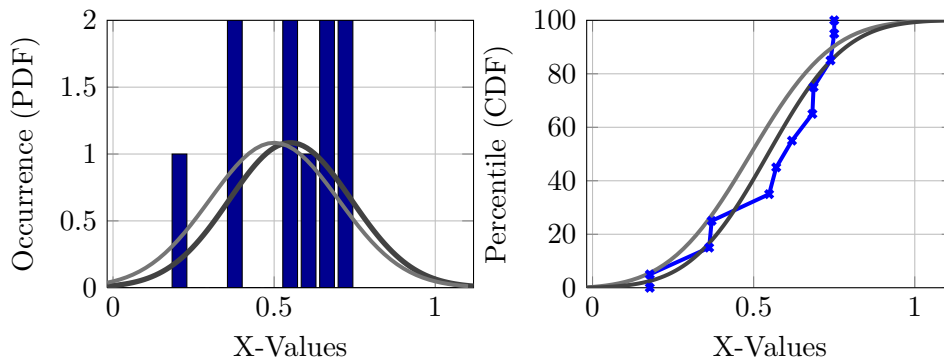
Figure 2.1: Exemplary comparison of PDFs (left) and CFDs (right) for a normally distributed random vector $\mathsf{X} = \{0.68, 0.62, 0.57, 0.75, 0.69, 0.55, 0.36, 0.37, 0.74, 0.18\}$ with $\bar{\mathsf{X}} = 0.5$ and $\sigma_{\mathsf{X}} = 0.2$. Analytic (light grey) and fitted (dark grey) functions are given along with the counts and estimated percentiles (blue).

limits (UCL, LCL) around a center line (CL) for a number of consecutive measurements. For the SHM framework, these measurements are CPs from incoming data instances during the testing phase. For a detailed, educational introduction to quality control, see e.g. [128]. Among many others, so-called $\bar{x}$-control charts are widely used to monitor the mean of a control variable. When several measurements are combined to rational subgroups it is also possible to monitor the parameter's variability.

For $\bar{x}$-control charts, the CL is defined as the variable mean $\bar{\mathsf{X}}$ or $\mathsf{X}_{50\%}$, and UCL/LCL are defined in terms of the parameter's standard deviation σ_{X} with

$$
\begin{aligned}
LCL &= \bar{\mathsf{X}} - A_{L,n_{rs}}\sigma_{\mathsf{X}} &= \mathsf{X}_{\alpha/2\%} \\
UCL &= \bar{\mathsf{X}} + A_{U,n_{rs}}\sigma_{\mathsf{X}} &= \mathsf{X}_{(1-\alpha/2)\%}.
\end{aligned}
\tag{2.88}
$$

$A_{L,n_{rs}}$ and $A_{U,n_{rs}}$ are scalar factors depending on the subgroup size n_{rs}. Obviously, $A_{L,n_{rs}} = A_{U,n_{rs}}$ is valid for symmetric distributions such as the normal distribution. Using Equation 2.88, one has two options to determine the control limits for a given set of training data: 1. Through evaluation of a fitted PDF e.g. an estimate of the mean and standard deviation and accordingly estimated constants for $A_{L,n_{rs}}$ and $A_{U,n_{rs}}$ using Equation 2.87. 2. Defining a confidence interval through α and estimating the percentiles $\mathsf{X}_{\alpha/2\%}$ and $\mathsf{X}_{(1-\alpha/2)\%}$.

Evaluation of a control chart for a new variable (CPs from data instance in testing) is equal to performing a hypothesis test on the variable: If $LCL < \mathsf{X}_i < UCL$ the structure from which the data was captured is assumed to be in a healthy state ($\mathcal{H}_0$-Hypothesis). If $LCL > \mathsf{X}_i$ or $\mathsf{X}_i > UCL$, the structure is assumed to be possibly damaged, the $\mathcal{H}_1$-Hypothesis. It should be noted that there is always a α-percentage of parameters which lie outside the boundaries for a healthy system. In the benchmark case, in which the correct state of the structure is known, control charts can be evaluated against the correct hypothesis: All testing data instances are plotted in the control chart and correct and wrong decisions can be counted and divided by the total number of healthy and damaged data instances. Two types of errors are commonly distinguished with false positive (FP) indications and false negative (FN) indications. Many other nomenclatures for those errors exist as shown in Table. 2.2 [2, 40, 57, 128, 130].

Table 2.2: Present nomenclature in literature for the errors and results of hypothesis testing.

False positive (FP) in %	**False negative (FN)** in %
Synonyms:	Synonyms:
Type I Error (engineering)	**Type II Error** (engineering)
Producer's risk (production)	**Consumer's risk** (production)
	1-detection rate or **1-power**
1-specificity (medicine)	**1-sensitivity** (medicine)
1-true negative (TN) with FP+TN=100%	**1-true positive** (TP) with FN+TP=100%
$\mathcal{H}_1$ at $\mathcal{H}_0 := \mathcal{H}_{10}$ with $\mathcal{H}_{10} + \mathcal{H}_{00} = 100\%$	$\mathcal{H}_0$ at $\mathcal{H}_1 := \mathcal{H}_{01}$ with $\mathcal{H}_{01} + \mathcal{H}_{11} = 100\%$

It should be noted that those counts or percentages strongly depend on the chosen value for α, since it defines the value range for X being linked to a healthy condition. Accordingly $\mathcal{H}_{10}$ and $\mathcal{H}_{01}$ must be understood as a function of α:

$$\mathcal{H}_{10} = \mathcal{H}_{10}(\alpha) \quad \mathcal{H}_{01} = \mathcal{H}_{01}(\alpha) \in [0,100]. \tag{2.89}$$

If these parameters are analyzed for different α-values, receiver operating characteristic (ROC) curves can be drawn.

2.7.3 Receiver Operating Characteristic Curves

Originating from the field of medicine, where HT is present in the form of diverse medical checks, ROCs can be used to evaluate the over-all performance of a test through a variation of the confidence interval. The curve is defined by detection rate $\mathcal{H}_{11}(\alpha)$ over false alarm rate $\mathcal{H}_{10}(\alpha)$ as a two dimensional vector $ROC(\alpha)$:

$$ROC(\alpha) := \quad [\mathcal{H}_{11}(\alpha), \mathcal{H}_{10}(\alpha)] = \quad [1 - FN(\alpha), FP(\alpha)]. \tag{2.90}$$

As a result, ROCs can be used to select an optimal operating point. Figure 2.2 (right) shows typical ROC-curves for two CPs, with distributions given in the left sub-plot, evaluated for different α-values. Start and end of these curves at $ROC(\alpha = 0) = [0,0]$ and $ROC(\alpha = 1) = [100,100]$, respectively, are fix points from theory: If $\alpha = 0$, the confidence interval covers (theoretically) the whole parameter range and all monitored parameters will fall into it. As a result, there will be no false alarm but also no damage detection, so the point lies in the lower left corner of the ROC-diagram. In contrast $\alpha = 1$ denotes a confidence interval with zero width. Accordingly all monitored parameters will lie outside the boundaries and the detection rate will be 100% but also the false alarm rate will be at 100%. A straight line from (0,0) to (100,100) represents a ROC characteristic which is "completely useless" [2] for a differentiation between healthy and potentially damaged data instances. The more the curve tends towards the upper left corner, the better the test performance. A perfect discrimination is located at (0,100), and accordingly all damaged sets are identified without any false positive alarms. This is only achievable if there is no overlap of parameter distributions from healthy and damaged sets in the analyzed data. An optimal curve starts at the lower left corner, goes straight up to the upper left and horizontally to the upper right. The trend to the upper right is inevitable since a growing α and hence a smaller confidence interval will lead to false positive alarms at a certain point.

The given example in Figure 2.2 (left) shows a parameter distribution for the healthy state $\mathcal{H}_0$ for both CPs and two distributions in the damaged state. It is obvious that CP1-values from the damaged state strongly overlap with the healthy parameters while CP2 performs much better. Accordingly the ROC-curves in Figure 2.2 (right) differ significantly: For CP2, it directly reaches a 100% detection rate, going over to the upper right with a constant detection rate of 100%, and an increasing number of false positive alarms with increasing α. CP1 in contrast is not able to distinguish between the two states perfectly and the ROC-curve runs below the CP2 curve for all
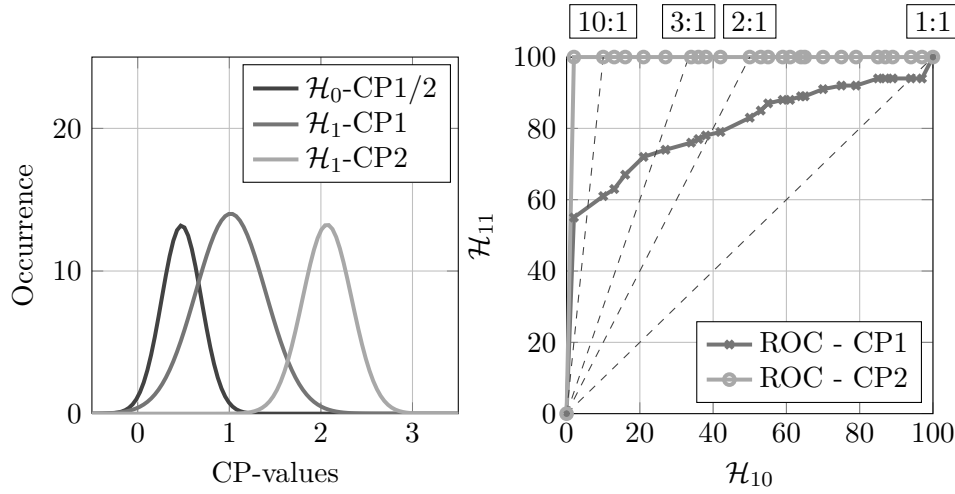
Figure 2.2: Parameter distributions (left) for the healthy state of CP1 and CP2 ($\mu = 0.5; \sigma = 0.2$) and the damaged state for both CPs (CP1: $\mu = 1; \sigma = 0.4$ and CP2: $\mu = 2; \sigma = 0.3$), 100 random parameter each. ROC-curves per CP are given for different α-values $[0, 0.02 : 0.04 : 0.98, 1]$ in the right plot. Newly introduced performance lines given for 2:1, 3:1, and 10:1 ratios.

investigated α-values. Performance lines are introduced for a better visual interpretation of the curves.

From this investigation, a scalar metric for ROC-curves and hypothesis test performance can be defined with the area under the curve (AUC)' [2]:

$$\mathcal{A} = \int\limits_{0}^{100} ROC(\alpha)d\alpha. \tag{2.91}$$

It is obvious that in the general real world case, an analytical formulation for the ROCs is not available and Equation 2.91 has to be implemented through numerical integration. Values between the points on the ROC curve derived for discrete α-values are unknown. Hence, an estimate is necessary to calculate an AUC. Since for a finite number of test sets, the ROC curve increases monotonically, not strictly monotonic, step-functions can be used as lower and upper boundaries and linear interpolation, as implemented for this work, as a compromise. The larger the area below the curve, the better the performance. Boundaries are given by Akobeng [2] with: $\mathcal{A} > 0.9$ indicating high accuracy, $0.9 > \mathcal{A} > 0.7$ indicating moderate accuracy, and $0.7 > \mathcal{A} > 0.5$ for low accuracy. Another performance indicator is the maximum distance between ROC-curve and the diagonal, dubbed Youden index ($\mathcal{J}$) [2, 217], with

$$\mathcal{J} = max\{\mathcal{H}_{11}(\alpha) - \mathcal{H}_{01}(\alpha)\}. \tag{2.92}$$

A second parameter that can be taken out of an ROC curve is the minimum distance to the optimum in the upper left corner, $\bar{\mathsf{d}}$. It is simply calculated as

$$\bar{\mathsf{d}} = min\{\sqrt{\mathcal{H}_{10}(\alpha)^2 + \mathcal{H}_{01}(\alpha)^2}\}. \tag{2.93}$$

All three parameters provide a global index for a comparison of HT. $\mathcal{J}$ and $\bar{\mathsf{d}}$ will also result in an optimal value for α for a single point on the ROC-curve. Both parameters will be used to compare different combinations of ML, CP, and HT as outlined in detail in the following chapter (see 3.4).

3 Novelties and Benchmark Studies

To this point motivation for structural health monitoring has been given and existing approaches for the automated extraction of modal parameters and SHM have been presented in Chapter 1. Further, the theoretical background for the following studies was given in Chapter 2. Before investigating results of OMA and SHM for large-scale structures, this chapter gives a detailed description into the TEMP procedure used in combination with SSI for OMA, and the SHM framework with its subsequent steps of machine learning (ML), condition parameters (CP) and hypothesis testing (HT). TEMP is exemplarily applied to a data base of the New Carquinez bridge. Exemplary plots used for analysis are introduced before the chapter closes with an application within an exemplary public database, generated from the LANL 4-DoF system, a small scale physical model.

3.1 Accumulated Energy as Condition Parameter

The accumulated energy (AE) in Equation 2.46 is the integral of a power spectral density over frequency (see Equation 2.5) and serves as an indicator for energy distribution within a certain frequency range of a given signal. Following 2.46 and 2.47 $E_{yy}(\omega_i)$ ranges form 0 to 100 %, linking each increasing frequency bin with a cumulative energy level. The value for $E_{yy}(\omega_k)$ denotes the percentage of energy that is present in the signal up to ω_k. Vice versa, once $E_{yy}(\omega_i)$ is calculated, the frequency ω_{e_j} where a given energy level $e_j \in [0,100]$ is crossed can be calculated. Figure 3.1 shows the PSD of a channel (left) and the corresponding AE (right). Accordingly, n_e discrete frequencies $\tilde{\omega}_j$ can be identified within a certain energy interval $[e_a - e_b], e_a < e_b \in [0,100]$. The condition parameter for channel i is then defined as the mean frequency value for a certain energy interval:

$$CP^{E_{yy}}_{(i),[e_a-e_b]} = CP^{E_{yy}}_{i,k} = \frac{1}{n_b} \sum_{j=1}^{n_a} \tilde{\omega}_j. \tag{3.1}$$

k indicates the interval number and n_a and n_b the indexes at the beginning and the end of the interval, respectively.

Since this frequency depends on the energy distribution within the spectrum being measured, the resulting mean frequency per energy section takes changes in the whole frequency range into account instead of tracking single peaks of a spectrum (e.g. modal frequencies). This derivation differs from the one in [208] where AE is built from spectra and its centroid is tracked or visual inspection is performed. The parameter has also been used e.g. for shape analysis [41] and to characterize earthquakes in time domain [192].
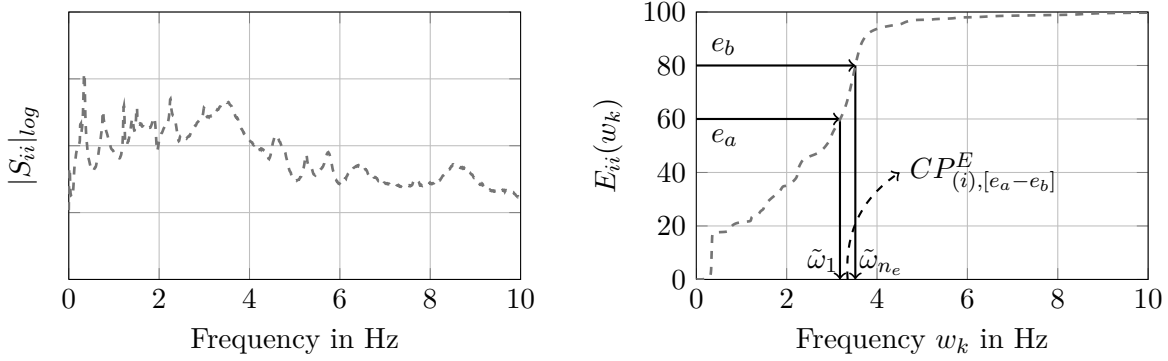
Figure 3.1: Power spectral density (left) and accumulated energy (right) for a single data-channel. In the right plot, the estimation of the $CP^E_{(i),[e_a-e_b]}$ is indicated through lower and upper energy bound e_a and e_b, the according frequency range and finally the mean frequency between $\tilde{\omega}_1$ and $\tilde{\omega}_{n_e}$.

$CP^E_{(i),[e_a-e_b]}$ is a scalar for a single channel, accordingly an $m \times 1$ vector results for a single data instance with m channels. If several energy sectors are included each channel results in a vector and each data instance in a CP matrix. Further, the parameter was extended to include not only auto-correlations but also cross-correlations to use information between sensor positions. This results in an accumulated energy matrix where $CP^E_{(i,j),[e_a-e_b]}$ is the frequency corresponding to the energy interval $[e_a - e_b]$ for the accumulated energy resulting from the cross-correlation between channel i and j. Through this correlation m^2 values result from m channels. To reduce the dimensionality all cross-correlations between channel i and all other channels are averaged. Accordingly, information for the correlation between channel i and all other channels is merged. Through this procedure $2m$ parameters result from m channels, dubbed $CP^{E_{xy}}_{i,j}$. 'xy' indicates the cross correlations used for estimation. Only one of the two will be indicated in labels of plots.

3.2 TEMP: Triangulation-Based Extraction of Modal Parameters

In long term SHM and online monitoring, the computational demands of automated extraction of modal parameters becomes a critical issue, as thousands of data instances have to be analyzed or computation has to be relocated to wireless sensor nodes. In this context, the extraction of modal parameters is applied to the solutions of the system identification step (dubbed $\mathcal{S}$), which is carried out by e.g. SSI, collected in stabilization diagrams. It is not argued that the quality of the extracted frequencies, damping-values, and mode shapes strongly depends on these solutions. In fact, the advantage of the presented procedure lies in the way the results are extracted and can be stated by the number of comparisons needed: The known procedures comprise time-consuming calculation steps since clustering is applied to the (very) large set of solutions $\mathcal{S}$, where each possible pair of poles is investigated (see 1.5). If $\mathcal{S}$ is comprised of n solutions, this leads to $(n^2 - n)/2$ comparisons for each metric. The approach introduced here, dubbed triangulation-based extraction of modal parameters (TEMP), uses triangle objects of a Delaunay-triangulation in the frequency-damping-plane for a comparison of neighboring solutions

only. The triangulation results in $2n - 2 - b$ triangles[1]. Three comparisons are calculated on each triangle resulting in only $3(2n - 2 - b)$ comparisons. The Delaunay-triangulation is a well known, robust technique that leads to a unique solution. This results in a strongly reduced computational effort and robust extraction results [77].

The procedure provides an easily traceable solution for both improving the stability-diagram and grouping the solutions by connected triangles. Finally, each cluster might comprehend several paths (modes), detected as graphs through each cluster. Not every solution in a cluster will necessarily participate in a mode, which is an advance on most clustering approaches which assume each cluster to be a single mode ignoring possible mode splits. This triangulation based approach further enables a general display of the distribution of solutions from parametric system identification procedures and parameter sensitivities by triangle dimensions indicating different stability diagram characteristics for e.g. SSI and VAR.

For path estimation, the set of modes/solutions $\mathcal{S}$ (see 2.3 and 2.4), calculated from the preferred system identification procedure, with $n_{\mathcal{S}}$ solutions, serves as the initial set[2]. The presented procedure is organized as follows (Symbols $\hat{\,}$ and $\hat{\hat{\,}}$ indicate reduced solution sets):

1. Reduction of $\mathcal{S}$ to $\hat{\mathcal{S}}$ by weighted Mean Phase Deviation (MPD).

2. Building a *Delaunay*-Triangulation in the f-ζ-plane (frequency-damping) of $\hat{\mathcal{S}}$.

3. Reduction of $\hat{\mathcal{S}}$ to $\hat{\hat{\mathcal{S}}}$ by triangle dimensions.

4. Division of remaining solutions by connected triangles into sub sets $\hat{P}_i \in \hat{\hat{\mathcal{S}}}$.

5. Identification of stable paths for each sub set $\hat{P}_i$.

6. Reduction of path objects by their length.

Initially, all modes in $\mathcal{S}$ are tested to exist in complex conjugate pairs, and one half of the solutions is kept since each pair lies on the same point in the frequency-damping or frequency-model orders space. Further, mean phase deviations (MPD, Equation (2.36)) for all remaining solutions are calculated and all solutions with mode shapes exceeding the criterion ϕ_{crit} are rejected. Then, the remaining solutions $\hat{\mathcal{S}}_i$ are compared in the frequency damping plane to reduce the number of solutions. In this plane the set of points $\hat{\mathcal{S}}^{f,\zeta} := \{\hat{\mathcal{S}}_1^{f,\zeta}, \ldots, \hat{\mathcal{S}}_{n_{\hat{\mathcal{S}}}}^{f,\zeta}\}$ is defined by frequency and damping of each solution. Assuming that $\hat{\mathcal{S}}^{f,\zeta}$ is in *general position*, which means that no four point of $\hat{\mathcal{S}}^{f,\zeta}$ lie exactly on a circle, a unique *Delaunay*-Triangulation $\mathcal{D}(\hat{\mathcal{S}}^{f,\zeta})$ can be performed [43]. The procedure is very efficient and can be accessed e.g. using built-in functions of Matlab. The *Delaunay*-Triangulation is a special case of many possible triangulations for $\hat{\mathcal{S}}^{f,\zeta}$ where the minimum angle (of all triangles) of the triangulation is maximised. A set of n_{Δ} triangles $\Delta_i \in \Delta$, each holding a unique set of points $\hat{\mathcal{S}}_l, \hat{\mathcal{S}}_m, \hat{\mathcal{S}}_n \in \Delta_i$, is the result of this triangulation. For each

---

1   Where b is the number of vertices (points) on the convex hull.

2   A basic criterion for physical solutions is their existence in conjugate-complex pairs. Since frequency and damping are equal for both of these solutions, only one of the pair is considered for path identification here.

Δ_i, the distances between the corner nodes in frequency and damping can be calculated with (2.31) and (2.32) , see also Figure 3.2. The distances are denoted by

$$\Delta_{i,\delta f} = \left[d_{f_{0,l,m}}, d_{f_{0,l,n}}, d_{f_{0,n,m}} \right]; \qquad \Delta_{i,\delta\zeta} = \left[d_{\zeta_{l,m}}, d_{\zeta_{l,n}}, d_{\zeta_{n,m}} \right]. \tag{3.2}$$

Further, the MAC values of (2.33) between the three points serve as a third indicator. It follows

$$\Delta_{i,\delta MAC} = \left[\mathrm{MAC}(\mathcal{S}_l^\psi, \mathcal{S}_m^\psi), \mathrm{MAC}(\mathcal{S}_l^\psi, \mathcal{S}_n^\psi), \mathrm{MAC}(\mathcal{S}_n^\psi, \mathcal{S}_m^\psi) \right]. \tag{3.3}$$

When all triangle dimensions have been calculated, thresholds can be applied to determine a sub set of Δ, denoted $\hat\Delta$, in which each $\hat\Delta_i$ has proper dimensions. According to frequency, damping and MAC, three critical values f_{crit}, ζ_{crit} and MAC_{crit} are defined. The values for damping and frequency are expressed in percent and define the maximal relative divergence within a triangle. For MAC, the criterion defines a minimum MAC-value. Finally, the criterion if a triangle Δ_i belongs to $\hat\Delta$ can be formulated as follows:

$$\Delta_i \in \hat\Delta \text{ if } max \begin{bmatrix} \dfrac{max(\Delta_{i,\delta fs})}{min(\mathcal{S}_l^{f_0}, \mathcal{S}_m^{f_0}, \mathcal{S}_n^{f_0}) f_{crit}} \\[2ex] \dfrac{max(\Delta_{i,\delta\zeta})}{min(\mathcal{S}_l^\zeta, \mathcal{S}_m^\zeta, \mathcal{S}_n^\zeta) \zeta_{crit}} \\[2ex] \dfrac{min(\Delta_{i,\delta MAC})}{MAC_{crit}} \end{bmatrix} \leq 1 \tag{3.4}$$

If this condition is fulfilled, the triangle is sufficiently small and all solutions have similar Eigenvectors.

To illustrate the procedure, Figure 3.3 shows the initial triangulation (blue) in the frequency-damping-plane for an arbitrary ten minute data instance originating form the wind turbine in 5. As initial $\mathcal{S}$ solutions of SSI-Data(50) are used[1]. Each corner node of a blue triangle represents one solution/mode of the system identification procedure. To clarify the triangulation, only the lower frequencies from 0 to 5Hz are plotted. Further, green circles mark the corners of remaining triangles after frequency and damping criteria have been applied. Finally red crosses indicate solutions that remain after MAC values have been checked within the triangles. It is clearly visible how this procedure reduces $\mathcal{S}$ to the dense regions with low damping values. Without the need to reduce $\mathcal{S}$ by *hard* criteria such as maximal damping values, the low damped modes remain in $\hat\Delta$[2]. All mentioned operations can be executed using vector operations and hence suit Matlab very well, resulting in a very fast computation.

The set of points that builds $\hat\Delta$ is called $\hat{\hat{\mathcal{S}}}$. To divide the subset $\hat{\hat{\mathcal{S}}}$ into groups of connected

---

1   model orders from 1 to 200 are considered, reduction through a maximum MPD of 25° was applied before triangulation.

2   As long as a mode participates in a single triangle with proper dimensions it remains in $\hat{\hat{\mathcal{S}}}$.
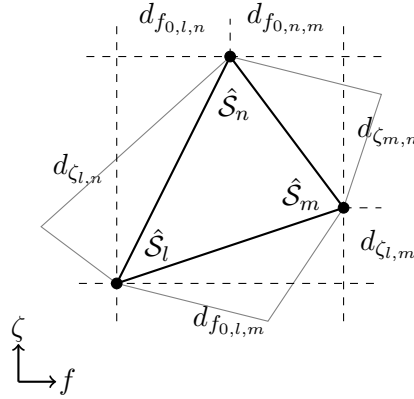
Figure 3.2: Triangle object in frequency-damping-plane used in TEMP-procedure with frequency and damping distances between corner points of triangle. Triangle sides also represent MAC-comparisons between corner-nodes.

points, the triangulation is very useful as well. Starting with a set of three points of an arbitrary triangle $\hat{P}_{start} := \hat{\mathcal{S}}_l, \hat{\mathcal{S}}_m, \hat{\mathcal{S}}_n \in \hat{\Delta}_i$, further points, belonging to triangles that contain one or two points of the initial point set, can be added to $\hat{P}_i$. The search is continued for the increased set of points/triangles until no additional triangles containing points of the set, can be found. The identified triangles are erased from $\hat{\Delta}$ and the procedure is repeated until no triangles are left and all points are allocated to specific $\hat{P}_i$[1]. For the initial triangulation this procedure would collect all points in one $\hat{P}_i$. Since many triangles have been erased, gaps between the triangles will let this procedure split the complete set of points. Accordingly, $\hat{\mathcal{S}}$ is divided into $n_{\hat{\Delta}}$ sub sets $\hat{P}_i$. Figure 3.4 shows the result of this procedure for $\hat{\hat{\mathcal{S}}}$ from Figure 3.3. Again, the initial triangulation is plotted as a reference, colored circles indicate the different $\hat{P}_i$.

For each $\hat{P}_i$ the path identification algorithm can be run: Initially, all points from $\hat{P}_i$ with the highest model order are understood as different path-objects. Then, a loop runs over all other (lower) model orders n_k contained in $\hat{P}_i$, collecting solutions with the appropriate model order. Within those loops, the closest solution to a path-object (in a frequency, damping, and MAC sense, fulfilling f_{crit}, ζ_{crit} and MAC_{crit}) is appended to an object. One solution can hence be added to two different path objects to merge them[2]. This results in a number of path-objects per sub set $\hat{P}_i$. To distinguish between these objects, their length (indicating how many model orders a path involves) serves as indicator. A last criterion removes all paths with a number of model orders lower than $\hat{P}_{crit}$ defines. It is suggested that a path-object should contain at least 50 % of the total number of model orders.

The reduction of $\hat{\hat{\mathcal{S}}}$ is plotted in the frequency-model order-plane in Figure 3.5. The upper plot shows the initial set of solutions. This set is also given by the blue triangulation in Figure 3.3 and Figure 3.4, here after application of the phase criterion ϕ_{crit}. The very same solutions are displayed as standard stabilization diagram in the upper plot of Figure 3.5. In this example,

---

[1] It should be noted that this routine does not work with the call of *neighbouring* triangles since these have one side in common, here the connection of only one point is sufficient.

[2] If one solution is added to two different path-objects both objects will add the same solutions in further loops.
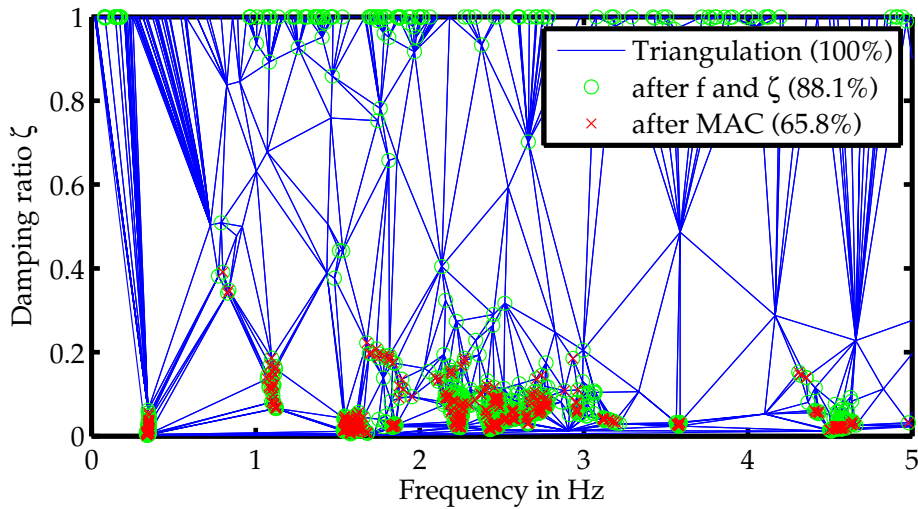
Figure 3.3: Triangulation for SSI-results calculated for a 10 minute data instance. Reduced number of solutions after applying f_{crit}, ζ_{crit} marked with green bullets and solutions after applying MAC_{crit} marked with red crosses.
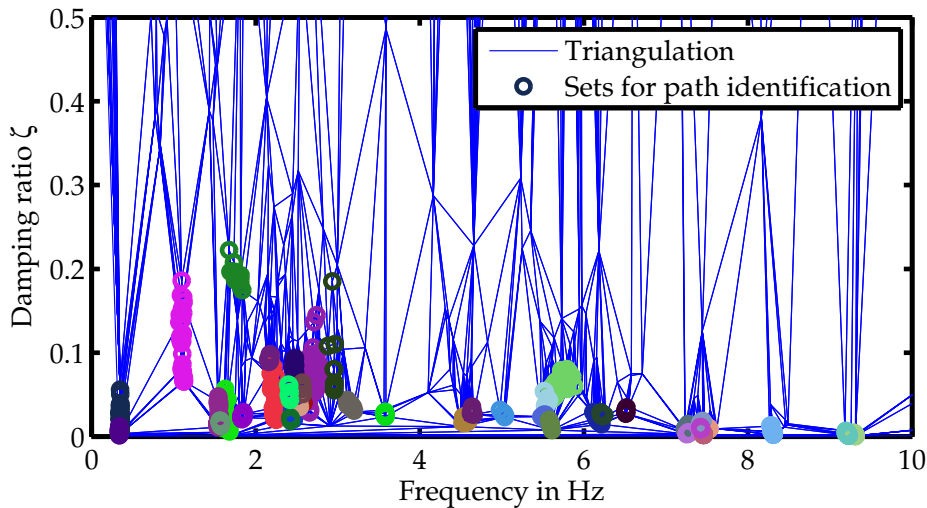
Figure 3.4: Final, separated triangle cluster $\hat{P}_i$ during TEMP-procedure, indicated through different colors. Stable paths are subsequently identified within each $\hat{P}_i$.

a majority of the solutions is located below 10 Hz with further accumulations at 12, 19.5 and 24 Hz, respectively. After the reduction, the lower plot results. It is clearly visible that a fair amount of *noise* is erased from the stability plot and that certain paths occur. The remaining set is split through grouping connected triangles as indicated by bullets in Figure 3.4. Each group is separately taken for the path-identification procedure. Finally, Table 3.1 gives an overview of all used criteria with a brief description and minimal/maximal values.

It is clear that the quality of reduction is closely related to the choice of the reduction criteria. Different values for ϕ_{crit}, f_{crit}, ζ_{crit} and MAC_{crit} will influence the number of remaining solutions $\hat{\hat{\mathcal{S}}}_i$. If each criterion is varied over its value range, the trend of the amount of remaining solutions indicates the distribution and sensitivity of the addressed modal validation parameter. For this

Table 3.1: TEMP criteria for modal parameter extraction at LANL 4-DoF system.

Criterion	Description	Min	Max
ϕ_{crit}	Criterion for mean phase divergence within a single Eigenvector. Used to reduce initial set of modes/solutions $\mathcal{S}$.	$0°$	$45°$
f_{crit}	Relative frequency difference between two solutions in %. %-value based on smallest frequency within triangle (for triangulation procedure) or smaller frequency between two points (for path identification). Used to reduce $\mathcal{S}$ based on triangulation & path identification	0	∞
ζ_{crit}	Relative damping difference between two solutions in %. %-value based on smallest damping within triangle (for triangulation procedure) or smaller frequency between two points (for path identification). Used to reduce $\mathcal{S}$ based on triangulation & path identification	0	∞
MAC_{crit}	MAC value between two solutions. Used to reduce $\mathcal{S}$ based on triangulation & path identification	0	1
$\hat{P}_{crit}$	Minumum number of model orders participating in path object. Used for path identification	1	p_{max}
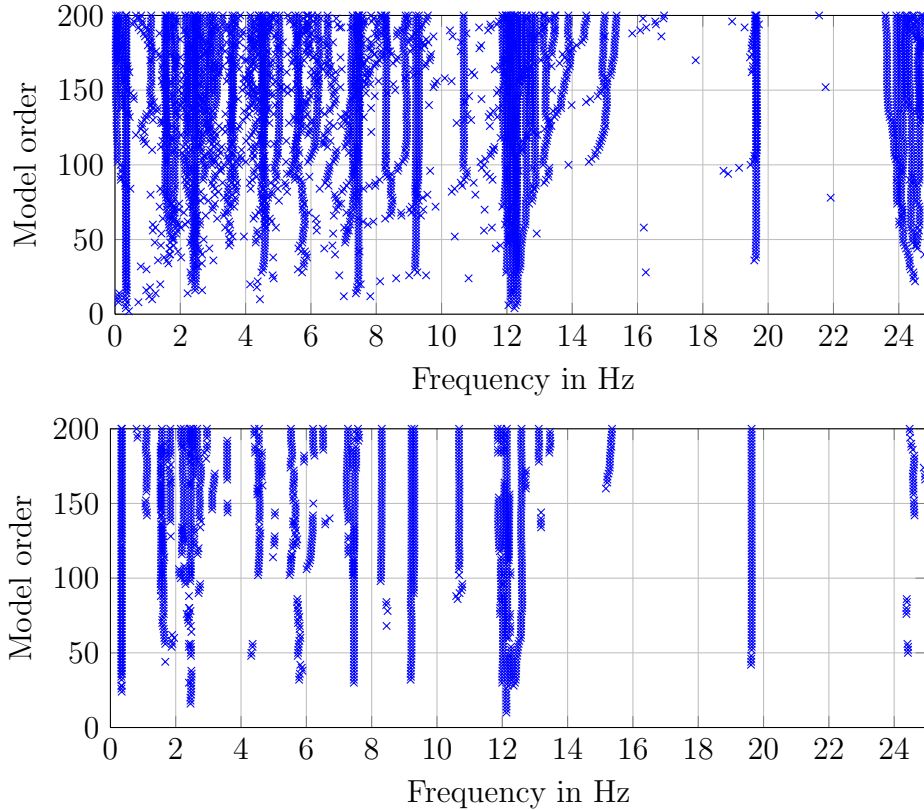
Figure 3.5: Initial stabilization diagram from SSI-Data ($\mathcal{S}$, upper plot) and cleared stabilization diagram after TEMP ($\hat{\mathcal{S}}$, lower plot). Reduction through phase-, frequency-, damping-, and MAC -criterion, with a threshold of 25°, 5 %, 75 % and 0.1, respectively.

purpose, solutions of 300 system identifications based on SSI and VAR are analyzed in [77]. Here, differences and statistical properties can be investigated.

It is stated that an automated extraction of modal parameters should be based on the detailed knowledge of the validation parameter's statistical distributions. Only if the parameter distributions/sensitivities for a given system identification method with fixed sets of model orders do not change for several data instances, inner, statistical values can be taken for a reliable automation. If the statistical distributions of the criteria differ from normal distributions, and hence the estimation of statistical parameters becomes more costly, parameter-percentiles serve as a easy to interpret boundary.

3.3 Application of TEMP to the Database of New Carquinez bridge

The New Carquinez Bridge (NCB), officially named Alfre Zampa Memorial Bridge, is a suspension bridge of 1056 m length that crosses the Carquinez Straight in Vallejo, CA, north of San Francisco. The main span has a length of 728 m with two side spans of 147 and 181 m, carried by two hollow concrete towers of 120 m height. A continuous orthotropic steel box girder forms the deck of the bridge. It was completed in 2003 as a part of the seismic retrofit program of the Bay Area Toll Authority. Today, it supports four lanes of westbound traffic on freeway I-80 between Sacramento and San Francisco. Due to the high risk of seismic hazards, the California Department of Transportation as the bridge operator, is required to decide about the safety of reopening the bridge after any seismic event. Hence, a monitoring system was put into place.

In the summer of 2010, the Laboratory for Intelligent Systems and Technologies, University of Michigan, implemented a wireless long-term structural (health) monitoring system on the NCB. For the monitoring, different sensors divided into three sub networks (N for north, S for south, and T for tower) were installed as displayed in the upper graphic of Figure 3.6. In total, the wireless monitoring system supports 33 tri-axial accelerometers, 9 strain gages, 3 string potentiometers, 1 GPS node and 3 weather stations (which include thermometers, anemometers and wind vanes). The lower left and lower middle picture in Figure 3.6 display these weather stations and wireless sensor nodes. The *Narada* sensor nodes [190], including those carrying accelerometers, are attached magnetically to the bottom of the deck, outside the girder. All nodes are powered by solar panels. The data collection times were changed after a couple of months from 4:00, 8:00, 12:00, 16:00, and 20:00 h to 2:00, 6:00, 10, 14:00, 18:00, and 22:00 h (as can be seen in subsequent figures). A validation and benchmark comparison to a wired sensor system can be found in [102]. First insights into modal properties and a comparison to FEM were analyzed in [101] and [83].

In this section, sensor nodes from the southern sub network (S1 to S9 in Figure 3.6) are used to perform the automated extraction of modal parameters by TEMP (see Chapter 3.2). To do so, SSI is first run and poles for model orders between 100 and 300 are extracted in steps of two. These results are evaluated by the introduced TEMP procedure. Each data instance is composed of nine bi-axial acceleration sensors resulting in 18 channels. Measurements were taken with a sampling frequency of f_s=20 Hz over a period of 480 s. A custom designed 4-pole Butterworth
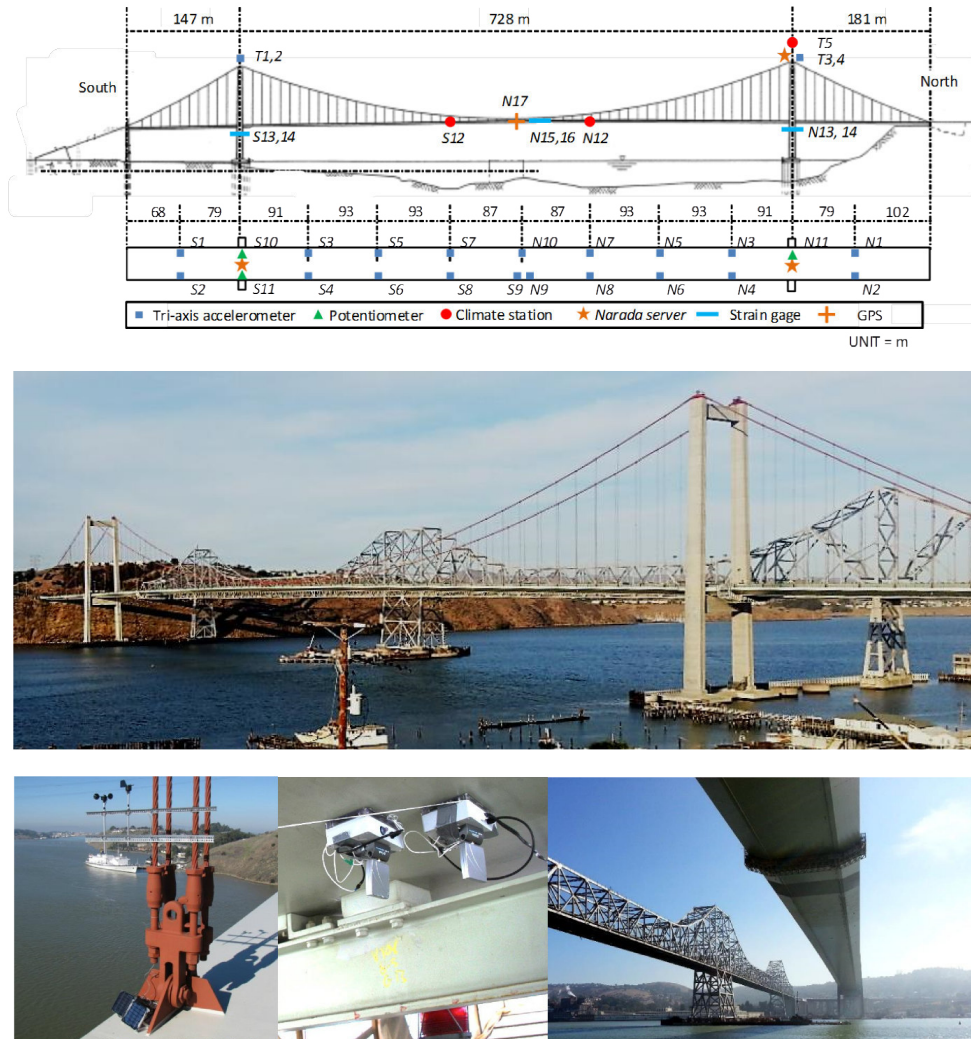
Figure 3.6: Structure and data acquisition system for the New Carquinez Bridge. Side view and sensor locations are given in the upper plot, the middle plots shows a side view from south, and a weather station, sensor nodes and a bottom view are given in the bottom row (left to right).

filter is used as a combined DC reflection and anti-alias filter configured with a pass-band from 0.001Hz to 10 Hz. Results from TEMP were compared to a knowledge based approach in [222], showing very good agreement but also highlighting that certain modes are less present in one of the two sub network. Settings for the TEMP application in this section are as follows: Shifs: 80 Model orders: 100 to 300, $\phi_{crit} = 17.5°$, $f_{crit} = 1.5\%$, $\zeta_{crit} = 35\%$, $MAC_{crit} = 0.9$, $\hat{P}_{crit} = 50$[1].

In total, 1158 data instances were analyzed. TEMP-parameters are kept constant for every data instance. Results of the automated procedure are shown in Figure 3.7 (left). Even though modes were identified up to 10 Hz, a close-up to the range of 0 to 1 Hz is chosen since the main

---

1   The number of shifts results from the estimated lowest mode at 0.18 Hz which has a period of 5.55 s and hence 111 samples. To cover about 70% of the samples 80 shifts are necessary. Due to the 18 channels, a state space model order of 36 results. This order should be well overestimated with chosen orders of 100 to 300. Values for MPD, frequency, damping, and MAC are empirical values recommended for large-scale structures. An overview for TEMP settings for all investigated structures is given in Table 6.1

global bending modes are present in the range up to 1 Hz (see [83]). It can be seen that all modes are identified very constantly over the different data instances and that only a few spurious modes lie between the desired physical modes. This is underlined by sharp peaks in the very left plot for mode occurrence over frequency. Some symmetric modes are not identified from the signal due to insufficient amplitudes. Over the different data instances, between 20 and 35 solutions result as physical modes from TEMP. Here some data instances stick out, where distinctively fewer solutions are calculated. Further, fewer solutions are identified from data instance 400 onwards, where a system update was performed and less spurious solutions result (upper plot).

In order to track the structure's modes over time, one can make repeated use of the TEMP procedure: Data in Figure 3.7 (left) can be used for path identification to track modes over the different data instances. The data instance number is simply interpreted as model order and TEMP can be applied to all the solutions. Results can be seen in the right plot of Figure 3.7, where different modes are indicated by different colors reaching over all the analyzed data instances. Due to noise in the data, colored excitation, path-split or path merging, spurious solutions might result from single data instances. These solutions might pollute the overall results. Through the repeated application of TEMP, similar modes can be extracted for analysis. Also, if modes should switch position in frequency, these can be traced with the comparison of damping and MAC. The option of path-detail exploration also provides the ability to track changes in mode shapes over time. It should be noted that TEMP-criteria should be adjusted for this analysis to allow for stronger fluctuations between data instances – Depending on the measurement interval it is obvious that changes in frequency, damping, and mode shape might be more distinct between data instances than within a single measurement.

Mode shapes for all eight modes, indicated in Figure 3.7 (right), are given in Figure 3.8. It should be noted that measurements represent the southern sub-network of sensor nodes; accordingly mode shapes reach up to the middle of the bridge and repeat themselves from that point on towards the northern end of the NCB. All measured degrees of freedom are indicated by red arrows. Additionally, fix points are included into the plot at both ends of the side span where bearings constrain the structure's movements.

The modes with mean frequencies at 0.194 Hz (upper left), 0.257 Hz (upper right), 0.363 Hz (2nd row left), 0.48 Hz (2nd row right), and 0.644 Hz (4th row left) represent global, vertical bending modes of the bridge with an increasing number of maxima and some torsional content. For the highest bending mode at 0.644 Hz the two adjacent maxima on the left move in the same direction, indicating that the spatial solution might be too low to capture this mode correctly, possibly missing a maximum between nodes, or the phase information is erroneous. The mode at 0.18, 0.53, and 1.04 Hz (1st row left, 3rd row right, and 5th row right) form the first three horizontal bending modes. The mode at 0.557 Hz (4th row left) is dominated by the side span where both vertical measurements show the largest absolute amplitudes. It should be noted that this mode is close to one mode referred to as a mix between symmetric and antisymmetric vertical bending at a frequency of 0.561 Hz in [83]. Finally, the mode at 0.743 Hz (5th row right) is the first antisymmetric global torsion mode where points on either side of the bridge deck move in opposite directions. It should be noted that the side span does not continue the torsional
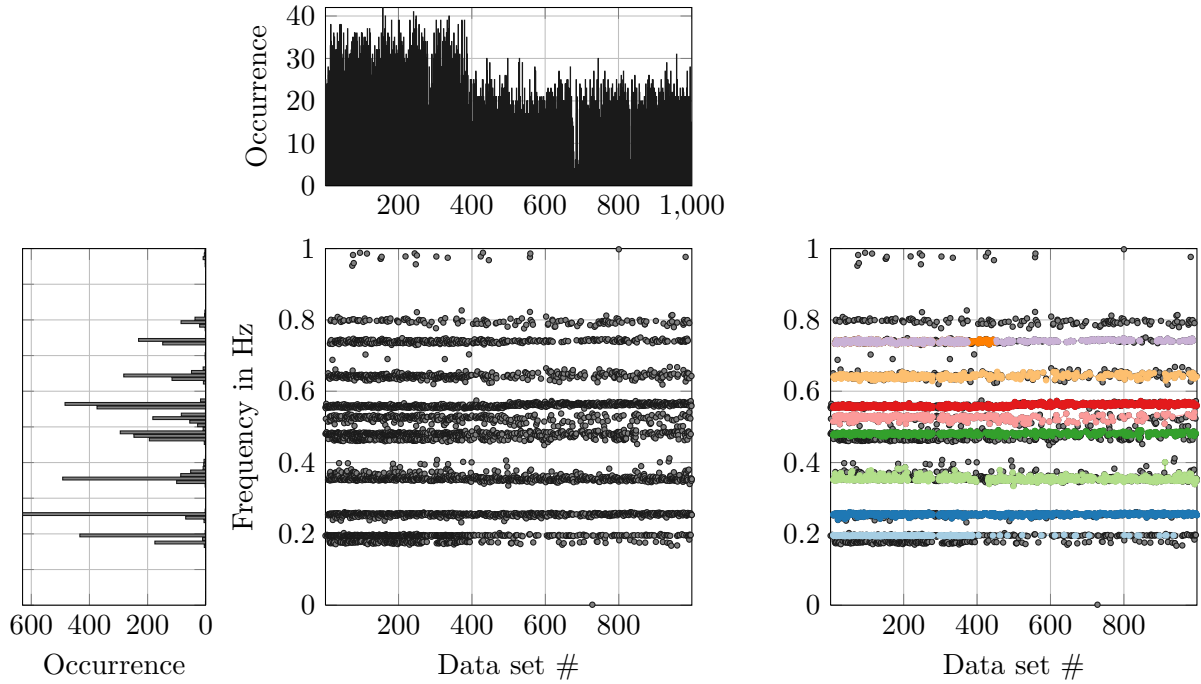
Figure 3.7: Overview of automatically identified modal frequencies for 1000 data instances using TEMP method (2nd from left) along with occurrence of frequencies (left) and number of solutions for modal parameters per data instance (top). Results from a second evaluation by TEMP are given in the right plot. Different colors indicate the different modes over the analyzed data instances

movement.

To gain an insight into the influence of EOCs on the modes, frequencies and damping values are analyzed over five different EOCs using standard box-plots for one mode in Figure 3.9. Within the figure, wind speed, wind direction, temperature, hour of the day, and mean maximum acceleration are analyzed. If a bin contains less than 10 values, e.g. if less than 10 data instances with solutions for those modes exist in the EOC-range, the bin is omitted in the plot. Accordingly the number of bins might vary between the different modes. Values indicated at the bins mark the mean values per bin.

Figure 3.9 shows the EOC influence on the first global bending mode. The mode has a major maximum at the middle of the main span and two small maxima at the side span and at the beginning of the main span. With an increase in wind speed the mean resonance frequency drops by 0.5% before slightly increasing with stronger wind back to 0.178 Hz (1st row). Damping ratios follow a similar trend, slightly decreasing before increasing again. The wind direction (2nd row) also has a minor influence on frequency and damping. Only the frequency follows a slight trend reaching a maximum at the 82.5 degree bin. Temperature influences manifest most strongly in the damping values (3rd row). For lower temperatures around 11 degrees Celsius mean damping values lie above 1% and rise up to 1.5%. With an increase in temperature, damping drops down to a third with 0.5% for temperatures higher than 17 degrees. Usually an increase in temperature would be considered to coince with an increase in damping. The hour of the day reveals a higher frequency at 4 am night time and lower frequencies for day time, indicating more traffic load
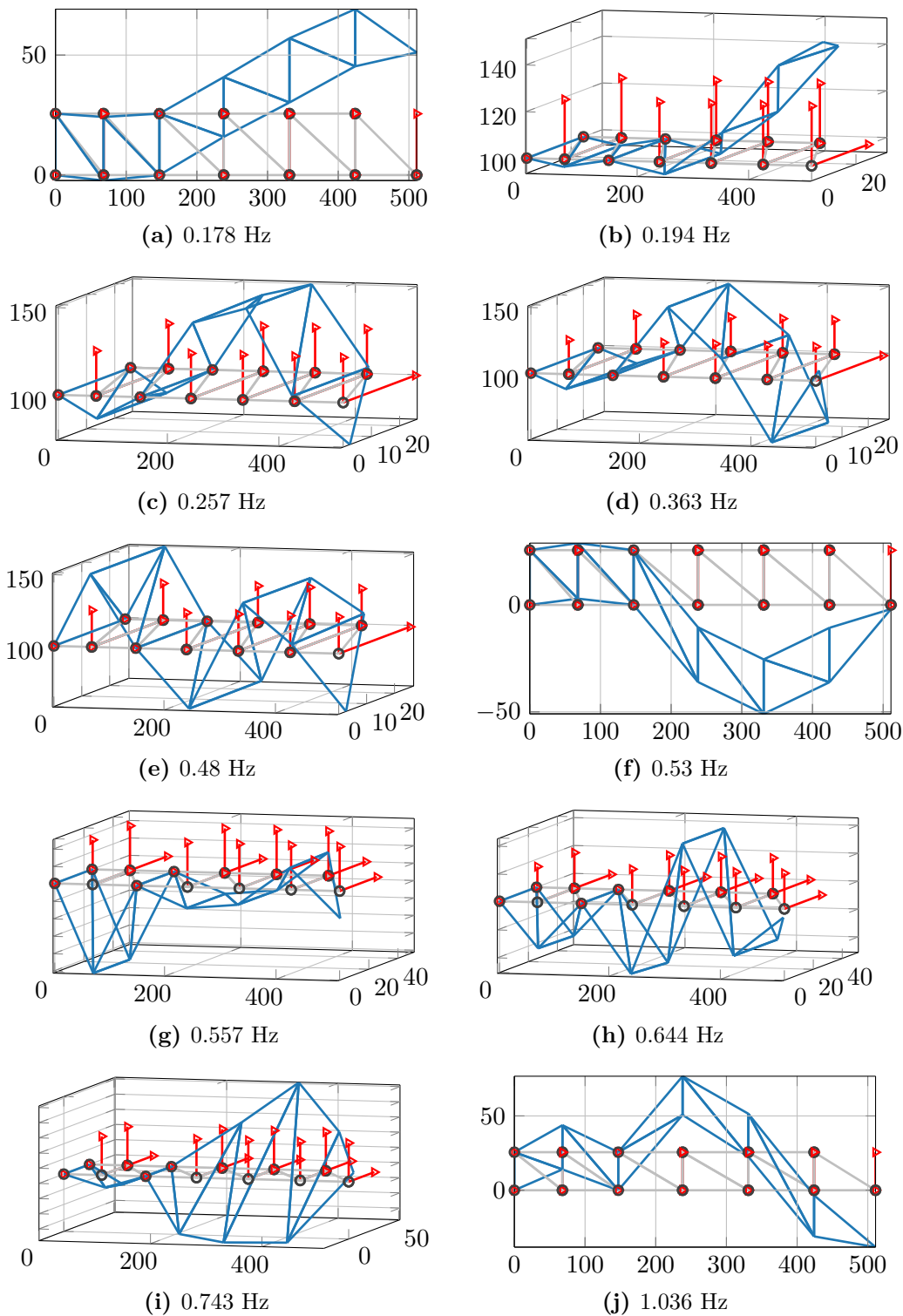
Figure 3.8: Identified global bending and torsion modes for NCB at mean frequencies of 0.178, 0.194, 0.257, 0.363, 0.48, 0.53, 0.557, 0.644, 0.743, and 1.036 Hz (left to right, top to bottom). Mode shapes are extracted from data instance # 17 (07.12.2012; 08:00 am).

during the day (4th row). Further, the first modal frequency seems to decrease slightly with an increase of acceleration amplitude indicating non-linear behavior (5th row).

For this benchmark example, TEMP proved to be an effective tool for aiding the automated processing of dynamic bridge response data. The automated analysis enables a statistical evaluation of identified modes through e.g. box-plots. Here, EOC dependencies are revealed and aid subsequent analysis and validation of simulations and numerical models. Overall, temperature changes reveal the most significant effect on the analyzed mode. Nevertheless, different EOCs correlate and further analysis is necessary to investigate changing dynamics. The knowledge of EOCs which affect the structures behavior and those who do not, can be included in the SHM process as aid for decisions regarding which EOCs can be employed in machine learning.
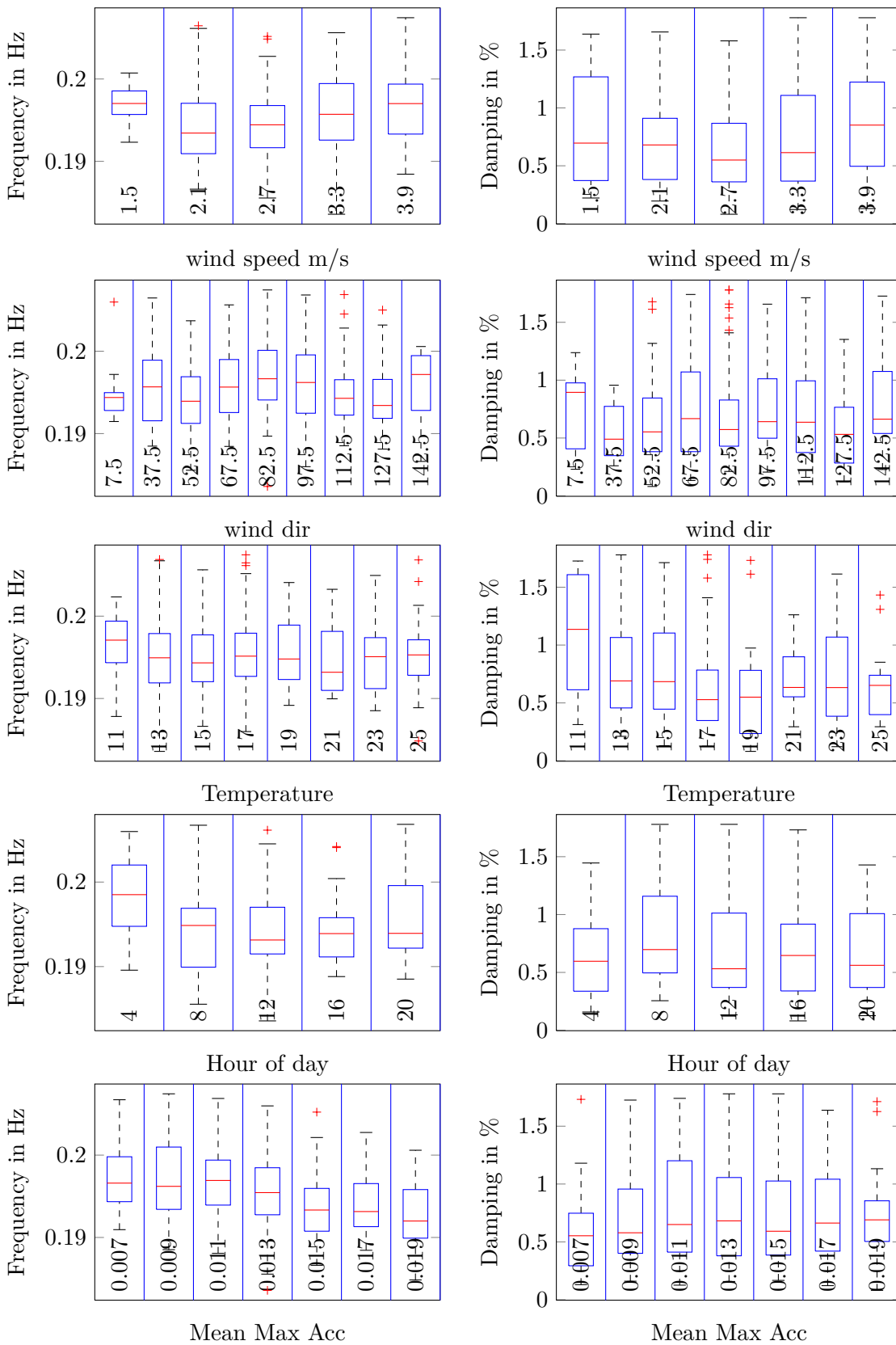
Figure 3.9: Dependencies of modal frequency and damping for first NCB bending mode at 0.194 Hz.

3.4 A SHM Framework – How to Estimate SHM Performance Holistically

This section will give an insight into the different steps of the proposed modular SHM framework. To realize this task and following Montgomery [128], a differentiation is desired between "chance cause of variation", the variation due to natural variability, and "assignable causes", changes due to system abnormalities. Approaching the problem of monitoring a mechanical structure, Deraemaeker et al. [46] state a general relation between *input* (*EOCs* and resulting loads) and *output* $\mathcal{Y}$ (CPs) through an unknown mapping of functional $f(\bullet)$ with

$$\mathcal{Y} = f(EOCs) + g(\eta). \tag{3.5}$$

$g(\eta)$ represents an unknown residual term from damage and noise effects and $\mathcal{Y} \in \mathbb{R}^{\bar{m} \times k}$ is the state matrix, with $\bar{m}$-dimensional CPs and k training sets. Providing a sound and reliable formulation for $f(\bullet)$ and to minimize $g(\eta)$ is the main task in SHM. This formulation will be extended to cover all necessary steps for an SHM application. The main focus of the proposed framework is damage detection (SHM-level one), e.g. to separate normal from abnormal states and the performance evaluation of different ML-CP-HT combinations. If an abnormal state is detected, the possibility of damage localization (SHM-level two) can be addressed.

Postulating a valid data acquisition, four different steps are defined: Data selection, machine learning (ML), condition parameters (CPs), and hypothesis testing (HT) (see Figure 3.10). This is motivated by the SHM axioms and the following statements:

1. **No evaluation can be performed without a parameter to judge on (CP).**
2. **No decision on a parameter can be taken without a threshold (HT).**
3. **No threshold can be defined without a basis of data instances even if only a single data instance or a single data group is used (ML).**
4. **No basis can be defined without data selection.**

Hence, the following points of variation occur during application:

1. **Training data, in count and selection of training sets.**
2. **Machine learning, in type and setting of applied techniques.**
3. **Condition parameters, in type and settings for the extracted parameters.**
4. **Hypothesis testing, in probability density functions and confidence intervals.**

Since there is no underlying mechanical model of the structure involved, it is applicable to any given mechanical structure from which dynamic responses can be measured. For complex, large scale structures it is widely accepted that a measurement of the single time instance will not be sufficient as reference. Hence, most of the recent SHM-procedures as well as this framework consist of a so called training or base-line phase (indicated by solid lines in Figure 3.10) and a testing or monitoring phase (dotted lines in Figure 3.10).

ML, as a tool to learn the systems behavior during healthy states, is applied to the training database by utilizing attributes of each data instance ($\mathcal{D}_i^{\mathbf{EOC}}$). These can either be values

extracted from the measured response time series or, more commonly, additionally collected EOCs. A CP can be any value derived from the recorded time series per data instance. The definition of *relative* and *absolute* CPs is based on the CP formulation: If by definition a second data instance is needed to calculate the CP for a certain set, the CP is categorized as *relative.* Absolute CPs in contrast are directly derived from a single data instance. Modal frequencies for example are absolute CPs, if a frequency difference is used, they become relative CPs.

This does not contradict the statements above since both CP types are compared to the training phase during HT. The distinction is more of a practical kind since the implementation effort for relative CPs is higher[1] and they prohibit supervised ML. It should be noted that the order of ML and CPs might be reversed depending on the applied scheme, e.g. for machine learning techniques that neglect EOCs or supervised machine learning. Further, HT is understood as both building a probabilistic model for CPs during training with respect to machine learning and evaluating new incoming data instances with respect to these probabilistic models. The result is a hypothesis test with a decision about whether the structure is healthy or not.

Once CPs are calculated for all data instances, their distribution (e.g. within clusters) can be calculated and confidence intervals serve as thresholds for future data instances to differentiate between healthy or unhealthy states:

- Training phase
  - **Data acquisition**: Initial database composed of valid and sound data instances;
  - **Machine learning**: Training with data under differing system states[2];
  - Estimation of **condition parameters**;
  - **Hypothesis testing**: Setting up **probabilistic models** for CPs with respect to ML;
- Testing phase
  - **Data acquisition**: New, incoming data instances (usually 10 min. blocks for OWTs);
  - **Machine learning**: Data instance assignment and integration;
  - Calculation of **CP(s)** (if necessary, with respect to machine learning);
  - **Hypothesis testing**: Evaluation of CP(s) within probabilistic model(s);

Many different approaches can be implemented to achieve these SHM steps (see 1.3.2 to 1.3.3 and 2.5 to 2.7), in Figure 3.10 represented through (a-c),(A-C), and (𝔞-𝔠), respectively. If the structure is considered healthy during a monitoring phase, the base-line phase can be extended by further data instances to increase reliability. Based on the decision of whether the structure is in a healthy or abnormal (potentially unhealthy) state, further SHM-levels may be investigated.

Following the framework from Equation 3.5, where a state matrix is defined as function of EOCs and noise, an extension leads to a global description of SHM:

$$
\begin{aligned}
ML &= f(EOCs, CP) + g(\eta) \\
CP &= f(EOCs, ML) + g(\eta) = \tilde{\mathcal{Y}} \\
HT &= f(ML, CP) + g(\eta)
\end{aligned}
\tag{3.6}
$$

---

1   Since relative CPs need a reference for their estimation, a change in ML and hence a (possible) change in data classification leads to the need of a re-estimation of those parameters for every ML setting.

2   This step is often also referred to as data normalization and might be applied subsequently to the estimation of condition parameters, depending on the procedure chosen.
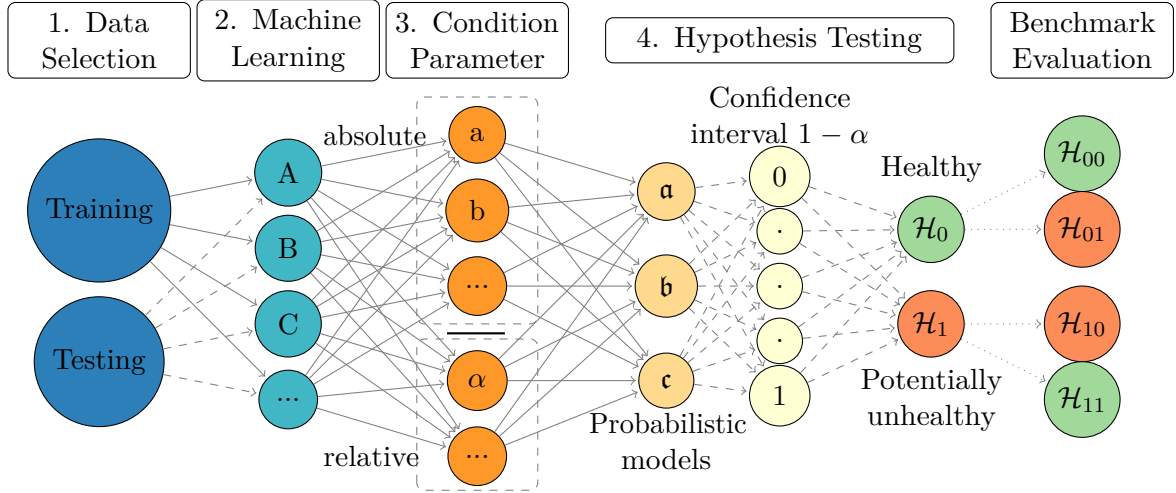
Figure 3.10: Modular SHM framework: Training and subsequently testing data instances are analyzed through a combination of machine learning algorithm, damage parameter and probabilistic model to draw a decision about the state.

Again, $g(\eta)$ represents an unknown residual term from damage and noise effects and $\tilde{\mathcal{Y}}$ is a modification of the state matrix. Machine learning becomes a function of EOCs and noise, CPs are indicated in grey since they are only involved when supervised ML is applied. CPs are defined as a function of EOCs and noise, former denoted as state matrix (see Equation (3.5)). If relative CPs are used, the dependency also includes ML (grey). Hypothesis testing as the final step depends always on ML and CP. During operation, the SHM procedure results in a series of hypothesis tests. The number of tests depends on the number of applied ML procedures and settings, the number of different CPs and the number of HT variations. The resulting, binary decision $\mathcal{H}$ is always a function of ML, CP and HT and can be defined as

$$\mathcal{H}_{n,k} = \mathcal{H}(ML, CP, HT) = \begin{cases} \mathcal{H}_0 & \text{for} \quad \text{Healthy states} \\ \mathcal{H}_1 & \text{for} \quad \text{Abnormal states} \end{cases} . \tag{3.7}$$

$\mathcal{H}_{n,k}$ is the HT result for data instance n under the k-th ML-CP-HT-combination. In general, there is no information about how well the SHM framework performs, no matter which techniques are chosen in the single steps.

However, if the monitored structure can be damaged or modified artificially, as for the examples given in Chapter 3.5 and 4, or abnormal states are known in the testing phase, the SHM procedure can be evaluated both for false positive (FP, $\mathcal{H}_{10}$ in Figure 3.10) and false negative (FN - $\mathcal{H}_{01}$ in Figure 3.10) HT results. Further, if the training phase is sufficiently long and the structure remains healthy, which is mostly proven through conventional inspections, the hypothesis tests of the SHM framework can be checked against false positive alarms, since they should not exceed the confidence intervals chosen.

3.4.1 Training Phase

Machine Learning

Starting with the initial step after data collection and validation, many different options exist for machine learning. It is emphasized that the assumption of a healthy, or normally behaving, structure during the training phase must hold. In Chapter 2, four variants are discussed with manual classification, k-means, affinity propagation and least squares support vector machines. While the latter is a supervised learning method (dependencies between EOCs and CPs are trained) all other approaches can be used as unsupervised techniques with EOCs as their input. Figure 3.11 shows the exemplary applications of these variants. Here a two dimensional, normalized EOC vector of wind speed and rotor speed is considered. It is advisable to normalize each EOC to neglect different weighting through distance measures in the EOC space. For manual classification, this step can be omitted. The following normalization by median and maximum absolute value is performed per EOC before automated clustering:

$$\tilde{x}_i = x_i - p_{50}(x) \qquad\qquad \hat{x}_i = \tilde{x}_i/max(|\tilde{x}|) \in [-1,1] \qquad\qquad (3.8)$$

Here, x_i is an EOC value for data instance i, $p_{50}(x)$ is the median of the EOC vector (all data instances participating in the training phase), and $\hat{x}_i$ is the scaled EOC.

In case of a *base classification* (upper left in Figure 3.11) all data instances are put into a single cluster where no distinction is made by EOCs. Sometimes this case is referred as a technique that overcomes machine learning, but is basically the most simple example of it. For easily separable EOCs, manual classification can lead to a proper separation of data instances, as given in the upper right plot of Figure 3.11. Here, four non-overlapping clusters result. Nevertheless, with an increasing number of input EOCs, manual classification will become impractical. An example for automated clustering is given in the lower left plot of Figure 3.11: Each color indicates a cluster resulting from affinity propagation. In contrast to manual clustering, each data instance which is part of the training phase is automatically assigned to a cluster. If one decides for unsupervised ML and further for data clustering, there are a vast number of different classification procedures available at this point. Affinity propagation by Dueck [52], as introduced to SHM in [77], has the potential to provide a well performing and fast solution.

Independent from the chosen procedure, the step of data classification or clustering results in the assignment of data instances from the training phase to a certain cluster. This assignment can be stored e.g. in a vector for each classification variation, later denoted as ML^X (see Table 3.2). Different manual borders as well as different settings[1] for affinity propagation or k-means will result in different assignments. Hence, each realization (potentially) results in a different number of clusters, with differing cluster sizes.

If a supervised machine learning technique is chosen, such as a realization of neural networks

---

1 Settings can either concern parameters that need to be set for the procedure itself, e.g. cluster number for classical approaches or the preference for affinity propagation, or also the number and type of EOCs used.
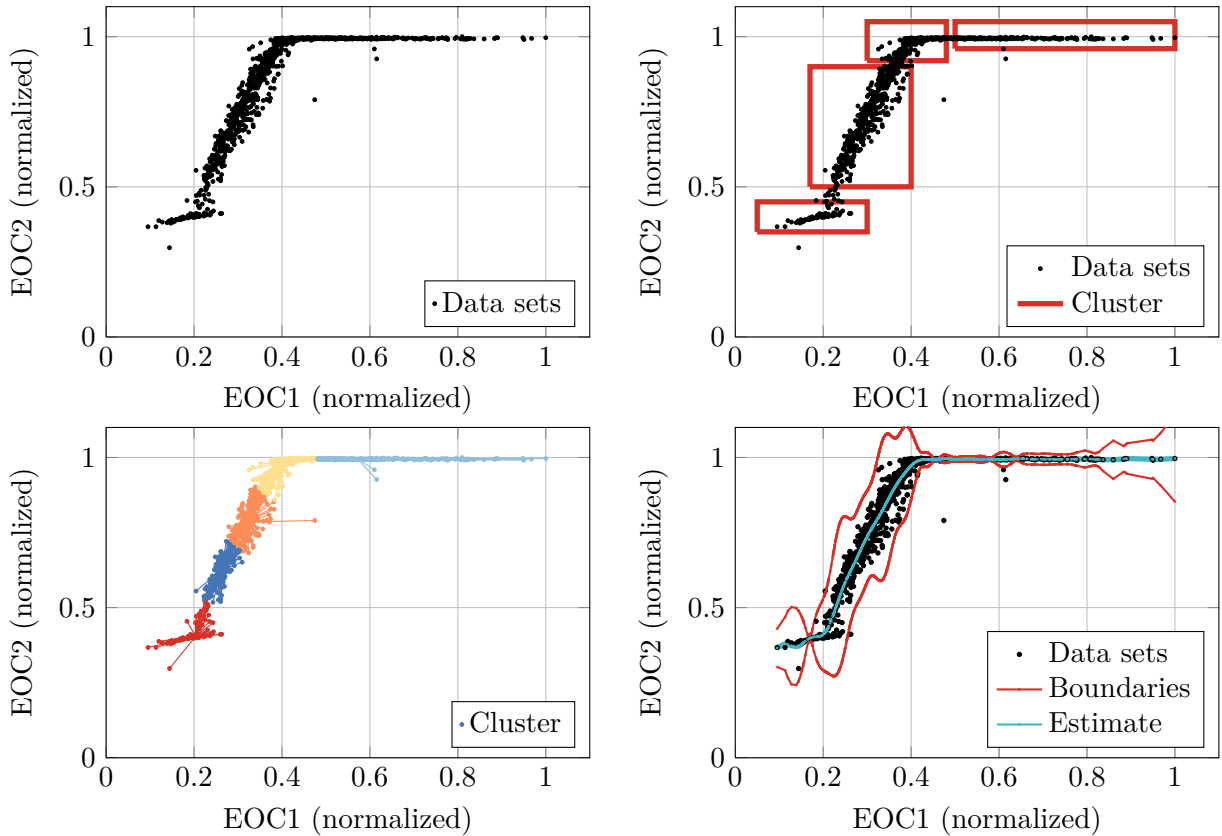
Figure 3.11: Exemplary machine learning cases for *base classification* (upper left), manual classification (upper right), k-means or affinity propagation (lower left), and regression analysis (lower right) in a two-dimensional, normalized EOC-space. Data distribution shows a typical distribution for rotor speed over wind speed of a pitch-controlled, multi-MW wind turbine.

or regression analysis, the dependency between EOCs and CPs is trained. The lower right plot of Figure 3.11 shows a least-squares support vector regression for the example data instances. It should be noted that EOC2 (rotor speed) is assumed to be a CP (goal value) here. The procedure results in a forecast (blue line) for the CP (EOC2), depending on the input given by EOC1. Additionally, the procedure provides varying confidence intervals which depend on the input variable (red lines). The input parameter can be multi dimensional, resulting in CP spheres. (LS-)SVM are a handy tool for well correlated processes with no ambiguities. Also the input-output relation should not contain gaps. Additionally the definition of proper reference data instances for relative condition parameters, is more difficult to realize since both, input (EOCs) and output (CP) are needed simultaneously for supervised ML.

Superior performance of AP compared to standard k-centers clustering was already stated. Figure 3.12 shows results for the comparison of cluster quality by the mean Euclidean distance between the cluster center and nodes for AP and k-centers, seven EOCs are used as input[1]. Analysis is carried out for four training set sizes and different numbers of cluster each. For a fixed

---

1 Rotor speed, wind speed, nacelle position, wind direction, turbulence intensity, temperature, and air pressure

number of clusters, AP calculates the desired solution iteratively. Further, AP was run a single time and k-centers 10,000 times. AP is able to outperform the classical clustering approach for almost all displayed cases with a single run. Only for 1008 data sts and very high numbers of clusters k-centers is able to lead to better results than AP. Accordingly, AP is favored.

As stated before, due to these limitations and the desire to use relative CPs and accordingly unsupervised machine learning procedures, *base classification*, manual classifications and affinity propagation are used to investigate SHM performances within the presented framework. Table 3.2 gives an overview of the nomenclature and variables.

Condition Parameters

After the ML step is performed, absolute and relative condition parameters can be calculated. The calculation of absolute CPs is independent from ML since the parameters result from the data instance itself. In contrast, relative parameters necessitate the definition of one or more reference data instances and hence depend on the ML instance. While for absolute parameters ML only defines the separation into clusters, new relative parameters have to be calculated for every ML instance due to the dependency on reference sets (clusters). Table 3.3 gives an overview of the investigated parameters, the nomenclature, description, input variables and references to theory and definitions.

Hypothesis Testing

Once all desired CPs have been calculated for all training data instances and ML in stances, probabilistic features per cluster and classification can be calculated. These serve as basis for hypothesis testing and control charts in the latter testing phase. Basically, a number of CP values form a discrete probability density function (PDF) within each cluster. If desired, a continuous PDF can be fitted to this sample. Figure 3.13 shows the difference between the *base classification* and a classification by affinity propagation for the example data instances from Figure 3.11 for an absolute CP[1]. A sophisticated classification has the potential to reduce the CP variation within

Table 3.2: Used machine learning techniques in SHM framework with nomenclature, input parameters, description, and reference.

Symbol	Description	Input Variables	Ref
Machine Learning Procedures			
ML^{Man}	Manual data classification	EOCs with boundaries or vector with data instance assignment.	
ML^{AP}	Clustering algorithm using message passing between data instances.	p - Preference for data instances; Number and type of EOCs.	2.5.2

1　If a relative CP was used, the right hand plots would differ since different references would result from the single cluster and five cluster in the upper and lower plot, respectively.

Table 3.3: Used condition parameters in SHM framework with nomenclature, input parameters, description, and reference.

Symbol	Description	Input Variables	Ref
Absolute CPs, calculated for each channel separately (locally), except modal frequencies CP^{f_i}.			
$CP^{Max}_{(i)}$	Signal maximum per channel	-	
$CP^{\sigma}_{(i)}$	Signal standard deviation per channel	-	Eq.(2.43)
$CP^{\gamma_1}_{(i)}$	Signal skewness per channel	-	Eq.(2.44)
$CP^{\gamma_2}_{(i)}$	Signal kurtosis per channel	-	Eq.(2.45)
CP^{f_i}	Modal frequencies per data instance	N_{shift} - Number of blocks/shifts in Block-Hankel-Matrix, N_{Orders} - Model orders for stabilization diagram, and $krit$ - TEMP parameters	P.60ff
$CP^{E_{yy}}_{i,[e_a-e_b]}$	Frequencies linked to accumulated energy levels per channel	$N_{intervals}$ - Number of intervals for energy/frequency.	Eq.(3.1)
$CP^{E_{xy}}_{i,[e_a-e_b]}$	Frequencies linked to accumulated energy levels for all cross correlations with channel i	$N_{intervals}$ - Number of intervals for energy/frequency.	Eq.(3.1)
Relative CPs, calculated for all channels at once (globally).			
CP^{R^2}	Measure of difference between data simulated by VAR and measured data per data instance	p - Number of backward time steps taken.	Eq.(2.69)
$CP^{\mathcal{M}}$	Test value of M-Box-Test for data simulated, per data instance	p - Number of backward time steps taken.	Eq.(2.76)
CP^{ε}	Summed residual vector of Hankel-Matrix multiplied by reference Nullspace	n_{shift} - Number of blocks/shifts in Block-Hankel-Matrix, n_{is} - number of non significant (right) columns in left SVD-matrix, defining the size of Nullspace.	Eq.(2.55)
CP^{γ}	Subspace based damage residual for data instance	n_{shift} - Number of blocks/shifts in Block-Hankel-Matrix, n_{sig} - number of significant (left) columns in left SVD-matrix, and n_b - number of sub blocks.	Eq.(2.64)
CP^{MSD}	Distance measure using an arbitrary combination of CP in vector form	Combination of the above	
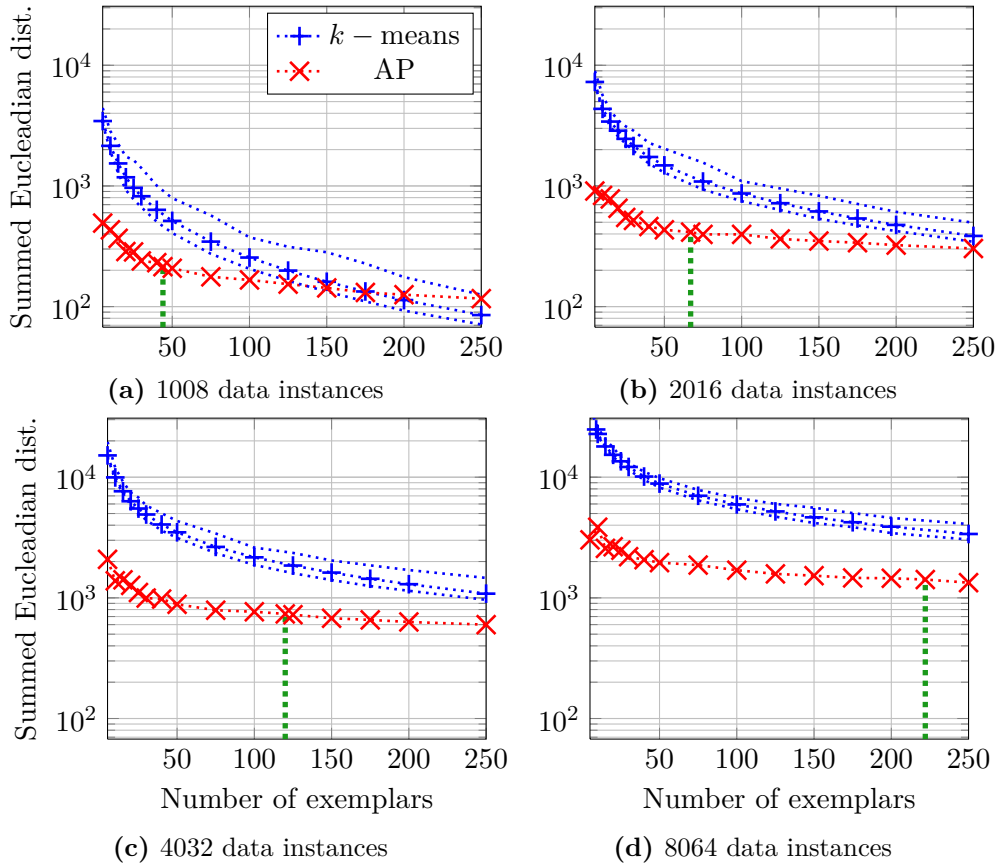
Figure 3.12: Mean euclidean distance between cluster centre and corresponding datums for different numbers of exemplars and training data instances quantities. Solutions for a single AP–run and 10,000 runs for k-centers (mean, minimal and maximal results given). Green, dashed lines indicate sets with automatically chosen numbers of exemplars by AP.

each resulting cluster, compared to the overall variation. Further, a damaged structure under EOC combination x might behave as the intact structure under EOC combination y. In this case the damage is masked by variations due to EOCs.

Since the fitted distributions serve as boundary estimators for hypothesis testing, it is important to extract good estimates for upper and lower control limits (UCL/LCL) as discussed in Chaper 2.7. Both depend on the assigned cluster, chosen confidence interval, and distribution type.

It is obvious that for the artificial case in Figure 3.13, five clusters in the lower right plot (ML^{AP}) result in a better description of the five overlaying distributions compared to the single cluster in the upper right plot (ML^{Man}). E.g. a CP value from a damaged structure of 10 would be close to the center of the fitted distribution for ML^{Man}, while it would probably be indicated as outlier with the distributions in ML^{AP}. Accordingly, the SHM performance based on five clusters will be better in the testing phase where each new data instance is assigned to a cluster by EOCs (here EOC1 and EOC2) and control limits are taken from the individual cluster.

Next to the CPs, the ML decision influences the performance of a hypothesis test for a new data instance. Nevertheless, further decisions have to be made to extract boundaries (upper and lower control limits, UCL/LCL). As depicted in the right hand plots in Figure 3.13, only a
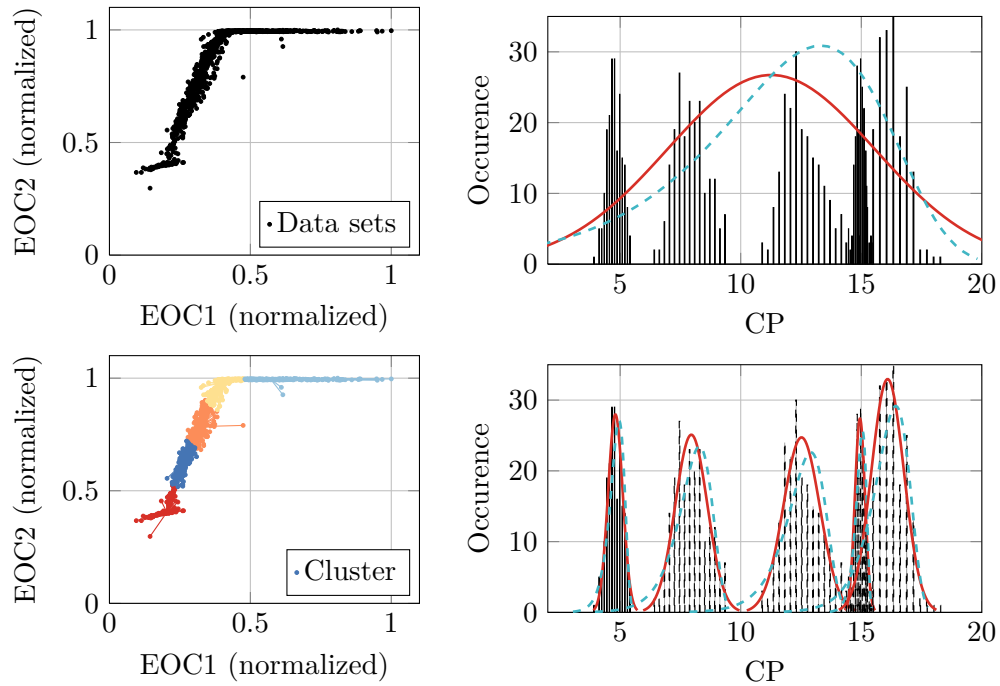
Figure 3.13: *Base classification* with a single cluster (upper left) and classification by affinity propagation with several clusters (lower left) for exemplary training phase. According discrete density functions over clustered CPs are given in plots on the right hand side. Continuous PDFs for a normal (solid) and extreme value distribution (dashed) are included for a single cluster (upper right) and five clusters (lower right).
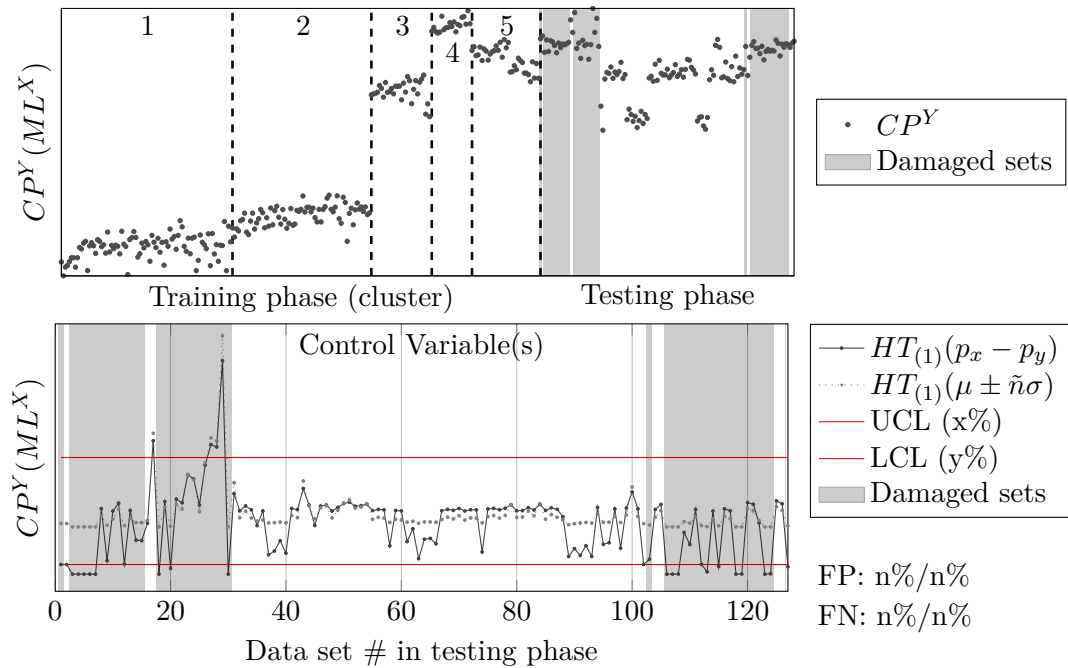
Figure 3.14: Exemplary plots for absolute CP values during training and testing (upper plot) and normalized, multi-reference x-bar-control chart for evaluation during testing phase (lower plot).

discrete sample of the true parameter distribution exists. The sample size is directly influenced by the size of the training phase and the number and characteristics of clusters resulting from machine learning. Once the sample per cluster is defined by ML and CP, one has to draw limits based on an assumption for the distribution type. Here the distribution type (normal, extreme value, discrete etc.) and the desired confidence interval form the two main variables. In this case only Gaussian normal- and discrete distributions will be investigated. It should be noted that the precision that can be achieved formally depends on the sample size.

3.4.2 Testing Phase

After the training phase and hence after ML and CP estimation, new data instances are analyzed in the testing phase. Each data instance is therefore assigned to a cluster in each ML variation ML^X and the desired PDF can be built for each CP^Y. The upper plot in Figure 3.14 shows an exemplary plot for a single $CP^Y(ML^X)$-combination over the training and testing phase. Again, five clusters appear in the training phase in which CP^Y takes on different value distributions in each cluster. CP^Y values for the testing phase are plotted chronologically in the right part of the upper plot. Phases in which known abnormalities or damage (in the benchmark case) are marked with grey patches. It can be seen that the complete parameter range during the test phase is covered by the range of the training phase. Only the comparison within the correct cluster (1 to 5) reveals abnormal CP^Y values.

For the testing phase of the SHM framework, a well known tool for process observation can be utilized by using control charts (lower plot in Figure 3.14). Every new data instance is assigned to its corresponding cluster in the training phase by its EOCs. For each cluster possibly different parameter distributions result which CP^Y, denoted X_i, is compared to. It is convenient to define a normalized control chart with $LCL = -1$, $UCL = 1$ and $CL = 0$ in the spirit of a standardized normal distribution. Therefore, X_i is normalized to

$$\hat{\mathsf{X}}_i^{\mathcal{D}} = \begin{cases} \dfrac{\mathsf{X}_i - \mathsf{X}_{50\%}}{\mathsf{X}_{50\%} - \mathsf{X}_{\alpha/2\%}} < 0 & \text{for} \quad \mathsf{X}_i - \mathsf{X}_{50\%} < 0 \\[3mm] \dfrac{\mathsf{X}_i - \mathsf{X}_{50\%}}{\mathsf{X}_{(1-\alpha/2)\%} - \mathsf{X}_{50\%}} > 0 & \text{for} \quad \mathsf{X}_i - \mathsf{X}_{50\%} > 0 \end{cases} \tag{3.9}$$

for a discrete distribution by percentiles and

$$\hat{\mathsf{X}}_i^{\mathcal{G}} = (\mathsf{X}_i - \mu_i)/(\tilde{n}_i \sigma_i) \tag{3.10}$$

for a Gaussian distribution. X_i represents the CP for a data instance i from the testing phase, depending on ML^X if a relative CP is investigated. Further, the percentiles $p_{n,i}$, mean μ_i, and standard deviation σ_i have to be calculated with respect to the current data instance. Through the normalization in Equation (3.9), UCL and LCL lie at $+1$ and -1 for any data instance and CP-ML combination. It is important to take the scaling of the CPs into account since these might range over various orders of magnitude. For some analysis it aids the inspection of control charts to use logarithmic scaling, as applied in Section 3.5. In such a case the absolute value of the

control variable is used and both control limits lie at $+1$.

After application of Equation (3.9), a normalized control chart can be plotted for all new parameters (CPs from new data instances). The lower plot of Figure 3.14 shows the control chart normalized through 3.9 and 3.10 and hence a normalized version of the testing phase in the upper plot. Again, grey areas mark damaged data instances and red lines indicate UCL and LCL (± 1). If the control variable remains between these lines, the structure is assumed to be healthy. If it exceeds these limits, potentially abnormal dynamic behavior is detected ($\mathcal{H}_0$ and $\mathcal{H}_1$ in (3.7)). The two lines result from two different distribution assumptions; one from a Gaussian normal distribution (dashed) the other from a discrete distribution (solid). In the benchmark case, the information about detection rate (100-FN) and FP can be used to evaluate the performance of a certain $ML^X - CP^Y - HT^Z$-combination though FP/FN percentages (indicated at the lower right of the lower plot).

Based on the knowledge of FP and FN percentages, performance maps are introduced to evaluate the quality of a given $ML^X - CP^Y - HT^Z$-combination in a normalized manner. Figure 3.15 shows such a performance map with the false alarm rate (FP) in % on the x-axis and the detection rate (1-FN) on the y-axis. Each $ML^X - CP^Y - HT^Z$-combination results in a point on this map. It should be noted that maps are drawn for a single HT type here, e.g. for a discrete or a Gaussian normal distribution. To distinguish between the different combinations, different markers indicate different ML types and numbers indicate different CPs. Hence, a marker-number combination uniquely defines a $ML^X - CP^Y - HT^Z$-combination. Results can be interpreted as in receiver operating characteristics (ROCs) in Chapter 2.7.3. Performance maps can be extended to ROCs if confidence intervals are varied for an analyzed combination. The area under the (ROC-) curve (AUC) will be used as final performance indicator in the presented SHM framework.

It is suggested to add the performance lines from Figure 3.15 to the ROCs to facilitate the visual inspection. An evaluation by the AUCs of ROCs can be used to evaluate performance for
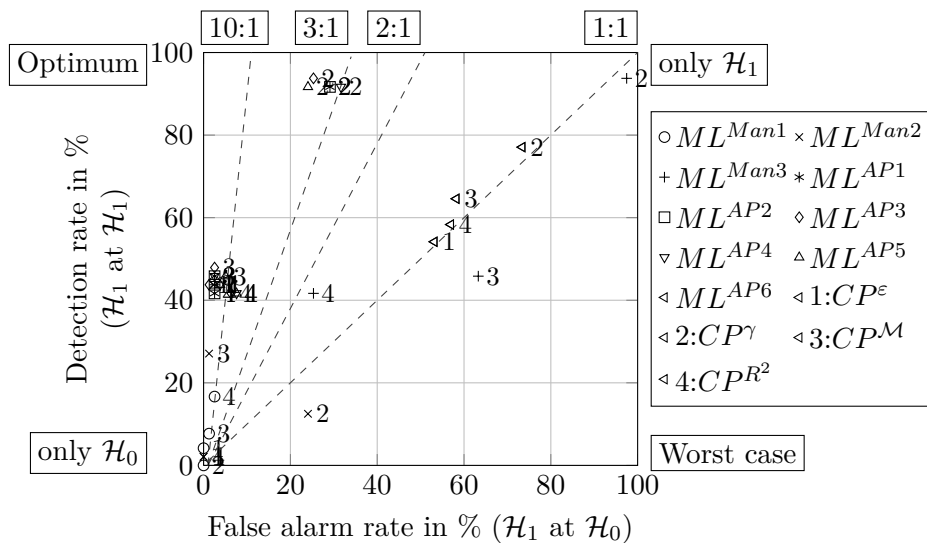
Figure 3.15: Examplary performance map for SHM framework. Different ML types are indicated by different symbols, different CPs by numbers.

different damage scenarios separately or for different damage scenarios at once. The analysis always leads to the optimal setting for all damage scenarios present in the testing data instances: If the testing data contains e.g. 100 damaged data instances, next to another 100 healthy sets, and 90 of the damaged sets represent a severe damage scenario, the other a very small, most ML-CP-HT combination will start off with a detection rate of 90%. Still, the procedure will optimize the SHM framework to the one realization which additionally identifies the 10% of data instances with less severe damage. In other words, it is not prohibited to mix different damage cases in the testing data instances, keeping in mind that some might be easier to identify than others. For instance this can be observed in the control charts of the subsequent example as long as all ML-CP-HT scenarios are compared for the same data instances.

3.5 Concept Validation: Monitoring of Three-Story Building Structure

The following section will outline the application of the modular SHM framework to a benchmark database that is publicly available and is provided by the Engineering Institute of Los Alamos National Laboratories[1]. A description of the structure and test setup is followed by the extraction of modal parameters through the TEMP procedure. Finally, the different steps of the SHM framework are illustrated and different data, ML, CP and HT combinations will be evaluated by their performance.

3.5.1 Experimental Set-up

The structure analyzed is a three story frame with base excitation, sliding on rails in a single direction as depicted in Figure 3.16. Each plate (30.5 x 30.5 x 2.5 cm^3) is connected to the adjacent one by four columns (17.7 x 2.5 x 0.6 cm^3). A shaker excites the structure unidirectionally at the base plate, where a load cell is mounted to measure the applied forces. Further, a column is suspended from the middle of the upper floor reaching down to a bumper on the floor below in order to simulate non-linear damage scenarios. On each of the four plates, an acceleration sensor is installed. The shaker excites the structure by a band-limited random white noise in the range of 20-150 Hz with an excitation level of 2.6 V.

Forces and time series for 17 different states were recorded, see Table 3.4 for a description. Each state consists of 50 data instances, each measured with 320 Hz over a period of 25.6 s. Hence, each set consists of five channels (one load cell and four acceleration channels) with 8192 samples. In state # 1, the structure remains in the initial setup. During states # 2 & 3, additional masses of 1.2 kg were clamped on the base and first floor, respectively (about 19% of the total mass of a floor). These mass changes can be understood as a change due to EOCs, e.g. floor loading in a building. The first three states will be dubbed base-line condition in the following discussions. During states # 4-9 the structure's stiffness was altered (later referred to as linear-damage). Here, a single and then two columns on the shaker facing side were replaced on

---

each floor by columns with half thickness, resulting in a stiffness reduction of 87.5 % per column ($k \propto d^3; k_{red} = (d_2/d_1)^3 = 0.5^3 = 12.5$). In states # 10 to 14, the bumper is installed and the gap between bumper and suspended column is reduced from 0.20 to 0.05 mm resulting in an increase of non-linearity (later referred to as non-linear-damage). Finally, in states # 15 to 17 non-linear damage are combined with additional mass loading, simulating damage under changing EOCs. Further details on the setup, equipment and data can be found in [59] and [60].

Data from the three-story building structure has been the subject of several past scientific publications: The original report from LANL by Figueiredo et al. [59] contains extensive descriptions of the experimental set-up along with different examinations. Recently Farrar and Worden [57] put the results from the original report into a broader SHM context and evaluated the overall performance.

The extensive initial report implies a set-up and data description, machine learning, and investigation of several condition parameters as well as hypothesis testing approaches. Modal frequencies and damping values are estimated through the complex mode identification index and further used as damage sensitive features (see Table 3.6 for a comparison to the new results). An AR-model is fitted to time series of channel 5 (4 in this study) and AR-parameters are used to predict time series for all states. The difference between prediction and measurement are plotted in Shewhart X-Bar control charts in subgroups of four. Confidence intervals are chosen to 3σ based on state #9 in Table 3.4, two AR-Models (AR(5) and AR(30)) are implemented. It is shown that the AR(30) performs better, nevertheless state 16 is not identified as damaged. Further, the approach only accounts for channel four (most affected on 3rd floor) and control limits are not drawn with respect to the complete training phase. Using prediction errors from an auto-associative neural network (AANN) as CPs, trained on channel four of the healthy data instances, results are improved and state #16 is also classified as damaged. Through the usage of
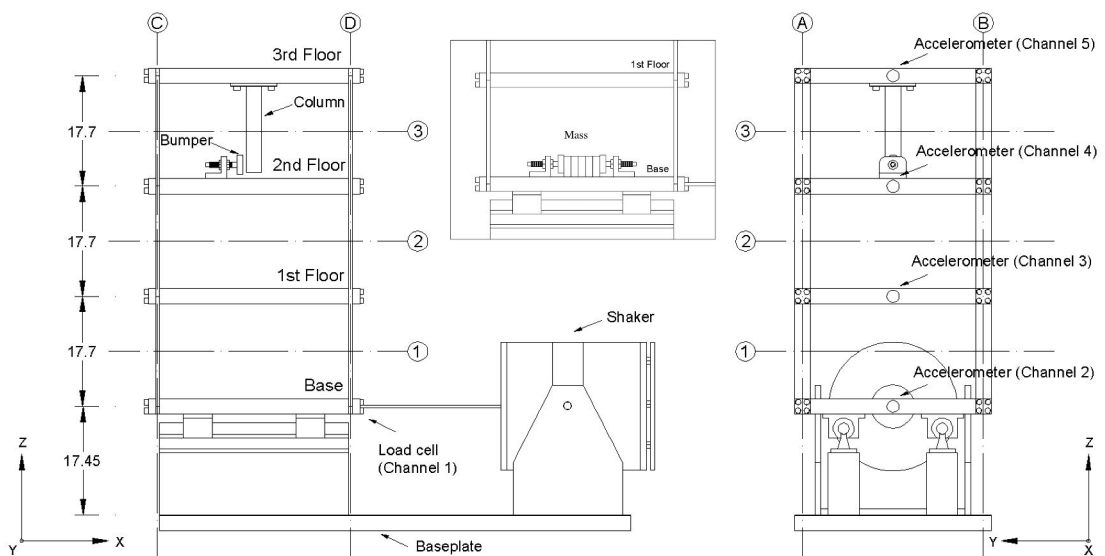
Figure 3.16: Experimental sep-up for LANL three-storey building structure with side views and detail for mass mounting (source: [59]). Since the load cell is not included, channels 2 to 5 in this figure are referred to as channel 1 to 4 in this study.

Table 3.4: Overview of System states for LAN 4-DoF system (⋆Originally treated as healthy states.)

Label	Set	Condition	Description
State 1	1 -50	Undamaged	Baseline condition
State 2	51 -100	Undamaged	Added mass (1.2 kg) at the base
State 3	101 -150	Undamaged	Added mass (1.2 kg) on the 1st floor
State 4	151 -200	Damaged⋆	Stiffness reduction in column 1BD
State 5	201 -250	Damaged⋆	Stiffness reduction in column 1AD and 1BD
State 6	251 -300	Damaged⋆	Stiffness reduction in column 2BD
State 7	301 -350	Damaged⋆	Stiffness reduction in column 2AD and 2BD
State 8	351 -400	Damaged⋆	Stiffness reduction in column 3BD
State 9	401 -450	Damaged⋆	Stiffness reduction in column 3AD and 3BD
State 10	451 -500	Damaged	Gap (0.20 mm)
State 11	501 -550	Damaged	Gap (0.15 mm)
State 12	551 -600	Damaged	Gap (0.13 mm)
State 13	601 -650	Damaged	Gap (0.10 mm)
State 14	651 -700	Damaged	Gap (0.05 mm)
State 15	701 -750	Damaged	Gap (0.20 mm) and mass (1.2 kg) at the base
State 16	751 -800	Damaged	Gap (0.20 mm) and mass (1.2 kg) on the 1st floor
State 17	801 -850	Damaged	Gap (0.10 mm) and mass (1.2 kg) on the 1st floor

the Mahalanobis square distances for AR(5/30)-models as CPs, even better results are achieved. Here, also state #16 is correctly classified as damaged.

In [57][60], the investigated data is also used to carry out a linearity study through a comparison of FRF magnitudes under different excitation levels for the healthy and damaged structure. A strong non-linearity results for the non-linear-damage. Further, the performance of different ML algorithms, namely AANN, factor analysis, Mahalanobis squared-distance and singular value decomposition is demonstrated[1]. FP and FN errors are summarized for all four approaches resulting in total errors of less than 3.8%, favoring the AANN procedure.

In [61] a VAR(15)-model is used in combination with the MSD to identify damage. As in the literature mentioned before, a base line clustering with a single cluster in the training phase is used. The model order was estimated by AIC and state #15 and 16 remain difficult to be correctly accounted as damaged. The analysis also includes approaches with only two/one data channel(s), resulting in a slightly better detection rate. Zhan et al. [218] use the first nine states to apply a model based parameter identification to capture stiffness and mass changes with some success.

---

1 the latter two are not understood as ML techniques in this work but as CPs based on a single cluster.

The available damage states in the data base reach from a small to quite severe changes in the structure's dynamics and both linear and non-linear scenarios can be investigated. Making the provided database a valuable benchmark for new CPs and HT approaches. In summary, many different condition parameters were already applied to the data and state #16 turns out to be the most difficult for damage detection since the non-linearity is the weakest and additional masses influence the behavior. Further, in present studies classification is not applied, and the task of damage localization and the influence of different hypothesis testing approaches remains an open task. Among others, these points will be investigated in the next section.

3.5.2 Data Analysis

In this section, the benchmark database is used to verify the presented system identification procedure, the SHM framework and condition parameters. Main settings for the analysis are listed in Table 3.5: The analyzed database consists of 850 data instances grouped into 17 states (50 data instances each). Each data instance holds measured output data from the four accelerometers at a sampling rate of 320 Hz, input force measures are not included. States #1-3 serve as the training phase, while state #4-17 are understood as damaged. Ten data instances of states #1-3 are kept to account for false positive detection. Hence, 120 data instances are used for training and 730 for testing. In contrast to past studies, stiffness changes are understood as damage. As a result, state #1 can serve as reference for states #4-14, state #2 for state #15 and state #3 for #16 and 17.

Since the different states are well known in this example, no automated machine learning is necessary. Two manual classifications are further analyzed: 1. A so-called base line classification with a single cluster for the complete training phase and 2. A classification with three clusters according to the known system states in Table 3.4. Several CPs are calculated for those two ML options and for each CP and ML, hypothesis testing is carried out. Here a Gaussian and a discrete distribution by percentiles are analyzed. For both, a ROC is calculated with the confidence intervals noted in Table 3.5. The following points will be investigated for the different settings:

- How does the TEMP procedure perform on the data?
- Is there a difference between one cluster (no EOCs included) and the manual classification with three clusters according to EOCs?
- Which damage type (linear, non-linear, EOC + non-linear) is detected through the CPs?
- If damage is detected, does the CP amplitude allow for a relative quantification?
- Is it possible to localize damage without the use of a numerical model?

Table 3.5: Settings for SHM scheme at LANL 4-DoF system. Comments on parameter settings are given at appropriate points in the text.

Number of channels:	4 (@ 320 Hz)	Data sets in training:	120 [1:40, 51:90, 101:140]
Total number of data sets:	850	Data sets in testing:	730 [41:50, 91:100, 141:850]
Number of ML types:	2		
ML Names:	$'Man_1'$ $'Man_2'$		
Number of clusters:	1 3		
Reference EOCs:	State Added mass		

Settings for condition parameter(s):

CP^{f_i}:   Shifs: 70   Model orders: 100 to 300

                $\phi_{crit} = 12.5$ $f_{crit} = 1.5$ $\zeta_{crit} = 35$ $MAC_{crit} = 0.9$ $\hat{P}_{crit} = 50$

$CP^{E_{yy}}_{i,j}$:   Number of energy bins = 10

CP^{ε}:   Shifts = 16   Non-sign. col. = 4

$CP^{\mathcal{M}}/CP^{R^2}$: AR-Model Order = 16

CP^{γ}:   Shifts = 4   Sign. col. = 12   Blocks = 25

Analyzed distribution types: Discrete, Gaussian

Confidence interval - α-values for hypothesis testing: [0.1:0.1:2, 2:1:20, 20:2:40, 40:10:90]%

3.5.3 Operational Modal Analysis

Modal parameters were calculated using the TEMP presented in 3.2, input parameter settings can be found in Table 3.5[1] for CP^{f_i}. Table 3.6 shows averaged results for frequency and damping for 50 data instances in state #1. Results from the initial study are stated as reference. As expected, agreement between frequencies is very good while estimates for damping values do differ more. It should be noted that damping decreases with increasing frequency. Figure 3.17 shows the according mode shapes for the 4-DoF system from a single data instance in state #1. Modes c to e are the first three bending modes of the structure while the low frequent mode at 9.1 Hz is linked to a rigid body motion. It results from the connection between shaker and structure and is not addressed subsequently. Further, the mode at about 20 Hz seems to be an effect of the band limited input excitation being between 20 and 150 Hz. This mode appears in the same shape as the first bending mode. S-plane plots of the modes can be found in Section A.1, here all DoFs align well in the complex plane, but none of the modes lies on the real axis. This proves the complexity of a mode shape being an inferior extraction parameter.

More details about the modes reveals Figure 3.18(a), where all TEMP solutions between 0 and 80 Hz are plotted over the analyzed 850 data instances. If TEMP is applied to these solutions, and

---

1   After the inspection of PSDs from different data instances and channles a lower frequency of interest of $f_{min} = 5$ Hz was determined (see Figure 3.18(c)). Accordingly the number of shifts was chosen to $70 > 64 = f_s/f_{min} = 320/5$. The number of model orders as well as criteria f_{crit}, ζ_{crit}, and MAC_{crit} are empirical. The MPD criterion ϕ_{crit} could be set to a low value of 12.5 due to the laboratory surrounding. $\hat{P}_{crit}$ should be chosen to one half to a fifth of the given model orders, 200 in this case. Explanation on CP settings will be given in the corresponding subsections

Table 3.6: Averaged TEMP results for data instances 1 to 50 (state #1) and reference results from LANL report [59] in braces.

	f_{01} rigid body mode	f_{02} excitation noise	f_1 1st bending	f_2 2nd bending	f_3 3rd bending
f in Hz	9.6	21.2	30.7 (30.7)	54.4 (54.2)	71.2 (70.7)
ζ in %	9.3	4.9	3.8 (6.3)	2.1 (2.0)	0.78 (0.97)

(a) 9.1 Hz **(b)** 19.8 Hz **(c)** 29.7 Hz

(d) 53.9 Hz **(e)** 71.5 Hz
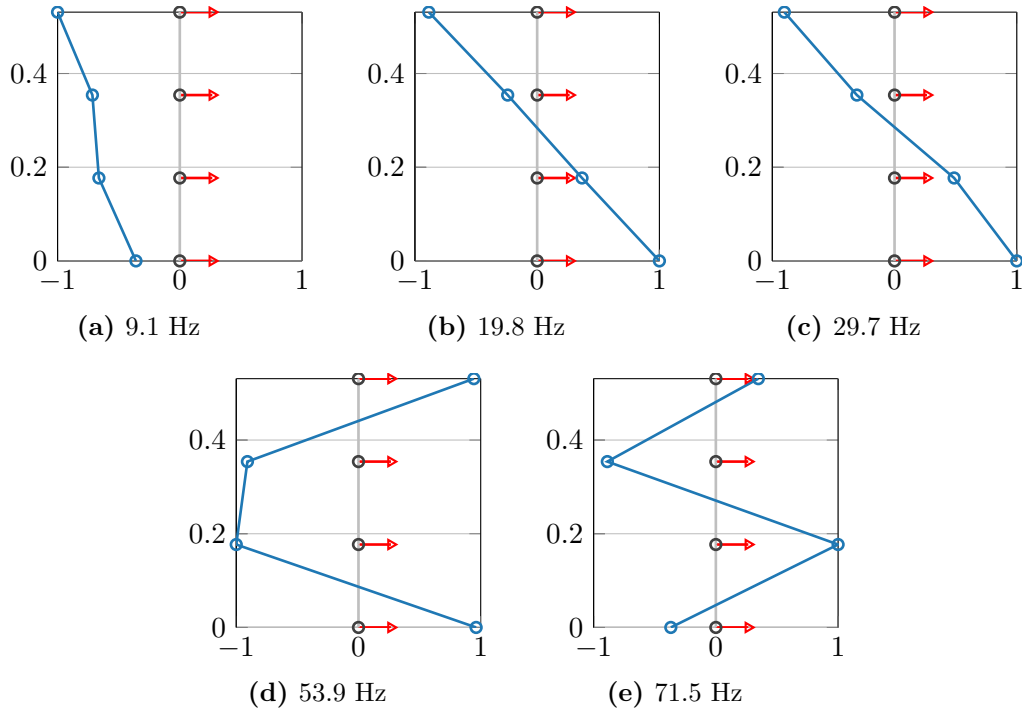
Figure 3.17: First five identified global bending modes at LANL 4-DoF system from data instance 'state01_05'. See Appendix A.1 for s-plane plots.

the data instance number is understood as model order, path objects can be extracted to track the modes over the different data instances (see Figure 3.18(b)). In addition, Figure 3.18(c) holds the averaged PSD for selected states. The rigid body mode is identified at a constant frequency for the first ten states (set 1 to 500), with less identifications in state #7. In states #11 to 17 the identification is disturbed by increasing non-linearities. The mode at 20 Hz, which is not mentioned in the initial report, is constantly identified over all data instances with a fairly large scatter in frequency. This mode will not be included as CP here.

The second bending mode at around 54 Hz reveals some interesting insight in connection with the PSDs plotted in Figure 3.18(c): In 3.18(a), there is notably more scattering for the identification during states #4, 6, 8, and 9, even indicating two close modes for f_2 in states #4 and 8. The spectra confirm this result. Here, for states #4 and 8, the second mode clearly shifts down and switches from a single peak to two (red circles in Figure 3.18(c)). This is most probably a result of the asymmetric damage that is introduced by only altering the stiffness of a single

column. Which results in torsional movements additional to the main bending mode. Accordingly, the effect is not present for states #5 and 7 and only slightly in state #9 where two columns are damaged each. For state #10 with a very low non-linearity, the spectrum is almost similar to the first state. For stronger non-linearities in states #14 and 17, some transformations can be seen at the peak of the second and third mode.

It is obvious that even for such a simple structure as the investigated 4-DoF model, changes in dynamic characteristics due to damage and/or EOCs might be complex and difficult to predict, especially the alterations of the dynamic behavior, in this case visualized by PSDs, is not limited to simple frequency shifts. Due to system changes new peaks will occur and energy will shift from one frequency band to another. Here, the combination of SSI and TEMP is able to identify varying numbers of modes at differing frequencies over the complete database. Further, TEMP can also be used to track modes over the database for the extraction of modal frequencies, damping, and mode shapes as CPs. In that case, the set number is used as model order for the path identification. It should be noted that since in TEMP the occurrence in conjugate-complex pairs is one of the initial checks in the routine, the conjugate complex matrix of all solutions has to be added (see Chapter 3.2).

3.5.4 Application of the SHM framework

In the following section, results from the SHM framework's application to the outlined benchmark database will be shown. Since the structure's states are well known and documented, machine learning in an automated manner can be omitted. Hence, one source of variability can be omitted and data variation, condition parameters as well as hypothesis testing remain to be analyzed. Nevertheless, two different ML set-ups are introduced for a comparison: 1. "Man1" - A so-called base-line classification, where the complete training phase is understood as a single cluster. This attempt is always used when EOCs are disregarded. 2. "Man2" - A clustering that is orientated on the system states where separate clusters are formed for states #1 to 3, respectively. Accordingly, the difference between absolute and relative CPs becomes obvious in this example as well. First, trends and control charts will be discussed for selected CPs, each for both ML settings and a fixed confidence interval and a Gaussian and discrete distribution in hypothesis testing. Subsequently, performance of all settings will be compared by different ROC metrics.

Absolute Condition Parameters

In the following, two examples of absolute CP are chosen for a detailed discussion.

Skewness As a measure of asymmetry the skewness is a CP that potentially indicates non-linearities in the structures dynamic behavior. Figure 3.19 shows the $CP^{\gamma_1}_{(i)}$ trends for all four measured channels over the 850 data instances in the first and second sub-plot. On the left, the training phase is separated by orange vertical lines. For the second sub-plot, three vertical lines indicate the three clusters during the training phase. For each cluster and CP, the parameter distribution is indicated by red symbols displaying major percentiles. On the right side, the
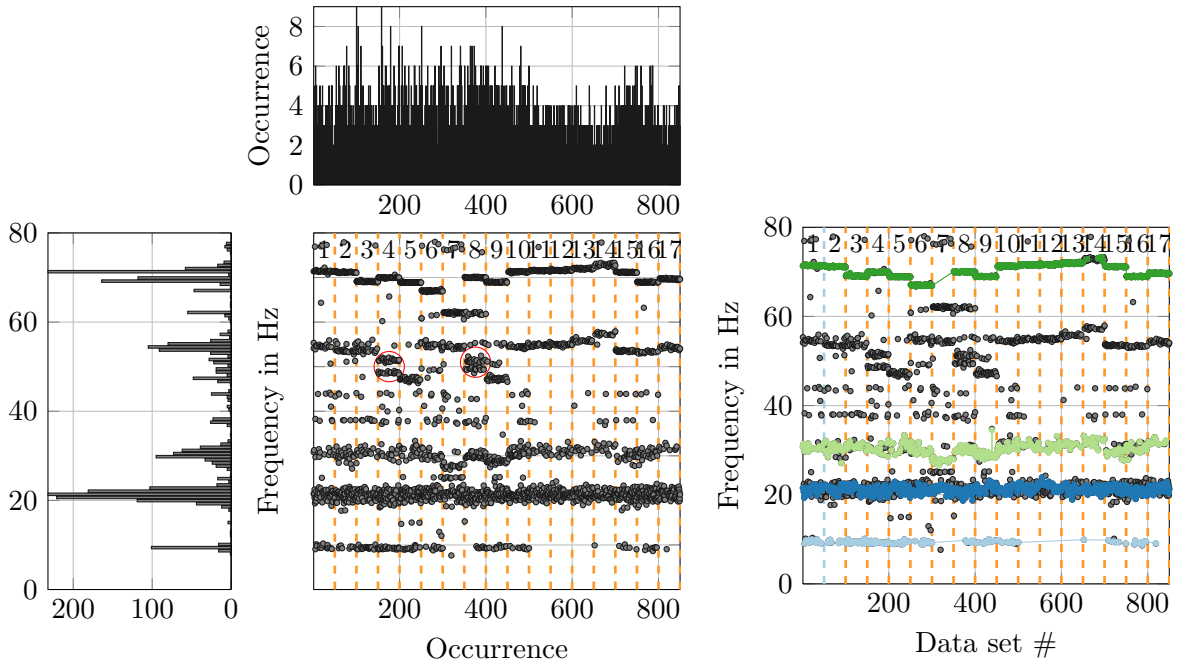
(a) TEMP results over all data instances in databas with occurrences over frequency and data instance.

(b) Path objects for different modes, identified by TEMP from (a)
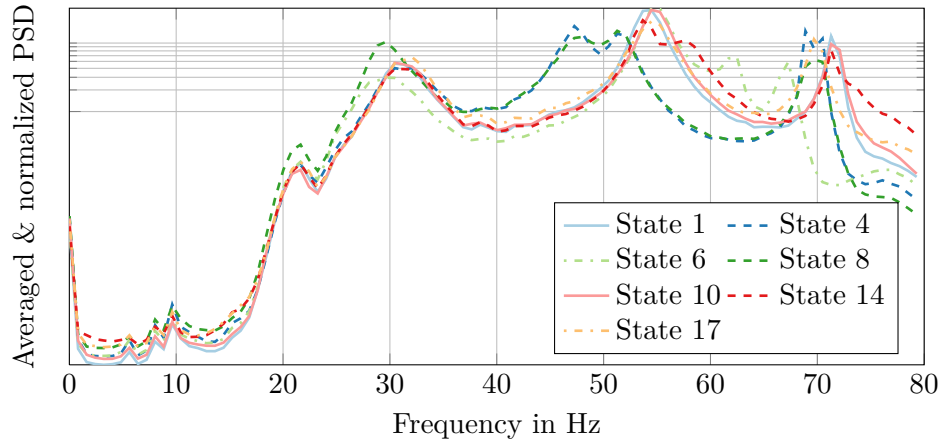
(c) Averaged and normalized Energy content by PSDs for different system states.

Figure 3.18: Overview of automatically identified modal frequencies for all 379 data instances using TEMP method in (a) along with occurrence of frequencies and number of solutions per data instance. Automatically extracted path objects given in (b). The change in dynamic behaviour between different states is visualized by PSDs in (c)

testing phase is visualized, where the grey shading indicates damaged data instances for states #4 to 17. Here, parameter trends are similar between sub-plot 1 and 2 for this absolute Cs, since its estimation does not rely on reference data instances. For relative CPs, these plots will differ accordingly.

In sub-plot 3 and 4 (from top), control charts for both ML set-ups are drawn based on the CP trends in sub-plot 1 and 2, respectively. Again, grey shading indicates damaged sets. Additionally, vertical dashed orange lines indicate the different states. Here, numbers on top indicate the

state #. For state #1 to 3, only 10 sets each are used in the testing while for states #4 to 17, 50 sets are used. It should be noted that the vertical scaling is set logarithmic to aid the visualization. Hence, outliers below the LCL and above the UCL lie above +1. This concept of data presentation is repeated for all selected CPs.

For the first 500 data instances the skewness has no relevant peaks for all four channels. Values range around zero, indicating a symmetric distribution of acceleration values in each time series. From state #11 (set 501) on, the skewness increases for channel 3 and decreases for channel 4 ($CP_{(3)}^{\gamma_1}$, $CP_{(a)}^{\gamma_1}$). These sensors are located at the second and third floor of the structure, right where the impact between bumper and column is introduced. This indicates that an increase in non-linearity through a smaller gap results in an increase of higher acceleration values on the second floor and smaller accelerations on the third floor. Channels two and one ($CP_{(2)}^{\gamma_1}$, $CP_{(1)}^{\gamma_1}$) show only minor trends towards negative skewness values for data instance 600 to 700. For state #17 results are similar to state #13 (also a gap size of 0.1 mm) with slightly smaller amplitudes.

Both control charts show a similar picture: All healthy states lie predominantly within the limits but also states with a linear damage set-up (4 to 9, data instance 31 to 430) lie within the control limits for a large number of data instances and are falsely-classified as healthy. From state #10 to 14, where non-linearity is introduced, data instances are increasingly identified as damaged, both for the assumption of a Gaussian and discrete distribution. For state #15 and 16 only a few sets lie outside the control limits, state #17 is again correctly identified as damaged. Two distinct differences can be seen here: 1. the classification into three clusters ("Man2") leads to a slight amplification of the control variables. 2. The analysis through percentiles as a discrete distribution leads to slightly stronger outlier than the assumption of a Gaussian distribution in states 11 to 14.

In this example, the skewness is a good indicator for non-linear damage cases, with increasing amplitude as the level of non-linearity increases. Also, damage localization can be realized using the tracking of amplitude and sign shift of the CP. Through an easy computation, it is an attractive CP for SHM frameworks. Data flagged as damaged with more sophisticated CPs could be analyzed by the skewness in a second step in order to indicate the type of damage present.

Accumulated Energy Figure 3.20 for $CP_{i,9}^{E_{yy}}$ is organized in the same manner as Figure 3.19: The upper two sub-plots show CP trends the lower two control charts. Both, for "Man1" (upper and 3rd plot) and "Man2" (2nd and 4th plot). In total, eight parameters result from the four measured channels, four auto- and four summed cross-correlations. Here, only the control charts based on percentiles are displayed to preserve clear charts. For the analysis, ten equally spaced energy bins are investigated per channel (see Table 3.5). $CP_{j,9}^{E_{yy}}, j = 1,2,..4$ as the best performing parameter is chosen for a detailed investigation over all j channels.

For the sake of lucidity control charts are only plotted for the analysis through a discrete distribution by percentiles as compared to the Gaussian distribution, results were of equal or better quality. As described in 3.1, eight CPs result from four measured channels in the control charts, where $CP_{1,9}^{E_{yy}}$-$CP_{4,9}^{E_{yy}}$ result only from autocorrelation and $CP_{1,9}^{E_{xy}}$-$CP_{4,9}^{E_{xy}}$ include also cross-correlations between channels.
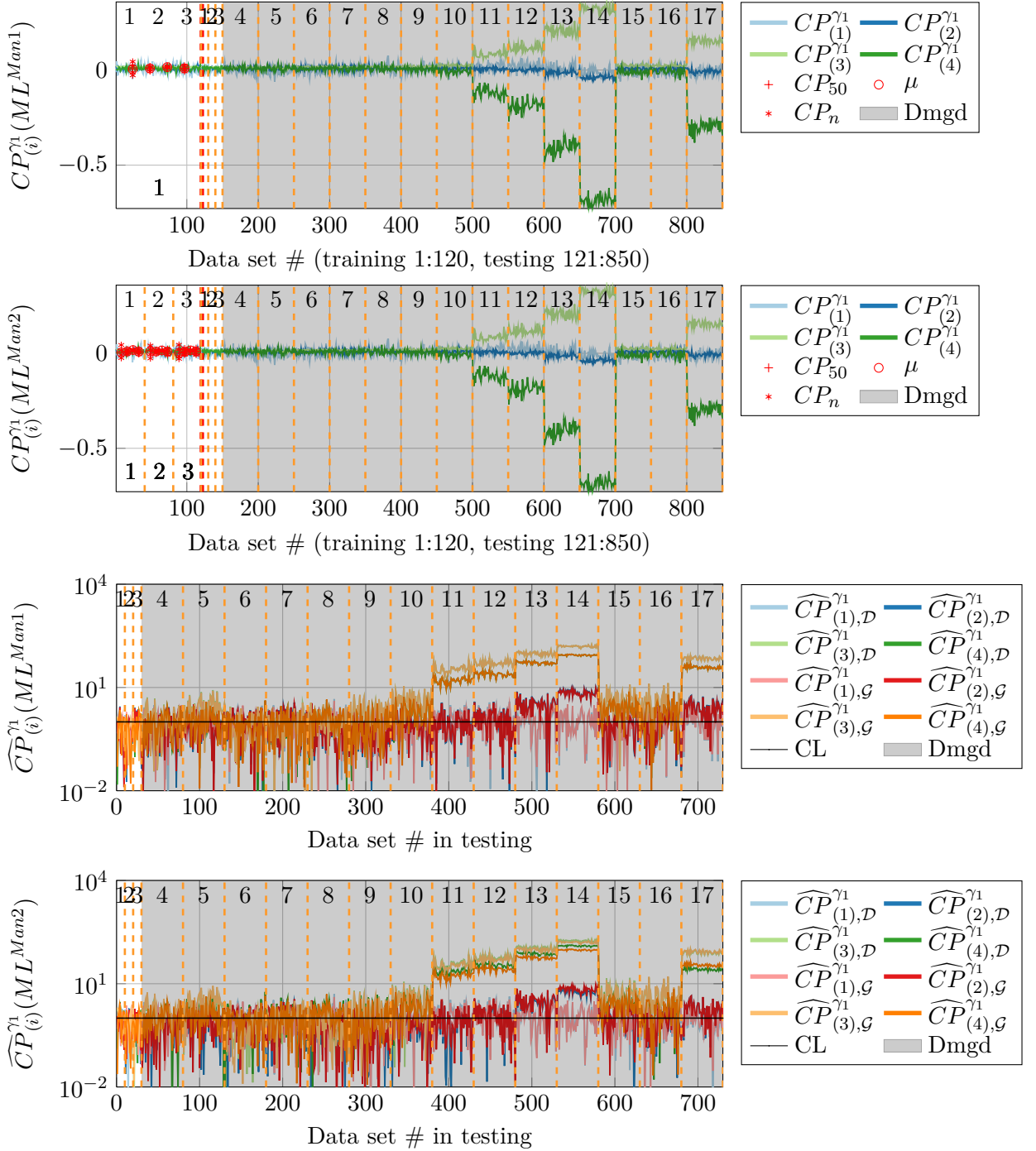
Figure 3.19: Absolute CP trends (upper two plots) and normalized control charts (lower two plots) for CP^{γ_1}, given for ML set-up "Manual1' (upper and 3rd plot) with one cluster and "Manual2" (2nd and 4th plot) with three clusters. Numbers on the upper edge indicate reference states from Table 3.4. Training and testing data is separated by a red line in the upper two plots and parameter distributions in each cluster during training are indicated by red symbols (+,o,*). It should be noted that both control limits lie at $+1$ for the lower two plots due to logarithmic scaling.

Values per channel of $CP_{i,9}^{E_{yy}}$ range from 50 to 120 Hz (see 1st and 2nd plot in Figure 3.20). The parameters react to the different system states and mostly clear plateaus are visible in blocks of 50 data instances each. It can be seen that between one cluster in "Man1" in sub-plot 1 and three clusters in "Man2" in sub-plot 2, CP variation within clusters can be reduced during training, especially for channel 2 and 3. This leads to more accurate control limits. Comparing both control charts in sub-plot 3 and 4, this results in a strong amplification of the parameter sensitivity. For "Man2", state #4 already exceeds the control limits distinctively, while control variables remain within the limits for "Man1" in this state. All other linear damage (states#5-9) are identified as damaged through "Man2". With only a base line classification in "Man1", many of the linear damage cases are classified as healthy.

Investigating sub-plot 4, even a damage localization results from the CPs: for states #4 and 5 (damage between base and 1st floor) $CP_{2,9}^{E_{yy}}$ has a maximum amplitude, for states #6 and 7 (damage between 1st and 2nd floor) $CP_{2,9}^{E_{yy}}$, $CP_{3,9}^{E_{yy}}$ and $CP_{4,9}^{E_{xy}}$ have maximum amplitudes, and for states #8 and 9 (damage between 2nd and 3rd floor) maximum amplitudes also result from $CP_{3,9}^{E_{yy}}$ and $CP_{3,9}^{E_{xy}}$. Overall the damage location between 2nd and 3rd floor is identified with less distinct amplitudes in the control variables.

Non-linearities in states #10 to 14 can be detected for a maximum gap size of 0.15 mm (state #11). Leading to the conclusion that a gap size of 0.20 mm lies above the sensitivity of the CP. Accordingly, the CP has trouble in identifying the first two states (15 and 16) with a combination of added mass and gap of 0.20 mm. The last scenario with a smaller gap and additional EOCs is identified again. Positively, for smaller gaps a localization is possible since $CP_{3,9}^{E_{yy}}$ and $CP_{3,9}^{E_{xy}}$ result in the most distinct outlier.

It should be noted that for all linear damage cases, the mean frequencies for the tracked accumulated energy levels decrease, indicating a shift of energy to lower frequencies in the spectrum. For non-linear damage in contrast, frequencies increase indicating an energy shift to higher frequency ranges. This follows the physical understanding of both damage scenarios since non-linearity, present through impact loading, has distinctively high-frequency contents compared to the normal movement, excited by the shaker. On the other hand, through the degradation of stiffness in the linear damage cases, the system becomes softer with content in lower frequency-ranges.

Being an excellent parameter for linear damage and damage localization as well as indication of non-linear damage, accumulated energies have the potential to add important knowledge to a SHM system. Further the parameter has low computational costs and provides a physical meaning.

Relative Condition Parameters

The calculation of relative Cps becomes more complex compared to absolute CPs as CP^{γ_1} or $CP_{(i,9)}^{E_{xy}}$. While CP^{γ_1} has no parameter to be set and $CP_{(i,9)}^{E_{xy}}$ requires only a number of energy bins, SSI and VAR based parameters necessitate the estimation of more complex initial parameters or settings (see Table 3.3). Selected parameters are given in Table 3.5. These can again be derived
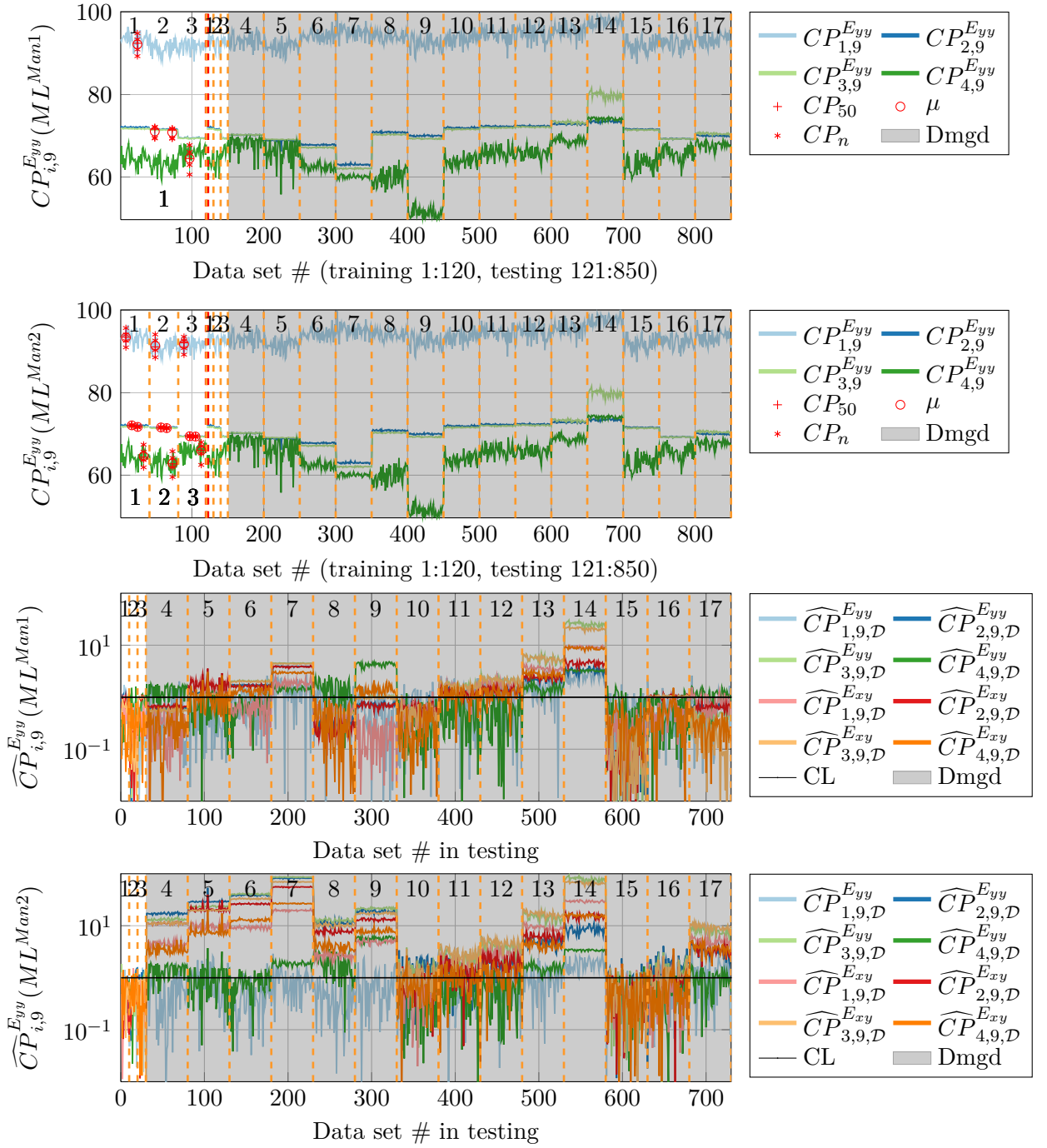
Figure 3.20: Absolute CP trends (upper two plots) and normalized control charts (lower two plots) for $CP_{(i,9)}^{E_{yy}}$ and $CP_{(i,9)}^{E_{xy}}$, given for ML set-up "Manual1' (upper and 3rd plot) with one cluster and "Manual2" (2nd and 4th plot) with three clusters. Numbers on the upper edge indicate reference states from Table 3.4. Training and testing data is separated by a red line in the upper two plots and parameter distributions in each cluster during training are indicated by red symbols (+,o,*). It should be noted that both control limits lie at +1 for the lower two plots due to logarithmic scaling.

from a rough estimation of the lowest frequency of interest f_u and the sampling frequency f_s.

For $CP^{\mathcal{M}}$ and CP^{R^2} the VAR model order p could be chosen to the number of samples needed to cover one oscillation of the lowest frequency of interest with $p = f_s/f_{min} = 320/20 = 16$. As mentioned by Haake [75], it can be sufficient to cover about 70% of the oscillation for good system identification results.

For the SSI based parameters CP^{ε} and CP^{γ} the number of shifts n_{shift} to build the Block Hankel matrix could be interpreted in a similar manner as p and was chosen accordingly. Recalling the size of the Hankel matrix is $n_{shift} * m$ wich is split into significant and insignificant columns, hence $n_{shift} * m = n_{sig} + n_{is}$.

n_{sig} should be equal the (state space) model order of the physical system, a first guess leads to $n_{sig} = 2m = 8$ since four channels are measured. Unfortunately, a continuous system is not limited in the model order and Figure 3.18 already revealed that some damage cases might lead to pole splits and an increase of the model order. n_{is} could be directly calculated through $n_{is} = n_{shift} * m - n_{sig} = 16 * 4 - 8 = 56$. Nevertheless, n_{is} and n_{sig} could also be chosen to violate this equation since both are used for separate parameters. The block size needs to satisfy statistical independence between blocks, for a lowest frequency of 30 Hz $N_b = 320/30 \ = 11$ samples as block length would result.

For the given benchmark example, it is possible to perform parameter studies on these variable to estimate optimal settings with respect to AUCs. These studies are carried out to validate the theoretical assumptions (see Figures 3.21, 3.24, and 3.25) before parameter trends and control charts are investigated for optimal parameter settings in Figures 3.22, 3.23, 3.26, and 3.27.

VAR-Residues   In contrast to statistics and accumulated energies, the residues from VAR-models result in a scalar CP for each data instance since all channels are taken into account at once. Both, $CP^{\mathcal{M}}$ and CP^{R^2} will be investigated here. Figueiredo et al. [59] suggest an AR-model order of 15 based on AIC. To investigate the model, a parameter study based on the evaluation of ROCs was performed. The AUC values are used as an indicator (see 2.7). Figure 3.21 shows the results for AR-model orders from 1 to 40 for all four ML-HT combinations and both CPs (left and right sub-plot). The analysis is run with 120 training sets as described in 3.5 for every analyzed AR-model order. A maximum value of 1 for the AUC indicates perfect separation of healthy and damaged states. It is clearly visible that for both CPs, classification "Man2" (dark blue and green) with three clusters in the training phase outperforms "Man1" (light blue and green) with a single cluster. After reaching a peak for $CP^{\mathcal{M}}$ and $p = 4$ performance decreases for "Man1". For higher model orders the AUC stabilizes a bit above 0.8. In the case of CP^{R^2} (right plot), the performance of "Man1" is even worse with stronger fluctuations for low model orders below $p = 10$ with a stabilization around 0.7 for higher model orders.

For $CP^{\mathcal{M}}$ and 'Man2', the AUC reaches 1 for $p = 2$ for CP^{R^2} a minimum model order of 5 is needed. For increasing model orders AUC values constantly remain at 1 for both CPs and 'Man2'. On the safe side, a model order of 16 was chosen on the safe side as model order for further detailed investigations.

Figures 3.22 and 3.23 are organized as above for skewness in Figure 3.19: The upper two
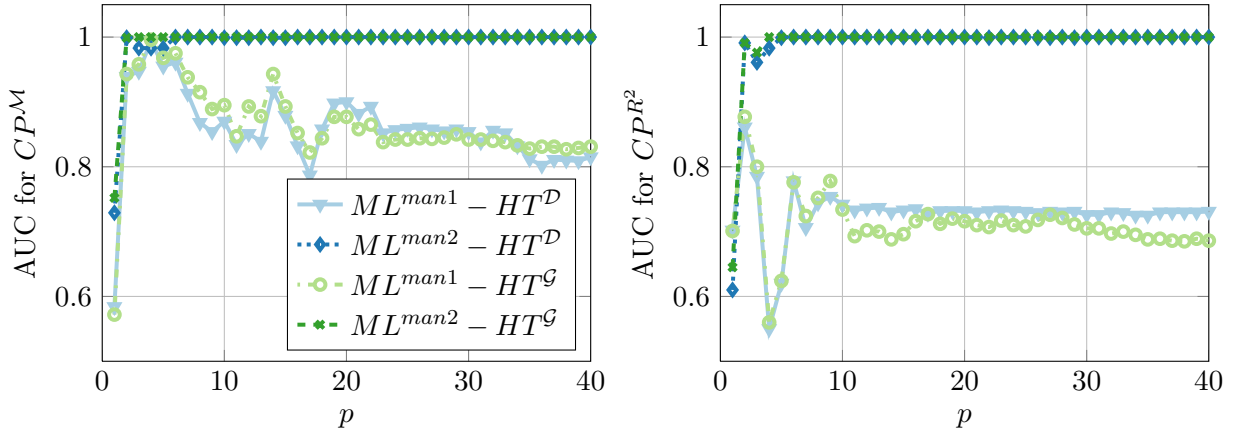
Figure 3.21: Parameter study for VAR-based $CP^{\mathcal{M}}$ (left) and CP^{R^2} (right). Different ML-HT combinations analyzed over AR-model orders from 1 to 40.

sub-plots show CP trends for "Man1" and "Man2", respectively. The lower to plots show the control charts. Compared to absolute CPs, the difference in the classification within the training phase results in differences of the absolute values of the CPs (compare sub-plot 1 and 2 in Figure 3.23 and Figure 3.22). For both CPs, the values are reduced significantly for the training phase in "Man2" ($10^{5.5}$ to 10^5 and $10^{0.5}$ to 10^{-1}), indicating a better inner-cluster agreement of the measured data. Further, a strong amplification of the control variables is achieved using three clusters in comparison of sub-plot three and four in Figure 3.23 and Figure 3.22, respectively: For $CP^{\mathcal{M}}$ from maximum values of 4 to around 15 and for CP^{R^2} from maximum values around 10 to 600. Both parameters lack the possibility of damage localization as they combine all measured channels.

CP^{R^2} shows clear distinction in parameter amplitudes for each measured state. Even within the training the additional masses change the CP values, if a single cluster is used as in "Man1" (upper sub-plot in Figure 3.22). Within the linear damage cases in states #4 to 9 for both ML set-ups, damage at columns between base and 1st floor (#4/5) seem to have a similar influence as between 2nd and 3rd floor (#8/9) (see sub-plot 2 and 4 in Figure 3.22). Damage between 1st and 2nd floor result in larger CP values indicating stronger damage even if the extent of the damage is similar. For the non-linear damage in states #10 to 17, an decrease of the gap coincides with an increase of the CP. Here, the difference between 0.2 and 0.15 mm (#10/11) seems more distinct than for the other reductions. Overall, building the control limits with the use of a Gaussian distribution leads to more distinct outliers in the control charts and hence a better distinction. If the clusters are not separated in the training, the variations in the training are large which results in a misclassification of data instances from states #4, 10 to 12, 15, and 16. Using "Man2" all damaged states are classified correctly with states #10, 15, and 16 lying closest to the control limits. CP^{R^2} proved to be a very valuable CP for the benchmark example, displaying perfect performance and an indication of the damage extent.

$CP^{\mathcal{M}}$ is an excellent parameter to detect damaged states if three clusters are used during the training phase, too. In Figure 3.23 the control chart in sub-plot 4 gives a clear distinction

between states #1 to 3 and 4 to 17. With a single cluster in the training phase, states #4 and 16 lie directly on the UCL and data instances from states #10 and 15 are misclassified as healthy. Another useful result of "Man2" is the constant amplitude for similar damage cases in states #4, 6, and 8 as well as in states #5, 7, and 9 for a single and two replaced columns, respectively. A decreasing gap size is also quantified by a clear trend of $CP^{\mathcal{M}}$ in states #10 to 14.

As for CP^{R^2}, a Gaussian distribution leads to an improved distinction in the control charts. Accordingly, $CP^{\mathcal{M}}$ also performs perfectly for the analyzed data and damage quantification is possible. Both parameters have their advantage: While CP^{R^2} is able to distinct more clearly between healthy and damaged, $CP^{\mathcal{M}}$ gives a better quantification of damages.

SSI-Residues   In a similar manner as VAR based CPs, the estimation of SSI based CPs depends on different input variables. As described in Table 3.3, CP^{ε} depends on the number of shifts n_{shift} in the Hankel matrix and the number of insignificant columns n_{is} of the Nullspace. CP^{γ} depends on n_{shift} and further on the number of significant columns n_{sig} and the block length N_b. As in the VAR case, optimal parameter values are not exactly known a priori. Hence, parameter studies are carried out to optimize AUCs, before the performance of the two CPs are discussed by means of control charts and ROCs.

As mentioned above, n_{shift} and n_{is} need to be set for CP^{ε}. In Figure 3.24 the AUC is plotted for different parameter setting of CP^{ε}, the assumption of a Gaussian distribution, and classification "Man2" as optimal combination from their former absolute CPs is used here. Figures for the remaining three combinations ("Man1", percentiles) can be found in Chapter A.2. 400 different combinations of n_{shift} and n_{is} reveal a broad picture of the performance here. Again, 120 training sets and 730 testing sets are used in the same manner as for the absolute CPs. Blue areas with no AUC values indicate parameter boundaries, e.g. n_{is} needs to be smaller than or equal to $n_{shift} * m = n_{shift} * 4$.

In agreement with the theoretical derivation, high AUC values can be seen around $n_{shift} = 16$ (14 to 17) over all analyzed n_{is} values. Here values lie above 0.9, indicating a good overall performance of the parameter. According to the theoretical estimation optimal values of n_{is} can be calculated by $n_{is} = n_{shift} * m - n_{sig} = n_{shift} * 4 - 8$. For $n_{sig} = 3$, 4, 5, 6, and 7 $n_{is} = 4$, 8, 12, 16 and 20 result. Those points lie in a region of poor performance that stretches as a band from the top left downwards to the right in Figure 3.24 (orange to yellow). The high AUC values for $n_{shift} > 8$ and $n_{is} <= 20$ indicates that the model order of the analyzed system is in fact larger than 8. Local optima can be found at $(n_{is}, n_{shift}) = (1,16)$, (4,16), (8,15), and (9,15) all reaching AUC=0.95 indicating a (theoretical) number of significant columns of $n_{sig} = m * n_{shift} - n_{is} = 63$, 60, 52, and 51, respectively. From these optima, the combination (4, 16) was chosen for later analysis since n_{is} influences the computational cost and should be kept low while a value of 1 was assumed to be too small.

The parameter study for CP^{γ} is more complex since a third variable, N_b, has to be taken into account. Variables n_{shift} and n_{sig} can be estimated in the same manner as for CP^{ε}. Figure 3.25 holds the AUCs for CP^{γ} for a variation of n_{shift} and n_{sig} for eight different block lengths N_b. Again, the assumption of a Gaussian distribution and classification "Man2" are shown. It should
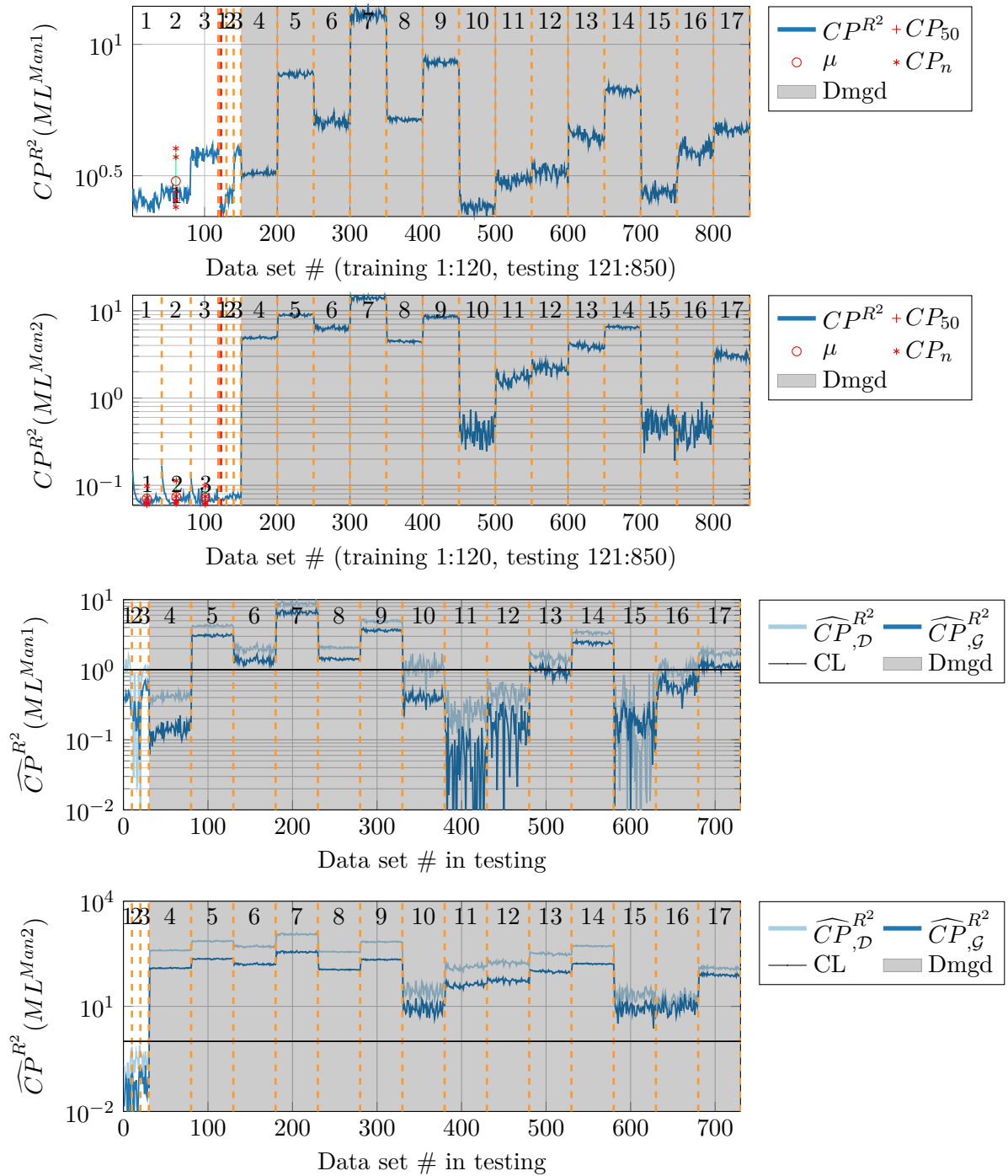
Figure 3.22: Absolute CP trends (upper two plots) and normalized control charts (lower two plots) for CP^{R^2}, given for ML set-up "Manual1' (upper and 3rd plot) with one cluster and "Manual2" (2nd and 4th plot) with three clusters. Numbers on the upper edge indicate reference states from Table 3.4. Training and testing data is separated by a red line in the upper two plots and parameter distributions in each cluster during training are indicated by red symbols (+,o,*). It should be noted that both control limits lie at +1 for the lower two plots due to logarithmic scaling.
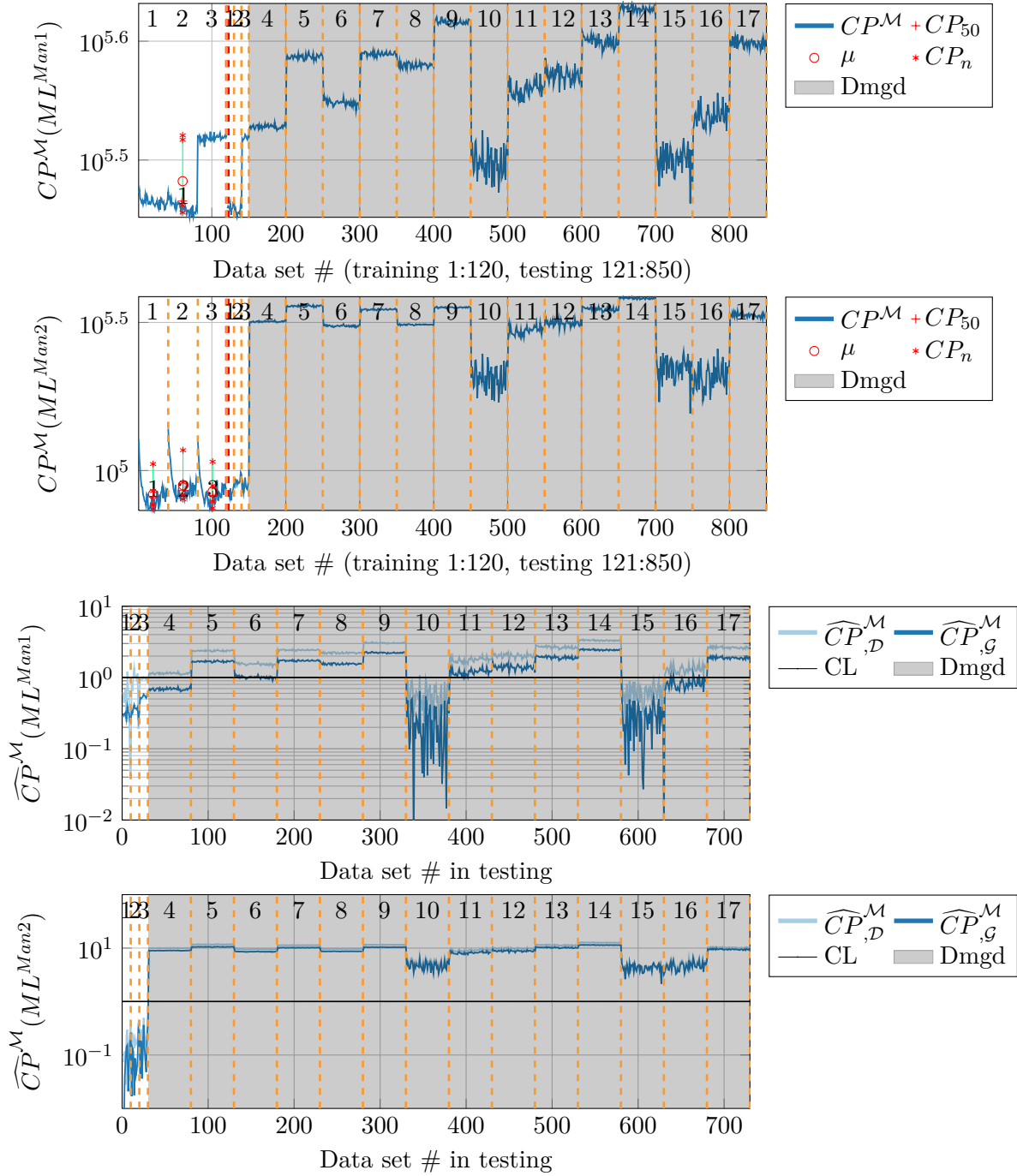
Figure 3.23: Absolute CP trends (upper two plots) and normalized control charts (lower two plots) for $CP^{\mathcal{M}}$, given for ML set-up "Manual1' (upper and 3rd plot) with one cluster and "Manual2" (2nd and 4th plot) with three clusters. Numbers on the upper edge indicate reference states from Table 3.4. Training and testing data is separated by a red line in the upper two plots and parameter distributions in each cluster during training are indicated by red symbols (+,o,*). It should be noted that both control limits lie at +1 for the lower two plots due to logarithmic scaling.

| n_{shift} \ n_{is}	1	2	3	4	5	6	7	8	9	10	11	12	13	14	15	16	17	18	19	20
1	0.68	0.58	0.62	0.72																
2	0.69	0.65	0.72	0.65	0.7	0.79	0.84	0.76												
3	0.9	0.82	0.79	0.68	0.77	0.78	0.7	0.7	0.72	0.78	0.76	0.77								
4	0.9	0.92	0.91	0.89	0.88	0.81	0.85	0.78	0.81	0.74	0.77	0.73	0.7	0.72	0.72	0.71				
5	0.87	0.89	0.88	0.89	0.87	0.87	0.87	0.8	0.79	0.69	0.65	0.65	0.72	0.71	0.85	0.68	0.72	0.74	0.8	0.8
6	0.86	0.87	0.9	0.9	0.9	0.83	0.84	0.84	0.83	0.79	0.67	0.64	0.64	0.62	0.68	0.71	0.72	0.69	0.67	0.65
7	0.89	0.86	0.87	0.84	0.83	0.8	0.8	0.8	0.76	0.77	0.75	0.77	0.79	0.79	0.65	0.69	0.67	0.69	0.66	0.74
8	0.91	0.92	0.92	0.9	0.92	0.92	0.92	0.92	0.92	0.91	0.91	0.89	0.88	0.89	0.94	0.9	0.87	0.81	0.76	0.8
9	0.93	0.92	0.92	0.93	0.91	0.91	0.92	0.91	0.91	0.92	0.91	0.91	0.91	0.91	0.92	0.92	0.92	0.91	0.91	0.89
10	0.94	0.91	0.9	0.93	0.93	0.93	0.92	0.92	0.94	0.94	0.94	0.93	0.93	0.94	0.94	0.94	0.93	0.93	0.93	0.91
11	0.9	0.89	0.91	0.92	0.91	0.92	0.94	0.92	0.91	0.91	0.93	0.93	0.93	0.93	0.93	0.93	0.93	0.93	0.93	0.91
12	0.92	0.88	0.9	0.89	0.9	0.88	0.9	0.9	0.91	0.91	0.9	0.91	0.9	0.9	0.91	0.91	0.91	0.91	0.91	0.92
13	0.88	0.89	0.89	0.88	0.88	0.88	0.89	0.87	0.87	0.88	0.88	0.89	0.88	0.88	0.88	0.9	0.89	0.89	0.89	0.9
14	0.93	0.93	0.93	0.92	0.91	0.92	0.93	0.92	0.92	0.92	0.93	0.93	0.94	0.94	0.93	0.93	0.93	0.93	0.93	0.93
15	0.94	0.92	0.94	0.94	0.93	0.93	0.94	0.95	0.95	0.94	0.94	0.94	0.94	0.94	0.94	0.94	0.94	0.93	0.93	0.93
16	0.95	0.93	0.93	0.95	0.94	0.93	0.92	0.93	0.93	0.93	0.93	0.93	0.93	0.94	0.94	0.94	0.93	0.94	0.94	0.93
17	0.91	0.91	0.92	0.91	0.93	0.93	0.93	0.92	0.92	0.92	0.93	0.93	0.93	0.92	0.91	0.92	0.92	0.92	0.93	0.93
18	0.9	0.88	0.88	0.91	0.89	0.9	0.9	0.9	0.91	0.9	0.89	0.89	0.89	0.91	0.91	0.92	0.92	0.92	0.92	0.92
19	0.9	0.88	0.9	0.92	0.88	0.89	0.91	0.91	0.91	0.91	0.92	0.92	0.89	0.91	0.89	0.92	0.91	0.91	0.91	0.91
20	0.91	0.93	0.92	0.94	0.94	0.93	0.91	0.92	0.93	0.92	0.93	0.91	0.91	0.91	0.91	0.89	0.9	0.91	0.92	0.91
21	0.85	0.91	0.93	0.91	0.91	0.9	0.9	0.9	0.9	0.91	0.92	0.92	0.91	0.9	0.9	0.88	0.86	0.86	0.87	0.86
22	0.87	0.87	0.9	0.9	0.9	0.88	0.89	0.89	0.89	0.88	0.88	0.9	0.91	0.89	0.89	0.9	0.89	0.87	0.87	0.87

$HT^{\mathcal{G}}(CP^{\varepsilon}(ML^{man2}))$

Figure 3.24: Parameter study for CP^{ε} at 4-DoF system. AUCs are shown for different model orders n_{shift} and number of insignificant columns n_{is}. Best performing combination ML^{Man_2} with the assumption of a normally distributed variable is given here, remaining three combinations are given in Figure A.2.

be noted that numbers in the fields are given in values from 0 to 100 instead of 0 to 1 for the AUC for a better displayability. The remaining three plots for all other ML-HT combinations can be found in Chapter A.2. In total, 1768 runs were performed to investigate performances, sub-plots are given for different block lengths N_b.

N_b was derived to be chosen appropriately to assure statistical independence between data blocks. Recalling the lower band limit of 20 Hz and a lowest eigenfrequency of 30 Hz, results in a block length of 10 to 20. Since with short block lengths the number of blocks and hence the computational costs increase, $N_b = 10$ was taken as a lower boundary for the study and larger block lengths should be tested for their performance.

Upon looking at all sub-plots in Figure 3.25, a general pattern can be seen: A region of bad performance on the lower right grows from $N_b = 50$ (second row, left plot in) to $N_b = 250$. For $N_b = 25$ this region disappears and emerges again for $N_b = 10$. An overall comparison of different N_b settings can be made by averaging the AUC values over all parameter combinations per sub-plot (M_b), indicated in each title. Here $N_b = 25$ clearly performs best. Further, regions of good performance (AUC>0.8) form a more or less distinct 'r'-shaped character in the n_{shift}-n_{sig} parameter space. The vertical line of this 'r' contains well performing combinations but maxima with an AUC>0.96 can only be found in the 'arch'. Regions of best performance are located close to the parameter boundaries on the upper right side. This indicates that really the majority of the SVD matrix should be considered as being significant and that the real model order is larger or equal to eight. Further, optimal model orders n_{shift} are lower than for CP^{ε} with values between 3 and 8. This is indicating that dynamic changes due to damage manifest in higher frequency regions of the measured spectrum since e.g. $n_{shift} = 4$ result in $320/4 = 80$ Hz for f_{min}. Since an
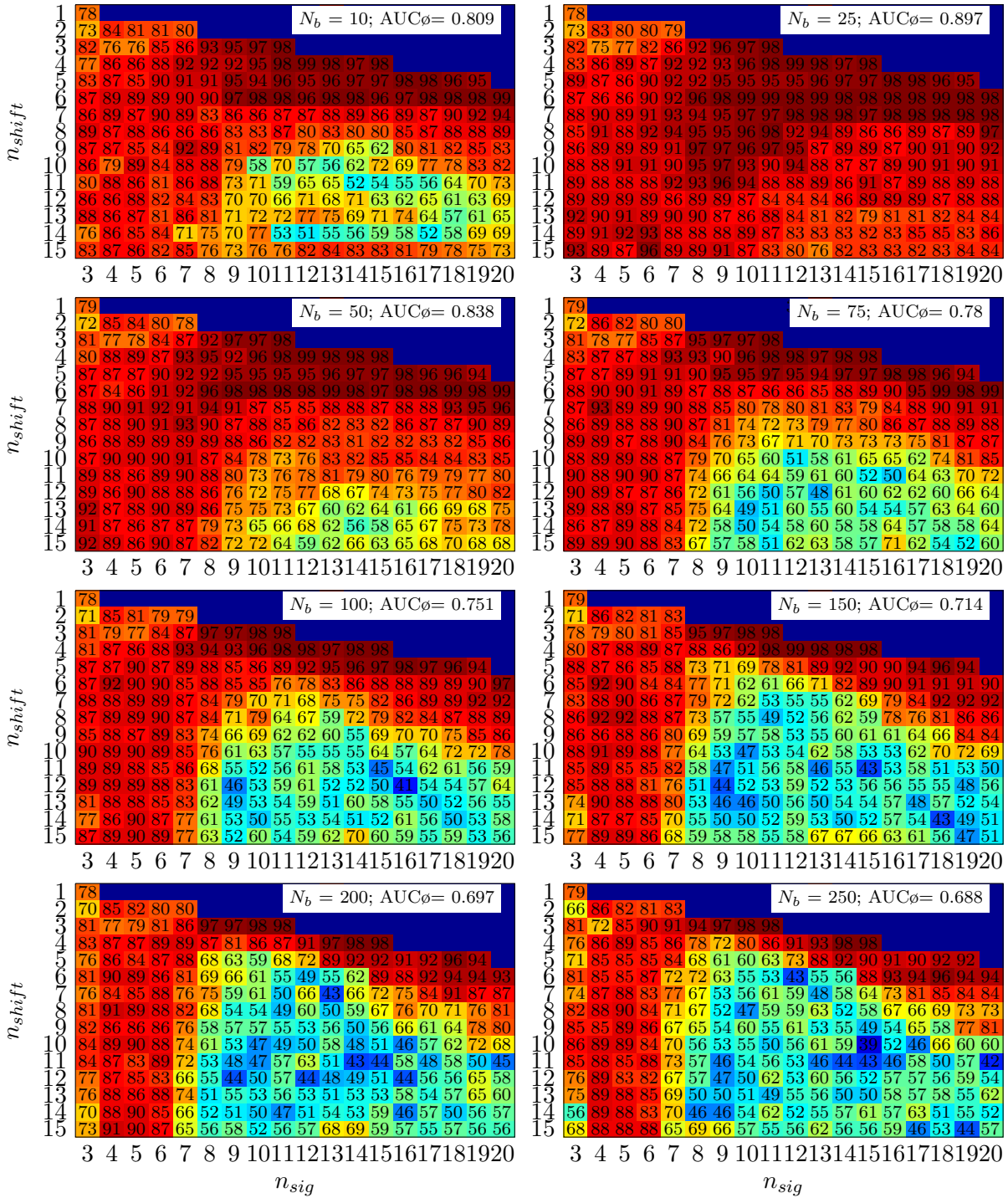
Figure 3.25: Parameter study for $HT^{\mathcal{G}}(CP^{\gamma}(ML^{Man_2}))$ over different model orders N_{shift} (Block size of Hankel-matrix), number of significant columns (N_s), and number of samples per block (N_b). It should be noted that for a better displayability the AUC is ranging form 0 to 100 instead of 0 to 1. Best performing combination ML^{Man_2} with the assumption of a normally distributed variable is given here, remaining three combinations are given in Figure A.3, A.4, and A.5.

increased computational cost goes along with an increase of both, n_{shift} and n_{sig}, a combination of $(N_b, N_s, N_{shift})=$ (25, 12, 4) was chosen (AUC=0.99).

Analogous to the aforementioned CPs, CP^ε and CP^γ are analyzed using control charts in logarithmic scaling given in Figure 3.26 and Figure 3.27, respectively. As for the relative CPs $CP^\mathcal{M}$ and CP^{R^2} difference in the absolute CP values between "Man1" and "Man2" can be seen between the 1st and 2nd sub-plot. For CP^ε, values can be reduced from 10^{-3} to 10^{-5} (1st and 2nd sub-plot in Figure 3.26) and for CP^γ from 10^5 to 10^2 (1st and 2nd sub-plot in Figure 3.27). Both indicate a strong increase of inner cluster similarity for three clusters in "Man2". This fact also manifests in the performance within the displayed control charts: outlier amplitudes for both CPs are strongly increased from sub-plot 3 to 4. For "Man1", CP^ε only indicates state #5, 9, and 11 to 14 as damaged and only under the usage of percentiles. For " Man2" in contrast, only states #15 and 16 and the first sets of #10 remain undetected. A similar picture results for CP^γ in Figure 3.27: For "Man1" states #4 to 9 as well as 13, 14, 16 and 17 are indicated as damaged and performance is again improved for "Man2". Overall, CP^γ performs better than CP^ε here. In the case of "Man2" in sub-plot 4, only state #10 and 16 remain in a false indication. In terms of HT, the discrete distribution performs better for CP^ε while a Gaussian does for CP^γ (light blue compared to dark blue).

For CP^ε the stiffness reduction for one column between the base and 1st floor (#4) as well as 1st and 2nd floor (#6) is indicated correctly as less severe than for the reduction in two columns (#5 and 7). Nevertheless, amplitudes are reversed for damage between the 2nd and 3rd floor (#8/9). The increase of non-linearity follows a clear trend with larger CP^ε values the smaller the gap gets. CP^γ indicates all linear damage correctly, having stronger amplitudes for damage at both columns (#5, 7, and 9) than in one column (#4, 6, and 8). Here the damage between 2nd and 3rd floor (#8/9) results in slightly larger CP amplitudes. The increase in non-linearity is again indicated correctly. The least severe, combined damage scenarios in #15 and 16 are only handled well by CP^γ.

As explained above, the evaluation for false positive alarms and damage detection rate for many control charts based on different confidence intervals leads to receiver operating characteristics (ROCs). Figure 3.28 shows such ROCs for CP^{R^2} (upper plot) and CP^γ (lower plot), respectively. Confidence intervals were varied as indicated by α values in Table 3.5. Again, all four ML-HT combinations are plotted: "Man1" is indicated by light blue, "Man2" by dark blue, an underlying Gaussian distribution is indicated by dotted and a discrete distribution by solid lines. Optimal points on the ROCs per classification in terms of Youden index ($\mathcal{J}$) and maximum distance to diagonal ($\bar{\mathrm{d}}$) are indicated as well.

It is obvious how both parameters indicate better performance if they act on data that was clustered during training (dark blue lines, "Man2"): ROC curves run closer to the upper left corner than for the base line classification. CP^{R^2} even runs through the upper left corner, showing optimal performance. A difference between the assumption of normally distributed parameters and an estimation by percentiles is not visible for "Man2". For "Man1" the discrete version performs better in the upper right region where very large false positive rates have already been reached.
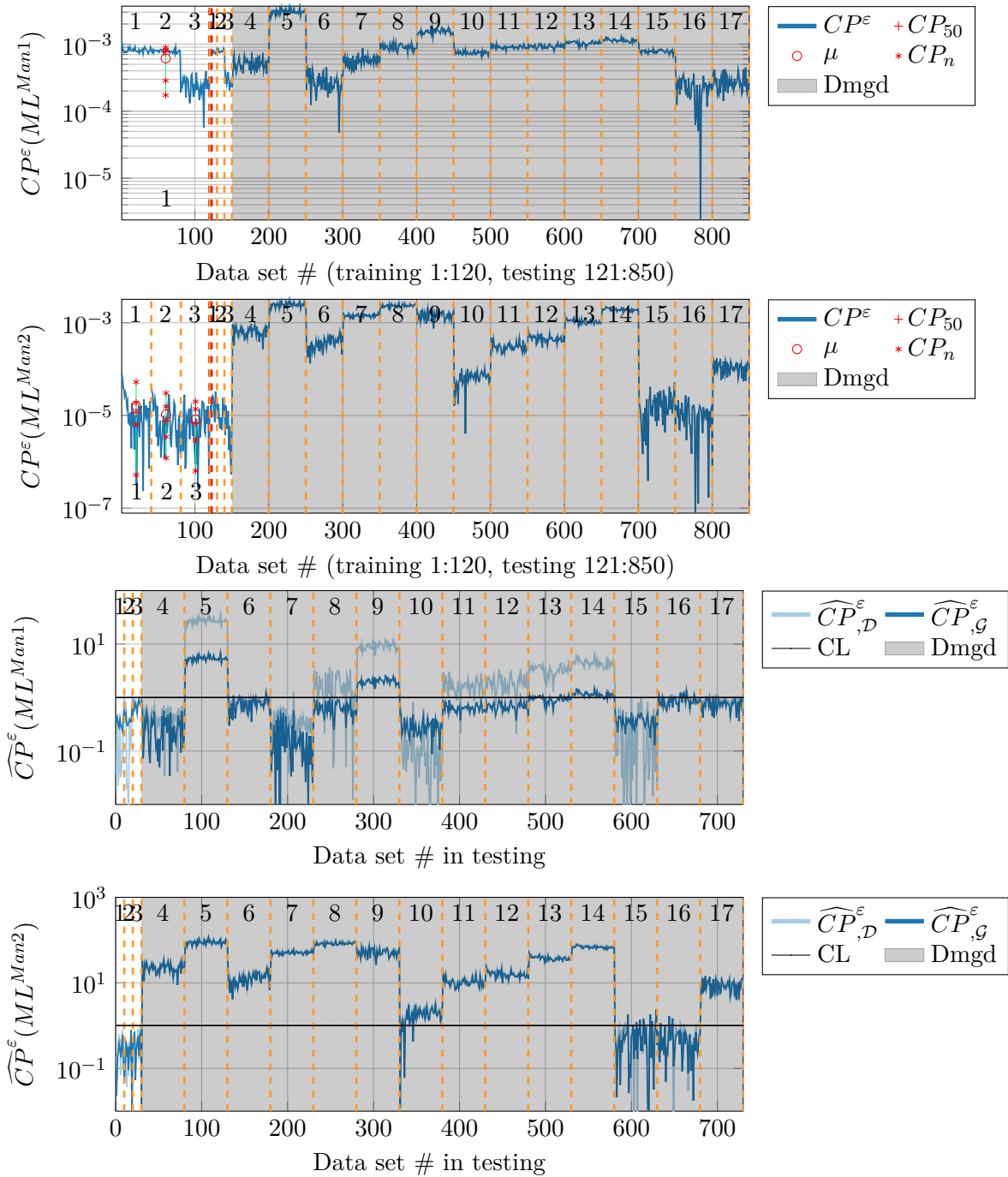
Figure 3.26: Absolute CP trends (upper two plots) and normalized control charts (lower two plots) for CP^ε, given for ML set-up "Manual1' (upper and 3rd plot) with one cluster and "Manual2" (2nd and 4th plot) with three clusters. Numbers on the upper edge indicate reference states from Table 3.4. Training and testing data is separated by a red line in the upper two plots and parameter distributions in each cluster during training are indicated by red symbols (+,o,*). It should be noted that both control limits lie at $+1$ for the lower two plots due to logarithmic scaling.
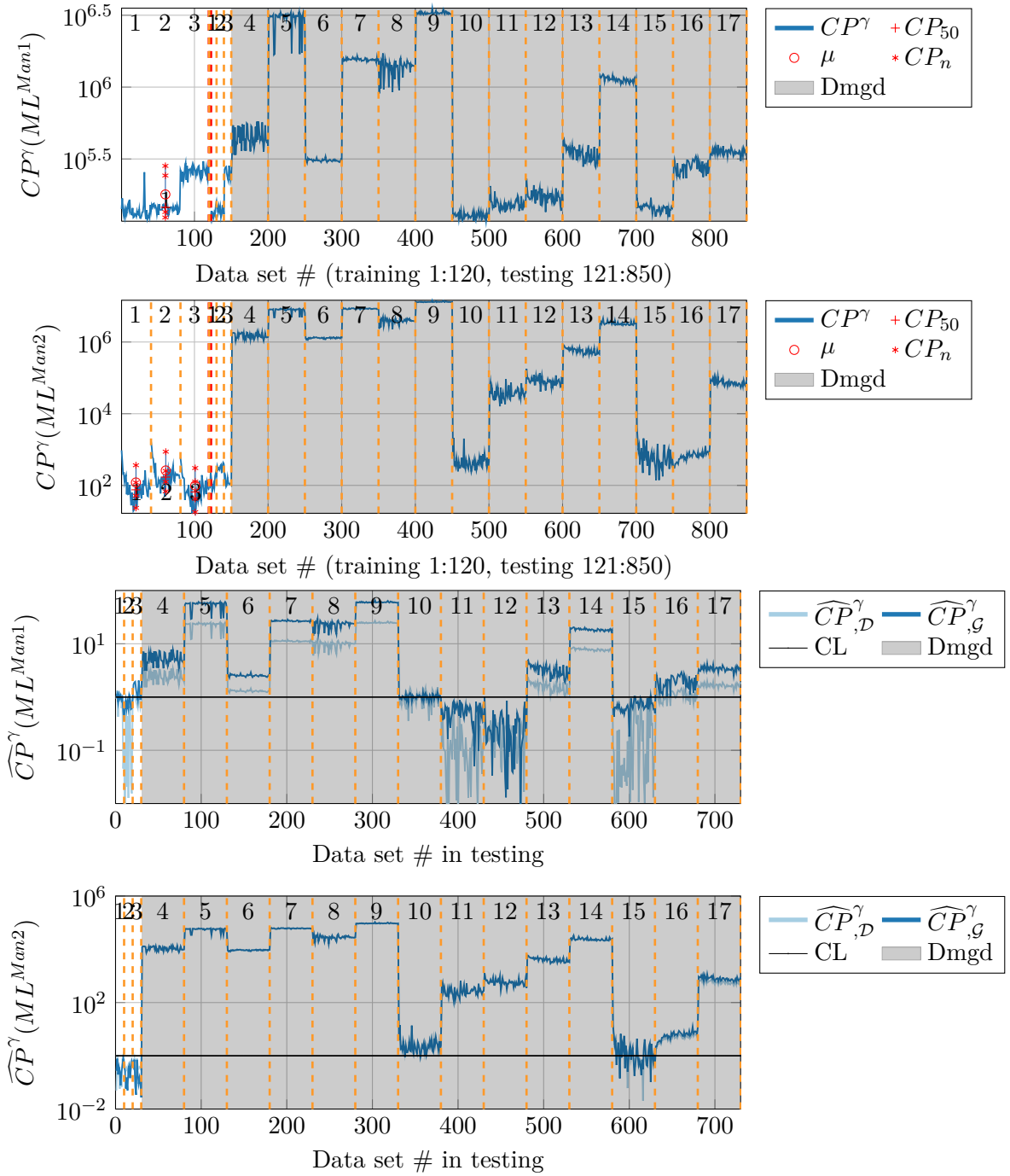
Figure 3.27: Absolute CP trends (upper two plots) and normalized control charts (lower two plots) for CP^γ, given for ML set-up "Manual1' (upper and 3rd plot) with one cluster and "Manual2" (2nd and 4th plot) with three clusters. Numbers on the upper edge indicate reference states from Table 3.4. Training and testing data is separated by a red line in the upper two plots and parameter distributions in each cluster during training are indicated by red symbols (+,o,*). It should be noted that both control limits lie at +1 for the lower two plots due to logarithmic scaling.
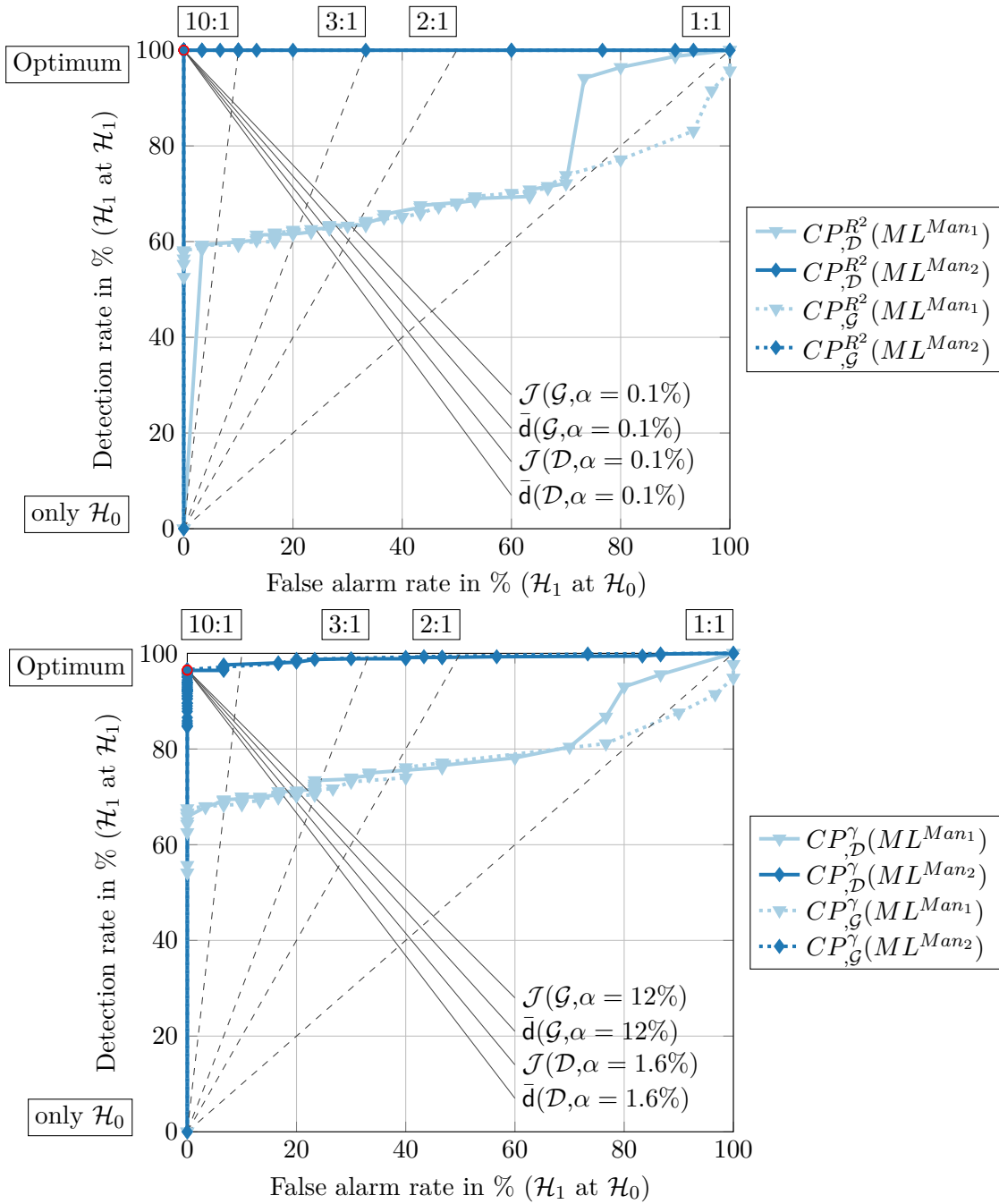
Figure 3.28: ROCs for CP^{R^2} (upper plot) and CP^γ (lower plot). Classification "Man1" is indicated by light blue, "Man2" by dark blue, an underlying Gaussian distribution is indicated by dotted, a discrete by solid lines.

It is another important insight to investigate the distribution of different points on the ROCs. Since the confidence interval is defined by $1 - \alpha$, small α values indicate a wide interval, which is desired. For CP^{R^2} optimal points are reached at a small α value of 0.001 (0.1%) while for CP^{γ} a larger value of 0.016 (1.6%) is necessary to result in the best performance for this parameter. While ROC curves for CP^{R^2} start of with high detection rates, ROCs for CP^{γ} approach their optimum with rising α values, indicating a better separation of CP values between healthy and damaged by CP^{R^2}. As discussed before, these plots provide a very useful tool for interpreting the performance of an ML-CP-HT realization.

Finally, it was noted that for all relative CPs (both, VAR and SSI based) parameter trends in the training phase of "Man2" show a decrease towards the middle of each cluster with a subsequent increase of CP values (see second sub-plot in Figure 3.22, Figure 3.23, Figure 3.26, and Figure 3.27). This is most possibly a result of averaging all reference matrices from each cluster. The structure is subject to continuous changes during data acquisition, e.g. a warm up or equipoising of the structure-shaker system, which alter the system's dynamics over time. Hence, data instances from the middle of each cluster fit best to the averaged references.

Performance Overview

For a final comparison of selected CPs, results from all ROCs are combined in Table 3.7. Results for further CPs, such as time series statistics and other accumulated energy levels, are given in Table A.1 in Chapter A.2. The first four columns of Table 3.7 show AUCs for different ML-HT combinations (two classifications "Man1" and "Man2" and two distribution types). Values >0.7 are underlined whereas values >0.9 are written within a box. Further, maxima per CP (line) are set bold. The last four columns indicate single points on the ROCs with best performance with respect to $\bar{\mathsf{d}}$ and $\mathcal{J}$. Points belong to the best performance in column 1 to 4 (bold) and corresponding α values are given. A small α indicates a wide confidence interval (1-α) and vice versa. If a CP is able to separate well between healthy and damaged states, a small α results.

All CPs, except modal parameters, achieve a performance with AUC values > 0.9. $CP^{\mathcal{M}}$, and CP^{R^2} even perform perfectly (AUC=1). For accumulated energies ($CP_{i,j}^{E_{yy}}$ and $CP_{i,j}^{E_{xy}}$), parameters from cross-correlations outperform the auto correlated channels 2 and 3 (see lower two blocks in Table A.1. Optimal α values for $CP_{2,9}^{E_{xy}}$ and $CP_{3,9}^{E_{xy}}$ lie at 0.18 and 0.14, respectively. Modal frequencies show a moderate to bad performance for damage detection, most feasible here is f_4 as the third bending mode. Optimal α values range from 0.05 to 0.5. All relative damage parameters display very good performance with a clear distinction in α values: While SSI based CPs perform best for α =0.17/0.38, both VAR-based CPs can be applied with a much wider confidence interval with α =0.01. As seen in the control charts in Figures 3.19, 3.20, 3.22, 3.23, 3.26, and 3.27, the best damage quantification was achieved through $CP^{\mathcal{M}}$. $CP_{i,j}^{E_{yy}}$ and $CP_{i,j}^{E_{xy}}$ display a good performance with AUC>0.9 and provide in addition the possibility of damage localization which the global CPs from SSI and VAR are lacking. The extension to cross correlations provides additional insight here.

To get a visual insight into the performance over the different damage scenarios, Figure 3.29

Table 3.7: ROC metrics for different CPs. Values >0.7 are underlined whereas values >0.9 are written within a box. Further, maxima per CP (line) are set in bold. An overview for further investigated CPs can be found in Table A.1

|	Man_1-$\mathcal{D}$	Man_2-$\mathcal{D}$	Man_1-$\mathcal{G}$	Man_2-$\mathcal{G}$	$\bar{\text{d}}$	α	$\mathcal{J}$	α
Absolute CPs:								
$CP_{2,9}^{E_{xy}}$	0.71	0.939	0.659	**0.941**	**85.3/3.3**	0.18	**84.6/0**	0.16
$CP_{3,9}^{E_{xy}}$	0.74	**0.945**	0.646	0.943	**87/3.3**	0.14	**87/3.3**	0.14
CP^{f_1}	0.473	**0.517**	0.464	0.497	60.3/53.3	0.5	60.3/53.3	0.5
CP^{f_2}	0.477	**0.518**	0.479	0.494	77.3/73.3	0.17	**89.4/80**	0.36
CP^{f_3}	**0.611**	0.599	**0.611**	0.567	76/50	0.05	**80.6/53.3**	0.13
CP^{f_4}	0.712	0.685	0.73	**0.778**	**84.1/26.7**	0.12	**84.1/26.7**	0.12
Relative CPs:								
CP^{ε}	0.764	0.946	0.681	**0.948**	**87.7/0**	0.17	**87.7/0**	0.17
CP^{γ}	0.798	0.988	0.774	**0.991**	**96.6/0**	0.38	**96.6/0**	0.38
$CP^{\mathcal{M}}$	0.879	0.999	0.893	**1**	**100/0**	0.01	**100/0**	0.01
CP^{R^2}	0.733	**1**	0.696	**1**	**100/0**	0.01	**100/0**	0.01

shows the damage detection results for all CPs in Table 3.7 over the test phase. The known reference is given in the first line. Here the first 30 sets are indicated as healthy, belonging to states #1-3, all remaining sets (states #4-17) are flagged red as damaged. The upper plot uses a discrete parameter distribution the lower one a Gaussian. All parameters except modal frequencies identify the healthy sets correctly, CP^{γ} has some trouble for the discrete distribution. Further, states #4 to 9 with stiffness reductions are also well identified by the majority of parameters. State #10 with the widest gap between column and bumper is always identified correctly by $CP^{\mathcal{M}}$ and CP^{R^2}. $CP_{,}^{E_{yy}}$, $CP_{,}^{E_{xy}}$, CP^{γ}, and CP^{ε} in contrast have difficulties. In these states, better performance is achieved under the assumption of a discrete distribution. States #11 to 14 with a decreasing gap width are identified correctly, only $CP_{2,9}^{E_{xy}}$ flags some sets as healthy. The combined states #15 to 17 are correctly identified by $CP^{\mathcal{M}}$ and CP^{R^2}, CP^{γ} performs better in using percentiles in terms of damage detection but also starts to suffer from false positive alarms.

Variation of Training Instances

To this point, variations in ML, CP, and HT have been analyzed, addressing point 2.) to 4.) of the initially stated variations within every SHM procedure. Hence, the effect of training data instances remains open. Figure 3.30 addresses this problem. Here, the six best performing CPs were selected to analyze the influence of the number of training sets and a random selection of those. Results are given for "Man2" with three clusters in the training phase and a Gaussian distribution from which confidence intervals are drawn. The number of training sets was varied in steps of five from 5 to 45 data instances. It should be noted that the number of training sets denotes the number of data instances taken from each of the three states during the training phase. For each of the nine training set sizes, 25 runs were performed in which the data instances were chosen randomly from the training data to investigate the influence of differing training sets. Results are plotted in standard box-plots. The median is indicated by a red bar, 25 and 75%
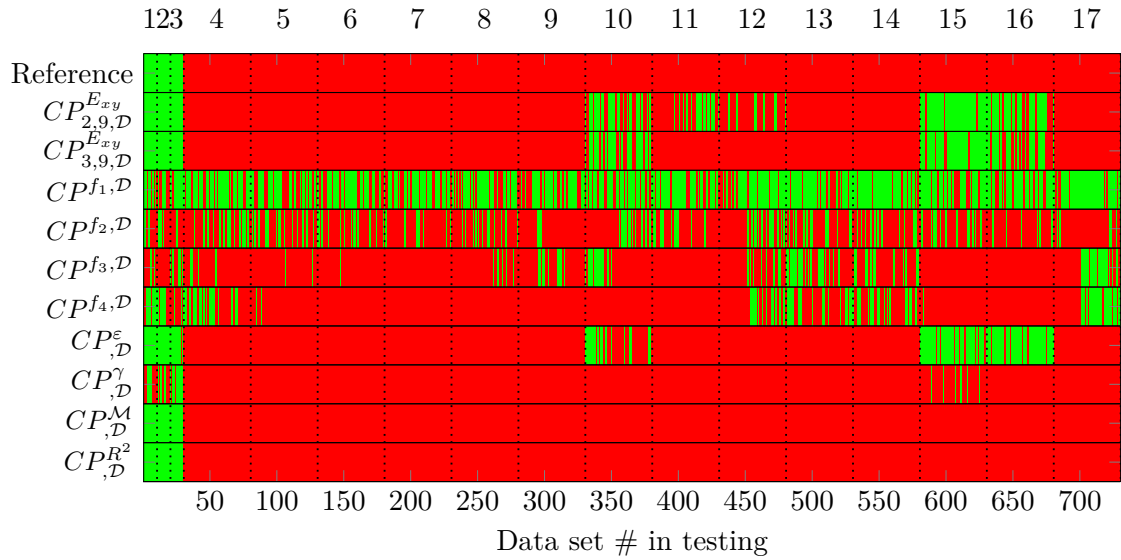
(a) Performance overview for different CPs based on percentiles.
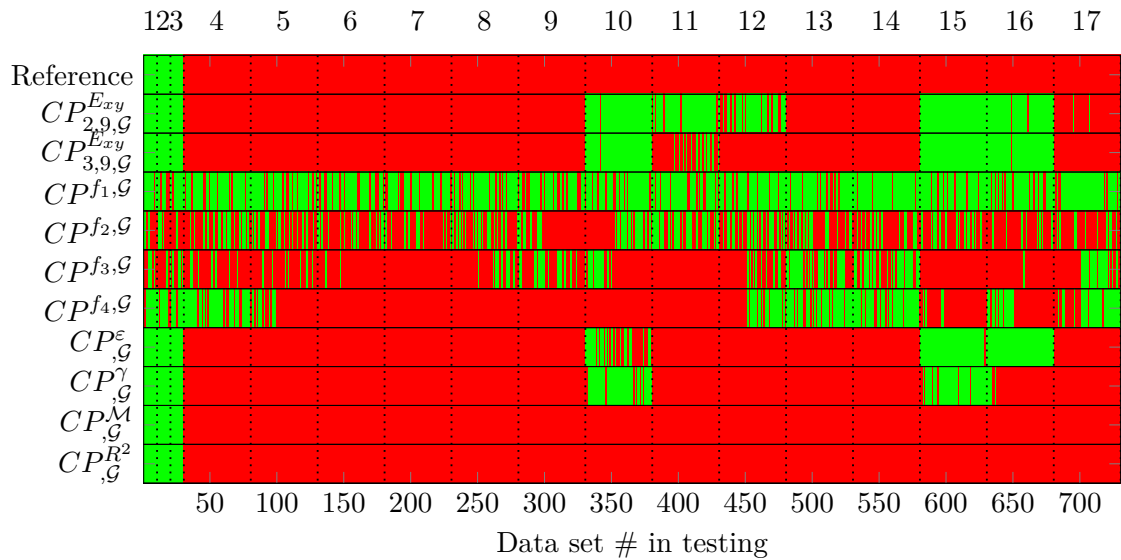
(b) Performance overview for different CPs based on a normal distribution.

Figure 3.29: Overview of damage identification for all CPs for 4-DoF system based on percentiles ((a)) and a normal distribution ((b)). Reference for the 730 data instances given in first row, red indicates a damaged and green a healthy state. Vertical lines and numbers on top indicate the 17 different states as given in Table 3.4.

percentiles by the blue box, 5 and 95% percentiles by the whiskers, and outliers by red crosses. This also affects the absolute CPs as well as the relative ones from SSI and VAR. The parameter range is a close up from 0.8 to 1.01, only for CP^ε (Figure 3.30(a)) the range was extended down to 0.7 due to an outlier for five training sets. The first row of Figure 3.30 ((a) and (b)) shows values for CPs from SSI, the second row ((c) and (d)) the two CPs from VARmodels and in the lower row two parameters derived from accumulated energies are given in (e) and (f).

Overall, there is a tendency of increasing AUC values with an increasing number of training sets with stronger and weaker characteristics. $CP^\mathcal{M}$ and CP^γ are the two CPs affected most, while $CP_{2,9}^{E_{xy}}$ and $CP_{3,9}^{E_{xy}}$ show constant behavior over all different numbers of training sets. While for CP^γ performance increases constantly with an increase of training sets, the other CPs seem to find an equilibrium at around 15 to 25 training sets from each state (45 to 75 data instances in total). CP^ε, $CP_{2,9}^{E_{xy}}$, and $CP_{3,9}^{E_{xy}}$ have an upper performance limit at around 0.95 the other three parameters (CP^{R^2}, $CP^\mathcal{M}$, and CP^γ) reach values up to AUC=1.

3.6 Conclusions

This chapter forms a central part of this thesis: It contains an outline of the presented evaluation framework for SHM performance plus the description of modal parameter extraction through TEMP and derivation of an extension of accumulated energies as CP. The application of all three points is given through benchmark examples.

Accumulated energies, as CP for SHM, are promising quantities since they combine the possibility of physical interpretation, as it can be done for modal parameters, with the consideration of the complete measured frequency spectrum, as for the residues from SSI and VAR models. An extension was presented in which summed power spectral densities of cross-correlations of sensor signals are used to derive the CPs, dubbed $CP_{i,j}^{E_{xy}}$. Improved performance results for this parameter in application to the given benchmark example of the three-story building structure.

Further, the triangulation-based extraction of modal parameters, short TEMP, is outlined. In this procedure, a Delaunay-triangulation in the frequency-damping-plane allows for a fast comparison and grouping of neighboring solutions in a stabilization diagram. A first application is provided by means of modal parameter extraction for a long-span suspension bridge. It is also included for derivation of modal quantities as CP within the SHM framework for the application on the three-story building structure. Two sets of initial criteria for TEMP are given and discussed in this chapter. These can be used as starting point for future research and applications.

Finally, the SHM framework for performance evaluation is derived based on the theoretical formulations given in Chapter 2. Its main constituents are the consideration of different machine learning techniques, different condition parameters and different probability distributions and confidence intervals for hypothesis testing. An overview of the techniques and parameters used is given in Tables 3.2 and 3.3 (pages 78 and 79). To allow for a variation of the confidence intervals, receiver operating characteristic curves are adopted and the area under their curves (AUC) is introduced as a performance criterion to the field of SHM. The framework also allows for a fast comparison of varying numbers and selections of training data
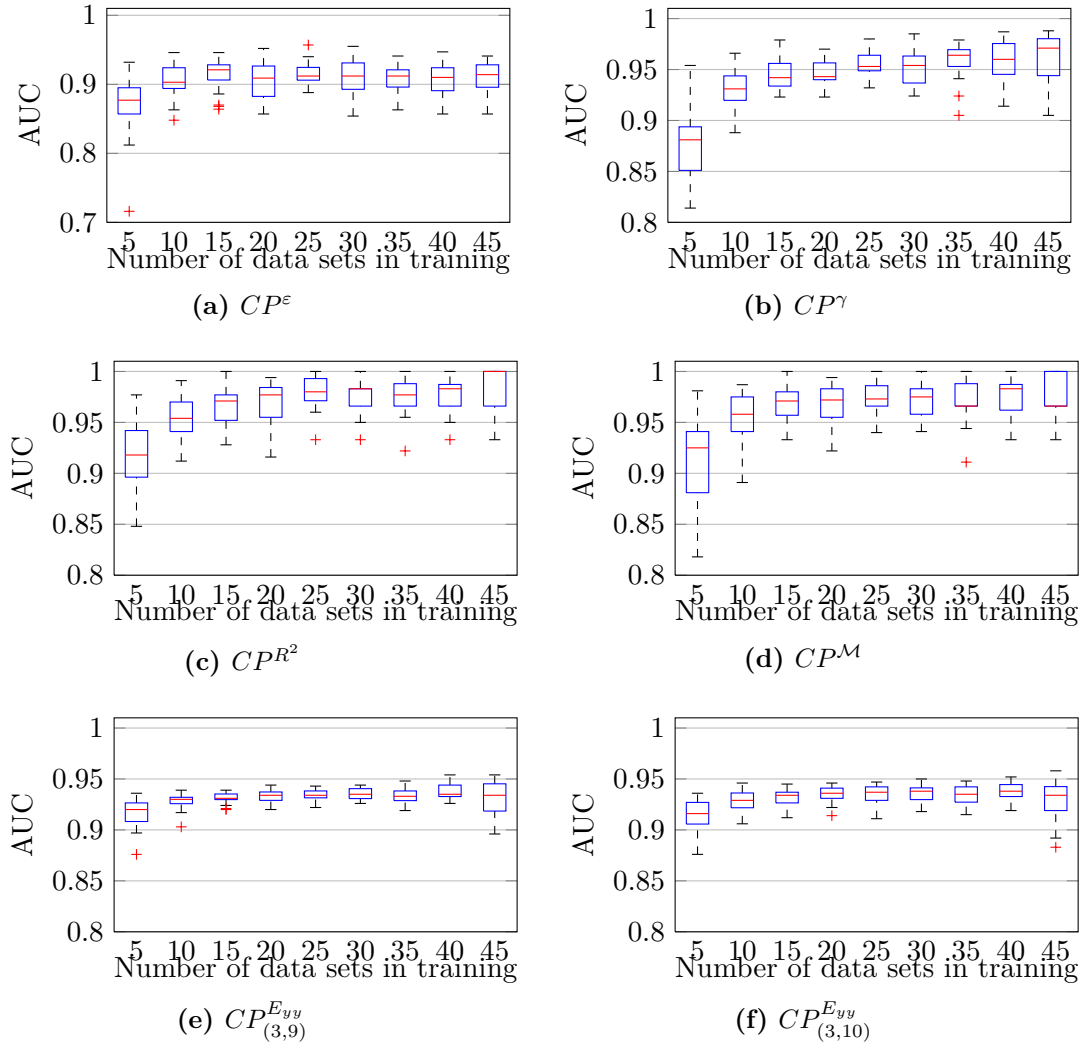
Figure 3.30: Condition parameter robustness against number and selection of training sets, evaluated by area under curve (AUC) of ROCs. Six CPs tested with selected, optimal parameter settings for different numbers of training data (5:5:45), 25 random selections were evaluated per set up. It should be noted that the number of training sets indicates the number of sets taken from each of the three healthy states (#1-3).

Considering this, the values of condition parameters must be understood with respect to machine learning ($CP(ML)$) and accordingly hypothesis testing with respect to machine learning and condition parameters $HT(CP(ML))$ as stated in Equations (3.6) and (3.7) on page 74.

Application of the SHM framework and an evaluation of performance is carried out using a benchmark database. It is publicly available and contains linear and non-linear damage scenarios on a base-excited frame structure. Damage detection and localization are successfully applied to the example and different combinations of SHM constituents are compared using the presented approach.

In general, the division of the training phase into three clusters improves the SHM performance significantly. For some CPs, it even facilitates damage detection. It should be noted that also the

relative CPs, which are sometimes claimed to work without ML or EOC compensation[1], benefit strongly from the ML step, e.g. manual clustering.

It is summarized that modal parameters are not feasible to detect damage. All four relative CPs (CP^{R2}, $CP^{\mathcal{M}}$, CP^{ε} and CP^{γ}) are able to detect linear an non-linear damage with high AUCs; CP^{R2} and $CP^{\mathcal{M}}$ result in slightly better performance. Another advantage of the VAR-based residues is the dependency on only one parameter while CP^{ε} and CP^{γ} need two and three initial parameters, respectively. The setting of these parameters is even more critical for the SHM performance of SSI based than VAR based CPs, since a safe side (larger model order p) can be chosen for VAR residues. A recommendation to estimate the parameters is given with respect to the number of measured channels m, sampling frequency f_s, and the lowest frequency of interest f_{min}:

$$p \gtrsim 0.7 * f_s/f_{min}$$
$$n_{shift} \approx f_s/f_{min} \text{ for } CP^{\varepsilon}$$
$$n_{shift} \lesssim f_s/f_{min} \text{ for } CP^{\gamma}$$
$$N_b \approx f_s/f_{min}$$
$$n_{sig} \gtrsim 2 * m$$
$$n_{is} \approx n_{shift} * m - n_{sig}.$$

Where f_{min} can be the lowest eigenfrequency, the first eigenfrequency considered as damage sensitive, or a band limit of a filter.

The newly formulated absolute CP based on accumulated energies performs almost as good as the more complex relative CPs and additionally provides the possibility of damage localization if calculated per measured channel. It is suggested to utilize the mean frequency between the 80 and 90% energy level as CP. The cross-correlation based $CP_{,}^{E_{xy}}$ performs slightly better than the formulation with auto correlations $CP_{,}^{E_{yy}}$.

For HT, results from discrete and normal distributions are very similar but the normal distribution is considered to be more robust. The number of training sets has influence on the achievable AUC level, it is suggested to use at least 15, better 20, instances per state the benchmark case. This number can also be transferred as minimum number of data instances per cluster for further analysis.

Over all, the applicability and validity of the approach are proven, establishing reasonable confidence that further analysis can be carried out in the same manner on different structures. To gain more belief in the used CPs and parameter settings, application will be presented in the following on a small-scale wind turbine with artificially introduced damage in (Chapter 4) and on an in-operation industrial-scale 5 MW wind turbine in Chapter 5.

---

1 In these cases a single cluster is used.

4 Monitoring a Small-scale Wind Turbine

Being of moderate size, the Los Alamos National Laboratories (LANL) wind turbine structure provides a link between small scale physical models and full-scale industrial power plants. Its dimensions are large enough to result in complex dynamic behavior under realistic loading and excitation while still allow for an application of artificial damage scenarios. For the measurement campaign, three main goals were set:

- Verification and *in-situ* test of *Martlet* wireless sensor nodes,

- dynamic characterization of the structure, through the triangulation based extraction of modal parameters (TEMP),

- application of the proposed SHM framework under challenging conditions and evaluation of performances.

For the design, performance, and evaluation of the *Martlet* wireless sensor nodes, it is referred to [93, 94]. The following sections will provide information on the structure itself, the data acquisition, identified dynamic characteristics and the application of the proposed modular SHM framework for performance evaluation. The set-up is very challenging for SHM since a new measurement chain is linked to a very limited collection of EOCs. Hence, this example must be understood as a validation under sub-optimal conditions rather than a proof of concept with perfect performance in all points.

4.1 The Structure

The subject of the study is a steel support structure for a Whisper 500 wind turbine. Located at a tech area of the LANL at about 2150 m elevation. The turbine is a two-bladed system with a rotor diameter of 4.5 m and a rated power of 3 kW at 10.5 m/s wind speed (peak power 3.2 kW at 12 m/s). Operational wind speeds reach from 3.4 m/s to max. 55 m/s. The nominal rotor speed is 500 rpm (8.2 Hz). A 12.2 m high steel structure carries the 70 kg heavy nacelle. For maintenance and experimental purposes, the whole tower can be tilted around a pivot point, which is located at a third of the tower height.

Figure 4.1 shows the overall structure with sensor positions (left), close up views of the bottom section, the tower in tilted position, and a bolt at the bottom (used to fix the structure in the upward position). The bolt was used to introduce damage to the structure by inserting a longer bolt with a spring. This changes boundary conditions slightly from fixed to only partially fixed and introduces additional non-linearities. An earlier experimental study, including a numerical
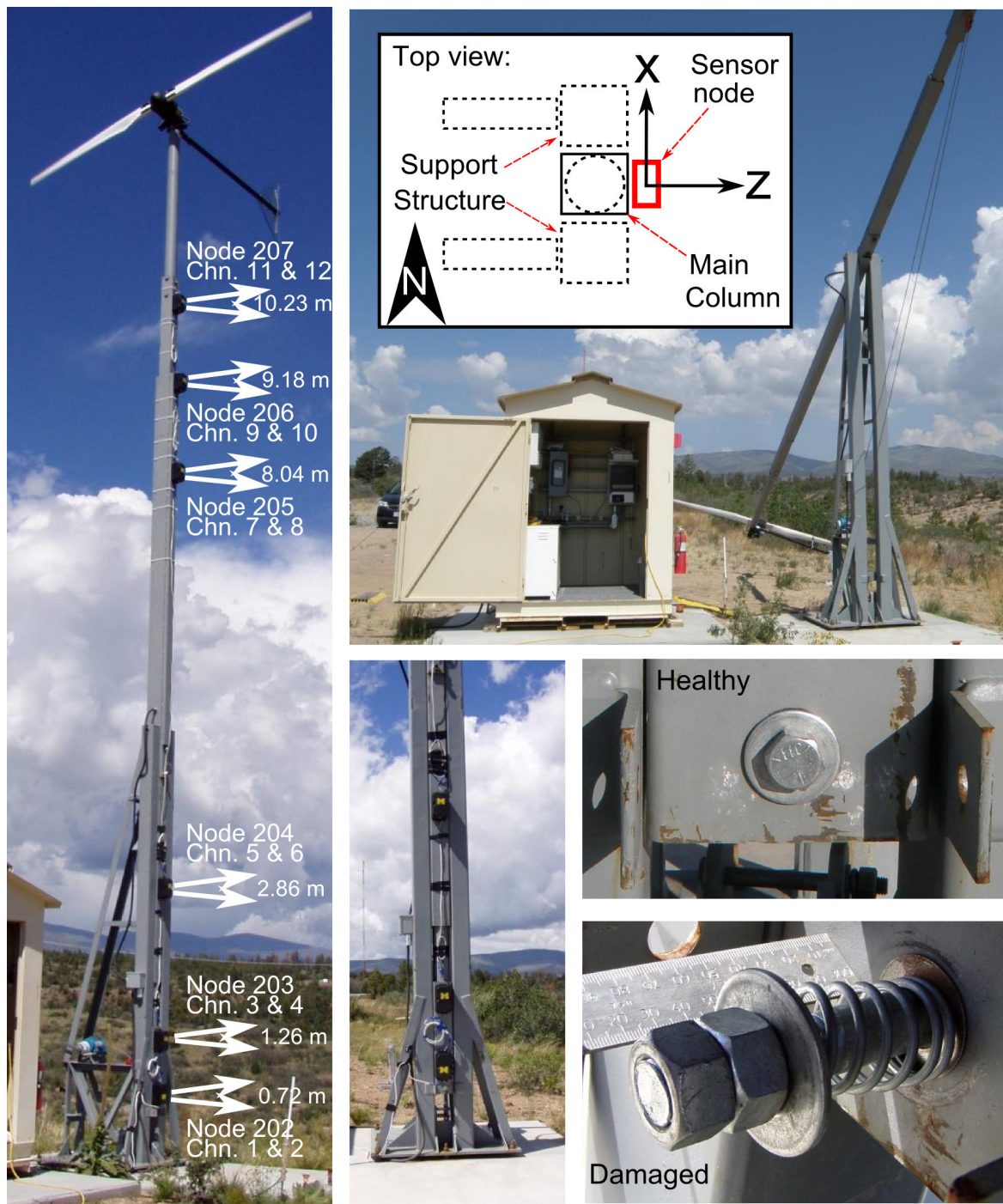
Figure 4.1: Wind turbine structure in erected position with six mounted sensor nodes, indicated by arrows (left). Turbine during tilting procedure with battery shed and schematic of top view with measurement directions (upper right). Close up of bottom sensor nodes (bottom middle) as well as healthy and damaged bolt state (bottom right).

model of the turbine, was published in [34]. In which the focus is put on the turbine's blades including modal analysis and the overall power production using a FAST model. Blade modes were identified at 9.1, 27.0, 33.4, and 75.5 Hz.

Each of the six wireless nodes consists of a tri-axial acceleration sensor (only the horizontal plane

in mounted position is recorded), power supply board, *Martlet* unit (see Kane et al. [93], Kane [94] for further details), and a board for sensor connection. The sensors were daisy chained and powered with 5 V from the wind turbine's battery bank. Data transmission to the base station was realized via radio.

During the test, the base station was placed in the weather proof battery shed. It consists of a raspberry pi for system control, crontab execution and data storage and a radio connected to the raspberry pi via USB, which controls the sensor network. A water proof outlet was used to connect the antenna and provide power supply for the sensor nodes.

As mentioned, the turbine tower can be tilted down via a wire crank for maintenance and experimental purposes as can be seen in Figure 4.1 (right). This feature was used to mount the upper three sensors above the pivot point (see arrows Figure 4.1 (left)). The lower three sensors were mounted below the pivot point, two close to the bolt and one further up in the middle of the lower field.

Additional information about weather conditions was taken from a weather station, located about 50 m north of the wind turbine. It is instrumented at four levels and located on the Pajarito Plateau in an open area, fetch within several hundred meters of the weather tower is over short grasses.

4.2 Data Aquisition

Sensor application and a first test run were performed in June 2013. First data instances were recorded on June 19th, 21st, 22nd, and 24th 2013. All of those data instances were collected under healthy conditions with the original bolt in place and the wire crank tightened.

A new base station was installed on September 13th. Data was collected in a second testing campaign on September 16th-18th 2013, both under healthy and damaged states. Damage introduction, manual stops and manual starts of the turbine were performed during the following times:

- 16.09.2013: 13:00-16:30 pm
- 17.09.2013: 09:15-11:55 am & 14:00-17:00 pm
- 18.09.2013: 09:15-12:47 pm

Beyond these time slots, data was automatically collected in five minute intervals under healthy conditions with 500 Hz or 1 kHz sampling rate for 23 s without the need for interaction. For the application of the SHM framework, data was sampled down to 100 Hz, only spectrograms are derived from the 500 Hz data instances. Each set was saved and transferred into Matlab-format with its name indicating the date and starting time of data collection.

Table 4.1 gives an overview of the collected data: On September 16th the turbine was under normal operation when the data collection started (13:00). For the first hour, data was collected under normal operation and additional handwritten notes for wind and performance were taken. Then, a first manual stop was performed and the bolt was exchanged to introduce damage. Subsequently the break was switched off. Then data was collected in the damaged state under normal operation. At the end, the break was again switched on and the original bolt was put back

into place. Finally, the break was switched off and data was collected under normal operation throughout the night (State 2 in Table 4.1). Since some data collection issues occurred, only data from 16:20 H on was used.

Table 4.1: Overview of database for LAN WT.

Label	Set	Condition	Description	Date and Time (DD.MM.JJJJ)
State 1	1	Damaged	Break on	16.09.2013; 16:20 h
State 2	2-200	Healthy	Normal operation	16.09.2013; 16:20 h - 17.09.2013; 9:20 h
State 3	201-215	Damaged	Spring installed	17.09.2013; 9:25 h - 17.09.2013; 11:25 h
State 4	216-237	Healthy	Normal operation	17.09.2013; 12:00 h - 17.09.2013; 14:21 h
State 5	238-250	Damaged	Break on + spring	17.09.2013; 14:40 h - 17.09.2013; 16:40 h
State 6	251-340	Healthy	Normal operation	17.09.2013; 18:15 h - 18.09.2013; 9:10 h
State 7	341	Damaged	Break switched on	18.09.2013 9:15 h
State 8	342, 343	Healthy	Normal operation	18.09.2013 9:40 h, 18.09.2013 9:45 h
State 9	344-349	Damaged	Break on + spring	18.09.2013; 9:55 h - 18.09.2013; 12:00 h
State 10	350-351	Healthy	Normal operation	18.09.2013 12:18 h, 18.09.2013 12:20 h
State 11	352	Damaged	Break switched on	18.09.2013 12:18 h, 18.09.2013 12:20 h
State 12	353, 354	Healthy	Normal operation	18.09.2013 12:34 h, 18.09.2013 12:43 h

On September 17th, wind was very low in the morning. The break was switched on while the rotor was not turning. Afterwards, the bolt was changed to the damaged state and the sampling frequency was set to 1 kHz to gain knowledge about higher frequency content in the signals. Wind picked up and data was collected under normal operations. Between 10:55 and 11:20 sampling rates were further increased and then set back to 1 kHz. Then, the break was switched on, the original bolt was installed and the sampling rate was set back to 500 Hz. The break was taken off and data was collected under normal operation for two hours in the healthy state. Later, the turbine was stopped and the damaged state was introduced again by inserting the longer bolt with the spring. After a short period the sampling frequency was increased to 1 kHz for 11 data instances, and then set back to 500 Hz. A stop and start was performed twice and during the second standstill, the original bolt was put back into place. The sampling frequency was also set back to 1 kHz and left at this value over night.

During the morning of the third day, a stop and start was performed under healthy conditions and a second stop was used to put the longer bolt with spring into place. One stop and start was performed under the damaged state, a second stop was used to decrease the spring length to 41 mm (51 mm before). In this state, a hammer was used to perform impacts during two data collection cycles. Then the break was released and normal operation in the damaged state was recorded. Finally, the brake was switched on and the original bolt was put into place. Another

stop and start was collected before the test was finished and all sensors were dismounted from the turbine.

It should be noted that the main wind direction is south which causes the tower to lean against the sub structure rather than the bolt or spring. Hence, the severity of the damage must be assumed to be very small for the overall dynamic behaviour. During the three days of testing, the wind constantly came from southern directions tending more to south-southeast for about the first 175 data instances before switching to more south southwestern directions for a short period. After about the first 30 to 40 data instances, the wind speed decreased significantly resulting in less excitation of the structure. The lower excitation level without significant rotor movement also influenced the automated system identification procedure accordingly less modes were identified during that period (see Figure 4.6).
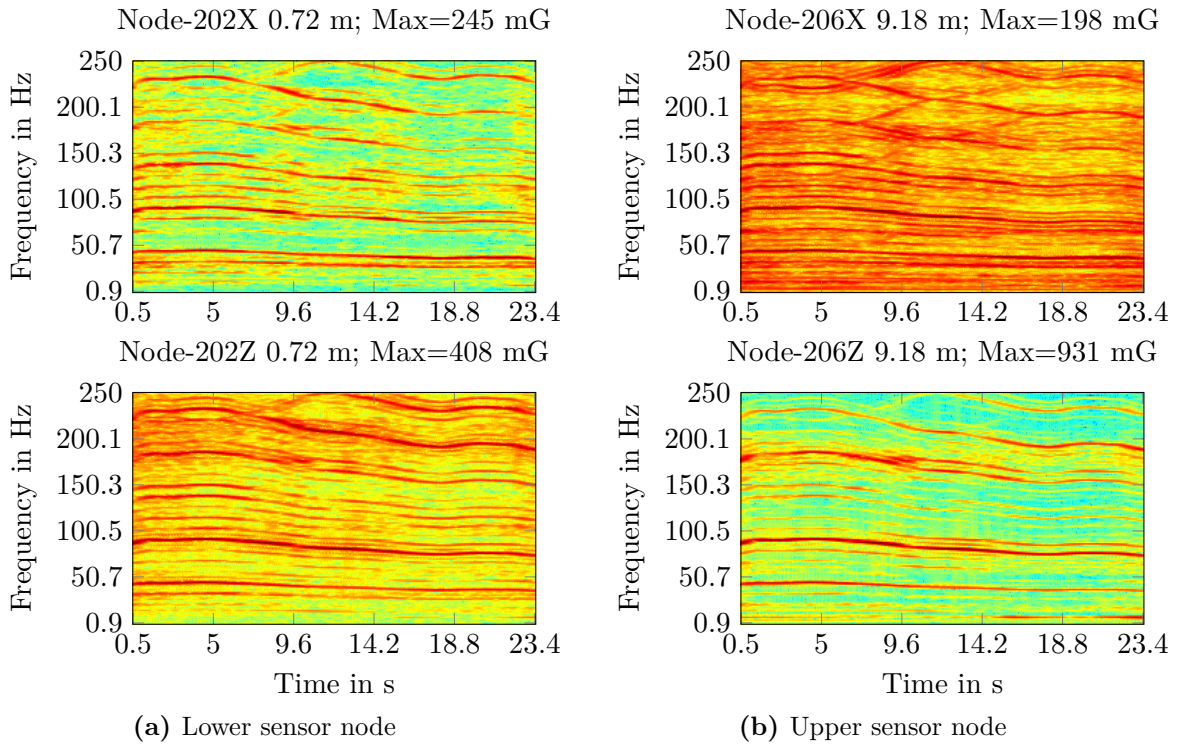
To provide easier accesses, data for all instances was saved in a single Matlab file. This file contains the raw data, environmental and operational conditions as well as further essential information (see B.1) and is named after the start time of data collection.

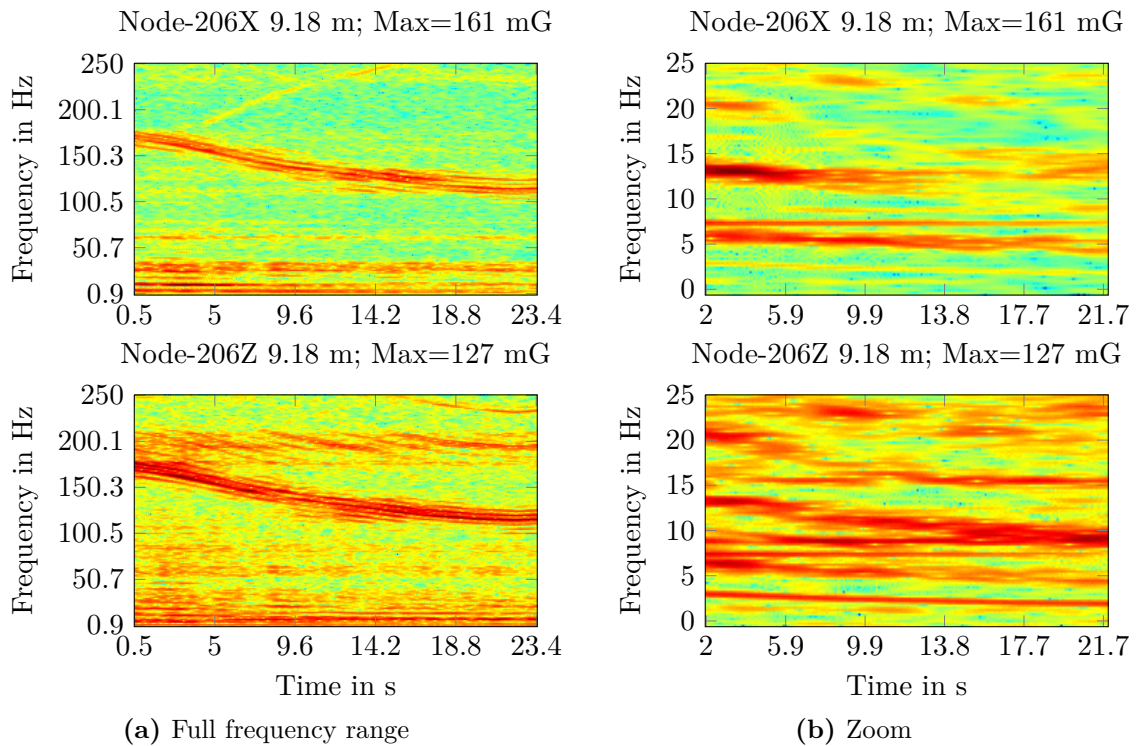## 4.3 Spectrograms and Modal Properties

Short time Fourier transforms, displayed in spectrograms, are used as a first tool to get an insight into the structure's dynamic behavior. These allow a visual inspection of changing frequency contents of a signal over time. Due to the limited recording length of each data instance, the successive Fourier transforms (512 samples each) is calculated with a large overlap of 500 samples). For a close-up to the lower frequency range (0-25 Hz), a higher frequency resolution was desired. Hence, the settings were changed to 2048 samples with an overlap of 2000 samples.

Figure 4.2 shows four spectrograms of two sensors (Node-202 and Node-206) in two directions each for normal operation under wind with a released break and without damage. It can be seen that for Node-206 and Node-202, the z-axis perpendicular to the wind direction (lower plot in Figure 4.2(b)) receives a higher excitation level by the southern wind than the x-direction. Wind speed variations result in variations of the rotor speed and in time variant frequency bands. The spectra in Figure 4.2 are full of harmonics with a number of side bands that range up to the Nyquist frequency of 250 Hz. Tracking these frequency bands, a slow decrease of wind and rotor speed can be read from the data recorded. Also, an aliasing effect can be seen in the lower right plot of Figure 4.2(b): A frequency band starts at around 225 Hz and behaves contrarily to the tendencies of all other bands until, at about half of the recording time, the band actually re-enters the observable frequency range. Similar phenomena can be seen for higher frequencies in the other spectrograms and are detected throughout the whole database.

The main reason for the strong harmonics and varying frequency content is obviously the rotor excitation. Also, the rotation speed adapts very fast to changing wind speeds and hence underlies significant fluctuations even within the rather short measuring period of up to 23 s. In Figure 4.3 a data instance with such a rotor speed change is depicted. A dominant frequency band with side harmonics can be seen, starting at about 170 Hz and decreasing over the measuring period to about 110 Hz (see Figure 4.3(a)). To verify frequency changes in the lower frequency range

Node-202X 0.72 m; Max=245 mG

Node-206X 9.18 m; Max=198 mG

Node-202Z 0.72 m; Max=408 mG

Node-206Z 9.18 m; Max=931 mG

(a) Lower sensor node

(b) Upper sensor node

Figure 4.2: Spectrograms during normal operation. Break is turned off, no damage is introduced and turbine turns under wind. data instance recorded on 17. Sep. 2013 14:05 pm.

Node-206X 9.18 m; Max=161 mG

Node-206X 9.18 m; Max=161 mG

Node-206Z 9.18 m; Max=127 mG

Node-206Z 9.18 m; Max=127 mG

(a) Full frequency range

(b) Zoom

Figure 4.3: Spectrograms with full frequency range and zoom during normal operation. Break is turned off, no damage is introduced and turbine turns under wind. data instance recorded on 16. Sep. 2013 19:30 pm

Node-206X 9.18 m; Max=330 mG

Node-206X 9.18 m; Max=13 mG

Node-206Z 9.18 m; Max=791 mG

Node-206Z 9.18 m; Max=16 mG

(a) Strong wind, undamaged

(b) No wind, undamaged

Node-206X 9.18 m; Max=303 mG

Node-206X 9.18 m; Max=8 mG

Node-206Z 9.18 m; Max=729 mG

Node-206Z 9.18 m; Max=6 mG

(c) Strong wind, damaged

(d) No wind, damaged
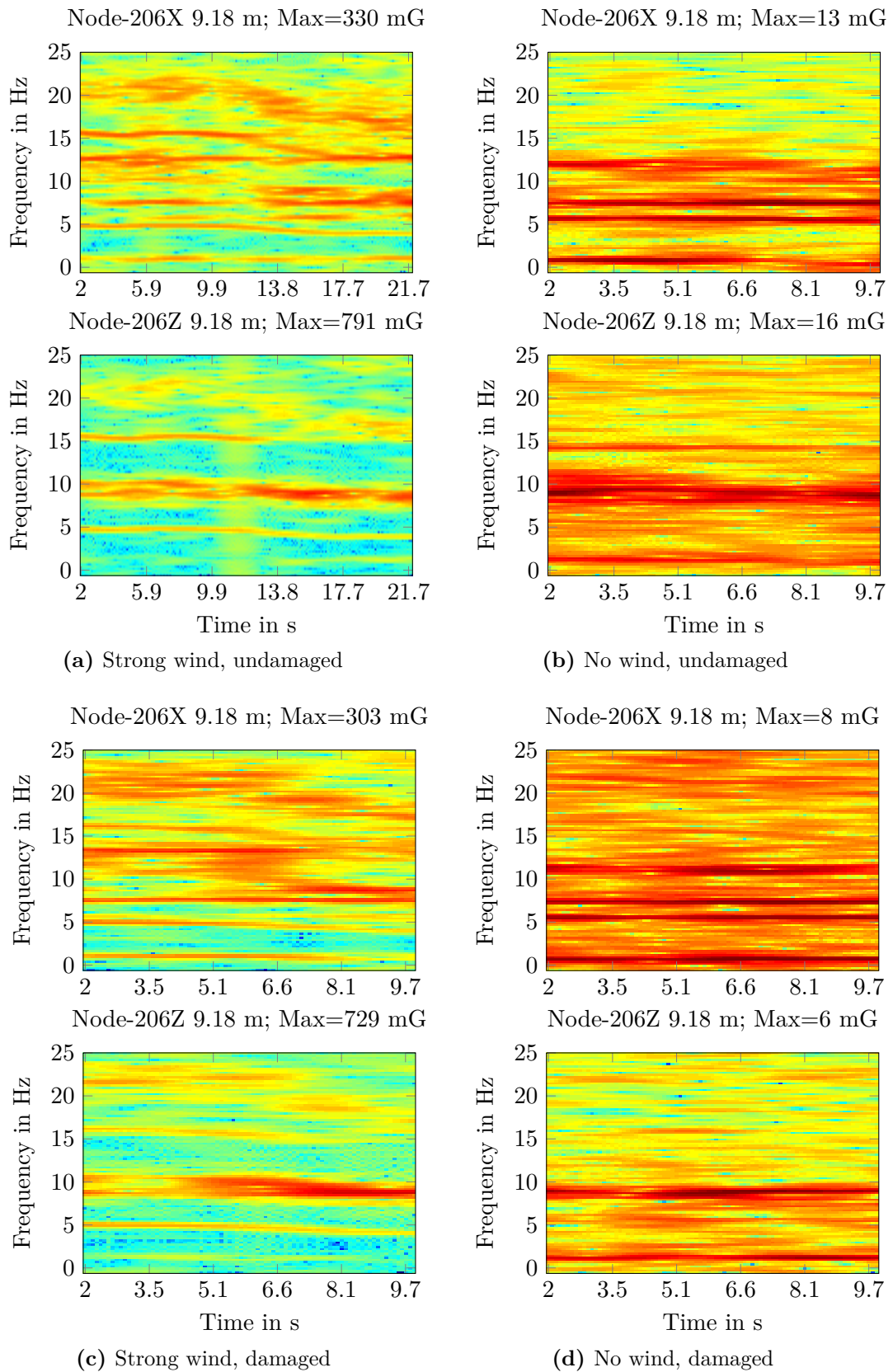
Figure 4.4: Spectrograms for x- and z-direction of node 206 at 9.18 m for undamaged state under wind 4.4a and without wind 4.4a. Spectrograms for the damaged scenario under wind 4.4c and without wind 4.4d. data instance recorded on 17.09.13 12:50, 18.09.13 11:57, 18.09.13 10:06, and 18.09.13 11:06, respectively.

(a) Break turned on, undamaged

(b) Break turned on, undamaged

(c) Break turned on, damaged

(d) Break turned on, damaged
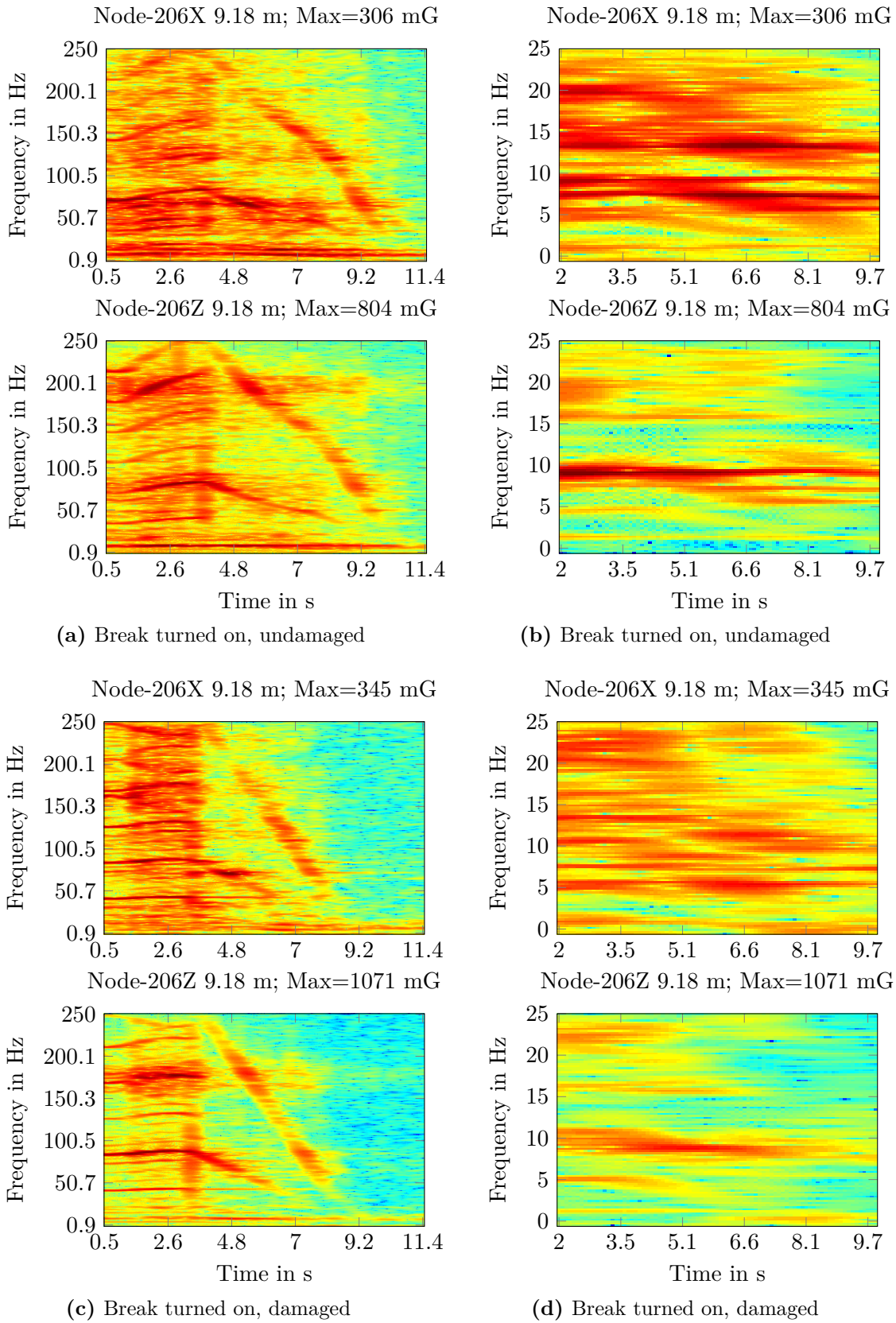
Figure 4.5: Spectrograms for dynamic behavior under break switch-on for complete frequency range (4.5a and 4.5c) and zoom from 0 to 25 Hz (4.5b and 4.5d). Break was truned on under healthy (4.5a and 4.5b) and damaged condition (4.5c and 4.5d). data instance recorded on 18.09.13 9:15, and 18.09.13 10:58, respectively.

and constant (modal) frequencies, a zoom for both measuring directions of Node-206 is given in Figure 4.3(b) (see also Figure 4.4 and 4.5 for spectrograms under healthy and damaged conditions with close-ups to the lower frequency band.).

Low frequency modes (between 1 and 2 Hz) only appear vague in Figure 4.3, for a more clear view see Figure 4.4(d). Below 5 Hz a varying band is present in both directions. A next constant line for both directions can be detected at around 7.5 Hz. For the x-direction, another constant frequency band, which is corrupted by a changing frequency, lies at about 6 Hz. In the z-direction the next constant band lies at about 9 Hz. Figure 4.4(b) and 4.4(d) display the constant frequency bands for the x-direction (1.5 Hz, 6 Hz, 7.5 Hz, and 12 Hz) and for the z-direction (2 Hz, 9.5 Hz, and 14.5 Hz) clearly. Spectrograms for data instances under an artificial switch-on of the wind turbine's brake are given in Figure 4.5. Both, full spectrum and zoom are given for Node-206. The brake's influence is clearly visible around 3.7 s when vibration amplitudes for frequencies up to 250 Hz drop and distinct harmonics of the rotor speed decrease to zero at about 8.2 s. Sub-figures 4.4(b) and 4.4(d) show the distinction between constant frequency bands and those driven by the rotor (harmonics).

The presence of many resonance frequencies with side bands distinctively complicates the system identification procedure. As a consequence, the analysis is limited to the very first modal frequencies which are already difficult to extract.

The TEMP method was introduced in Chapter 2. TEMP was used to automatically extract modal parameters for the discussed database with 354 data instances. Table 4.2 holds the applied criteria for the extraction[1]. Every data instance is opened and TEMP is applied to the raw stabilization diagrams from SSI-Data, based on all 12 channels. When data was sampled with more than 100 Hz, the sampling rate was reduced through omission of samples.

Table 4.2: TEMP criteria for modal parameter extraction at LANL WT[1].

N_{shifts}	N_{order}	ϕ_{crit}	f_{crit}	ζ_{crit}	MAC_{crit}	$\hat{P}_{crit}$
60	$2:2:200$	$30°$	5%	80%	0.88	30

After a run for all data instances, an overview of the resulting solutions can be plotted as given in Figure 4.6. The lower right sub-plot holds all identified modal frequencies over each data instance for a range of 0 to 40 Hz. This frequency range was selected for discussion of the first global bending modes. From this plot it is obvious that from set 50 to about 200 the procedure resulted in significantly fewer solutions than for all other data instances. This is emphasized by the upper plot, where solutions per data instance are counted. The number of resulting modes drops from a value around 30 to less than 5. It was noted that for these data instances the wind speed

---

1   The number of shifts results from the estimated lowest mode at 1.4 Hz which has a period of 0.7 s and hence 70 samples at $f_s = 100$ Hz. To cover 70% of the samples 50 shifts are necessary, a little larger number was chosen here. Due to the 12 channels, a state space model order of 24 results. This order should be well overestimated with chosen orders of 2 to 200. Values for MPD, frequency, damping, and MAC are again empirical values recommended for large-scale structures. An overview for TEMP settings for all investigated structures is given in Table 6.1

dropped below 3 m/s. Hence, the turbine was not spinning and potentially only low frequency modes are present due to external (wind) excitation. Another more likely cause for the lack of mode identification could be caused by the (too) low and fixed resolution, set for the on-board amplifier of the *Martlet*-node. With only small acceleration amplitudes, the signal is not properly gained and thus the effective number of bits, used for digital representation, is insufficient. Hence, content with higher frequencies and lower amplitudes is not sampled in the signal. TEMP shows a distinct advantage over conventional clustering since the number of resulting modes is not user defined as in many present automated system identification procedures.

As previously mentioned, the automated identification (under operation) suffers from the harmonics present in the input and hence a violation of the white noise input assumption for SSI. Nevertheless, if the left plot in Figure 4.6 is investigated, distinct peaks with more modes identified occur in the histogram: two peaks below 2.0 Hz, one around 6.0 Hz, one around 8.0 Hz, and one between 9.0 and 10.0 Hz. Two less distinctive peaks are present around 12-14 and 16 Hz. These results agree with the frequency bands in the spectrograms discussed above. For a characterization of the global modes a data instance which contains all of these solutions was desired. The second set, recorded on 19.09.2013 16:20 pm, holds solutions within the following frequency bands: 1.2-1.4 Hz, 1.65-2.1 Hz, 6.5-5.5 Hz, 7.5-8.3 Hz, and 8.7-9.7 Hz. Results for identified frequencies and damping values for this data instance are listed in Table 4.3. Additionally, in the range of 8.7-9.7 Hz, some spurious modes occur. These are assumed to belong to the first blade mode at about 9.1 Hz [34] and rotor excitation and are omitted.

Table 4.3: TEMP results for data instance two, recorded 19.09.2013 16:20 pm

	f_1	f_2	f_3	f_4	f_5	f_6	f_7
f in Hz	1.4	1.9	6.0	7.8	9.6	12.3	14.8
ζ in %	1.6	2.9	0.3	0.1	1.7	1.3	0.4

This single data instance is used to illustrate the functionality of the TEMP approach in detail. As in Figure 4.6, a focus is put on the lower frequency range up to 40 Hz for the sake of clarity.

As stated above, each sensor node captures accelerations in the horizontal plane through two orthogonal axes. Hence, three dimensional mode shapes can be derived from the system identification process. In the case of TEMP, the complex mode shape from the solution with the highest model order is taken from each path in the stability diagram derived within each data instance. Figure 4.7, along with Figure B.2 in Appendix B.2, gives an insight into the first seven global bending modes of the experimental wind turbine structure. Plots 4.7a, 4.7d, 4.7g, and 4.7j hold the top view to the turbine, the main axis of the mode shape can be identified. All other plots show side views for the x- and z-axis, respectively.

The first two modes at 1.4 and 1.9 Hz show typical first bending modes for a cantilevered beam, moving in orthogonal directions which correspond to the sensor axis. The fifth mode at 9.6 Hz is almost orthogonal to the third and fourth mode. Mode number three at 6.0 Hz and five at 9.6 Hz seem to form an orthogonal pair since both have small amplitudes for the lower sensors, depicting
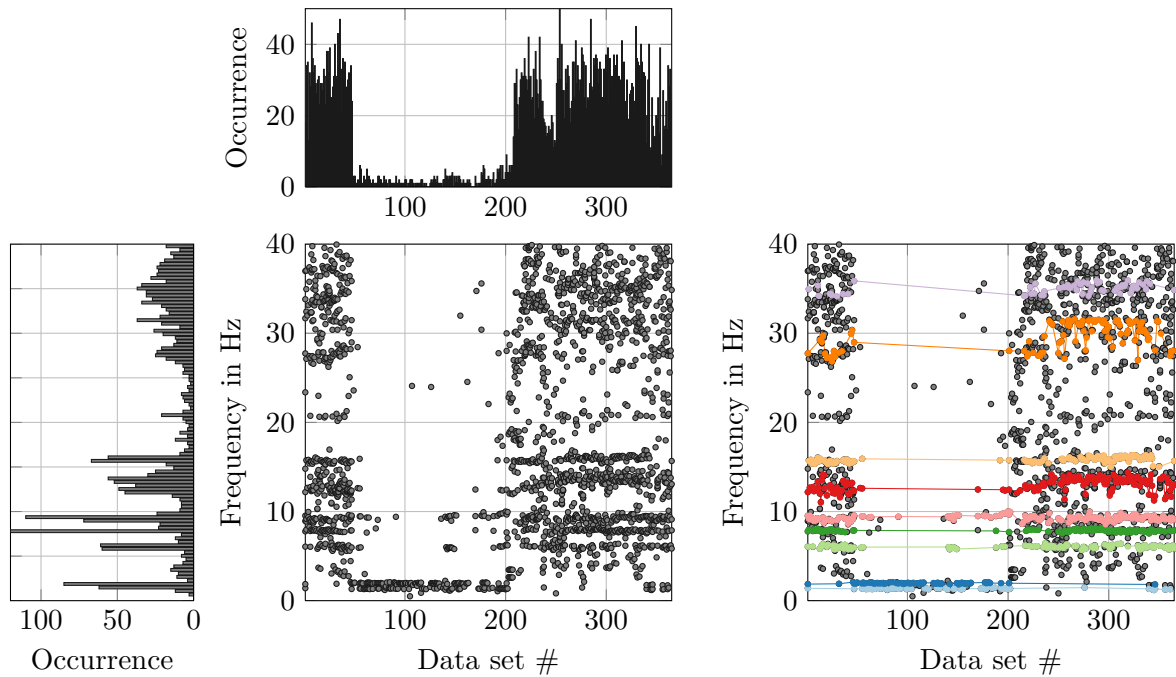
Figure 4.6: Overview of automatically identified modal frequencies for all 354 data instances using TEMP method (bottom middle) along with occurrence of frequencies (left) and number of solutions per data instance (top). Modal objects from a second run of TEMP over the complete database indicated by different colors (right)

a curve with a vertical tangent, typically for a cantilevered beam. Also, both have a maximum at the second highest node. In contrast, the fourth mode at 7.8 Hz has its maximum amplitude at the third highest node and the lower sensors curve as for a simply supported beam. Having two sensors on one level at the edges of the structure might reveal if mode four is a torsional. Again, the two highest modes form an orthogonal pair, too. Both have a zero crossing and two maxima. Mode six at 12.3 Hz appears oddly at the highest two sensor nodes since these almost have the same amplitude (see B.2d, B.2e, andB.2f).

As for the three story building structure, the complexity of a mode shape is not useful for the extraction of modal parameters. Again, most solutions align in the complex plane but do not lie purely on the real axis (see B.2). Hence MPD should be used to identify physical solutions.
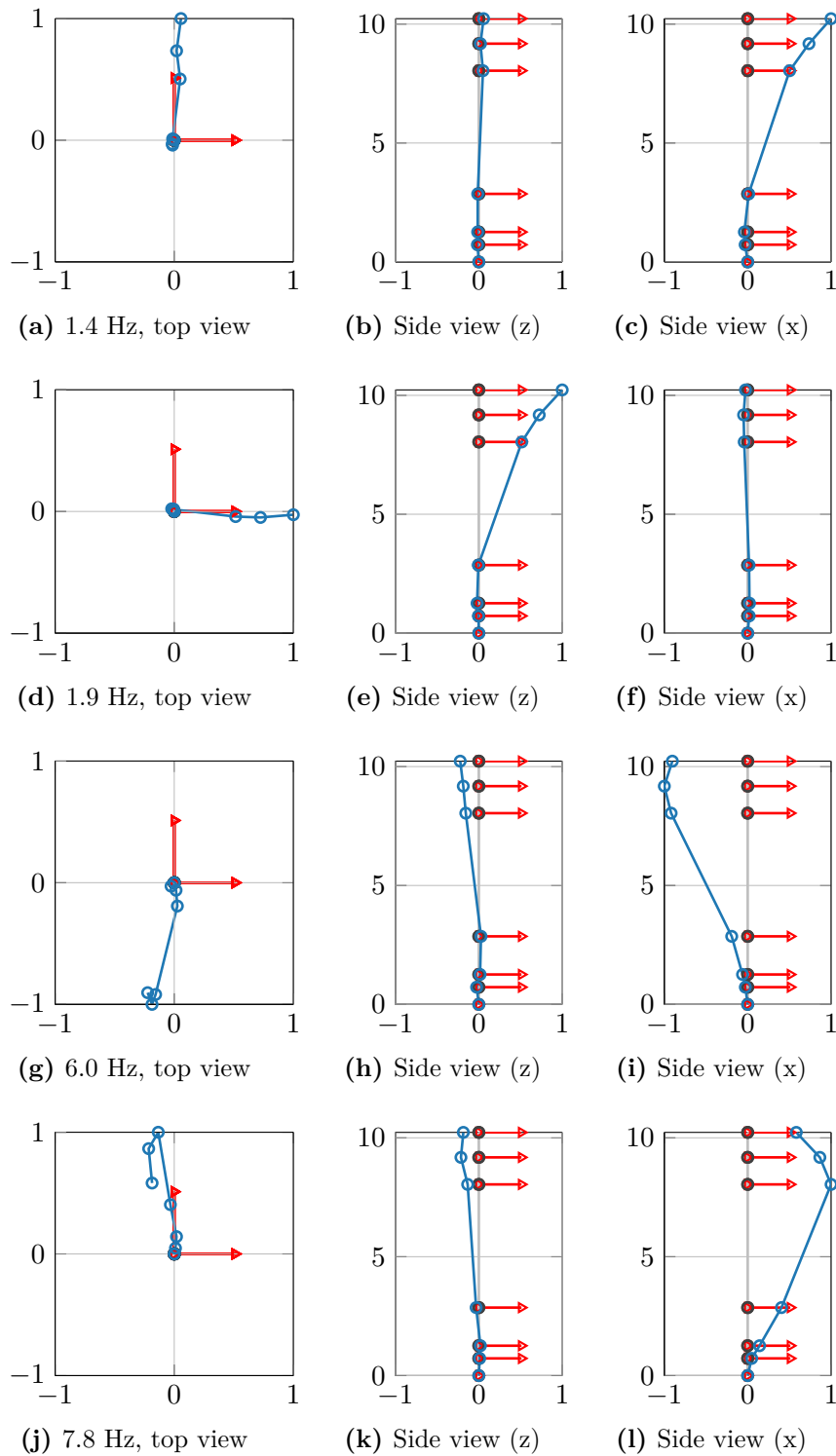
Figure 4.7: Identified global bending modes 1 to 4 for LANL wind turbine at 1.4, 1.9, 6.0, and 7.8 Hz with top and both side views. See Appendix B.2 for modes 5 to 7.

4.4 Application of SHM framework

For the application of the proposed SHM framework, the whole database as described above was used. An overview of the database by wind speed and temperature is given in Figure 4.8 (upper left). Here, artificially introduced brake scenarios and the loosened bolt are both understood as abnormal/damaged states. Further, the database is divided into learning and a testing phase (upper right in Figure 4.8). As stated, in Table 4.1, reversible damage was introduced multiple times. Training sets are drawn only from healthy sets covering the complete wind and temperature ranges.

The machine learning (ML) part was achieved using manual classification and automated classification through affinity propagation (AP). In the manual case, one reference classification and one by wind speed were used:

- *Manual1* or *Man1*: All training data instances form a single cluster (2nd row left in Figure 4.8).

- *Manual2* or *Man2*: Wind speed is used as a classification criterion for intervals from 12 to 16, 16 to 20, and 20 to 24 m/s (2nd row center in Figure 4.8).

Affinity propagation, as an automated clustering procedure, is used in four further cases, where the preference is set empirically to values of [-20,-10,-7.5,-5] resulting in [2, 4, 6, 7] clusters[1] based on wind speed and temperature information. Table 4.4 gives an overview of the different parameters used for SHM.

It is emphasized that the recording of rotor speed as a major system parameter has the potential to increase the performance of clustering and subsequently the SHM-performance significantly. The ML step results in six different variants of data clustering through which the comparison of CPs, and for relative CPs also their estimation, are defined. Table 4.5 gives an overview of the classification nomenclature and attributes[2]. The data instance separation in the temperature and wind speed plane for all six ML instances is given in the lower two rows of sub-figures in Figure 4.8.

For 'Manual1', all training CPs are taken to build the probabilistic model in a single cluster. Cluster sizes are indicated to provide information about the number of samples available for the construction of probabilistic models in the HT step during training. The following section will

---

1   Again, the smaller the absolute values of the preference (as gravity indicator), the more clusters will result from the AP procedure.

2   After the inspection of PSDs from different data instances and channels a lower frequency of interest of $f_{min} = 5$ Hz was determined. Accordingly the number of shifts was chosen to $60 \gg 20 = f_s/f_{min} = 100/5$. The number of model orders as well as criteria f_{crit}, ζ_{crit}, and MAC_{crit} are empirical. The MPD criterion ϕ_{crit} was set to a high value of 30 due to the in field conditions. $\hat{P}_{crit}$ should be chosen to one half to a fifth of the given model orders, 30 in this case. Selection of the different CP input variables goes along the introduced rules of thumb. $n_{shift} = f_s/f_{min} = 100/5 = 20$ is taken into account for CP^ε, n_{is} is chosen to a very low value of 2 here. For CP^γ, $n_{shift} = 7 < f_s/f_{min} = 20$ is a small value assuming significant changes in dynamics above 13 Hz and $n_{sig} = 10$ violates the rule of being equal to two times the number of sensors. The motivation lies in an excitation of mainly one sensor direction. For the VAR-based CPs, the model order was chosen on the safe side with $30 > f_s/f_{min} = 20$.
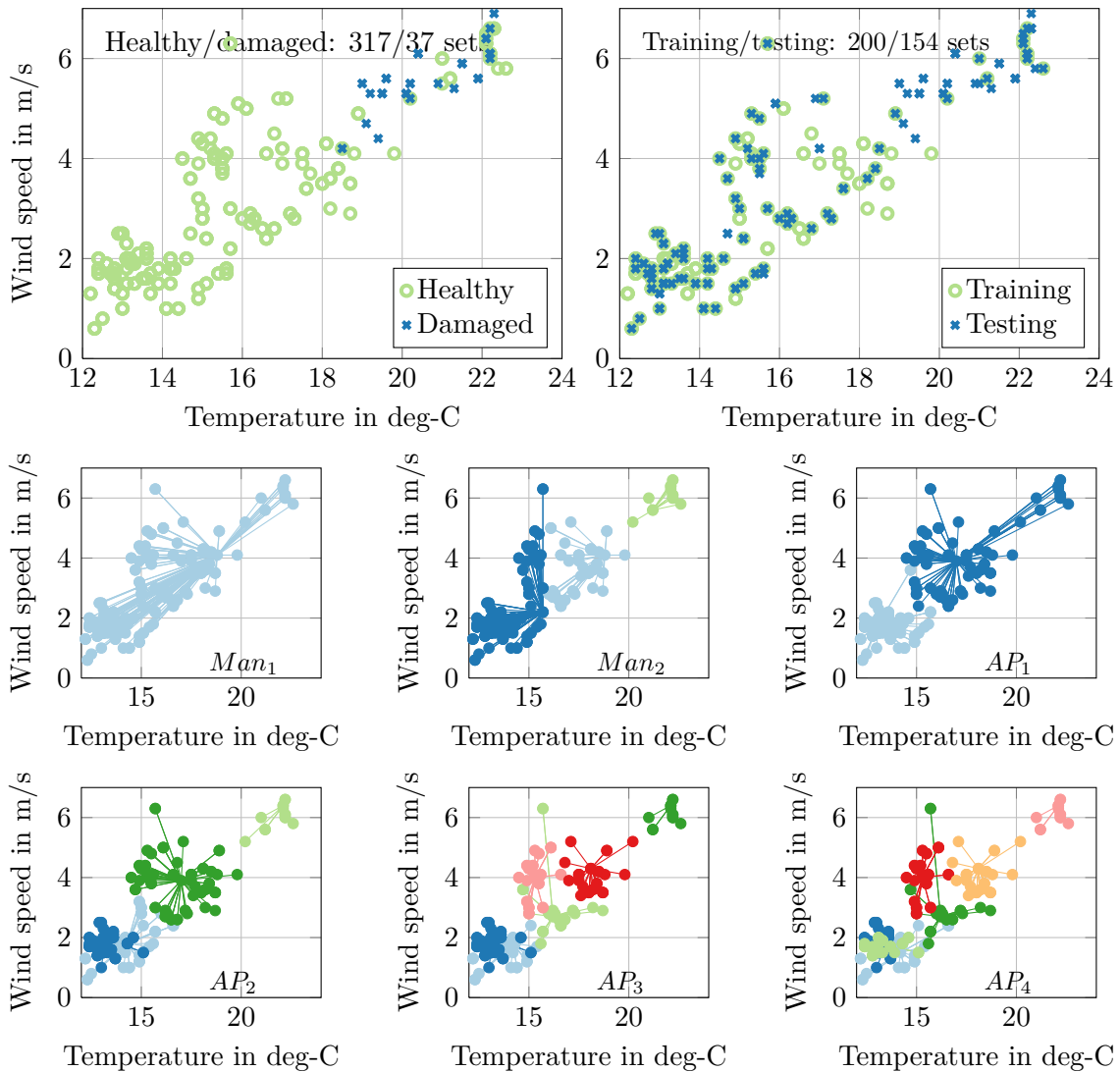
Figure 4.8: Complete analyzed database displayed over wind speed and temperature for healthy and damaged states (upper left) and training and testing (upper right). Clusters for the six analyzed ML setups are displayed in the lower two sub figure rows. It should be noted that three EOCs have been analyzed for "AP 1" to "AP 4" (temperature, wind speed and turbulence intensity, see Table 4.4). Hence, overlapping might occur in the 2d projections of the first two principal components.

show selected CPs during the training phase and control charts for a certain ML setting and confidence interval.

4.4.1 Selected Condition Parameters

Within this section, parameter trends and control charts for three CPs, one absolute and two relative, are investigated in detail before all implemented are compared with respect to AUC values. $CP_{i,9}^{E_{xy}}$ and $CP_{i,9}^{E_{yy}}$ are chosen because the energy interval between 80 and 90% showed good performance and further the ability to locate damage as demonstrated in the preceding example (see Chapter 3.5). One VAR based CP, CP^{R^2}, and one SSI based CP, CP^{γ}, are also taken into account here.

Table 4.4: Settings for SHM scheme at LANL WT

Number of channels:	12 (@ 100 Hz)	Data sets in training:	200
Total number of data sets:	354	Data sets in testing:	154

Number of ML types: 6

ML Names: $'Man_1'$ $'Man_2'$ $'AP_1'$ $'AP_2'$ $'AP_3'$ $'AP_4'$

Number of clusters:	1	3	2	4	6	7

Reference EOCs: Temperature; wind speed; wind speed stddev; wind direction

Settings for condition parameter(s):

CP^{f_i}: Shifs: 60   Model orders: 2 to 200

$\phi_{crit} = 30$ $f_{crit} = 5$ $\zeta_{crit} = 80$ $MAC_{crit} = 0.88$ $\hat{P}_{crit} = 30$

$CP_{i,j}^{E_{yy}}$: Number of energy bins = 10

CP^ε: Shifts = 20   Non-sign. col. = 2

$CP^{\mathcal{M}}/CP^{R^2}$: AR-Model Order = 30

CP^γ: Shifts = 7   Sign. col. = 10   Blocks = 100

Analyzed distribution types: Discrete, Gaussian

α-values for control chart figures: 1%

α-values for hypothesis testing: [0.1:0.1:2, 2:1:20, 20:2:40, 40:10:90]%

Table 4.5: Classification attributes for LANL WT

Classification name	ML^{Man_1}	ML^{Man_2}	ML^{AP_1}	ML^{AP_2}	ML^{AP_3}	ML^{AP_4}
Number of clusters	1.0	3.0	2.0	4.0	6.0	7.0
Minimal cluster size	200.0	14.0	95.0	14.0	13.0	13.0
Average cluster size	200.0	66.7	100.0	50.0	33.3	28.6
Maximum cluster size	200.0	133.0	105.0	80.0	55.0	39.0

Figures 4.9, 4.10, and 4.11 are arranged in the same manner as for the benchmark example in Chapter 3.5: The upper two plots show the absolute CP values for training and testing in dependency to a certain ML setup, written $CP^x(ML^y)$ (*"condition parameter x in dependency to machine learning instance y"*). For the training phase up to data instance # 200, on the left side of these plots, different clusters are separated with vertical lines (orange). Within a single cluster, data instances are plotted chronologically and vertical lines indicate the parameter distribution within the cluster by percentiles (+,*,o). For accumulated energies in Figure 4.9, four lines are displayed, one for each channel of the lowest two sensor nodes but all channels are included into the final comparison. The lower two plots show control charts for the same ML types as the upper two plots. Here, the 154 data instances from the testing phase are plotted chronologically. Each control chart for a certain CP is calculated and plotted with an optimal α value resulting from the corresponding ROC (see Table 4.6). Damaged data instances during testing are indicated by grey rectangles.

Anticipating the final stage of performance evaluation, Table 4.6 displays the performance indicator AUC for all investigated ML-CP-HT combinations. These values will be referred to in

the next sections.

Regarding accumulated energies, it was observed in the previous chapter that frequencies linked to energy levels between 80 and 90% have a high sensitivity to structural changes. Accordingly, $CP_{i,9}^{E_{xy}}$ and $CP_{i,9}^{E_{yy}}$ are chosen for further investigation at the LANL WT structure. Figure 4.9 shows results for two selected ML scenarios. Being independent from ML, the absolute $CP_{i,9}^{E_{xy}}$, results in exactly the same CP values in the two upper sub-plots. In this case data values are only arranged differently within the training phase. Values range from about 15 up to 45 Hz as mean frequencies for the energy interval. The percentiles per cluster indicate a reduction of parameter variability for most channels and cluster for ML^{AP_2} (second plot from the top). During testing (lower two plots), some outliers can be found around data instance #10.

Taking a variation of confidence intervals into account to calculate ROC curves, Table 4.6 indicates the performance for parameters $CP_{i,9}^{E_{xy}}$ (Table B.2 for $CP_{i,9}^{E_{yy}}$). Here, the base-line classification ML^{Man_1} results in a poor performance for both distribution types. ML^{AP_1} to ML^{AP_4} in contrast, performs better for $HT_{\mathcal{G}}$, reaching values of up to 0.828. For $CP_{i,9}^{E_{yy}}$ even higher performance rates of 0.852 are achieved and channels close to the damage location perform better than those further apart. Hence, the autocorrelated parameter has a better performance for this structure.

The VAR-based, relative CP^{R^2} showed perfect discrimination between healthy and damaged states in the benchmark example. In Figure 4.10, ML^{Man_1} and ML^{AP_2} are investigated for these parameters. As relative CP, values depend on the ML-step. This can be observed in the upper two plots of Figure 4.10, where the CP takes on different values. Again, clustering through AP (2nd plot from top) compared to 'Man1' (top plot) results in a reduced variability of the CP within most clusters. While for ML^{Man_1} most parameters during damaged states (grey boxes in the 2nd plot from the bottom) lie with the control limits, ML^{AP_2} leads to an identification of all sets during the first damage scenario. Most sets within the second damage interval are also classified correctly. For both ML-types, damage in the last scenario are difficult to detect. Again, control charts based on the assumption of a normal distribution (dark blue) perform better than those derived from percentiles (light blue). It is repeated that damaged sets exceed the UCL and not LCL due to the re-formulation of CP^{R^2} in Equation (2.70).

The SSI-based CP^{γ} is the second relative CP, and is displayed in Figure 4.11. In the upper plot, for a single cluster, the CP fluctuates during training and CP values during damaged states (right) lie in the training CP-range. For the four clusters in contrast (2nd plot from top), CP values clearly differ between clusters, spanning over a larger range than for the reference classification 'Man1' with values up to 10. Here, the third cluster has notably higher values than the others, indicating stronger changes in dynamic behavior for these data instances under similar conditions. In an industrial application, those states with higher uncertainties might be omitted to improve damage detection. In the testing phase, CP values around the first two damaged data instance groups have high values, too. Within the control charts in the lower two plots of Figure 4.11, ML^{Man_1} results in many FP alarms in the control chart, both for Gaussian (subscript $\mathcal{G}$) and discrete (subscript $\mathcal{D}$) distributions. Neither parameter curve differs strongly but most values during the last healthy section lie outside the confidence interval for $CP_{,\mathcal{G}}^{\gamma}$, leading to high false
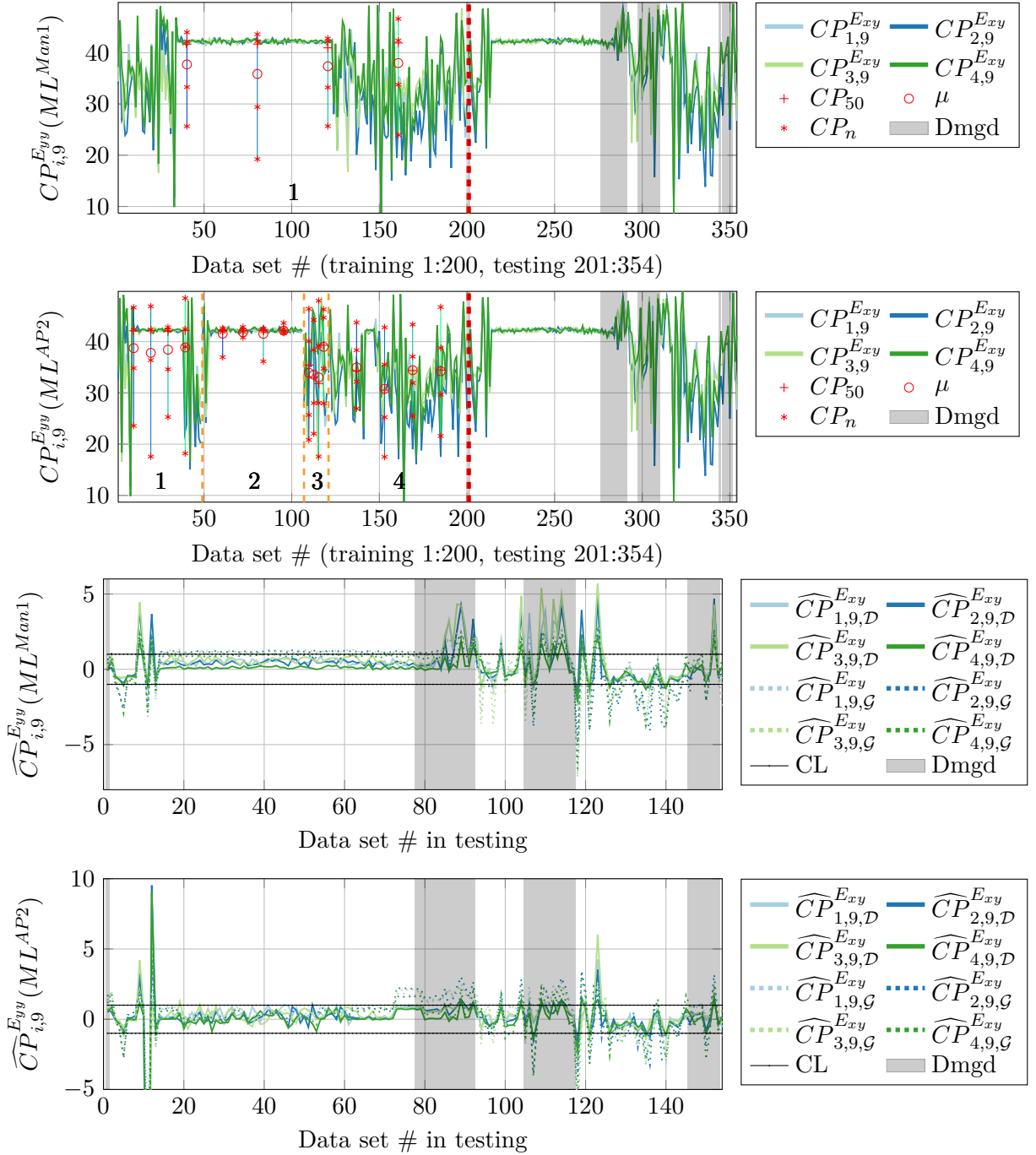
Figure 4.9: Condition parameter trends and control charts for $CP_{i,9}^{E_{yy}}$. Upper two plots show the absolute parameter trends the lower two plots the control charts for "Manual1" and "AP2" ML types, respectively. For control charts, hypothesis testing through a discrete distribution (subscript $\mathcal{D}$) and a Gaussian distribution (subscript $\mathcal{G}$) is analyzed. UCL and LCL located at ± 1 for $\alpha = 0.46$.
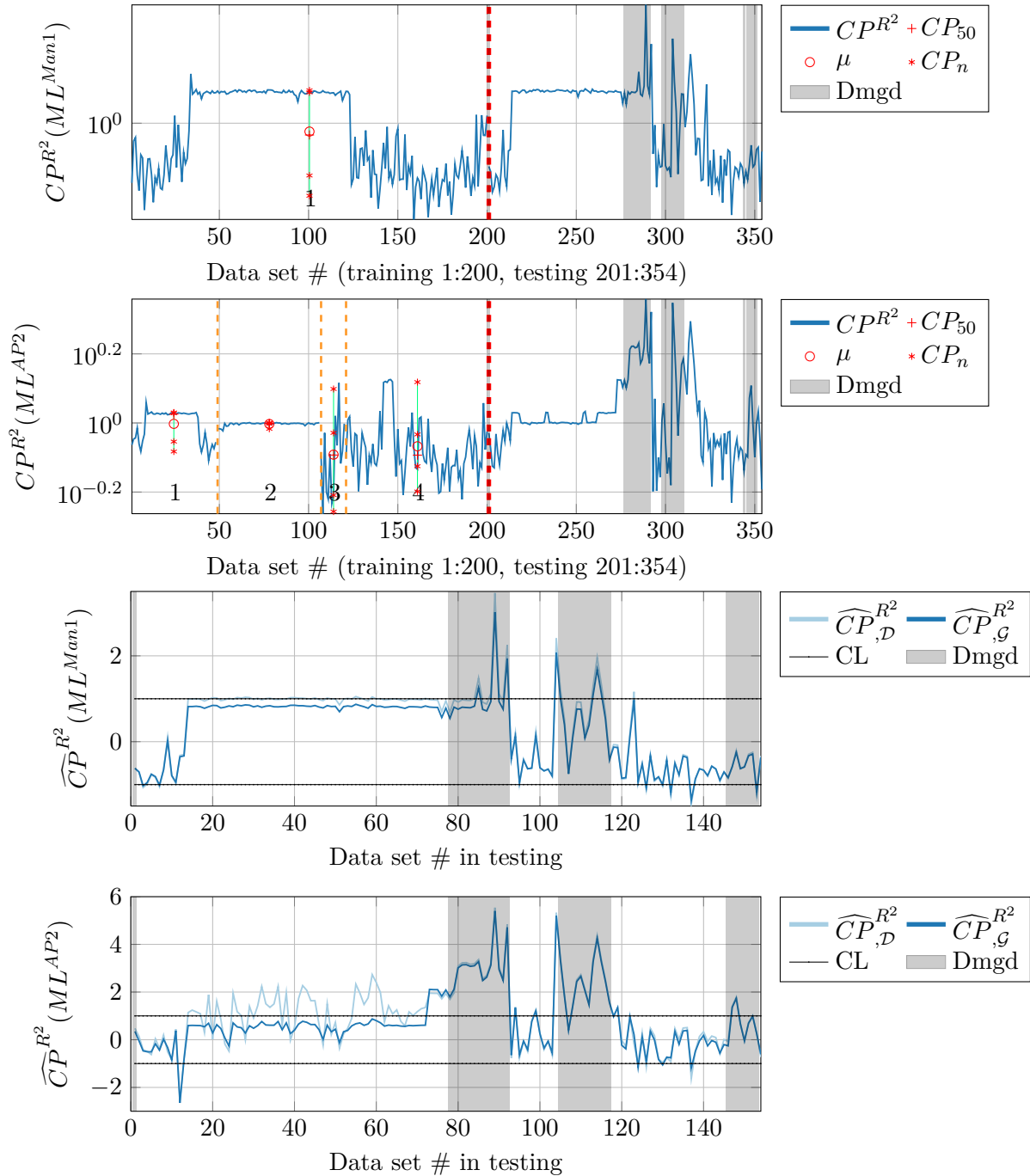
Figure 4.10: Condition parameter trends and control charts for CP^{R^2}. Upper two plots show the absolute parameter trends, the lower two plots the control charts for "Manual1" and "AP2", respectively. For control charts, hypothesis testing through a discrete distribution (subscript $\mathcal{D}$) and a Gaussian distribution (subscript $\mathcal{G}$) is analyzed. UCL and LCL located at ± 1 for $\alpha = 0.09$.

positive indication rates. For ML^{AP_2}, the performance is better. It should be noted that the parameter based on percentiles performs better (light blue). This curve also suffers from a high FP detection rate during the final healthy states around testing set 120 to 140. If a normal distribution is assumed, values during the first two damaged sections were close to the control limit showing a clear 'gap' in the chart but do not distinctively exceed the LCL boundary (dark blue in lowest plot of Figure 4.11). For $CP_{,\mathcal{D}}^{\gamma}$ the LCL is clearly exceeded. It must be noted that values exceed the threshold on the LCL which is not covered by theory, where less agreement with the references results in higher CP values for CP^{γ}.

Even though the absolute CP variation is smaller for CP^{γ} compared to CP^{R^2}, CP^{R^2} results in a better performance since CP values for damaged sets lie (mostly) out of the range of CP values in healthy states. CP^{γ} in contrast, results in CP values for damaged sets which lie close to or even within the range of CP values during healthy states (see second plot in Figure 4.10 and 4.11).

These control charts only display a small selection of possible tests to detect damage. Each control chart is drawn for a single confidence interval only and the visual inspection or extraction of false positive and false negative rates is not of general value for performance evaluation. Next, receiver operating characteristic curves are derived to complete the performance analysis.

4.4.2 Receiver Operating Characteristic Curves

To gain insight into the overall performance of the applied ML-CP-HT combinations this section utilizes ROCs to display detection rates (1-FN) over FP rates. Namely, ROC curves for the two relative CPs based on VAR-models and one ROC plot for a hybrid CP based on SSI- and VAR-residues which is simply a combination of the four CPs within a vector. The relative parameter is defined by the MSD between the reference vectors and the one of a new data instance (see Section 2.6.2). To derive the different ROCs, control charts for varying α-values are evaluated regarding false positive and false negative alarms. Figure 4.12 holds the different ROC curves for CP^{R^2} and $CP^{\mathcal{M}}$, respectively. In both plots, twelve lines are drawn for the six different ML-types (see Tab. 4.5) and for two distributions per ML-type. Normal and discrete distribution indicated by subscripts $\mathcal{G}$ and $\mathcal{D}$ in the legend. Each ML-type is indicated by a different colour. Marks indicate different α values, dashed lines belong to the normal distribution assumption solid lines to a distribution by percentiles. Optimal values with respect to the Youden-index and distance to the optimum ($\mathcal{J}$ and $\bar{\mathrm{d}}$) are indicated for both distribution types and according α-values are given.

Overall, ROC curves for $CP^{\mathcal{M}}$ in the upper plot lie close together, indicating more robust behavior against different classifications in the ML-step. The ROC for $CP_{\mathcal{D}}^{\mathcal{M}}(ML^{Man_2})$, clustered by wind speed, is worse, even lying below the diagonal. For all ML-types, the ROC based on a normal distribution (dashed lines, subscript $\mathcal{G}$) lie above the counterpart based on percentiles (solid lines, subscript $\mathcal{D}$) and hence, closer to the optimum in the upper left corner.

ML^{Man_1} is an exception here: in the range of lower detection rates (<40% on the y-axis) ML^{Man_1} outperforms the other classifications with very small FP rates. ML^{AP_1}, ML^{AP_2}, and ML^{AP_3} perform equally well. Depending on the desired maximum FP rate or performance ratio,
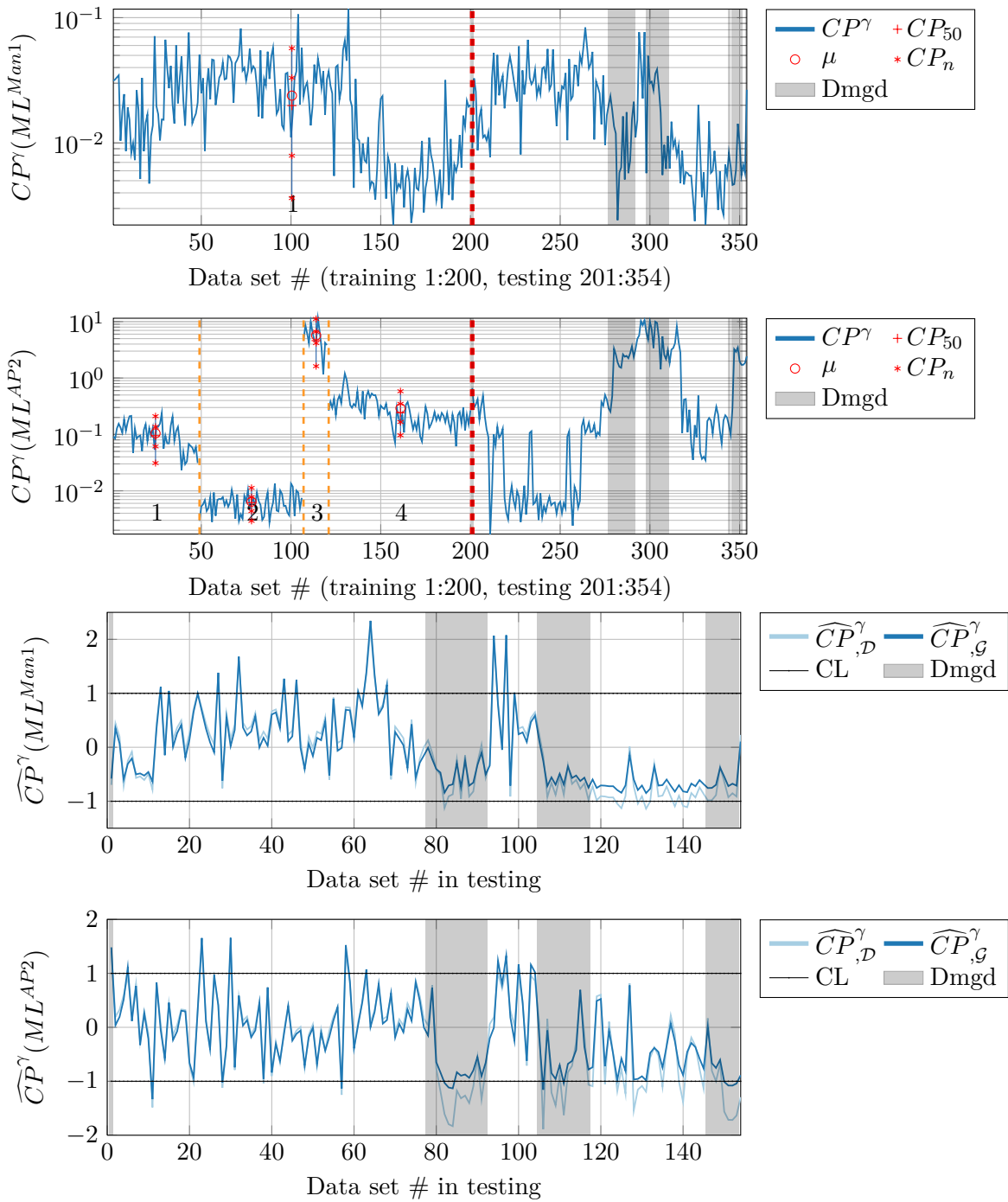
Figure 4.11: Condition parameter trends and control charts for CP^γ. Upper two plots show the absolute parameter trends, the lower two plots the control charts for "Manual1" and "AP2", respectively. For control charts, hypothesis testing through a discrete distribution (subscript $\mathcal{D}$) and a Gaussian distribution (subscript $\mathcal{G}$) is analyzed. UCL and LCL located at ± 1 for $\alpha = 0.22$.

one of these three classifications is suited best. Performance decreases for ML^{AP_4}: the ROC curve lies closer to the diagonal again. Most of the ROCs range slightly above the 3:1 performance line, only ML^{Man_1} reaches a 10:1 performance in the lower detection rate range.

The range for different ROC curves for CP^{R^2} is much larger than for $CP^{\mathcal{M}}$ (see lower plot in Figure 4.12). Hence, the dependency of this CP to ML is stronger and ML gains importance. Accordingly, if this parameter is included, EOCs and ML play an important role. Being least favorable, ML^{Man_1} and ML^{Man_2} lie on and below the diagonal respectively. Again, the Gaussian normal distribution leads to better performance than the discrete counterpart from percentiles for all ML types. The best values for CP^{R^2} lie around the 10:1 performance lines with a detection rate of 80% and only <8% false alarms for $CP_{\mathcal{G}}^{R^2}(ML^{AP_2})$ and $CP_{\mathcal{G}}^{R^2}(ML^{AP_3})$. ML^{AP_2} and ML^{AP_3} result in similar ROC curves with slight advantages for ML^{AP_2}.

Another important aspect which can be investigated by ROCs is the influence of the confidence interval. Since its width is defined by $1 - \alpha$, a small α corresponds to a wide interval. For $CP^{\mathcal{M}}$ points for different α values along the ROCs are distributed equally. Optima, denoted by red circles in the Figure 4.12 (upper plot for $CP^{\mathcal{M}}$), can be found for $\alpha = 1.5\%$ for a discrete distribution and $\alpha = 12\%$ for a normal distribution. For CP^{R^2}, points on the ROC curves start of with higher detection rates even for small α values. Optimal α values lie at 0.2, 0.9, and 4.0%, respectively (red circles in lower plot of Figure 4.12). This indicates a better separation of CP distributions between healthy and damaged states since a wider confidence interval can be chosen. This goes along with the results from ROCs in Figure 3.28 for the benchmark example.

Hybrid Condition Parameter using MSD As mentioned earlier, different condition parameters can be combined to form a hybrid parameter. To do so, the CPs values for a single data instance are stacked into a vector. If necessary, multi-dimensional CPs must be vectorized and/or reduced previously. The resulting vector is then analyzed by Mahalanobis square distances between a new data instance and the references of the cluster. The distance measure is then taken as new CP for evaluation. In the given example, the four relative CPs based on VAR and SSI residues CP^{R^2}, $CP^{\mathcal{M}}$, CP^{γ}, and CP^{ε} are combined. Figure 4.13 shows the ROC curves for the new, hybrid CP^{MSD}. In comparison to Figure 4.12 performance is increased, visible through a shift of most ROC curves to the left. Also, only very few points lie below the diagonal and more lie above the 3:1 performance line for CP^{MSD}. Maximum detection rates increase to about 90% for ML^{AP_2}. FP rates are slightly higher compared to the best ROCs from CP^{R^2}. It should be noted that an optimum is reached for the minimum α investigated (the widest confidence interval with $\alpha = 0.1\%$) and that, for smaller α-values, performance might increase due to smaller FP rates.

4.4.3 Final Comparison

Due to the usage of areas under receiver operating characteristics curves (AUCs) in the SHM framework, a normalized comparison between all different realizations, namely ML-CP-HT combinations, is possible. To do so, Table 4.6 holds the AUCs for all the investigated combinations. One CP is given per row. The first six columns hold results for discrete distributions used for
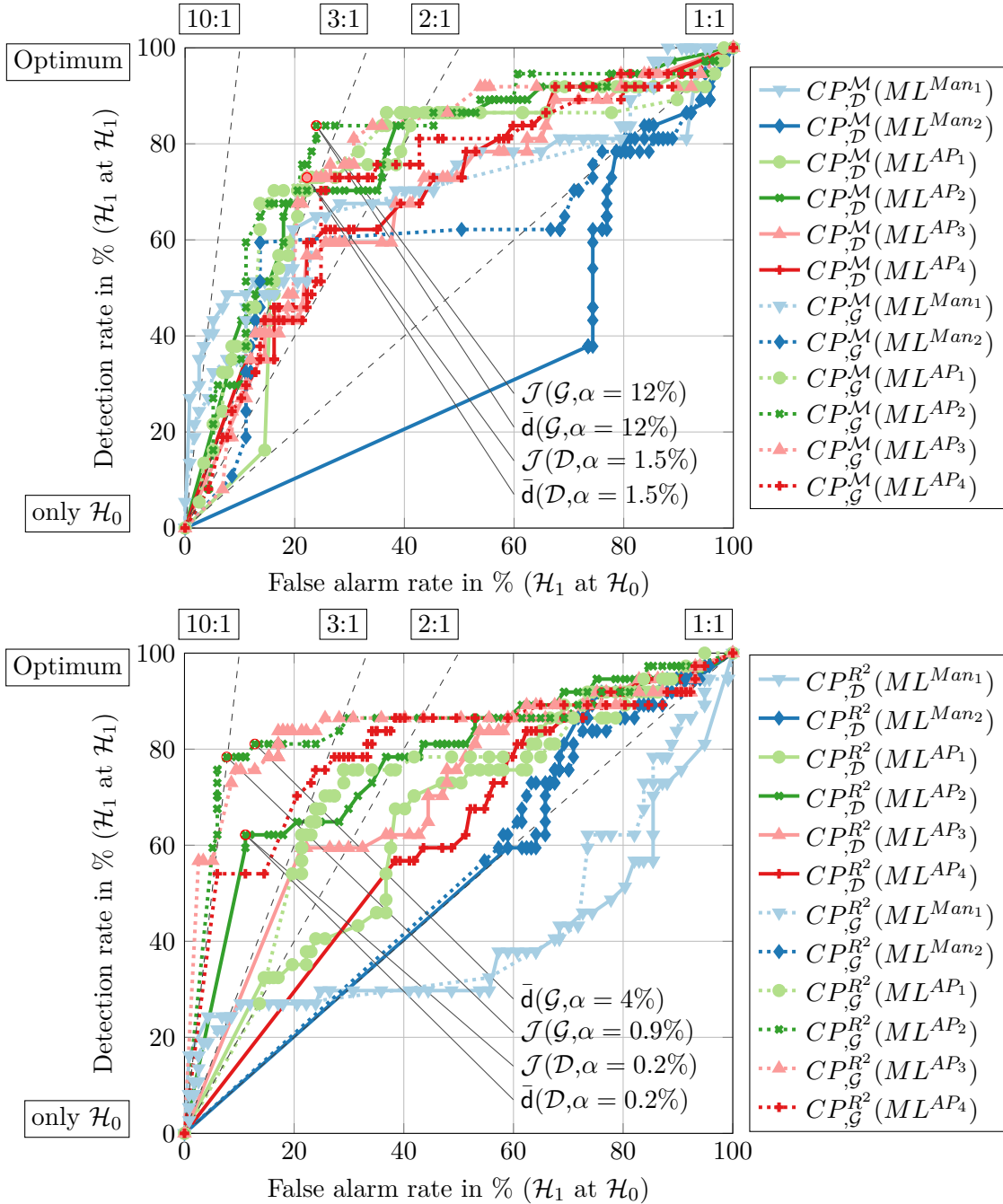
Figure 4.12: ROCs for CP^{R^2} (lower plot) and $CP^{\mathcal{M}}$ (upper plot). Classifications are indicated by different colors, an underlying Gaussian distribution is indicated by dotted, a discrete by solid lines. Optimal values with respect to the Youden-index and minimal distance to the optimum are marked as well ($\mathcal{J}$ and $\bar{\mathsf{d}}$).
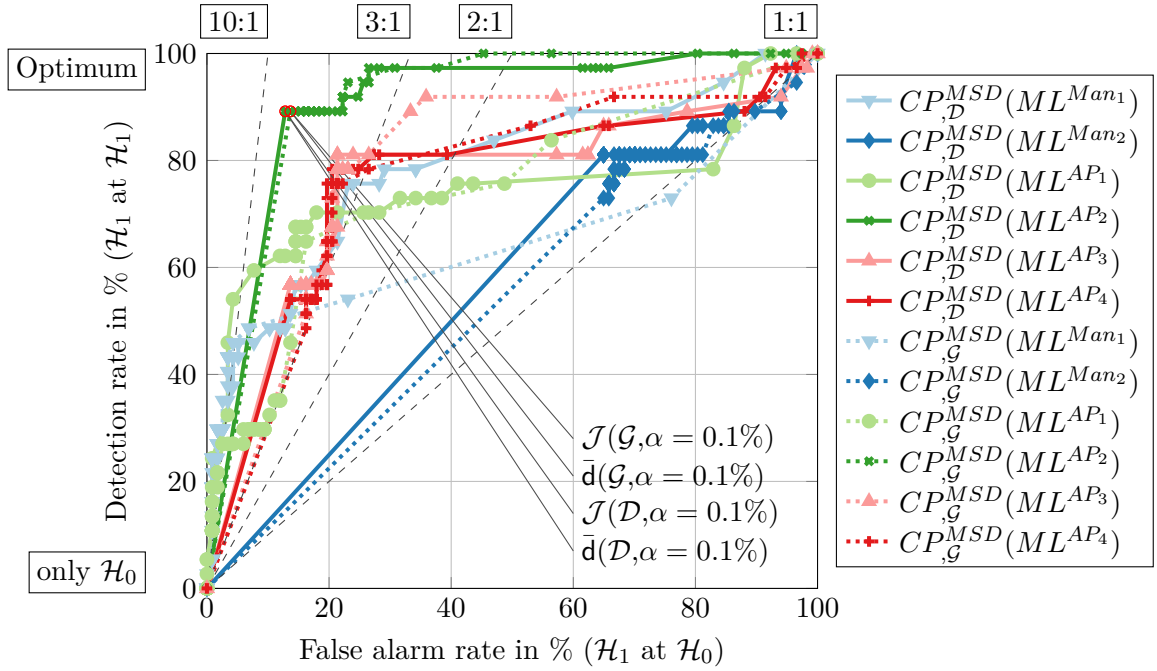
Figure 4.13: ROCs for CP^{MSD}. Classifications are indicated by different colors, an underlying Gaussian distribution is indicated by dotted, a discrete by solid lines. Optimal values with respect to the Youden index and minimal distance to the optimum are marked as well ($\mathcal{J}$ and $\bar{\mathsf{d}}$).

confidence intervals ($\mathcal{D}$), the columns 7 to 12 hold the AUCs for the assumption of a normal distribution ($\mathcal{G}$). The best AUCs per row are in bold, values above 0.7 are underlined, values above 0.9 set in boxes. In the last four columns, the optimal point $\bar{\mathsf{d}}$, its corresponding α-value, the Jouden-index $\mathcal{J}$, and its corresponding α-value are given respectively. Detection rates above 80% and FP rates below 10% are indicated with bold numbers.

Overall, optimal values for the CPs are located between column 7 to 12 for AUCs based on normal distributions. Only for CP^{γ}, the best performance is achieved under a discrete distribution assumption (column four, line four from bottom). Based on the extracted AUCs, the accumulated energy as CP can compete with the relative CPs for the analyzed example. ML^{AP_2} works best for relative CPs from SSI and VAR while ML^{AP_2} and ML^{AP_3} tend to work better for $CP_{i,9}^{E_{yy}}$ also, VAR-based parameters tend to work better than SSI-based residues in this case. The highest performance rates are indicated by channels 1 to 3 and 10 for $CP_{i,9}^{E_{yy}}$, giving the ability of damage localization applied between sensor node 1 and 2 (channels 1, 2 and 3, 4). Values for the cross-correlated accumulated energy CPs also have high AUCs for the first four channels (see Table 4.6). ML^{AP_1} results in the best performances. ML^{Man_1} is the least favorable ML setting, it provides no damage detection ability. This is in agreement with a core idea of this thesis: That a classification by EOCs aids performance or is even necessary to ensure damage detection. EOC correlation to absolute CPs, as accumulated energies or modal frequencies, can be used to choose optimal EOCs for classification as demonstrated in the next Chapter.

The Youden index $\mathcal{J}$ and optimal values $\bar{\mathsf{d}}$ result in quite high alpha values, indicating a difficult separation between healthy and damaged states. High detection rates for $\bar{\mathsf{d}}$ and $\mathcal{J}$ always go along

with fairly high false alarm rates (20-30%, 1st number in 4th-last and 2nd-last column). Both indicators for optimal operation point result in very similar α-values. As already mentioned, not every CP will work for all damage scenarios, especially given the difficult boundary conditions in this example. This underlines the strength of a multi-CP-based SHM framework, where some parameters indicate damage while others will not.

4.4.4 Variation of Training Instances

So far, the results displayed are based on a single realization of randomly selected training (and implicitly testing) data instances. To gain an insight into the dependency of performance on the selection and number of training data instances, these two parameters are varied for the best performing ML-type ML^{AP_2}. To do so, five different numbers of training sets, from 100 to 300 in steps of 50, are analyzed in Figure 4.14. If possible, due to the number of available training sets, 25 random selections for training and testing sets are realized each. Otherwise, some random selections are taken several times. It should be noted that the importance of damage detection, in contrast to the identification of healthy sets, increases with the number of training sets since only a limited number of sets for both types is available and only healthy sets can be chosen for training.

Hence, if more healthy sets are used in the training phase, less healthy sets remain for testing. Accordingly, the percentage of damaged sets increases in the testing phase, which in turn puts more weight on damage detection but also penalizes single FP alarms with a high percentage. With only ten healthy sets in the testing phase, each FP weights 10%, with a single set 100%. If only damaged states existed in testing, FP rates would always be zero and the AUC is purely dependent on the detection rate since all supporting points of ROC curves lie on the y-axis.

The different performances are evaluated in terms of AUC values from ROC curves. The 25 results for each training set size are displayed in box-plots in Figure 4.14. Values from 0.5 to 1 are displayed for all CPs, to guarantee similar scaling. Lower values are not of interest for monitoring purposes. The median is indicated by a red bar, 25 and 75% percentiles by the blue box, 5 and 95% percentiles by the whiskers, and outliers by red crosses.

CP^{ε} has a large scatter for each training set group size, indicating a strong dependency on the selection (see 4.14(a)). The parameter has a relatively constant performance for differing numbers of training sets, values lie around 0.7. In 4.14(b), CP^{γ} shows a strong dependency on the number of sets and has a large scatter for different selections. Performances are rather low for the given example with values below 0.8.

CP^{R^2} has a larger scatter for smaller group size during training (see 4.14(c)). For 250 and 300 training instances, the variation is reduced. This results from the fact that a number of 317 healthy sets are available for training, and accordingly the majority of utilized sets for the 25 random selections is similar if many sets are used for training. The parameter has a relatively constant performance for differing numbers of training sets. And even the highest median for only 100 sets in training. Values lie around 0.7, for 100 and 200 training sets the 75% percentile exceeds 0.8.

$CP^{\mathcal{M}}$ has the smallest scatter over different selections with an increase in performance for an increasing number of training sets, values range around 0.8.

Both $CP^{E_{yy}}_{(1,9)}$ and $CP^{E_{yy}}_{(2,10)}$ have a slight increase in performance if more training sets are used. In both cases the scatter remains constant with an increase in training sets. $CP^{E_{yy}}_{(2,10)}$ performs slightly better given the presented database. Overall, $CP^{E_{yy}}$ and $CP^{\mathcal{M}}$ have the best performance and the lowest dependency on the number and selection of training sets. CP^{MSD} in Figure 4.14(g) shows very good performance, reaching high values with 100 training sets already. An improvement is visible, with an increasing number of training sets up to 200. For 250 and 300 training sets, performance drops back to 0.8 most probably being influenced by the decreasing performance of both SSI-based residues.

4.5 Conclusions

The chapter presents the evaluation of a newly collected database from a small scale wind turbine, located at the Los Alamos National Laboratories, NM, USA. The structure allowed for an introduction of a small, reversible damage while displaying complex dynamic behaviour influenced by environmental and operational conditions. Newly developed wireless sensor nodes, namely the *Martlet* node, were utilized to collect bi-axial acceleration data at six levels. Damage was introduced by replacing a bolt through a spring at the bottom of the structure. The example was chosen to validate the extraction of modal parameter and damage identification under difficult circumstances. Hence, the results cannot be understood as a second proof of framework with perfect performance, e.g. AUCs of 1.

To begin with, data was analyzed by spectrograms. The extraction of modal parameters followed in a second step. Here the introduced TEMP procedure was successfully applied to the complete database in an automated manner. Even data instances with insufficient amplification of measured signals during low wind excitation can be used to identify the first two bending modes. Modal parameter estimation through TEMP works well with the stated empirical parameters along with a number of shifts for the block Hankel matrix calculated from $n_{shifts} \approx f_s/f_{min}$.

For the evaluation of SHM performance, using the proposed framework, the damage introduced is very small. Due to the dominant southern wind direction during data collection, the tower was excited sideways leaning against the sub-structure with almost no leaning against the bolt and spring. Accordingly, values from SSI and VAR parameters indicate damage but do not change strongly. In addition, EOC collection was limited and only available at a low frequency. The wind turbine, in contrast, follows the wind direction and speed very quickly, changing nacelle direction and rotor speed. Accordingly, wind might have changed direction or there may have been gusts, which are not displayed in the mean values of wind speed by the met tower close by, which would change the dynamic characteristics strongly. For future testing, the measurement of EOCs at higher frequencies is suggested. Especially the rotor speed is critical for harmonic excitation here.

Overall, taking into account the limited EOC availability and data collection through new, wireless nodes (prototypes), performance rates above 0.8 are quite promising, and show that
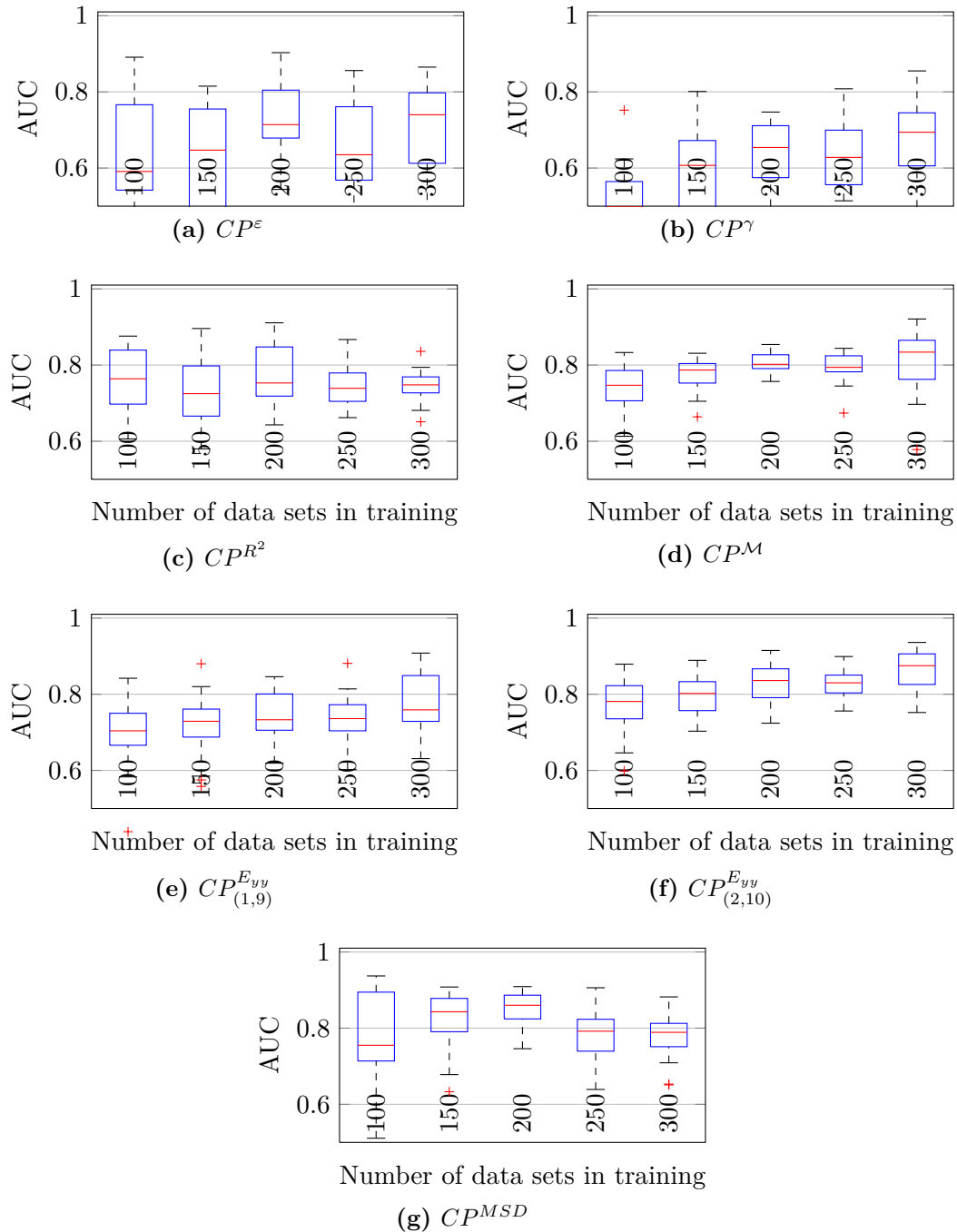
the CPs used are able to detect damage. It was shown that a base-line classification with a single cluster is insufficient for damage detection purposes, independently from CPs and HT. Best performances were achieved under the assumption of a normal distribution. In this more complex example, auto correlated $CP^{E_{yy}}_{(i,9)}$ perform slightly better than $CP^{E_{xy}}_{(i,9)}$. A localization is not as distinct as for the laboratory structure. Relative CP perform equal where CP^{R^2} performs best with respect to AUC values followed by CP^{ε}.

Again, the initial parameters to set give the VAR based parameter an advantage since those are easier to handle. For both, SSI and VAR, the calculation rules for initial parameters proved to work well (see Chapter 3.6). The combination of different CPs to a hybrid CP leads to more robust damage detection results (smaller α for optimum on ROC) and could even improve absolute performance to an AUC of 0.908. From training set variation a number of 200 training sets that should be used in this case results.

Overall, the proposed procedure of SHM-performance evaluation, again, proves to be of great value for the comparison of many different ML-CP-HT-combinations. The introduced performance lines in the ROC plots aid a quick inspection of the diagrams. The knowledge gained about TEMP and ML, CP, and HT settings will subsequently be transferred to the application of modal analysis and monitoring for an industrial size offshore wind turbine within the next chapter.

Table 4.6: Performance overview for LANL wind turbine. Area under curve values from receiver operating characteristic curves for different combinations of ML-CP-HT (columns 2 to 13). One CP is displayed per line. Optimal values, estimated through Youden-index and closest point to optimum are given as well (columns 14 to 17).

	$ML_D^{Man_1}$	$ML_D^{Man_2}$	$ML_D^{AP_1}$	$ML_D^{AP_2}$	$ML_D^{AP_3}$	$ML_D^{AP_4}$	$ML_G^{Man_1}$	$ML_G^{Man_2}$	$ML_G^{AP_1}$	$ML_G^{AP_2}$	$ML_G^{AP_3}$	$ML_G^{AP_4}$	$\bar{d}$	α	$\mathcal{J}$	α
$CP_{1,9}^{Exy}$	0.512	0.564	0.661	0.607	0.629	0.63	0.518	0.648	**0.796**	0.736	0.785	0.735	76/26	0.5	41/16	0.36
$CP_{2,9}^{Exy}$	0.515	0.622	0.73	0.632	0.664	0.666	0.464	0.668	**0.799**	0.741	0.772	0.738	**84**/24	0.5	38/17	0.4
$CP_{3,9}^{Exy}$	0.546	0.543	0.718	0.573	0.633	0.626	0.51	0.667	**0.792**	0.737	0.773	0.718	**81**/23	0.5	41/14	0.36
$CP_{4,9}^{Exy}$	0.543	0.438	0.613	0.441	0.547	0.533	0.447	0.445	**0.742**	0.619	0.729	0.664	**84**/35	0.7	35/22	0.5
$CP_{5,9}^{Exy}$	0.657	0.567	0.687	0.597	0.66	0.651	0.606	0.596	**0.797**	0.696	0.754	0.712	76/24	0.5	46/17	0.38
$CP_{6,9}^{Exy}$	0.583	0.498	0.606	0.498	0.592	0.604	0.501	0.493	0.701	0.645	**0.708**	0.668	76/34	0.7	49/30	0.6
$CP_{7,9}^{Exy}$	0.59	0.529	0.687	0.53	0.654	0.644	0.587	0.564	0.774	0.603	**0.779**	0.725	76/24	0.6	51/24	0.5
$CP_{8,9}^{Exy}$	0.587	0.556	0.72	0.569	0.667	0.661	0.557	0.539	**0.793**	0.631	0.78	0.739	**81**/27	0.6	51/26	0.5
$CP_{9,9}^{Exy}$	0.624	0.618	0.72	0.639	0.728	0.713	0.595	0.592	**0.788**	0.68	0.764	0.734	**84**/27	0.6	59/29	0.5
$CP_{10,9}^{Exy}$	0.637	0.667	0.737	0.649	0.752	0.756	0.627	0.681	0.817	0.742	**0.828**	0.799	**95**/30	0.7	59/21	0.4
$CP_{11,9}^{Exy}$	0.558	0.493	0.695	0.458	0.561	0.559	0.513	0.497	**0.765**	0.627	0.713	0.67	78/29	0.6	27/11	0.34
$CP_{12,9}^{Exy}$	0.618	0.522	0.652	0.551	0.606	0.613	0.558	0.616	0.731	0.7	**0.745**	0.712	**81**/33	0.6	65/34	0.6
CP^{f_1}	0.621	0.107	0.623	0.112	0.329	0.435	0.621	0.508	0.624	0.532	**0.644**	0.61	92/65	0.01	100/67	0.06
CP^{f_2}	0.679	0.126	0.679	0.15	0.361	0.446	0.675	0.697	0.675	0.697	**0.738**	0.686	100/52	0.01	100/52	0.01
CP^{ε}	0.372	0.742	0.575	0.745	0.655	0.654	0.469	0.771	0.513	**0.805**	0.781	0.668	76/14	0.5	8/4	0.7
CP^{γ}	0.448	0.164	0.336	**0.744**	0.613	0.645	0.522	0.099	0.346	0.694	0.576	0.617	76/25	0.22	89/93	0.9
$CP^{\mathcal{M}}$	0.711	0.355	0.731	0.77	0.677	0.694	0.697	0.607	0.768	**0.791**	0.753	0.716	**84**/24	0.38	65/24	0.32
CP^{R^2}	0.404	0.527	0.64	0.766	0.694	0.609	0.428	0.661	0.685	**0.851**	0.843	0.793	**81**/13	0.22	27/10	0.24
CP^{MSD}	0.788	0.569	0.747	0.903	0.755	0.759	0.65	0.537	0.746	0.908	0.798	0.76	**89**/14	0.001	81/68	0.11

Figure 4.14: Area under curve (AUC) values for investigated CPs for varying number of training sets. Seven CPs tested with selected, optimal parameter settings for different numbers of training data (100:50:300), 25 random selections were evaluated per set up. CP^{MSD} is based on CP^{R^2}, $CP^{\mathcal{M}}$, CP^{γ}, and CP^{ε}.

5 Monitoring the Adwen AD5-116

Having discussed a validation of the SHM framework and investigated an application on a small wind turbine with artificial damage, this chapter will complete the analysis with the investigation of an industrial-scale offshore wind turbine. An introduction of the structure and the test field it is located in, is followed by discussion of the system dynamics under changing environmental and operational conditions. The question of a proper classification of the different states for modal parameter prediction will then extend to an application of the proposed SHM framework.

5.1 Structure, Environment, and Data

In general, wind turbines have a rather slender and flexible structure with a high head mass in the nacelle and blades while the boundary conditions depend strongly on the foundation type. Large uncertainties in soil parameters, especially under drained conditions, and the aerodynamic behavior of the rotor still complicate numerical modeling, in particular for dynamic proposes which are addressed in monitoring tasks. Onshore, most turbines are based on lattice towers or monopiles on concrete foundations with ground anchors. Some older turbines with smaller nacelle heights are based on guyed towers. For offshore turbines, a variety of support structures exist, as displayed in Figure 5.1. While gravity foundations and monopiles are used for near-shore parks with smaller water depth, jacket foundations are used for deeper seas as well as tripod and tri-pile solutions. Jackets and tripods must be considered as especially stiff foundation types. Floating structures, such as tension leg platforms (TLPs), provide solutions for large water depth. Each support structure type comprises its own characteristics and damage scenarios. Accordingly, local monitoring tasks will strongly depend on the investigated structure while global approaches can possibly be applied to all foundation types.

For SHM purposes, three main types of possible damage sources are of particular interest. Grouted joints, serving as connections to the driven piles for offshore structures, were adapted from the oil and gas industry. Monopiles and tripiles are connected to the tower above sea level while jackets and tripods use grouted joints to connect the piles to the support structure right above the sea bed. Since the loading behavior differs strongly from large oil and gas platforms, long term behavior of these connections is of high interest. Further, welded connections occur at many different locations at on- and offshore structures. Due to many welded nodes, jacket structures play a particularly outstanding role here. Welding seams are considered to be potential starting points for cracks; fatigue could also be a problem here. Depending on the specific design, so called hot spots within the structure with maximal strain amplitudes form areas of special interest, where damage could have potentially more severe consequences. Each steel tower typically
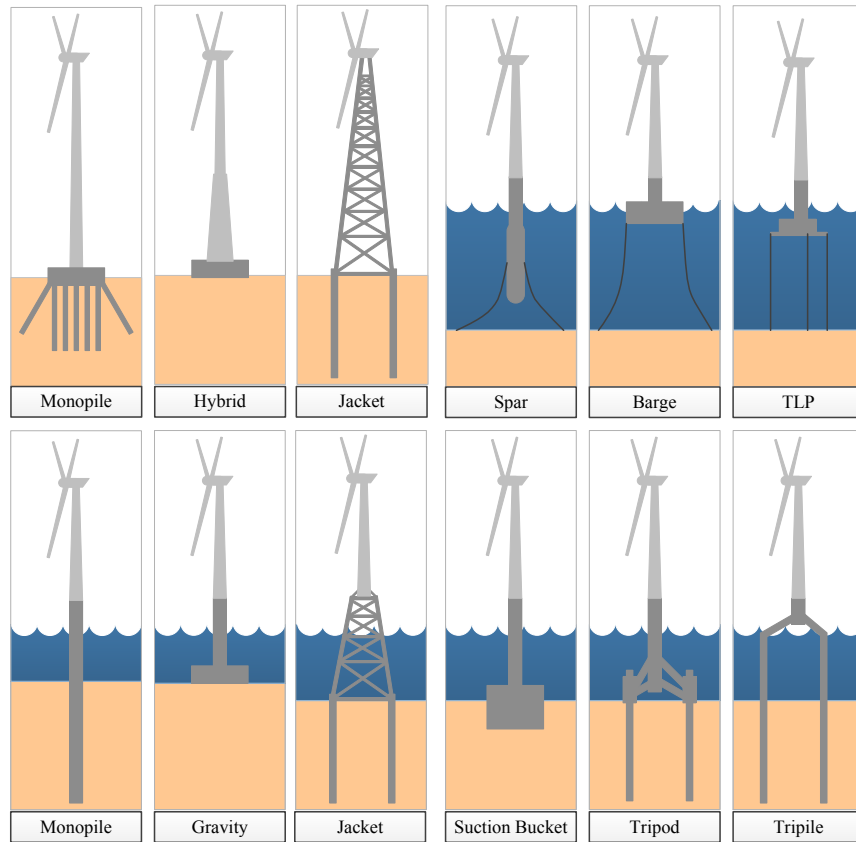
Figure 5.1: Typical supports structures for on- and offshore wind turbines. Support structures for onshore installation and floating solutions for deep sea installation in the upper row, structures for shallow and moderate water depth in the lower row.

consists of multiple sections, connected with a large number of bolts. Concrete towers, so far built only onshore, also consist of different sections of precast or in-situ concrete. These connections must be considered as critical points and are of high interest for monitoring approaches.

5.1.1 Adwen AD5-116 in *alpha ventus*

The test field *alpha ventus* was installed with a strong focus on research, represented by the RAVE (research at alpha ventus) initiative. During this pilot project, twelve offshore wind turbines were installed far away from the coast to test feasibility of design, logistics, installation and operation. The plants are located in the German Bight at the position [54°00′ N, 6°35′ E], about 45 km north of the Island Borkum (see lower left in Figure 5.2). Twelve turbines are installed, each with a rated output of 5 MW, among the largest wind energy converters classes on the market so far. Two different types of turbines and foundations – six REpower 5M turbines on jacket foundations and six Adwen AD5-116 turbines on so called tripods – form a rectangle of 3 by 4 plants (see upper left in Figure 5.2). The turbines were erected between 2009 and 2010 in about 30 m water

depth, exploring a completely new field for constructors and logistics. Energy production of all twelve converters was reported in April 2010. Two turbines, one of each type, were intensively equipped with over 1200 sensors, covering acceleration, inclination, and strain along with the measurement of operational conditions. Conventional sensor types are installed in addition with up-to-date approaches as optical sensors and prototypes to measure grout displacements. In mid 2010 the 1200 sensors started collecting data which is stored into an on-line database. In addition, the research platform FINO1, located close to *alpha ventus*, with a height of 105 m above lowest astronomical tide (LAT) collects environmental conditions, e.g. wind and temperature sensors installed on a lattice tower.

The studies presented focus on the tripod-based turbines in *alpha ventus*, more precisely on the Adwen AD5-116 plant *AV*07 (hereafter *AV*07). The right sub-plot in Figure 5.2 provides an overview of the structure with selected sensor positions. The hub height is 118 m (90 m above LAT), the 710 t heavy tripod spans 45 m from the sea bed, the nacelle and three-bladed rotor have a total weight of 349 tons. Along with the different tower parts, a weight of more than 1500 tons rests on the three piles. All forces are transmitted through the grouted joints. These connections between piles and pile sleeves at sea bed level are realized through injected high performance concrete. The diameter of the main column is 6 m with a wall thickness of only a few centimeters. At the indicated sensor locations (Level1 to Level6), two biaxial acceleration sensors are mounted at the same level on the northern and southern side of the tower (see Figure 5.2). The different sensor levels are at 26, 61.1, 71.2, 82.25, 96.5 and 110 m above the seabed. Accordingly, 24 channels at six different levels are present for data processing. Each data instance holds the structure's responses over ten minutes. With a given sampling rate of 50 Hz, 30.000 data points per channel and set result over the period of 10 min. In addition, wind speed, relative wind to nacelle direction, rotor speed, nacelle position, air temperature, air pressure, wind turbulence intensity, wave heights, and wave period as key EOCs are present for each data instance through ten minute mean values. These data instances will form the basis for the performed classification, system identification, and extraction of modal parameters and estimation of condition parameters in this chapter. The data structure is realized in the same way as the LANL WT example. In total, data over a period of 17 months was used here, resulting in 19,135 valid ten minute data instances[1].

5.1.2 Loading from Operation and Environment

WTs face highly complex loading scenarios in a harsh environment and, by definition, a WT is supposed to collect forces, rather than avoid them. In most cases, excitation frequencies up to 10 Hz are relevant for tower, nacelle and blades while for the electrical components, gear, and generator higher frequencies must be considered in condition monitoring (see 1.2). Gasch and Twele [68] define four major groups of excitation:

---

1   It should be noted that due to construction and maintenance data instances are missing. Further, data instances were not used when one key EOC, from the plant or FINO1, was missing, or acceleration data was erroneous.
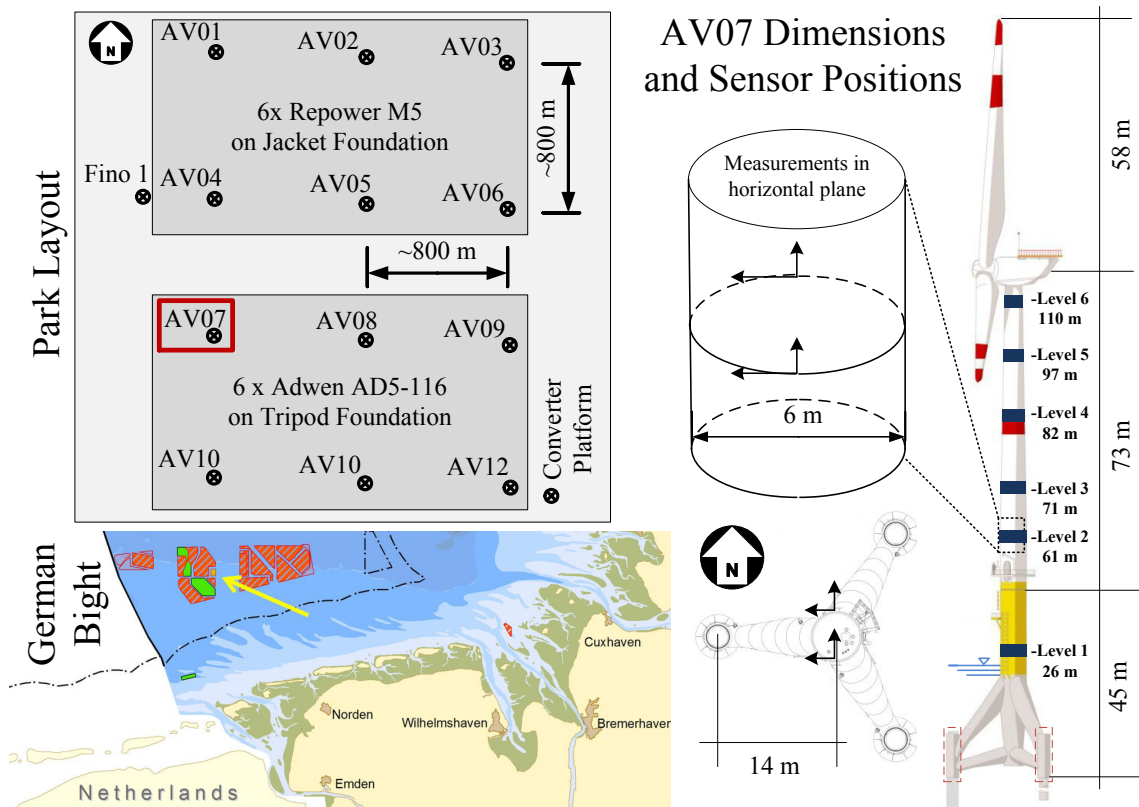
Figure 5.2: Location of test field *alpha ventus* (lower left) and park layout (upper left). Tripod structure with indicated sensor locations, measurement directions for each level and footprint of tripod (right plot). Grouted joints between piles and sleeves are marked with dashed red rectangles.

- Stationary forces from gravity, centrifugal forces, mean thrust, and wind.

- Periodic forces from mass imbalance, aerodynamic forces (wind profile, gusts), tower dam, sloped incoming flow, blade-tower passages.

- Stochastic forces from aerodynamic and hydrodynamic forces, and earthquakes.

- Transient forces from friction, braking, and earthquakes.

From the above mentioned excitation groups, periodic excitation from rotor blades plays an significant role for SHM. The revolving frequency is dubbed '1P', its nth higher harmonic 'nP'. 1P excitation mainly results from imbalances while 3P excitation results from the tower-blade passage and gusts. While imbalances can be influenced and reduced, the rotor harmonics will have to be dealt with. Higher harmonics of the base excitation frequencies, e.g. 1P and 3P, are therefore problematic as structural modes located at these frequencies can also be easily excited by these base frequencies. This happens not with each oscillation of the mode but with every n^{th} oscillation, where one blade passes the tower, it introduces new energy to the mode.

During the design process, the rated wind- and rotor speed are defined and excitation frequencies are known. For the AV07, the cut-in wind speed lies at about 3 m/s in 10 min average where

the turbine starts with 5 revolutions per minute (RPM) and reaches the rated rotor speed of 15 RPM at 10 m/s wind speed (see e.g. Figure 5.7 top, where 10 min mean values of wind speed are plotted over the rotor speed.). From that point on, the rotor speed is kept constant up to a wind speed of 25 m/s through pitch-angle variation of the blades. Accordingly, 15 RPM $= 15/60 \: [1/s] = 0.25 \: [Hz] = 1P$ and $3P, 6P,..., nP$ lie at $0.75, 1.5,..., n * 0.25$ Hz, respectively. Guidelines and codes usually call for structural modes not to be close to rotor excitation, e.g. $\pm 5\%$ around the 1 and $3P$-frequencies (see [70]). It will be seen subsequently that higher harmonics also play an important role in the operation of an (O)WT.

In addition to the rotor speed as a major operational effect, different environmental quantities influence the behavior of OWTs. Table 5.1 holds value ranges for selected EOCs measured at the $AV07$ site.

Table 5.1: Selected EOCs and their boundaries for $AV07$[1].

|	Rotor spd	Nacelle pos	Wind dir	Wind spd	Turbulence intensity	Temp.	Pressure	Wave freq	Wave H_s
	rot/min	Deg./°	Deg./°	m/s	-	°C	hPa	Hz	m
Min	0	0	0	0.196	0.0108	-4.04	841.6	0.03	0.02
Max	15	60	167.1	25.5	1.1	28.1	1039	0.59	7.25

Further, distribution for wind speed, wind direction, wave frequency and turbulence intensity are given in Figure 5.3. For the wind speed occurrence (Figure 5.3(a), top left), a Weibull distribution is fitted to the measured data. Clearly a mean wind speed around 8 m/s is visible. Main wind direction for the test field is South-West to South (Figure 5.3(a), top right). Here, maximum wind speeds above 20 m/s result from a long fetch over the English Channel. Wind from North also results in a small portion of strong wind since the German Bight is open to the North and allows the wind to build up over long distances. Most of the moderate wind up to 10 m/s occurs from South-Eastern directions, blowing from the mainland towards *alpha ventus*.

The turbulence intensity (I), defined as standard deviation of wind speed divided by the mean, both over 10 min, is an important factor for numerical simulations and turbine design. Figure 5.3b (left) displays measured turbulence intensities in a Box-plot along with different recommendations from codes. Here, the assumption of a constant value of 0.12, made by the Germanischer Lloyd (P.111 in [70]), does not capture peak values of I for wind speeds below 15 m/s (red crosses for outliers in Box-plot). In the IEC 61400-1 [90], I is defined with repect to a reference intensity I_{ref}. The given examples correspond to "higher" and "lower" turbulence characteristics. The values calculated for $I_{ref} = 0.12$ lie in good agreement with the 95%-percentiles of $AV07$ and thus build a good upper limit estimation.

---

1 It should be noted that for classification nacelle positions between 0 and 360° are not suitable since 0 and 360 define the same point. Consequently, the nacelle position is projected to a range of 0 to 60° exploiting symmetry. 0° equals a nacelle tip position above one tripod leg, 60° exactly between two tripod legs. Further, the wind direction is measured in relation to the nacelle position and can take on values from -180 to 180°. Here, only the absolute value is used.
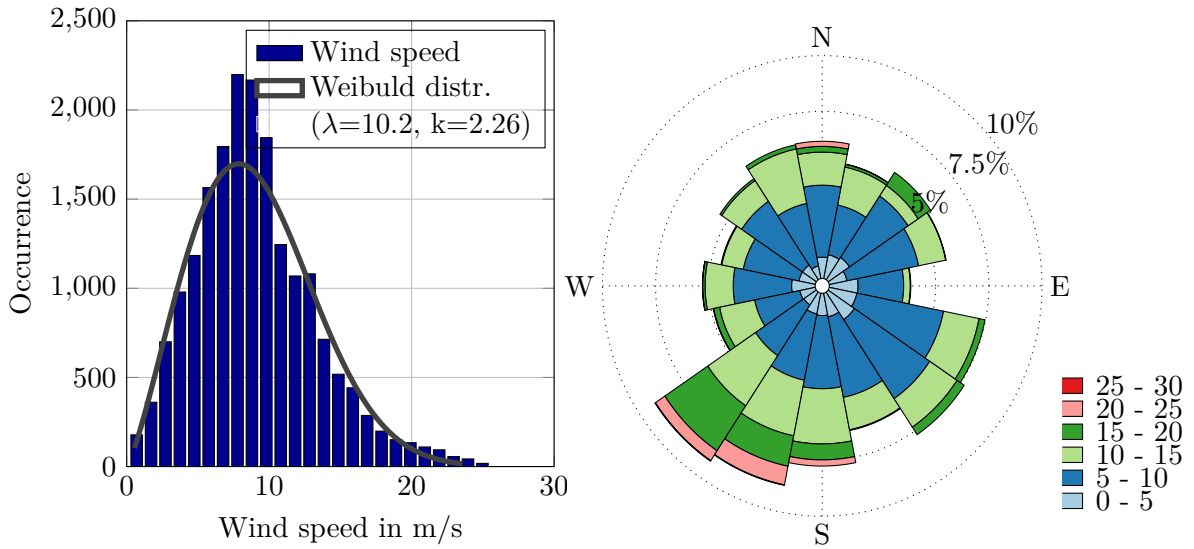
(a) Wind speed occurrence at *AV*07 site for 10 min mean values. Left: Occurrence with fitted Weibull-distribution, bin width 1 m/s and wind rose with wind speed intensities per section (right). Values in m/s, each section has a width of 22.5°.
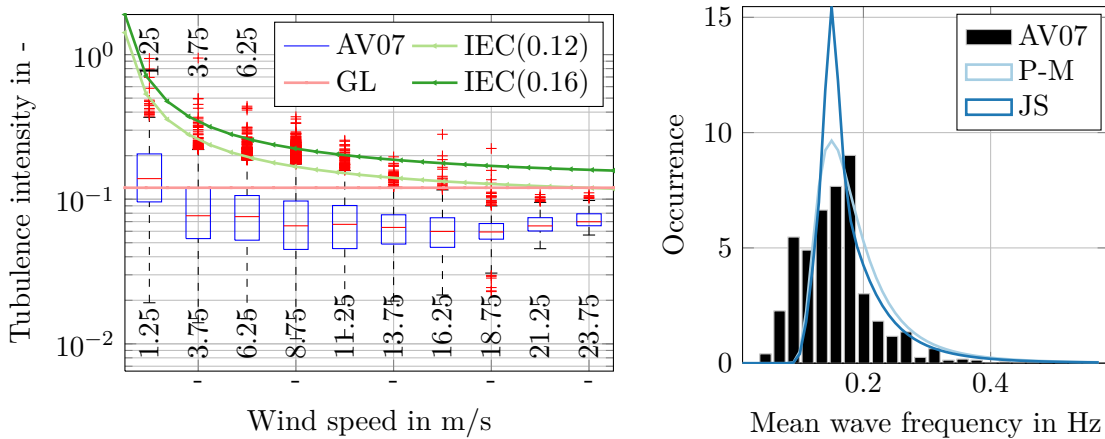
(b) Turbulence intensity over mean wind speed in comparison to different assumptions taken from the IEC 61400-1 and GL offshore guidelines (left). IEC(0.12) and IEC(0.16) indicate the values set for I_{ref}, center values for bins on the x-axis. Mean wave frequencies with a bin width of 0.02 Hz and comparison to a Pierson-Moskowitz (PM) and JONSWAP (JS) spectrum (right, $\gamma_{JS} = 2$).

Figure 5.3: Wind speed, -direction, turbulence intensity and wave frequency at *AV*07 site.

Finally, wave characteristics and tidal levels are considered to be able to interfere with the dynamics of offshore wind turbines. In *alpha ventus*, tidal levels underlie only a minor change with less than 1 m and hence do not influence the dynamics through e.g. added water mass. A distribution of mean wave frequencies is given in Figure 5.3b (right). Density functions for both, Pierson-Moskowitz (P-M) and JONSWAP (JS), are fitted as well. P-M gives a better fit here. It must be noted that these values always represent average values over time and, more importantly, over a three dimensional wave pattern. Therefore the wave frequency derived from mean periods must not be interpreted as strictly harmonic excitation as present from the rotor. Nevertheless, the measurements are in agreement with theoretical references such as in [87]. Here, a wide wave

spectrum is provided, ranging from astronomical tides with frequencies of 10^{-5} to 10^{-4} Hz over seiches, tsunamis, infra-gravity waves to wind generated waves between 10^{-1} to 10^{-0} Hz. Here, the "wind sea" has maximum energy at about 0.25 Hz. For the specific case at $AV07$ and the analyzed database, most data instances have a wave frequency below 0.2 Hz, well below the first modal frequency at 0.33 Hz.

The different stochastic, transient, and harmonic forces pose a challenge for operational modal analysis since the white noise assumption for system excitation is violated. Rotor harmonics play the main role here, wave excitation participates less, since the forces are acting at fairly low levels, especially for tripods where the lower part of the structure is very stiff. Temperature fluctuations on the sea are less distinct than for onshore WT with a continental climate. Still, a range of 30 °C is monitored and could alter material properties. The following section will investigate principal, global modes of the OWT. The identification of modes is followed by an investigation of EOC influence's on the structures dynamics.

5.2 Modal Analysis and Structural Dynamics

Automated modal analysis for all 19,135 10 min data instances as a core point of interest to gain knowledge of the system behavior is performed through the combination of SSI-Data and TEMP. For SSI-Data, 80 block shifts are used to derive model orders from 100 to 300 as initial input to TEMP. Further, criteria for TEMP are listed in Table 5.2[1]. For solutions from a single

Table 5.2: TEMP parameter for system identification at $AV07$[1].

n_{shifts}	N_{order}	ϕ_{crit}	f_{crit}	ζ_{crit}	MAC_{crit}	$\hat{P}_{crit}$
80	$100:2:300$	$32.5°$	3%	50%	0.95	50

data instance, TEMP takes about 4 seconds to run. It is advisable to store raw SSI results, to be capable of running TEMP with different settings subsequently without recalculating these results since this step takes the majority of time. A discussion of the TEMP process and mean distributions for triangle object attributes are presented in [77]. The following subsection will introduce the principal modes of the analyzed support structure, followed by an analysis of variations in dynamics, leading to the application of the SHM framework in section 5.3.

---

1 Again, the number of shifts results from the estimated lowest mode at 0.3 Hz which has a period of 3 s and hence 166 samples at $f_s = 50$ Hz. To cover 70% of the samples 117 shifts are necessary. Since the number of shifts is a major factor for computational costs and many data instances had to be analyzed, the feasibility of a smaller number was tested and 80 was chosen for n_{shifts}. Due to the 24 channels, a state space model order of 48 results. This order should be well overestimated with chosen orders of 100 to 300. Values for MPD, frequency, damping, and MAC are again empirical values recommended for large-scale structures. An overview for TEMP settings for all investigated structures is given in Table 6.1. It is suggested to test the TEMP performance on a small number of data instances before being applied to the whole data base.

5.2.1 Principal Modes in Standstill

An overview of the TEMP results for the complete database is presented in Figure 5.4. The middle plot on the bottom contains solutions from TEMP by rotor speed over frequency. Left and above, occurrences are given for solutions over rotor speed and frequency, respectively. In analogy to a (transposed) Campbell diagram, red lines in the center plot indicate rotor harmonics up to $99P$ in steps of $3P$. A close-up of 0-2 Hz is given in the upper right sub-plot. It can be seen how modal parameters are identified at some of the red lines, especially when close to a global bending mode. This indicates interaction and a transmission of excitation frequencies through the system identification due to colored excitation. Nevertheless, the upper bar plot reveals that distinct peaks result at the location of modal frequencies, which are identified more frequently. The right plot in Figure 5.4 holds solutions from TEMP over data instance numbers. Modal object-paths are indicated by colored lines. It should be noted that due to the large number of solutions ($>10^6$), TEMP was not used to extract the modes throughout the database. Instead, modes are tracked by frequency, damping and MAC within frequency bands. It is important to include the mode shape, since e.g. the two first bending modes, fore-aft (FA) and side-side (SS), lie very close together and the third bending modes in FA- and SS-direction interfere as well.

Mode shapes for selected modes are displayed as side views in the principal coordinate system, defined by rotor-axis and rotor-plane, in Figure 5.5 and 5.6. All modes are extracted under standstill and moderate wind speed. To derive mode shapes in the principal axis, extracted mode shapes had to be rotated by the mean rotor position of 10 min data instances. Another approach could be taken here with a projection (rotation) of the sensor signals for every orthogonal measurement sensor pair. For both approaches, it must be kept in mind that the nacelle position represents a mean value over 10 minutes. Three-dimensional views on the mode shapes, including the indication of the nacelle position are given in Figure C.2. In Figure 5.5 and 5.6, the first three global bending modes in each direction are displayed along with the first two torsional modes. For each mode, FA- and SS-views are displayed. The green and blue lines represent the northern and southern sensor locations, respectively. For global bending modes, these lines are in congruence (cf. 5.5(a) to 5.5(d), 5.6(a), and 5.6(b)). Torsional modes, in contrast, show anti-cyclical patterns between sensors located on a similar level (cf. 5.6(c), and 5.6(d)). It should be noted that for a clean torsional movement, theoretically only the tangential sensor location should indicate amplitudes (x-z-plane in Figure C.2(j) and Figure C.2(k)). In this case, also the orthogonal directions show amplitudes possibly due to bending and/or deformation present in the modes.

For both first bending modes, a clear distinction in FA and SS direction is possible. Although, the FA-1 shows some participation in the SS-direction for the chosen data instance. SS-1 shows almost exclusive movement in the rotor plane after rotation. Both second bending modes (FA-2, SS-2) clearly move in one plane each. The same accounts for FA-3 and SS-3 (Figure 5.6(a) and 5.6(b)) which show a very similar shape. The inclusion of blade movements for an derivation of rotor mode shapes could aid a distinction here. The two torsional modes in 5.6c and 5.6d show a different pattern. Here, sensors located on the same level move in opposing directions,
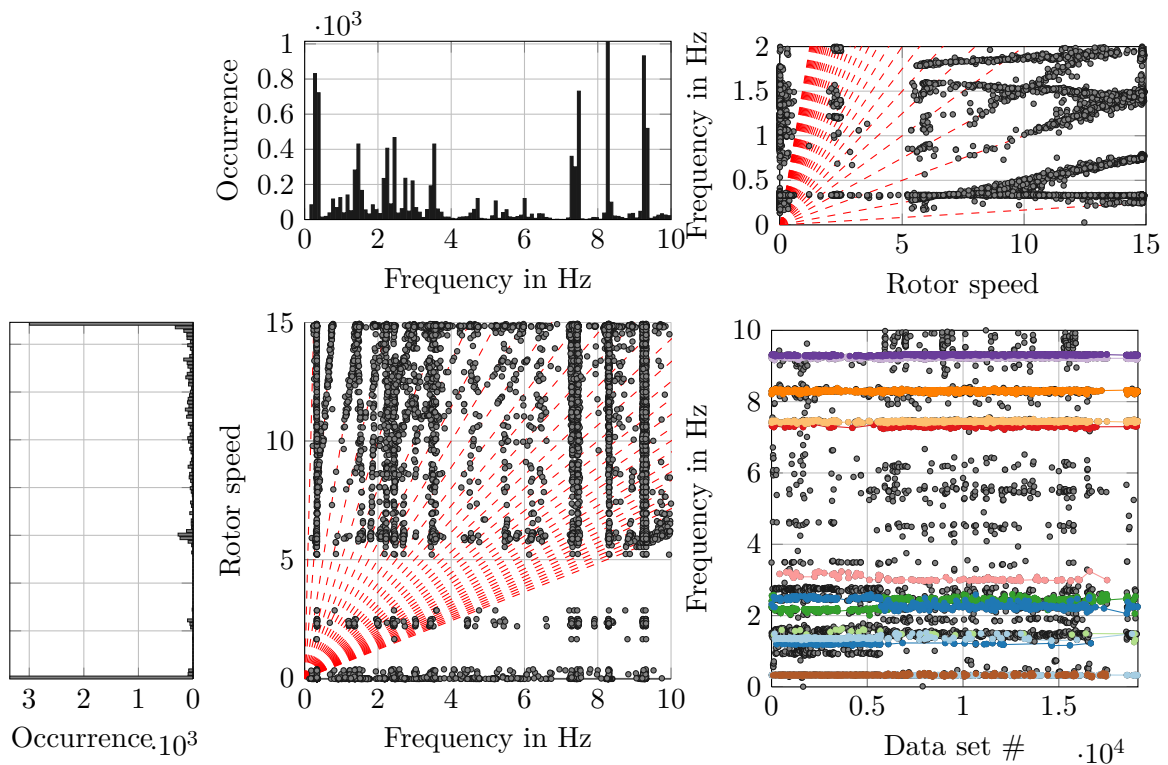
Figure 5.4: Overview of automatically identified modal frequencies for all 19,135 data instances using TEMP method (bottom middle) along with occurrence of frequencies (left) and number of solutions per data instance (middle top). Modal objects over the complete database indicated by different colors (bottom right). The upper right plots provides additionally a standard Campbell-Diagram up to 2 Hz.

indicating the torsional movement of the tower. T-1 shows different patterns in both planes. Mode shapes from each side (green and blue line) show no zero-crossing while for T-2 a single crossing can clearly be seen. It is noted that another mode with torsional tendencies was detected at a lower frequency of 1.19 Hz (T-0, see Figure C.1). FA-2, SS-2, and T-0 with less accuracy than the above mentioned and, for the bending modes, with a possible source in blade modes or interaction. Accordingly modes FA-1, SS-1, FA-3, SS-3, T-1, and T-2 are used subsequently for an analysis in different operational states.

It was observed that the extraction of the SS-1 mode was corrupted by the 3P harmonic, when passing its frequency band during run up. This mode is also more difficult to extract under operation and was less frequently identified by TEMP. Frequencies for identified modes for a data instance in standstill are given in the upper section of Table 5.3. The lower section contains frequency and damping ranges during operation. Results are taken from the analysis of different manually defined clusters. Clusters where the interference of mode and rotor harmonics were critical have been left out. In particular modes FA-1, FA-2, SS-3, and FA-3 show distinct frequency changes over 5%. Most probably as a result from changes of the rotor's mass of inertia due to rotation. For all modes, damping values have a range of about one order of magnitude between different states. Hence, the upper section of Table 5.3 does not hold damping values since values for a single data instance have very limited significance. Insights into the changing

(a) FA-1, $f = 0.33$ Hz

(b) SS-1, $f = 0.333$ Hz

(c) SS-2, $f = 1.37$ Hz

(d) FA-2, $f = 1.61$ Hz
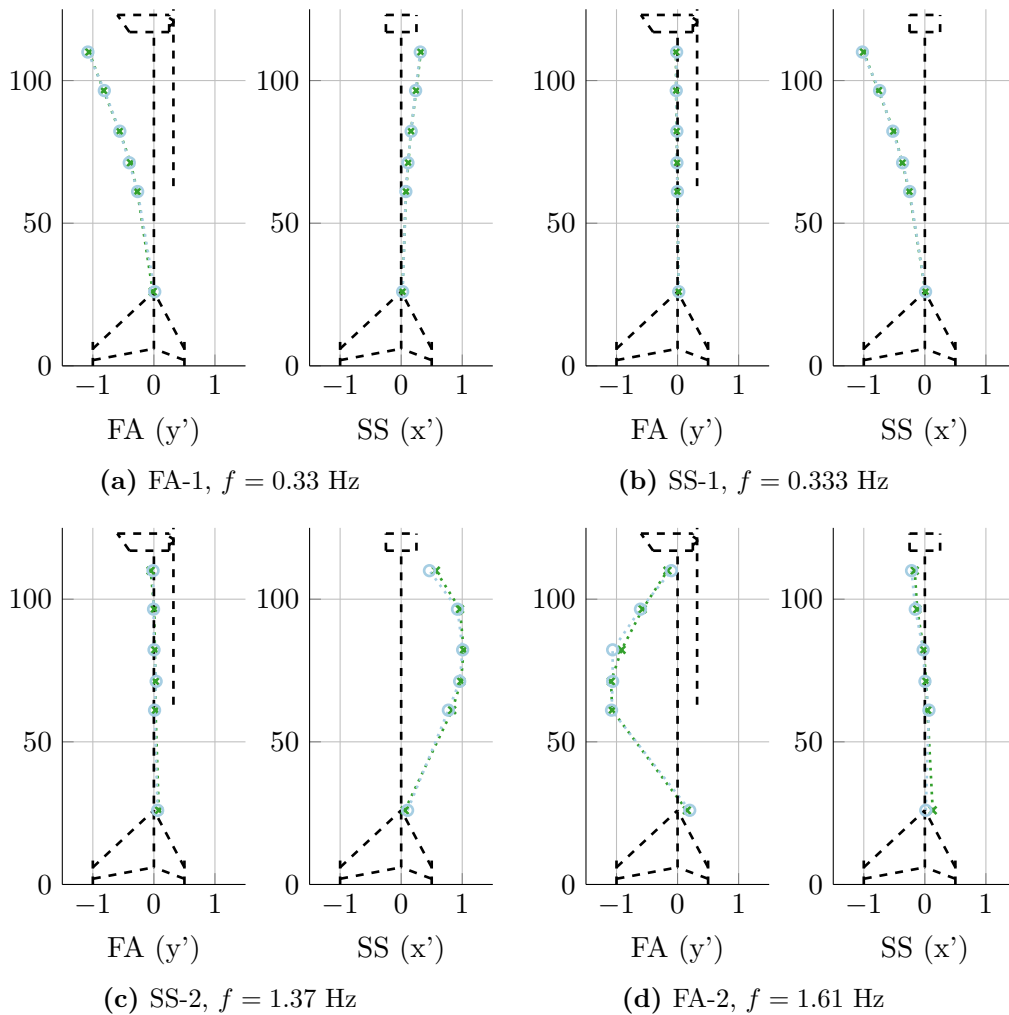
Figure 5.5: Three-dimensional, global mode shapes of offshore wind energy converter below 2.0 Hz including projections in global xz- and yz-plane. Rotated coordinate system indicates nacelle position, blue and turquoise the southern and northern sensors within the tower, respectively.

modal characteristics will be discussed in the next sub-section.

5.2.2 Changes of Structural Dynamics under EOC variation

Table 5.3 already indicated significant changes in modal properties for the offshore wind turbine $AV07$. These changes are of high interest for operators and designers since resonance phenomena could occur and damping estimates have a distinct influence on the design life-time. Before taking a detailed look at the dynamics of the first global modes, different operational states have to be defined. Figure 5.7(a) displays the well-known dependency between wind speed and rotor speed of the investigated wind turbine. Each dot represents a 10 min data instance. With slight alterations, it is applicable to most industrial scale turbines: From a certain wind speed on, the rotor picks up speed, here at about 5 RPM. With an increase in wind speed the rotor speed increases linearly, depending on the turbine control. At a certain (rated) wind speed, the rated rotor speed is reached, 15 RPM at about 11 m/s for the $AV07$. Due to pitch control of the blades,
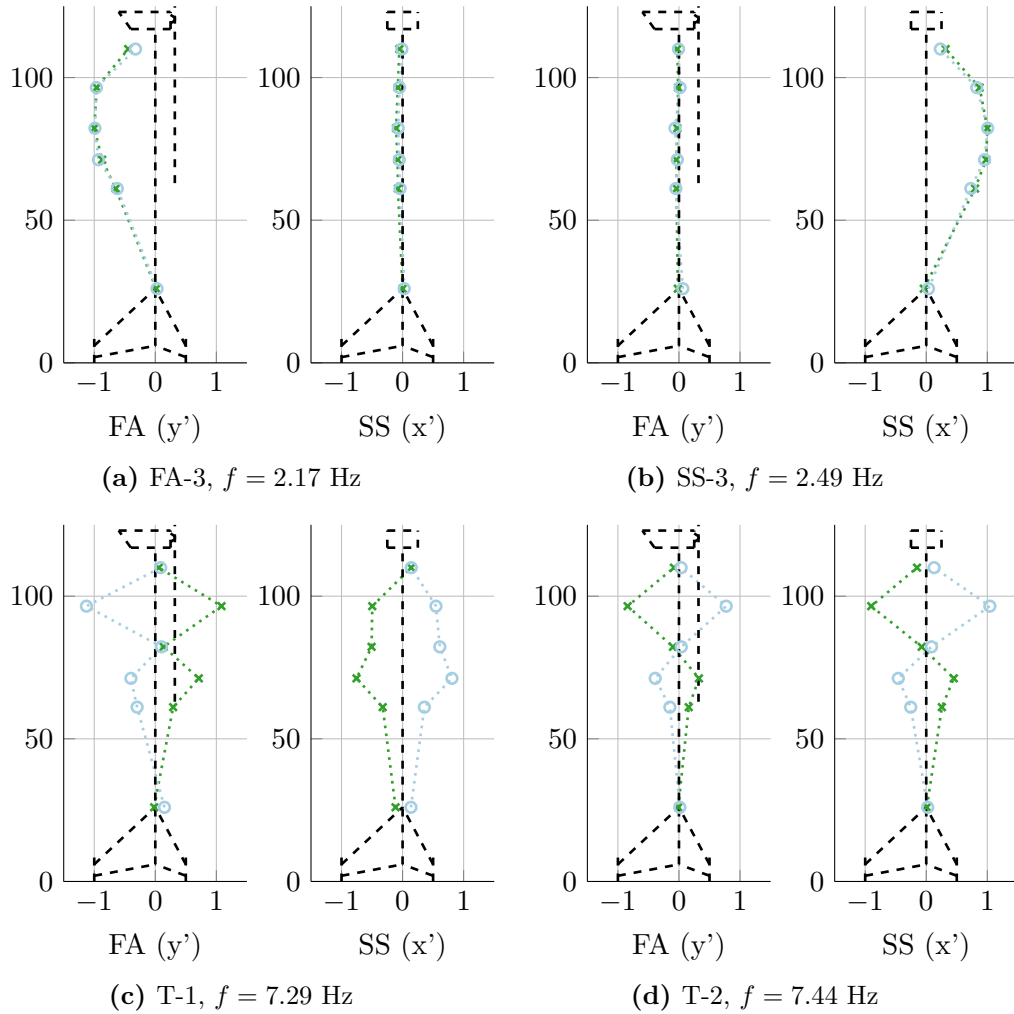
Figure 5.6: Three-dimensional, global mode shapes of offshore wind energy converter between 2 and 7.5 Hz including projections in global xz- and yz-plane. Rotated coordinate system indicates nacelle position, blue and turquoise the southern and northern sensors within the tower, respectively.

an increase in wind speed does not result in a higher rotor speed, and it is kept constant up to a cut-out wind speed of about 25 m/s. When the rotor cuts-out, e.g. for high wind speeds, the rotor speed is reduced again, resulting in a separate point cloud at the right hand side with about 2 RPM. Another cluster of data instances can be seen at 0 RPM over wind speed fro 0 to 16 m/s where the turbine is not in operation.

In [76] clustering of data instances by the main operational states of rotor and wind speed was introduced for an analysis of modal parameters: Main states are standstill, run-up, rated-speed, and pitch-controlled operation. Here, in each of the four clusters a linear regression is used to model the modal frequencies in dependency to further EOCs. Weijtjens et al. [206, 207] use similar clustering for operational states and apply linear and non-linear regression for frequencies of the FA-1 to 3 and SS-1 to 3 modes for a monopile OWT foundation, based on additional EOCs within each cluster. They define eight clusters by rotor speed and pitch angle. Pitch controlled operation above rated wind speed remains a single cluster here. The stiffening effect
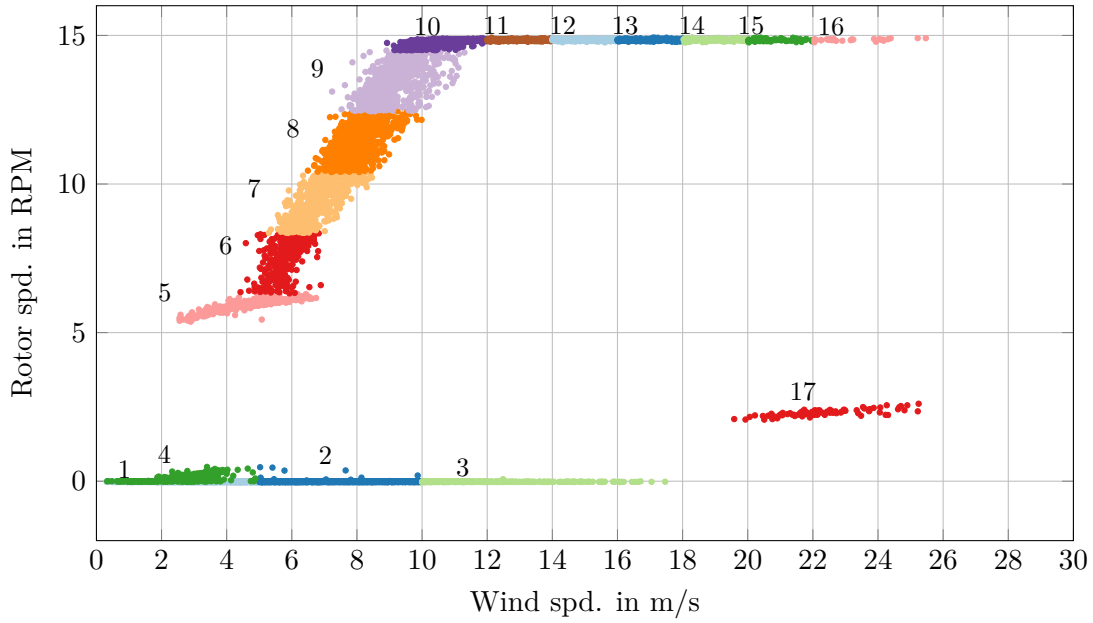
(a) Main Operational States of the OWT Adwen AD5-116, subsequently dubbed classification 'Manual2'.
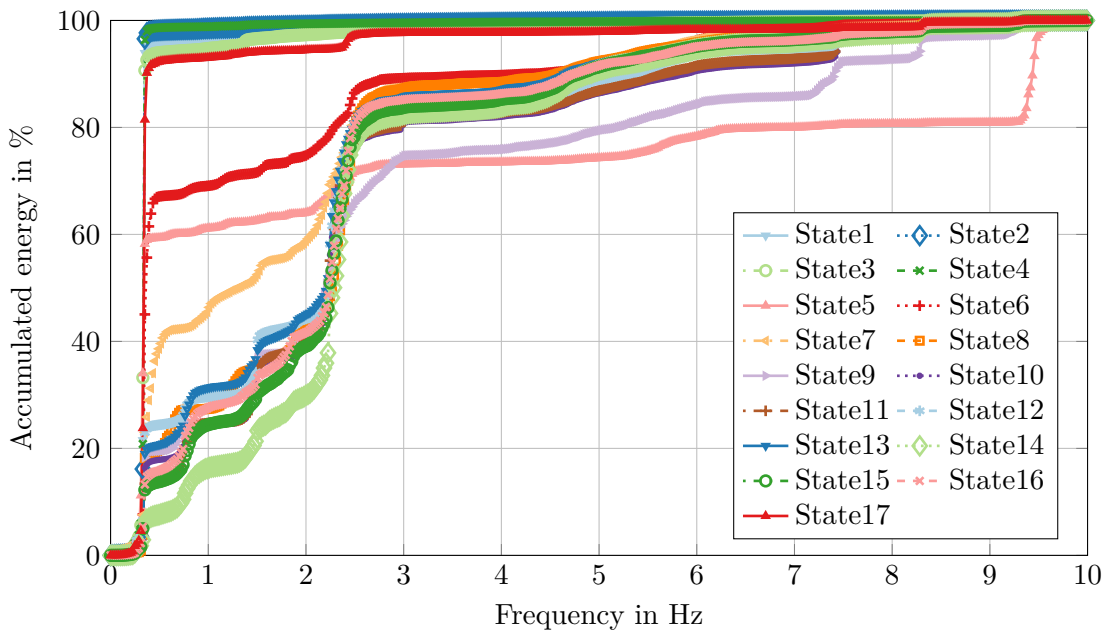
(b) Averaged energy distribution on level 5 under different operational states. Averaged over all four sensors on the level.

Figure 5.7: Main operational states and accumulated energies in such for $AV07$

Table 5.3: Results for TEMP extraction of modal parameters for *AV*07.

Mode[2]	FA-1	SS-1	FA-2	SS-2	SS-3	FA-3	T-1	T-2
Single data instance in standstill used in Figure 5.5 and 5.6								
Frequency [Hz]	0.33	0.333	1.37	1.61	2.17	2.49	7.29	7.44
Operational variation[3]								
Frequency [Hz]	0.32-0.34	0.33-0.334	1.34-1.38	1.43-1.61	2.15-2.50	2.17-2.50	7.26-7.35	7.41-7.50
Δf [%]	5.4	1.0	3.0	12.6	16.1	15.1	1.2	1.2
Damping [%]	0.3-4.2	0.2-1.3	1.5-4.0	0.5-6.0	0.4-2.7	0.8-6.2	0.3-2.2	0.3-2.2

of the J-tube, a structural component to guide and protect the power-cable, is revealed through data normalization (Weijtjens et al. [207]). Further, a raise in frequencies for the 2nd and 3rd FA and SS modes is detected during a second period of monitoring one year after the initial data was collected. In [206], damping ratios and frequencies are also investigated for the above mentioned operational states. The FA modes especially show a significant dependency on the rotor speed, as already theoretically indicated by Salzmann and Van der Tempel [167] and Valamanesh and Myers [195].

For the study presented, the classification of [76] and [206] is improved through division of clusters, as displayed in Figure 5.7(a): In total, 17 clusters[1] are defined for standstill (4 clusters, #1 to 4), run up (5 clusters, #5 to 9), rated speed (1 cluster, #10), pitch-controlled operation (6 clusters, #11 to 16), and cut-out (1 cluster, #17). Both, run up and pitch-controlled operation are split into several groups in comparison to the before mentioned references, respectively. Large variations in damping under differing pitch-angles (state 7 in [206]) are particularly reduced here. In [76], strong dependencies of the first modal frequency on rotor speed and wind speed exist. All clusters are defined by wind speed and rotor speed only, these two parameters also allow for a separation of different acceleration amplitudes as shown subsequently. Boundaries are given in Table 5.4. This classification will also be used as a classification 'Manual2' for the subsequent SHM analysis.

Before discussing frequency and damping variations between states for single modes, a general view is taken over the WT's dynamics. An important question for the dynamic analysis is: Which mode contributes most to the system's dynamic response? Using a conventional frequency spectrum, it could be difficult to tell quantitatively which modes contribute to the response most. To overcome this difficulty, accumulated energies are investigated instead. Figure 5.7(b) therefore

---

1 The notation cluster and state will be used ambivalent here.

2 **FA**: fore-aft in rotor axis-direction; **SS**: side-side in rotor plane direction; **T**: torsional around vertical z-axis.

3 From min. lower quartile (25%-percentile) to max. upper quartile (75%-percentile) in Figure 5.9 and C.3, respectively.

Table 5.4: State boundaries for classification 'Man1' by wind- and rotor speed for $AV07$.

State #		1	2	3	4	5	6	7	8	9
Rotor	Min	−0.30	−0.30	−0.30	−0.01	5.30	6.30	8.35	10.40	12.45
speed[1]	Max	−0.01	−0.01	−0.01	0.50	6.30	8.35	10.4	12.45	14.50
Wind	Min	0.0	5.0	10.0	0.0	2.0	4.0	5.0	6.0	7.0
speed	Max	5.0	10.0	18.0	5.0	7.0	7.0	9.0	10.0	11.5

| State #		10	11	12	13	14	15	16	17
Rotor	Min	14.5	14.7	14.7	14.7	14.7	14.7	14.7	1.8
speed	Max	15.0	15.0	15.0	15.0	15.0	15.0	15	2.8
Wind	Min	8.0	12.0	14.0	16.0	18.0	20.0	22.0	19.5
speed	Max	12.0	14.0	16.0	18.0	20.0	22.0	26.0	27.0

displays accumulated energies between 0 and 10 Hz, averaged for all four sensors at measurement level 5 (see 5.1), for the 17 different states in 5.7(a). 100 randomly chosen data instances are averaged per state. The sensor level was chosen since this position has high amplitudes in the three lowest mode shapes (cf. 5.5(a) to 5.5(d)). It was also observed that the majority of energy ($\gtrsim$99%), between the possible 0 and 25 Hz boundaries, is present between 0 and 10 Hz. In this plot, a steep gradient indicates large energy content at a frequency band.

The different states can now be split by their dynamic behavior, e.g. energy distribution between 0 and 10 Hz (accumulated energy). One group with similar behavior is formed of states 1 to 4 and 17. Here, the first FA and SS mode at 0.33 Hz are clearly dominant. In state 5 (pink) and 6 (red) energy shifts to the third bending mode and, for state 5, also the sixth mode above 9 Hz. This trend continues for state 7 (orange) where roughly similar amounts of energy are present in the first and third bending modes. States 8 to 16, the middle of run-up to end of pitch-controlled operation, form a second group with similar energy distribution: All have dominant energy jumps at the third bending modes above 2 Hz. State 9, right before rated speed, also shows energy in higher frequency modes at 7.5 and 9.5 Hz.

These general shifts in energy distribution between states are most probably caused by rotor excitation frequencies: At rated speed $9P$ lies at 2.25 Hz right between the two modes FA-3 and SS-3. Also, the $30P$ harmonic lies at 7.5 Hz at rated speed, right between T-1 and T-2. The 33P harmonic at 8.25 Hz lies close to the FA-4 bending mode. All of these harmonics introduce energy close to global bending modes. These general observations indicate the importance of taking higher rotor harmonics into account. Nevertheless, resonance phenomena are not known for the plant.

If these phenomena are investigated by standard deviation of acceleration signals on different

---

1   Due to aliasing effects of the sensor for rotor speed rotor speed values between -0.03 and -0.015 indicate a parked position here.
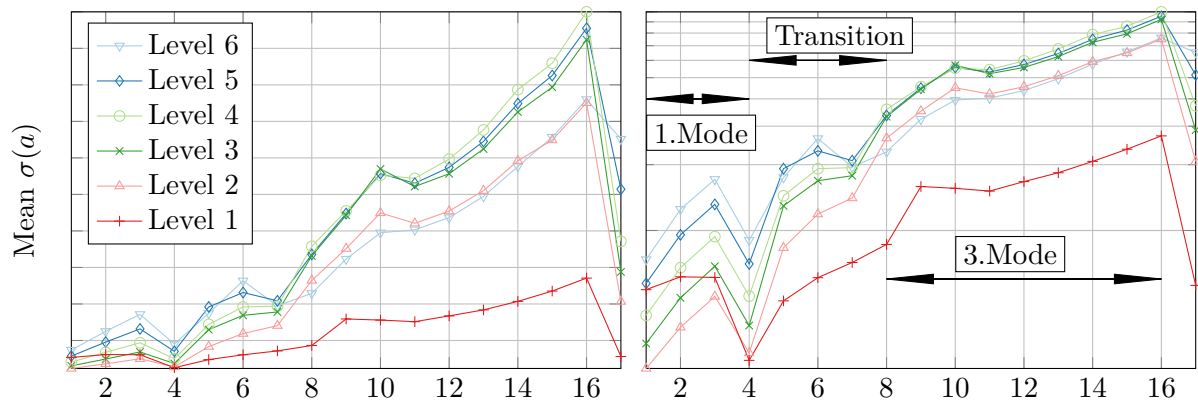
Figure 5.8: Median for the standard deviation of the investigated acceleration sensors on six different levels at $AV07$ for all 17 system states according to Figure 5.7(a). Values for all four sensors on each measurement level are averaged per data instance and subsequently for all sets within the cluster.

levels, a shift in amplitudes between measurement levels over different states can be revealed. Of course, the signal's standard deviation comprises all activated modes simultaneously and is used as measure of energy content in the signal. To illustrate this aspect, Figure 5.8 holds the median for the standard deviation of the investigated acceleration sensors on six different levels for all 17 system states. Within each state, all available data instances were used and median values for all four sensors on each level were averaged per data instance. The left plot in linear scale shows a general increase in acceleration levels: In standstill (state 1 to 3) acceleration levels increase with an increase in wind speed, level four with lower wind speeds has a reduced acceleration level. From state 5 to 16, acceleration levels increase significantly as expected. In cut-out (state 17) the amplitudes are reduced again.

The right hand plot in logarithmic scale reveals an insight into the acceleration amplitude ratios between the different measurement levels. Having in mind the three first mode shapes in both directions, the acceleration levels reveal distinct similarities: for states 1 to 4 acceleration amplitudes increase from level 2 to level 6 (indicated by flag '1.Mode'). Only accelerations at level 1 are not in the right order, probably due to additional excitation through waves at the sea level. Between states four and eight, a transition takes place where the acceleration amplitude on level 6 decreases. A second clear pattern results between states 8 and 16: Acceleration at levels 2 and 6 as well as at 3, 4, and 5 have similar amplitudes corresponding to the third mode shape. For state 17 the order switches back to the first mode. This examination confirms the conclusion drawn from Figure 5.7(b) on a global level: A switch in dynamic behavior from the first bending mode in standstill to the third bending mode being dominant in the acceleration signals during operation.

The conclusion on differing dominant modes leads to the question on how these modes can be characterized under changing EOCs. Before evaluating the data, a short reference to codes and present literature on the topic is stated.

In the IEC-61400-1 [90] structural damping of 1% critical damping and no aerodynamic damping are defined. The American Wind Energy Association (AWEA) and American Society of Civil

Engineers (ASCE) differentiate in their report damping in non-operational and operational states and recommend an assumption of 1% and 5%, respectively.

Valamanesh and Myers [195] use the software package FAST [135] to simulate FA and SS damping values for the 1.5 MW base-line turbine, developed by NREL [120]. Both, a flexible and rigid rotor are considered. Aerodynamic damping for the FA-1 mode increases linearly to 0.5% for standstill and takes on values between 4 and 5% for operational states.

Salzmann and Van der Tempel [167] compare different theoretical methods for damping estimation with numerical simulations for four wind turbines (Vestas V66, NEG Micon NM92, Vestas V90, 5.5 MW desktop design). For all scenarios, a linear increase of aerodynamic damping up to the rated wind speed results. Values range from 3.5 to 7%, depending on the WT. Above the rated wind speed, damping values drop by 2%, for two cases damping increases for higher wind speeds. In [170] damping ratios of FA-1 and SS-1 modes for a Vestas V90 3 MW OWT on a monopile foundation are extracted from measurements during an over-speed stop (comparable to the cut-out state 17). 1.05% in FA and 1.27% in SS-direction result from modal analysis, numerical simulations lead to values of 1.05% for both directions.
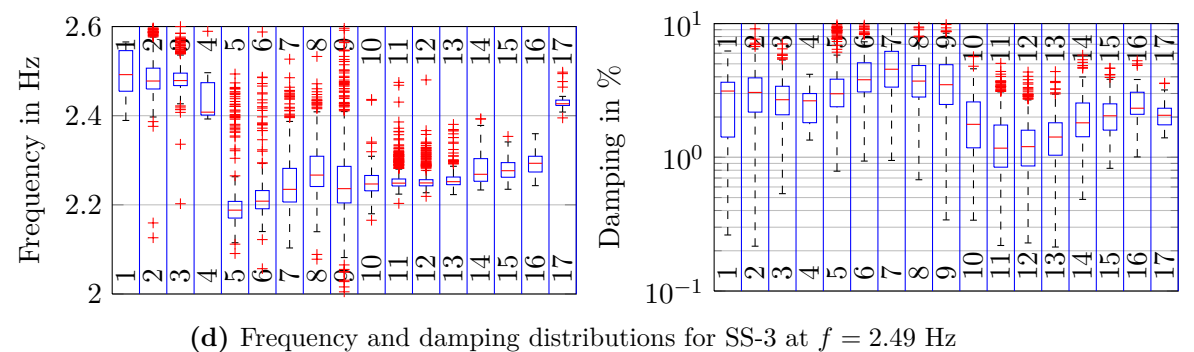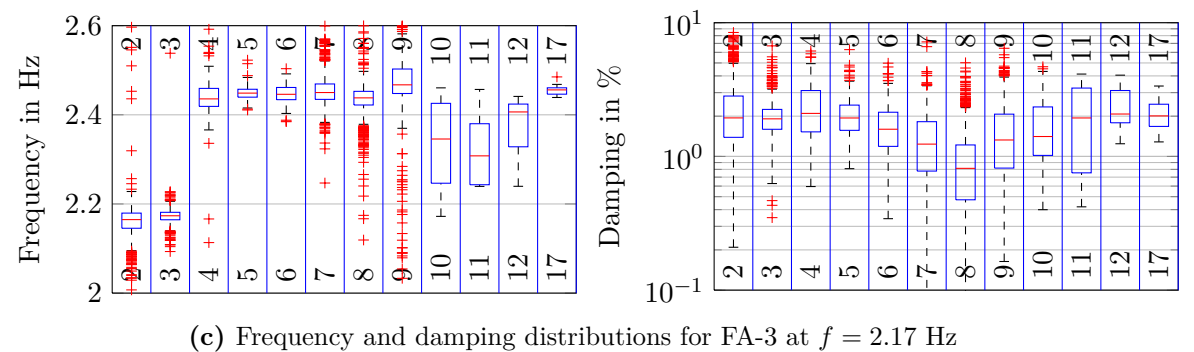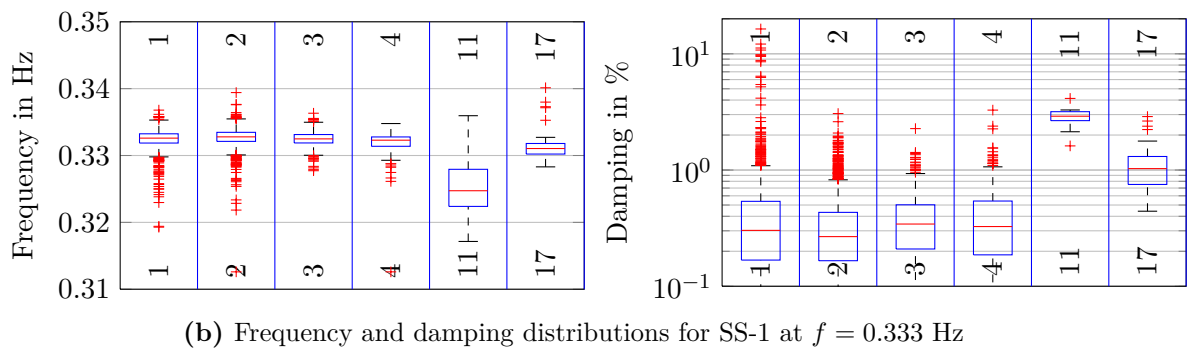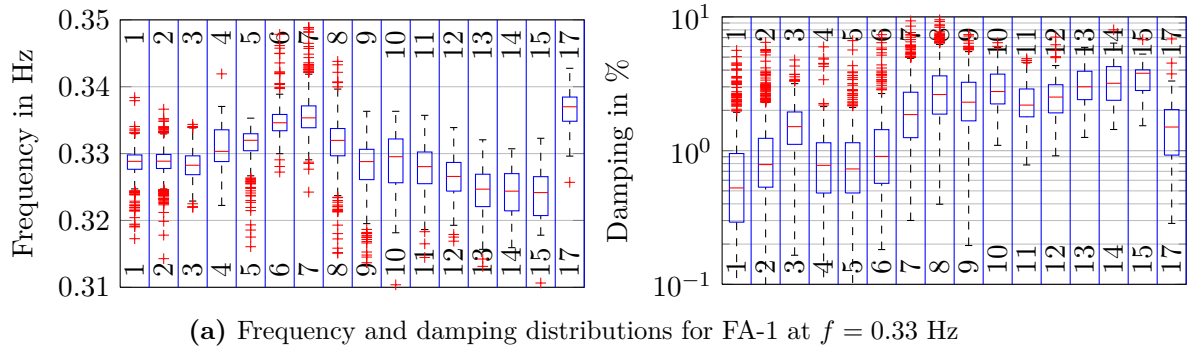
Damgaard et al. [42] analyze damping values of four different monopile-based wind turbines in different wind parks. Results for FA-1 damping values range from 2.34% to 2.59% in median and 1.43 to 1.75% for 5%-percentiles. Additionally a decrease of the modal frequency by 3 to 6% is linked to a rise in acceleration amplitudes. In the presented study, states 1 to 16 also represent an increase in acceleration (see Figure 5.8).

According to the presented references, modal damping and frequency are assumed to change from standstill to operation. To investigate the behaviour of the $AV07$, Figure 5.9 displays box-plots of frequency and damping over the different operational states. States with few identified modes or rotor interaction were left out here.

In Figure 5.9(a), the FA-1 frequency increases from standstill (states 1-3) to run up (states 5-7) before constantly decreasing for higher wind speeds and higher acceleration amplitudes (states 7 to 15). In the cut-out state the highest frequency values are extracted, resulting in a total range of 5.4% similar to what was reported in [42]. The frequency increase results from changes in the translational mass of inertia and the amplitude of the structure's movement. In a second phase, from state 10 to 15, the pitch of the rotor blades leads to a softening effect. A new observation is the increase in frequency for the cut-out state 17, where higher acceleration amplitudes are also present (cf. Figure 5.8).

Damping values display interesting behavior as well (see Figure 5.9(a), right). During states 1 to 3, damping increases linearly from 0.5 to 1.5%. The first states of the run up states, 4 to 6, show damping values below 1% which increase to 2% at state 10 and further, with a small gap at states 11 and 12, to 3% in state 15. The cut-out results in a decrease back to about 1.5% due to a lack of aerodynamic damping and as reported in literature. It is concluded that non-linear damping effects from larger dynamic amplitudes and aerodynamic damping add 1.5% critical damping which corresponds to 100% of the damping under standstill and low wind.

For mode SS-1 states 1 to 4, 11, and 17 were considered. In all other states interaction with rotor harmonics was present. Damping values stay at 0.3% below the damping of the FA mode

(a) Frequency and damping distributions for FA-1 at $f = 0.33$ Hz

(b) Frequency and damping distributions for SS-1 at $f = 0.333$ Hz

(c) Frequency and damping distributions for FA-3 at $f = 2.17$ Hz

(d) Frequency and damping distributions for SS-3 at $f = 2.49$ Hz

Figure 5.9: EOC influences on first bending mode of AV07 offshore wind energy converter below 2.5 Hz. Boxplots show mean (red line), 25% and 50% percentiles (blue box), 5% and 95% percentiles (whiskers), and outliers (red crosses, outside $\mu \pm 2.7\sigma$)

as expected. In state 11 and 17 damping jumps to 2 and 1%, respectively. Again aerodynamic damping and non-linear effects add substantially to the damping values. The modal frequency drops slightly in state 11 and 17. In general, damping values lie below theoretical values and other observations on monopiles. One reason could be a smaller activation of soil damping, compared to monopiles, since amplitudes at mud line level are smaller for tripod and jacket foundations due to their stiff structure.

The third bending modes SS-3 and FA-3 display a very interesting behavior as already indicated by large frequency variations in Table 5.3. Compared to each other, Figure 5.9(c) and 5.9(d) reveal a commutation of frequencies between standstill and run-up. In contrast to [206], the FA mode has a lower frequency during standstill than the SS mode. For these modes, the rotational mass of inertia and gyroscopic forces are crucial since the mode shapes have no large amplitudes at the nacelle but distinct rotation.

Damping values of FA-3 lie at about 2% for states 2 to 6 and decrease to 0.7% at state 8. SS-3 shows an increase of damping values up to state 7 before passing a die at state 12 and increasing again up to state 16. Nevertheless, FA-3 remains higher damped during states with rotor movement. It must be noted that especially for FA-3 and SS-3 the $9P$ and $12P$ harmonics pass the frequency bands of interest during states 7 to 9 and could potentially alter damping results. For these two modes, aerodynamic damping is not adding to the overall extracted damping values since no significant deflection of the rotor is caused in these modes. While the FA-3 mode recovers 2% damping in operation, the SS-3 mode's damping is cut into half which makes it a critical mode for fatigue. The low damping can also explain the dominant energy in this mode under operation as depicted in Figure 5.7(b).

Similar plots for frequencies SS-2, FA-2, T-1 , and T-2 can be found in Figure C.3. FA-2 shows stronger frequency and damping differences between standstill (state 1 to 3) and operation, damping values drop significantly below 1%. Again rotor interaction must be taken into account, these could cause low damping estimates. Frequencies for T-1 and T-2 increase during state 1 to 3, decrease up to state 10 and stay relatively constant for higher states. Damping values range around 1% critical damping. A distinct change in damping from state 9 to 10 can be seen. Here, SS-3 and T-2 drop and T-1 increases.

Recalling Figure 5.7 and 5.8, three main types of behavior occur during operation: a) the first bending mode is dominant in states 1 to 4 and 17, b) a transition period exists from state 5 to 7, and c) the third bending mode is dominating in states 8 to 16. Nevertheless, the division into several sub states for standstill, run-up, and pitch-controlled operation in comparison to [76] and [206] give further valuable insight into the dynamic behavior as displayed in Figure 5.9. The discussed changes in dynamic characteristics due to different operational conditions clearly show the necessity of a differentiation between these states for monitoring purposes, e.g. through machine learning. Also, the question of a proper separation between states arises here. The following section will outline the application of long-term monitoring to the $AV07$ with a focus on different ML realizations.

5.3 Application of SHM-Framewokr

After significant influences of EOCs on the dynamic behavior of the wind turbine have been shown in the last section, the SHM framework is utilized to gain further insight. The goal for its application within this section is twofold: The desire is to use the SHM framework to evaluate the influence of machine learning (ML) on the distribution of condition parameters (CP) without application of hypothesis testing (HT). The other to utilize abnormal states for a first condition identification step, using ML, CP, and HT, to see how beneficial the proposed line of action is for identifying deviations in the structural behavior.

To achieve these goals, the same database as for modal analysis and structural dynamics in Section 5.2 is used. Table 5.5 sums up the different settings for the SHM steps[1]. To decrease computational costs for parameter studies, the data instances are reduced to 12 channels and 4096 samples each. Two orthogonal channels from one sensor are selected on each level, for level 1 to 3 sensors from the southern side for levels 4 to 6 sensors from the northern side, respectively. A switch between north and south is included to capture torsional movements of the tower.

Table 5.5: Settings for SHM framework at $AV07$

Number of channels:	12 (@ 50 Hz)	Data sets in training:	1000
Total number of data sets:	19135	Data sets in testing:	1000
Number of ML types:	35	Maximum nuber of EOCs:	8
ML Names:	$'Man_1'$ - $'Man_3'$ $'AP_1'$ - $'AP_{32}'$		

Settings for condition parameter(s):

CP^{f_i}:   Shifs: 80   Model orders: 100 to 300

                $\phi_{crit} = 32.5$ $f_{crit} = 3$ $\zeta_{crit} = 50$ $MAC_{crit} = 0.95$ $\hat{P}_{crit} = 50$

$CP^{E_{yy}}_{i,j}$:   Number of energy bins = 10

CP^{ε}:   Shifts = 10   Non-sign. col. = 24

$CP^{\mathcal{M}}/CP^{R^2}$:   AR-Model Order = 25

CP^{γ}:   Shifts = 10   Sign. col. = 24   Blocks = 150

Analyzed distribution types: Discrete, Gaussian
α-values for control chart figures: 0.01
α-values for hypothesis testing: [0.1:0.1:2, 2:1:20, 20:2:40, 40:10:90]%

---

1   After the inspection of PSDs from different data instances and channels a lower frequency of interest of $f_{min} = 0.3$ Hz was determined. Shifts was chosen to 80 indicating a lower frequency of interest of 0.6 Hz. It was noted that with this number of shifts and model orders between 100 and 300, modes down to 0.3 Hz could be identified in a robust manner. This is assumed to correspond to the dominance of the primary bending modes, which are picked up by the numerical model even if low numbers of shifts are used. The criteria f_{crit}, ζ_{crit}, and MAC_{crit} are empirical. The MPD criterion ϕ_{crit} was set to a high value of 32.5 due to the in field conditions. $\hat{P}_{crit}$ should be chosen to one half to a fifth of the given model orders, 50 in this case. Selection of the different CP input variables goes along the introduced rules of thumb. The lowest damage sensitice frequency is set to 5 Hz. $n_{shift} = f_s/f_{min} = 50/5 = 10$ is taken into account for CP^{ε}, n_{is} is chosen to 24. For CP^{γ}, $n_{shift} = 10 = f_s/f_{min}$ and $n_{sig} = 24$ being equal to two times the number of sensors. For the VAR-based CPs, the model order was chosen on the safe side with $25 > f_s/f_{min} = 10$.

For training and testing 1000 data instances are used each. A distribution over wind and rotor speed of the included sets can be seen in Figure 5.10: Within the left plot all data instances are plotted, normal states correspond to data instances which lie in the clusters previously defined for examination of structural dynamics in Figure 5.7a. This classification is dubbed 'Manual2'. All data instances outside these clusters are assumed to be deviant in their dynamic behaviour.

It is emphasized that this definition was chosen due to the lack of actual structural damage. Hence, data instances marked in blue still belong to an intact and healthy structure. Deviation is only defined by abnormal EOC flags in terms of wind speed and rotor speed or controller deviations. These might result from the turbine being in a transition phase between states since EOC values represent 10 min mean values and would be difficult to identify by e.g. regression analysis between rotor speed and wind speed since the dependency between these two EOCs is not unique (a wind speed between 10 and 15 m/s can result in 0 or 15 RPM rotor speed). The right plot in Figure 5.10 shows both training and testing data instances (1000 each). It can be seen that training sets cover the whole range of normal states while testing sets also include the deviant states defined in the left plot of Figure 5.10.

In total, 35 different instances of ML (from reference, manual and AP) are analyzed with a maximum of 8 EOCs as input variables. As indicated in Table 5.5, the first three are manual classifications ('Man1' - 'Man3') followed by 32 classifications through affinity propagation (AP) named 'AP1' to 'AP32', differing in EOCs and preferences. Further details on ML will be given in the next sub-section. In the next block of Table 5.5, settings for the different CPs are given. CP^{f_i} exploits the same values as for modal parameter investigation in Section 5.2. Accumulated energies are again calculated and mean frequencies for ten energy intervals (j) extracted to serve as CPs, namely $CP_{i,j}^{E_{yy}}$ and $CP_{i,j}^{E_{xy}}$. For $CP^{\mathcal{M}}$ and CP^{R^2}, both VAR-based relative CPs, a model order of $p = 25$ is chosen. With a sampling rate of 50 Hz, this results in a $p/f_s = 0.5$ s long time span, covered by AR-coefficients and accordingly 2 Hz as lowest frequency of interest, right below the second bending modes FA-2 and SS-2. These modes dominate the structural behavior during operation and are considered to be authoritative.
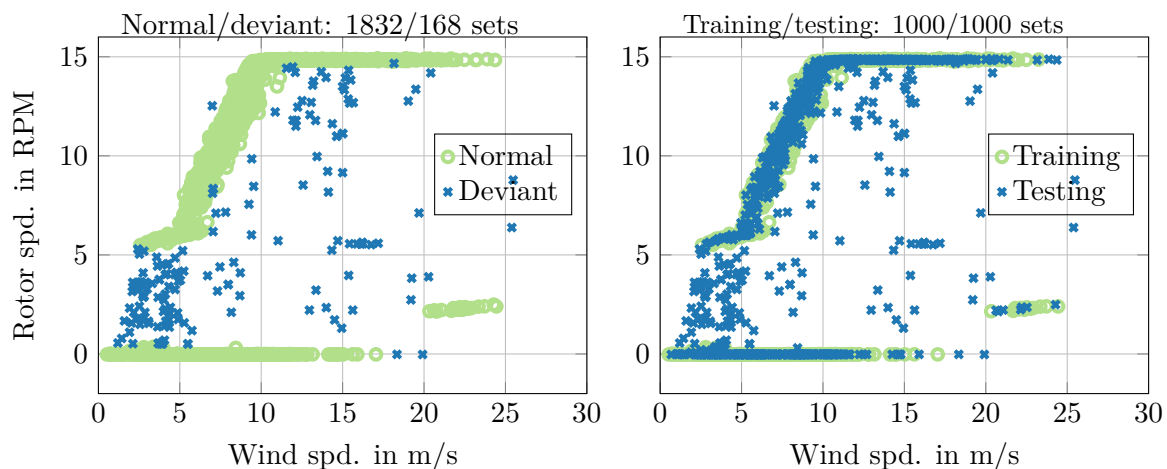
Figure 5.10: Overview of training and testing data instances for $AV07$.

For SSI-based residues CP^ε and CP^γ the same procedure as for the foregoing examples can be applied by definition of a lowest frequency of interest $f_{min} = 0.3$ Hz. n_{shift} follows to $f_s/f_{min} = 50/0.3 = 166.7$ which is obviously too large for an efficient computation.

Also, important changes in dynamics within the clusters are assumed to express themselves in higher frequency regions above 3-5 Hz and low values for n_{shift} already showed good performance in the benchmark examples. To allow the processing of many different SHM realizations, a (very) small number of 10 shifts is selected here. $n_s = 24$ significant columns represent the assumed state space model order with 12 channels in use. Further, a block size of 150 samples (3 s) is chosen to assure independence between data blocks after each rotor revolution. The chosen values do not represent the results of an optimization process since no actual damage scenarios are included in the database.

Finally, settings in the HT-step are listed. As before, a normal distribution is fitted to the CPs within each cluster and alternatively percentiles are calculated from the discrete samples. Control charts are calculated with a confidence interval of $0.99 = 1 - \alpha = 1 - 0.01$. For ROC generation, different α-values are included as given in Table 5.5: a:b:c denotes an interval with starting/ending point a and c, and interval size b. For later analysis, it is suggested to e.g. optimize the CP criteria with respect to the FP values.

5.3.1 Influence of Machine Learning

This sub-section will address the analysis of the ML influence on CPs. In this case AP, which showed good performance in the previous example, is used in the ML step. Along with this automated method, three different manual classifications (or ML instances) are analyzed:

- *Manual1* or *Man1*: All training data instances form a single cluster (upper left plot in Figure 5.12).

- *Manual2* or *Man2*: data instances are separated into 17 clusters as for the analysis of modal parameters (upper right plot in Figure 5.12).

- *Manual3* or *Man3*: Here, fewer clusters than in *Man2* are used. Standstill, run-up and pich-regulated operation are merged into a single cluster each.

Man1 represents the standard reference classification used in the previous examples. Again, it is included to demonstrate the superior performance if proper ML, in this case using AP, is included into the SHM framework. For AP, many different possibilities for a application exist. One is the combination of EOCs in number and type, the other is the *preference* value set for AP.

For absolute CPs, a dependency on EOCs can be drawn directly by analyzing the correlation coefficients between EOC and CP. For relative CP in contrast, analysis is more difficult since these parameters depend on the ML instance and a direct correlation to EOCs does not exist in a simple manner. To evaluate the dependency of these parameters, different ML instances are analyzed to investigate the influence on relative CPs.

As stated in Table 5.5, 1000 data instances are used in the training phase. These are drawn randomly from the 19,354 data instances in the database, except those flagged as 'deviant' from

normal operation. The following are present in the database: 1. Rotor speed, 2. Wind speed, 3. Nacelle position (relative), 4. Temperature, 5. Turbulence intensity, 6. wave heights (H_s mean of highest third), 7. Wave period, and 8. Relative wind direction. Wind and rotor speed show especially strong influences on dynamics and are considered to be appropriate for a first clustering of states, as executed for *Man2* and *Man3*. These two parameters represent the pitch action and angle indirectly and are included in the controller, too. The lack of pitch angle information, which was not present at the given point of time, should be corrected in future analysis. Nevertheless, detection of erroneous pitch information could be one of the goals for future SHM and hence application without pitch information is a valid scenario. Available EOCs are systematically used to derive different ML settings, as described subsequently.

To avoid the introduction of a lengthy table, different ML set-ups are displayed via a spy-plot in Figure 5.11a. Different EOCs are indicated on the y-axis, and different ML instances on the x-axis. A blue dot symbolizes the usage of a certain EOCs in the ML instance. On top, preference values for CPs are given. Vertical red lines separate different blocks: The first block is formed from the three manual classifications mentioned above. The second block is built by AP based on rotor and wind speed differing in preference values from -50 to -0.5 (AP1-AP5). Preferences should be varied in such an analysis over one or two orders of magnitude. The third block uses the same preferences as the preceding one but with all available EOCs (AP6-AP10). In block four, three EOCs are used. Rotor speed and wind speed provide the basis and instances vary in the third EOC included (AP11-AP16). In this block, all instances are calculated with the same preference of -5. Within the last block, a combination of four EOCs is analyzed (AP18-AP32). Again rotor and wind speed form the basis and all combinations for two of the remaining EOCs are investigated. AP17 was used as revisal for different results and will not be discussed further on.

The whole analysis was run ten times with 250, 500, and 1000 sets and randomly chosen training data instances each time. As a first result, a count of clusters can be investigated as shown in Figure 5.11b. Of course, the number of clusters is constant for manual classifications. An exception results when few data instances are used in training, as then some clusters might end up empty. In contrast, empty or almost empty clusters will not result from automatic clustering. For AP1-AP5 and AP6-AP10 a decrease in absolute value or preference results in an increase of cluster numbers as expected. When more EOCs are included, more clusters result. This is due to the relatively large distances between data instances in higher dimensional space even if normalized to [-1,1]. For future research, it is suggested to suppress this effect by introducing a scaled Euclidean distance measure by dividing the Euclidean distance by $\sqrt{n}$ for an n-dimensional EOC-space. Over the ten runs, cluster quantity stays fairly constant. In the third block, AP11, AP12 and AP15, representing the choice of nacelle position, temperature, and wave period respectively, result in larger numbers of clusters. A similar phenomenon can be investigated for the last block: All instances including the nacelle position, namely AP18 to AP22, result in higher cluster counts. The remaining instances behave quite similar. The outcome of more clusters with similarly EOC-dimensionality and preference indicates that the EOC 'nacelle position' seems to spread the data instance distribution more strongly. Similar phenomena are seen when the amount of
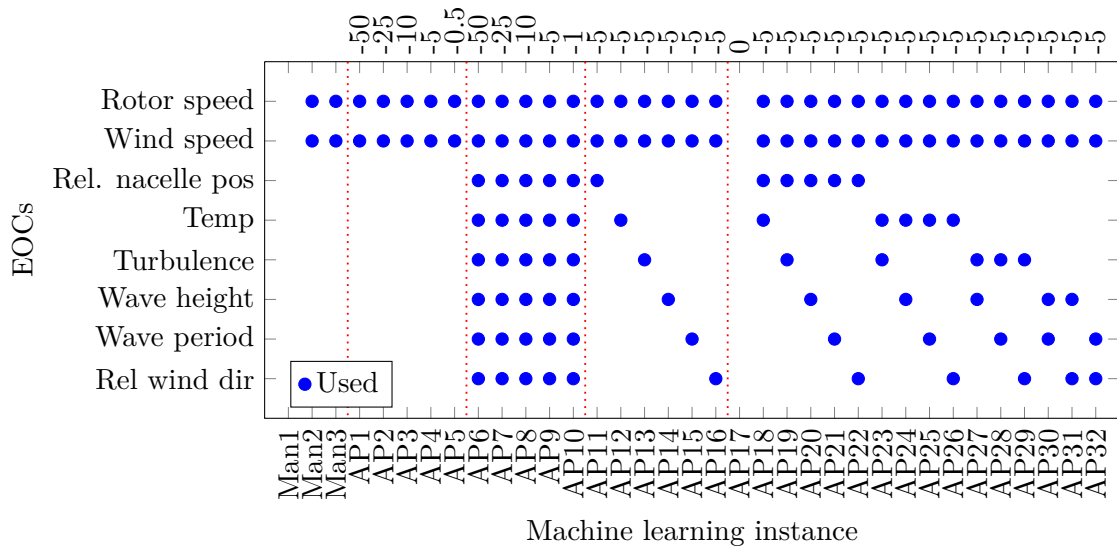
(a) Overview of machine learning set-ups for $AV07$
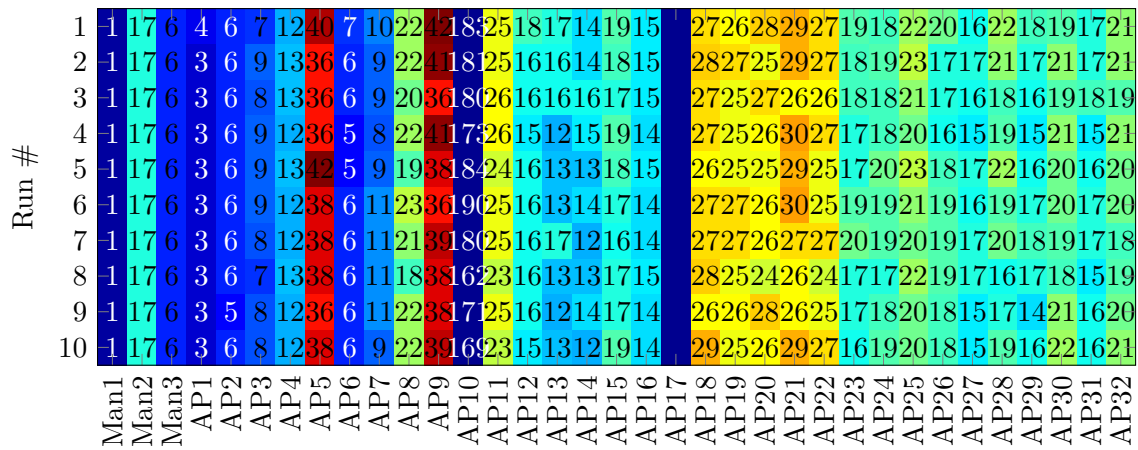
(b) Number of clusters for $AV07$; 1000 training sets

Figure 5.11: Overview of machine learning set-ups for $AV07$: Selected environmental and operational conditions per ML set-up indicated by blue dots (5.11(a)). Pereference, used for affinity propagation is indicated above each column. The settings are valid for all three investigated cases (250, 500, 1000 training sets). Number of clusters for different machine learning settings over ten runs with randomly chosen training data for $AV07$ (5.11(b)). 1000 training sets each. Analysis for 250 and 500 training sets are given in Figure C.5 and Figure C.6.

training data is reduced. In analogy to Figure 5.11b, Figure C.5 and Figure C.6 show cluster counts for 250 and 500 training sets, respectively.

To investigate the different outcomes, Figure 5.12 gives an insight into the six different ML instances AP4, AP5, AP11, AP13, AP26, and AP29. Again, each dot represents the 10 min mean values of one data instance. AP4 and AP5 base on 2 EOCs and different preference values, AP11 and AP13 base on three EOCs, one includes nacelle position one turbulence, and AP26 and AP29 are derived with four EOCs each. If more than two EOCs are included, the first two principal components are used as projection to display the cluster geometry. In the first row, the well-known curve of wind speed and rotor speed can be identified as in the case for manual

classification. Here the influence of a decrease in preference, from -5 (left) to -0.5 (right) is striking due to the number of clusters which increase from 12 to 40. For a two-dimensional space, AP mimics the manual classification (Man2, 12 clusters) well. Therefore, AP4 will serve as reference to *Manual2*.

With three and four EOCs in use, a principal component analysis of the normalized EOCs is used from which the first two principal components are plotted against each other to display the clusters (row two and three in Figure 5.12). The distribution of principal component clearly differs between AP11 (middle left) and AP13 (middle right), in which nacelle position and turbulence intensity are used, respectively. AP13 still shows a rotated picture of the original data distribution for AP4 and AP5 and hence rotor and wind speed. This is expected since turbulence intensity shows a clear dependency on wind speed as seen in Figure 5.3. The distribution of data instances in the PCA space differs strongly for AP 26 and 29. In the lower row, a T-shape is visible for both classifications. These examples show typical shapes for the database in question. As discussed before, the differing classification of the database results in different groups of data instances and thus in different groups of CPs. For relative CP in particular, as residues, the grouping strongly influences the CP values.

To investigate the influence of ML on the robust and well-performing CP^{R^2}, plots for CP-values during the training and testing-phase are used in Figure 5.13. For each cluster in the training phase, median, mean, and different percentiles indicate the CP distribution and are connected by a line[1]. These vertical lines can be used to give a first, visual estimation of variability. It is clear that variability is somehow linked to the number of data instances within a cluster. Large numbers of clusters will reduce variability but also the number of data instances in the single clusters and hence robustness in the decision process. A balance between these two factors is desired.

The reduction of variability between the reference classification Man1 (top plot in Figure 5.13) and the other classifications is obvious at first sight. Also, the cluster averages are reduced below $10^{-0.5}$ for most of the resulting classes in Man2, AP4 and AP13. Some classes for the three ML instances result in higher average CP-values. And hence consist of data instances with less agreement in dynamic behavior than clusters with lower CP values. Potentially, data instances during testing which fall in these clusters can be omitted in the SHM process. Another insight can be drawn by comparing cluster sizes between *Man2* and AP4 and AP13 (2nd to 4th plot in Figure 5.13): Since boundaries are fixed for the manual classification Man2 and data instances are drawn randomly from the database, it is not guaranteed that all clusters are filled equally and contain similar numbers of data instances. Hence more effort for a manual selection of training sets would have to be made to avoid this phenomenon. For AP, only a single cluster with very few data instances results (cluster #10 for AP4 and #7 for AP13). Inter-percentile ranges (IPR), as distance between 2.5% and 97.5%-percentile percentile values, can be calculated for each cluster. An average of all clusters in a single classification gives a proper indicator for the variance of a

---

1   2.5%, 25%, 50% (median), 75%, and 97.5%-percentiles are indicated.
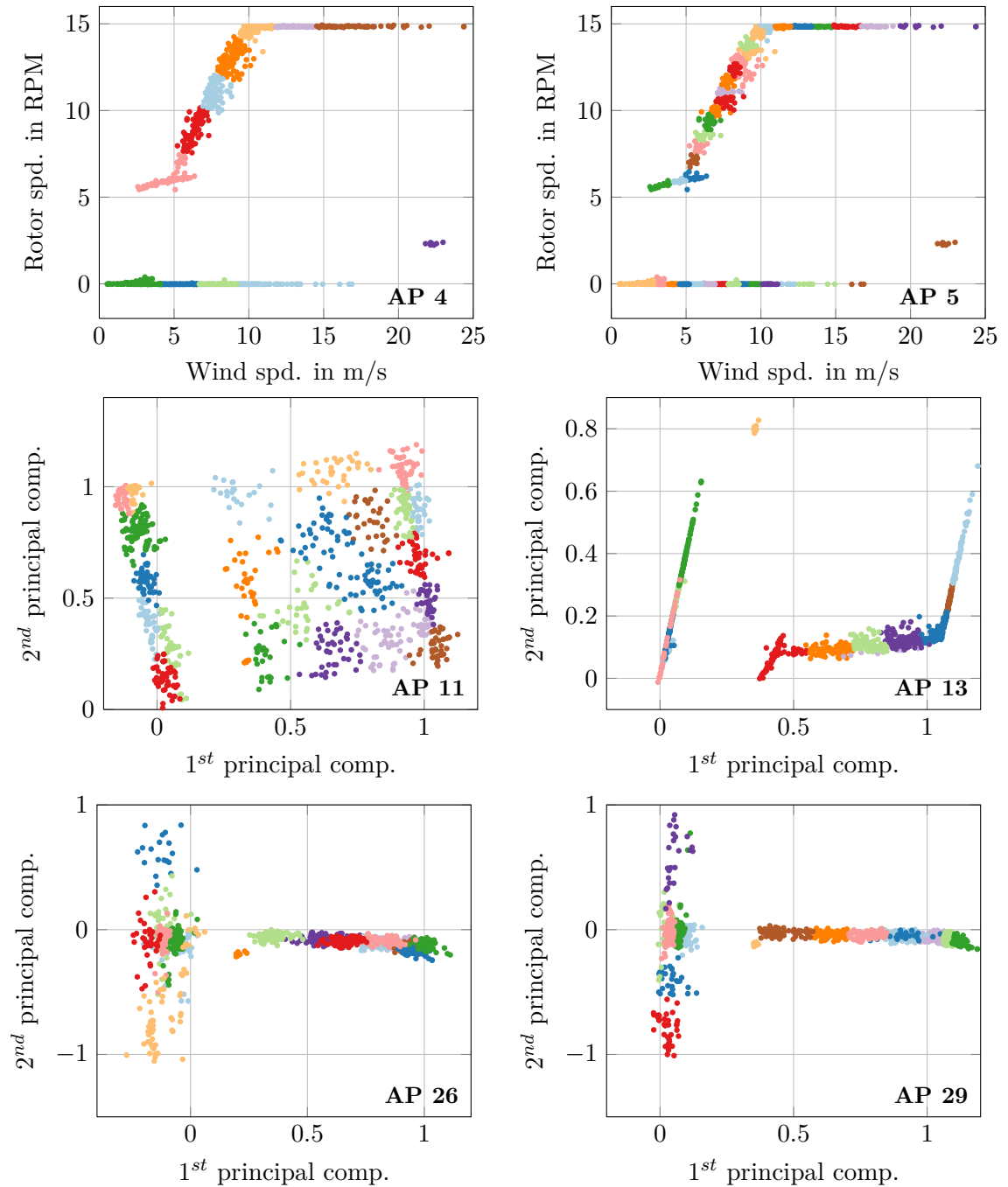
Figure 5.12: Different cluster geometries for ML instances at $AV07$: AP4 and AP5 constructed from two, AP11 and AP13 are constructed from three and AP26 and AP29 from four EOCs, respectively (row wise, top to bottom).
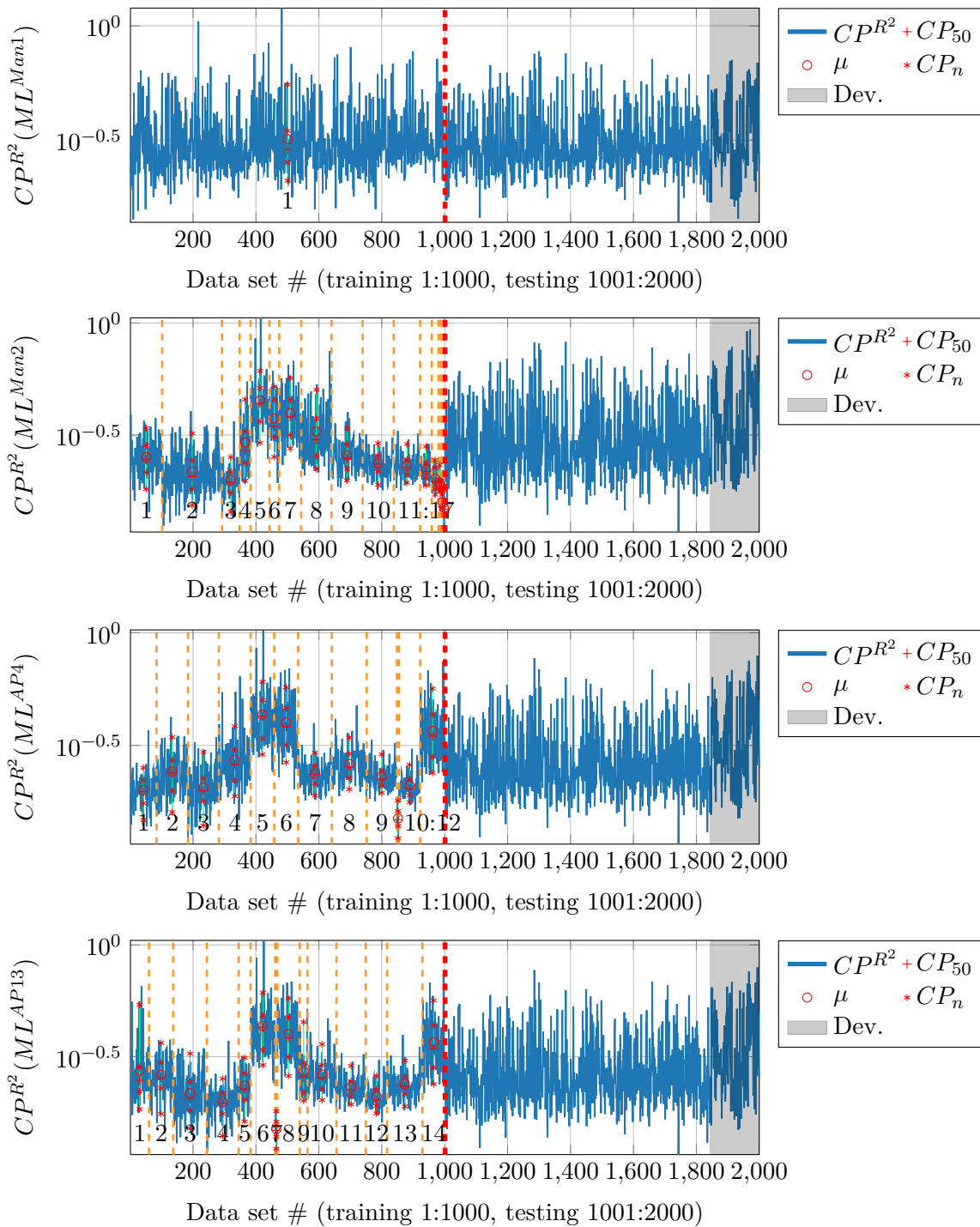
Figure 5.13: Influence of different ML instances on values of CP^{R^2}: Reference classification with a single cluster in training (upper plot), ML instance $Man2$ (2nd plot), AP4 and AP13. The left side represents the training phase, cluster seperated by vertical orange lines, the right side the testing phase including deviant data instances.

CP for a certain classification or ML instance.

For a broader understanding of how ML affects the estimation and distribution of CPs, averaged IPRs per CP and ML instance are investigated. Results for the ten runs with random training set selection are depicted in Figure 5.14: The plots hold the mean IPRs per classification for relative CPs from SSI and VAR. Additionally, CP^{MSP} is included, it is built from all four relative CPs. The upper plot holds all 10 runs, the lower the average values. All mean IPRs are normalized with respect to the base line classification *Man1*. Values below 1 indicate in average a reduced variability within clusters. Again, vertical red lines indicate the five different groups of ML instances. Recalling the five blocks, the first is constructed from manual classifications the second from AP with two EOCs and varying preference, the third with eight EOCs and varying preferences. In the fourth block, rotor speed and wind speed are combined with a third, in the fifth block with a third and fourth EOC. In both blocks, a constant preference of -5 is used. A strong dependency on the selected data instances can be seen for CP^ε in the upper plot. The remaining CPs behave distinctively more robust.

Within block 1, both manual classifications are able to reduce parameter variability significantly compared to the reference Man1. CP^{MSP} shows the strongest reduction. $CP^{\mathcal{M}}$, CP^{R^2}, and CP^γ behave similarly, CP^ε shows less reduction for Man3. It must be recalled that initial parameters for CP^γ and CP^ε were chosen only based on previous observations and might not be optimal. After the occurrence of damage, parameters could be re-calibrated for the damage scenario.

For block 2 and 3 a similar ranking is visible. $CP^{\mathcal{M}}$, CP^{R^2}, and CP^γ underlie moderate changes while CP^{MSP} and CP^ε change more drastically with the increasing number of clusters from AP1 to AP5 and AP6 to AP10. On average, CP^ε even results in values above 1 for AP1, AP2, AP6, and AP7. Parameter CP^ε strongly decreases from AP7 to AP8 reaching a mean IPR of 0.5. It can be concluded that the number of clusters has a distinct influence on the variability of relative CP as it was expected. A small number of clusters, below e.g. 12/13 for 1000 training sets in this case, is especially harmful for CP^ε.

Block four investigates combinations of three EOCs. It is obvious that IPR variations are less distinct than in the previous blocks and different CPs lie closer together, except CP^{MSP} which has small IPR values. Depending on the CP, different EOCs give here a slightly stronger reduction of mean IPRs: $CP^{\mathcal{M}}$ results in AP14 (wave height), CP^{R^2} in AP12 (with temperature), CP^γ in AP15 (wave period), and CP^ε also in AP12. AP13 is a good choice for all CPs. Overall, no strong improvement can be seen compared to AP4 where only the two main EOCs are included. Block 5 results in similar reductions of mean IPRs as block four. Mean values of IPRs lie right below 0.5 for CP^γ and CP^{R^2}. If CP^ε is taken as an indicator, AP18, AP23 to AP26 show a stronger reduction than the others, all linked to temperature as included EOC. A reduction of mean IPR to 0.5 compared to Man1 is possible for most ML instances, meaning the relative parameter distribution has only half the width.

Using the given modular framework of SHM, an analysis of many different realizations of ML-CP combinations is possible. From the observation above, regarding the influence of ML instance on the relative CPs, no strong reduction of mean IPRs can be achieved by adding more than the two initially used EOCs to the automated ML procedure. If desired, temperature and turbulence
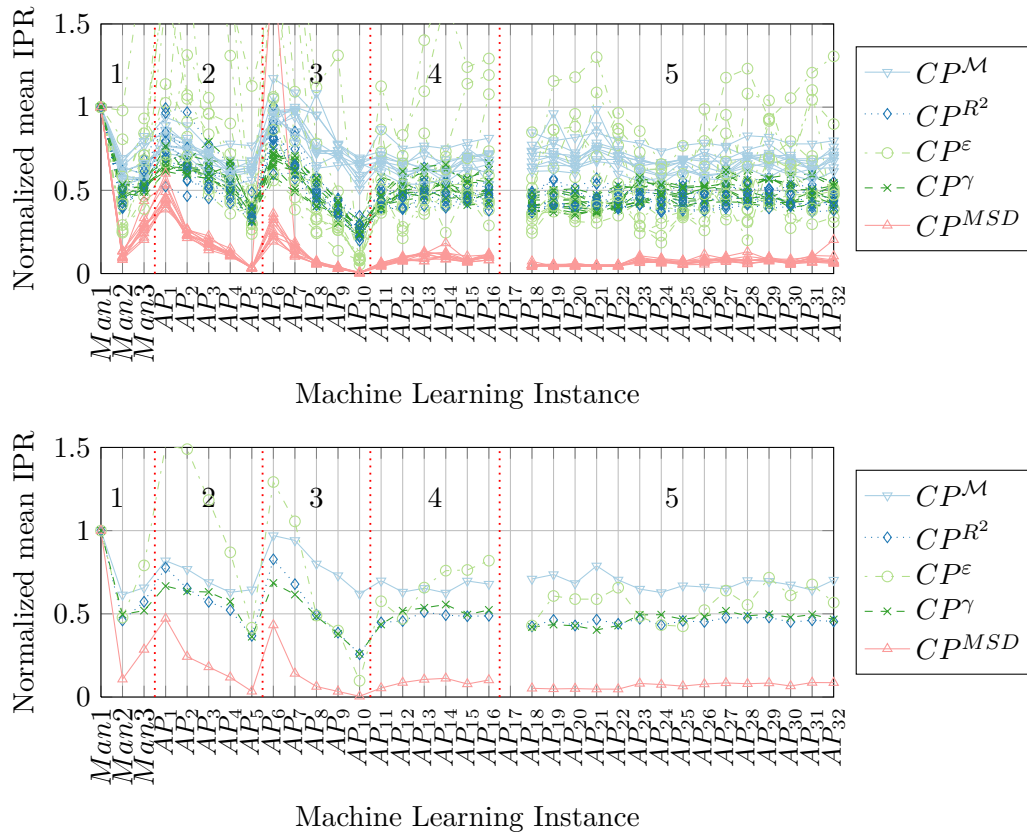
Figure 5.14: CP variation for different ML instances at $AV07$: Averaged inter-percentile-ranges (IPRs) for relative CPs from SSI and VAR, 10 runs with 1000 training sets each. All 10 values given in top plot, averages for 10 runs at the bottom. All values are normalized with respect to the reference ML instance Manual1.

intensity result as candidates for inclusion. For temperature, this is backed by investigations on absolute CPs, showing strong correlation with wind speed, rotor speed temperature and partially with wave height (see Figure C.4 for correlation coefficients between EOCs and absolute CPs for the complete database.). The next step leads to the estimation of SHM performance. In this case corresponds to an artificial case with the identification of deviant system states as defined in Figure 5.10, as discussed in the next section.

5.3.2 Detection of Deviant Operational States

Since no real structural damage is present for the wind turbine, the aim is to apply the SHM framework for a detection of deviant system states as defined in Figure 5.10. These states are identified by EOC values of rotor and wind speed. If a data instance lies outside any of the clusters defined in ML instance Manual2, it is flagged as deviant from normal operation. From the turbine's operational point of view it has to be stated that these deviations are a not linked to damages. This procedure is valid since it leads to a detection of differences in structural dynamics. If the deviant sets are included in the training, e.g. the complete wind speed - rotor speed plane is used, further deviations due to damages can be investigated. In other words: The definition of

normal operation is altered to reveal deviations of the structural response automatically through SHM.

The presented evaluation framework allows for a fast, general overview of how well each of the above mentioned ML instances in combination with different CPs, and HT settings, is able to identify these deviant states. In general, the example is run without the goal to detect 100% of the deviant data instances since some lie very close to the borders of Man2 clusters and might have minor differences in dynamic characteristics.

For the following investigation areas under the ROC curves are used. In the ML step, 35 different instances are included and 59 different CPs[1]. For each combination two different probability density functions are evaluated, with a normal distribution and discrete distribution by percentiles, resulting in $35*59*2 = 4,130$ combinations. To derive the analyzed AUCs, 105 different confidence intervals are used per ROC, resulting in more than half a million control charts being evaluated for false positive alarms and detection rates.

Figure 5.15 holds all AUC results for all ML-CP combinations and the assumption of a normal distribution. An overview for the assumption of a discrete distribution, not differing strongly from the normal distribution case, can be found in Figure C.10. In both cases AUC values, which have been displayed in tables in previous examples, are indicated by color. Dark red indicates high performances with AUC values around 0.8. One CP is plotted per row and one ML instance per column. White horizontal lines are utilized to separate the different parameters. Vertical lines indicate the five blocks from ML as discussed above. At the top, average performances for each ML instance, on the right average performance for every CP are given by mean AUCs, respectively. It should be noted that performance, as area under the ROC curve, includes correct identification of both healthy and deviant sets. Again, since some of the deviant sets lie very close to normal operation visually, these are probably not deviant. These sets will most probably not be identified, which is correct, but decrease the detection rate. Due to this fact, a detection rate of 100% is unrealistic in this case. This overview can now be addressed from two directions: One is the influence of ML on the performance, the other the investigation of different CP.

Performance by ML Some HT and performance independent insights into ML were already discussed in the previous section. In Figure 5.15, Man1 clearly results in the worst performance (1st column). This underlines again one basic theorem of this thesis, namely that a classification with more than one cluster is needed. In average Man2 and Man3 result in similar performances, well performing CPs tend to perform better under Man2, leading to the conclusion that Man3 has marginally too few clusters. In the next two ML blocks, performance increases from AP1 to AP5 and AP6 to AP10, being directly linked to the reduction in CP variability (see Figure 5.14). But, a slight decrease (average AUC 0.67 to 0.66) can be seen for AP5 and also for AP10. Still,

---

[1] 12 channels result in 24 values for accumulated energies for each energy bin (12 auto-correlations and 12 summed cross-correlations). Energy intervals 9 and 10 are displayed in 48 rows total. In addition two residues each, from SSI and VAR modes are inspected as well as six modal frequencies and one hybrid residue based on all four relative CPs.
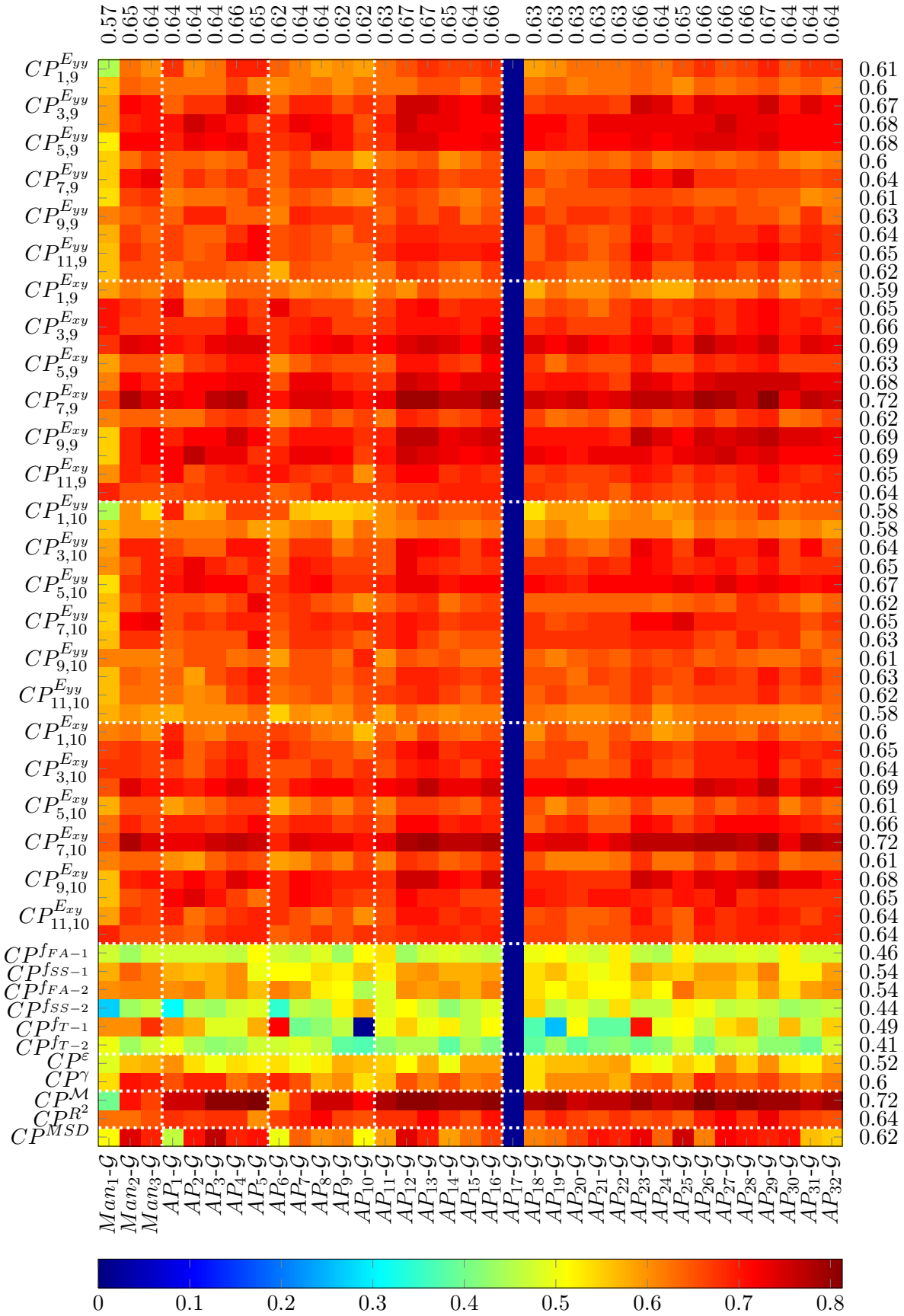
Figure 5.15: SHM performance overview for $AV07$: AUC values for 1.925 ML-CP-HT combinations. ML-CP combinations for the assumption of normal distributed parameters within each cluster. Only every 2nd y-label is set for $CP_{i,10}^{E}$ and $CP_{i,p}^{E}$ for readability. AP17 is excluded and padded with zeros.

performances does not drop strongly, indicating a robust behavior also with few data instances in a cluster.

In the 4th block, an additional EOC is included for ML. Investigating the average AUCs on top, a slight increase can be noticed compared to the first three blocks. Also, peak performances are reached for AP12, AP13, and AP16, underlining IPR observations. AP11, linked to the nacelle position, shows the lowest performance. Wave height and -period, included in AP14 and AP15 perform on a similar level as AP11. The last block with two additional EOCs to wind and rotor speed indicates no strong improvement: Average AUCs lie between 0.64 and 0.68 in the same range as for block four. AP18 to AP22, linked to the nacelle position, as well as AP30 to AP32, linked to wave period and wave height, perform less well. This inspection results in a favor to temperature, turbulence and relative wind direction above wave period wave height and nacelle position as input EOCs.

Performance by CP   Analysis of AUCs according to CP types will be discussed from top (accumulated energies) to bottom (hybrid CP by Mahalanobis square distance). Due to good performance in the previous examples, parameter $CP_{i,9}^{E_{yy}}$, $CP_{i,9}^{E_{xy}}$, $CP_{i,10}^{E_{yy}}$, and $CP_{i,10}^{E_{xy}}$ were chosen for investigation of accumulated energies. These four parameters track mean frequencies between 80 and 90% and 90 and 100% accumulated energy, respectively. $CP_{i,}^{E_{yy}}$ indicates accumulated energies from auto-correlated data, $CP_{i,}^{E_{xy}}$ for a summation of accumulated energies of all cross-correlations between channel x and all other channels. Both result in similar overall performances, reaching from 0.59 to 0.72 for $CP_{i,9}^{E_{yy}}$ and $CP_{i,9}^{E_{xy}}$ and 0.58 to 0.72 for $CP_{i,10}^{E_{yy}}$ and $CP_{i,10}^{E_{xy}}$. $CP_{i,9}^{E_{xy}}$ tends to perform better here, showing AUCs close to 0.8 (dark red). The introduction of cross correlations can increase the performance. Peak performances are dominantly found in the rows of $CP_{i,}^{E_{xy}}$ for both energy ranges. Specifically, parameters for cross-correlations 4, 6, 7, 9, 10 perform best. These are linked to measurement levels 5, 3, 6, 2, 2 and underline, with one exception, more distinct dynamics on levels 2 to 5.

Modal frequencies in contrast do not allow an indication of deviant states. Here performances range around 0.5 representing ROC curves on the diagonal of the performance map and hence the complete lack of the ability to distinguish between states. Regarding SSI-based residues, CP^{γ} performs better than CP^{ε} but both parameters do not reach high performance rates in this case. Perhaps since n_{shifts} was chosen too small. The correct tuning of all three parameters complicates the application. VAR-based residues in contrast, perform very well. An average value overall different ML instances of 0.72 for $CP^{\mathcal{M}}$ marks a peak value. $CP^{\mathcal{R}^2}$ does not perform as well, resulting in an average AUC of 0.64. Finally, CP^{MSD} shows strong fluctuations with partly very good and bad performance values. It is concluded that the hybrid parameter suffers from the non-optimal performance of the included SSI-residues CP^{γ} and CP^{ε}.

An exemplary evaluation of performances with respect to the identification of deviant system states can be carried out in a convenient way through the presented framework. Even allowing for an automation through identifying peak performances (AUCs) in the matrix displayed in Figure 5.15. In this case, AP4 and AP13 as well as AP26 und AP29 in combination with $CP^{\mathcal{M}}$ and $CP_{7,9}^{E_{xy}}$ can be considered as best performing alternatives. Selection of ML-instances also

relies on investigations of inner cluster CP variability by IPRs.

In combination, these results allow the exemplary visualization of SHM for the Adwen AD5-116 wind turbine. As stated in the introduction, no single CP will be able to solve all difficulties in SHM but rather a combination of different CPs with a sophisticated choice of ML and HT. To visualize a possible outcome of the SHM procedure Figure 5.16 shows a combination of $CP^{\mathcal{M}}$, CP^{R^2} and all 12 CPs $CP_{i,9}^{E_{xy}}$ along with fitted normal distributions: Identification of deviant states for the complete set of 1000 randomly chosen testing data instances is presented by indications per set in the well known rotor speed - wind speed - plane where deviate sets were defined. A hit per data instance results if one of the three CPs[1] indicates damage. In this spirit a robust detection results which does not overweight hits by a single CP. A normal distribution is assumed in HT.

This type of display goes along with the merging of CPs by Mahalanobis square distance but combines final results from CPs rather than merging them at an earlier stage. It is considered to be advantageous to point towards a probability of damage or deviation for a data instance, rather than a single black and white interpretation. If only a single CP gives an alarm, an outlier, covered by statistics, could have been occurred. If several CPs show hits, the probability of indication is more profound. In this case, most of the data instances in normal operation show zero or one hit. Most of the data instances with 2 and 3 hits lie away from the normal operation characteristic. This last step finalizes the use of the presented SHM evaluation framework summing up the many different paths that can be taken using ML, CPs, and HT towards a robust decision making and SHM visualization.
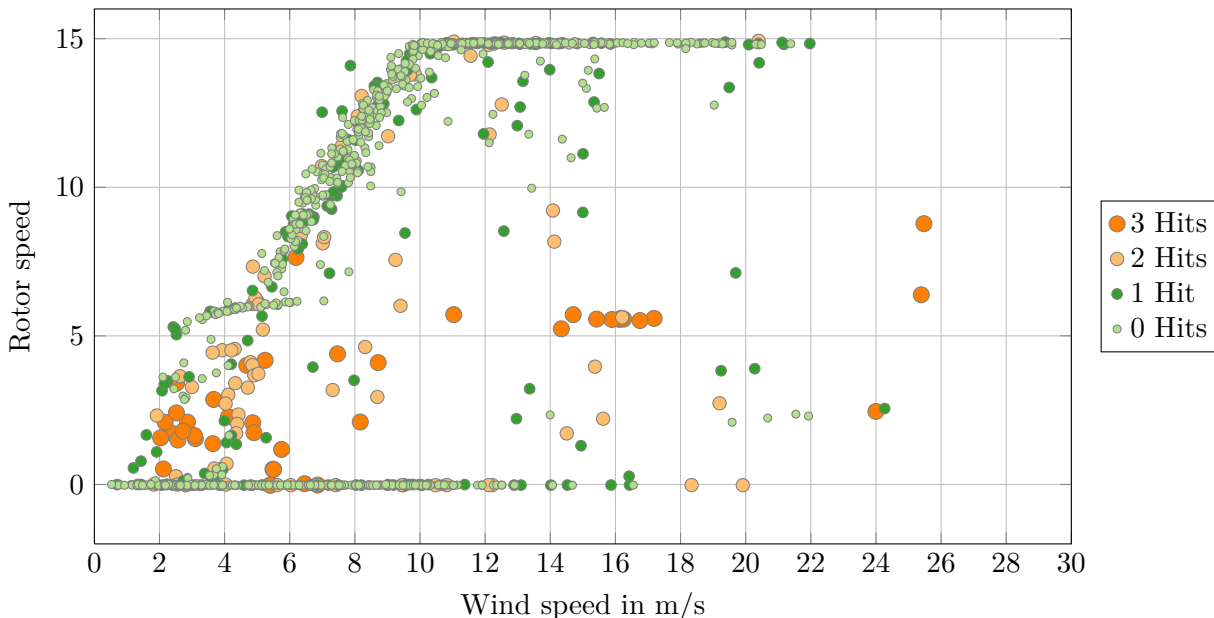
Figure 5.16: Final stage of SHM framework: Hits for possibly deviant data instances at $AV07$ in rotor speed - wind speed - plane. Included CP are $CP^{\mathcal{M}}$, CP^{R^2} and all 12 CPs $CP_{i,9}^{E_{xy}}$ (combined).

---

1   The twelve CPs for accumulated energy is summarized, if more than 6 indicate damage a hit results

5.4 Conclusions

Detailed analysis of modal parameters and dynamic behavior and application of the introduced SHM evaluation framework onto the 5MW Adwen AD5-116 (short *AV*07) offshore wind turbine is the subject of this chapter and its investigations. The RAVE-initiative (Research at *alpha ventus*) provides a large database of structural response data which was utilized to carry out the studies presented. More precisely, data over a period of 17 months, immediately after initial operation of the 12 plants, is used.

The first section names general aspects on the WT's dynamic behavior through accumulated energies, standard deviation of acceleration signals on different levels, and modal frequencies and damping. It is revealed that the rotor speed and wind speed have a distinct influence on the structure's dynamics. Modal frequencies underlie a change of several percent, damping values can change over one order of magnitude between standstill and rotation. In standstill, the acceleration amplitude influences the damping, e.g. of mode FA-1, which increases form 0.5 to 1.5%, and hence indicates non-linear behavior. Accumulated energies and acceleration standard deviation are used to prove a change in dynamic behavior from a dominating first bending mode in standstill to a dominant third bending mode when the rotor is turning. The shift to a dominating third mode can be explained by an increase of damping for the first (0.5 to 3.0%) and a decrease of damping for the third bending mode (3 to 1%). Close rotor harmonics introduce energy in this frequency region. In combination with the increase of damping under standstill with an increase of standard deviation of acceleration, soil damping can add 1% and aerodynamic 1.5% critical damping to the first mode in average. Overall, variability of modal parameters is stronger for in-operation states, especially right before the rated speed is reached.

These findings underline the common practice of avoiding interaction between bending modes and rotor harmonics. Even if taken care of in design, the interaction between 3rd bending modes along with a 6P excitation should be considered in guidelines and codes.

Regarding modal parameters, states with strong pitch action and possible interaction with rotor harmonics should not be considered to calibrate numerical models or extract values for design due to larger uncertainties. The extended manual clustering for modal parameter inspection allows for detailed investigations and is suggested to be applied similarly to all monitored foundation types of OWT to guarantee comparability.

Investigating the switch in dominant modes in acceleration signals, it is also important to remember acceleration being the second derivative of the displacement, which causes fatigue of the structure through strain. In the harmonic case, a double integration (from acceleration to displacement) is equal to multiplication of $1/\omega^2$. The acceleration amplitudes at 0.3 Hz are multiplied by a factor of $1/(2*\pi*0.3)^2 = 0.28$ while amplitudes at 2.17 Hz are reduced by a factor of $1/(2*\pi*2.17)^2 = 0.0054$, putting a strong weight on low frequent acceleration for fatigue.

ML improves performance from average AUCs 0f 0.57 to 0.67 since it leads to a reduced variability within the sub groups or clusters of each classification instance. Also, ML instances with an average of 15 to 20 sets per cluster and a normal distribution performed best. MOst important EOCs are wind speed, rotor speed and turbulence intensity.

Accumulated energies were able to perform equally to the more complex residues from SSI and VAR with average AUCs>0.7 over all analyzed HT instances. The Interval between 80 and 90% energy is most sensible for changes in the dynamic behavior. Also, the new cross correlated $CP^{E_{xy}}$ could outperform the autocorrelated $CP^{E_{yy}}$.

The derived guidelines to set initial parameters for relative CPs could be applied for the WT. For SSI based CPs, the parameter n_{shifts} was probably chosen too small which needs to be validated in future analysis. With the given settings, CP^{γ} outperforms CP^{ε}. Both are outperformed by the VAR based parameters with $CP^{\mathcal{M}}$ performing best. Also for the hybrid CPs based on Mahalanobis square distances, which are often claimed to omit the use of EOCs, it is stated the ML improves performance significantly from AUC=0.5 to AUC>0.7.

It is seen that modal parameters were not able to detect deviant states, possibly also due to interaction phenomena with rotor excitation. All other parameters do not suffer from this phenomenon. They naturally involve the rotor excitation since the complete (measured) spectrum is included. Accordingly, later states in the same operation point will have the same rotor excitation, causing no change to the overall dynamics. – Only a change in the response due to damage or non-trained EOCs is then detected.

Performance for the detection of deviant states is promising with AUC up to 0.8. The final combination of three CP-types ($CP^{\mathcal{M}}$, CP^{R^2}, and $CP^{E_{xy}}_{i,9}$) for optimal ML-instances ($ML^{AP_{26}}$) and Gaussian normal distributions within clusters show the feasibility of the presented framework for damage detection and a possible outcome for SHM applications.

6 Summary, Conclusions, and Outlook

6.1 Summary

Alongside the SHM levels and SHM axioms, a consistent evaluation of procedures is essential for research and industry. In this thesis, a variety of methods from different scientific fields are combined to contribute to the goal of a holistic evaluation of SHM performance. Along the way, more technical implementations were added to the core task.

First, a general introduction to SHM, a distinction to other monitoring fields and a description of SHM applications on (offshore) wind turbines is given. To pioneer the way for the suggested evaluation of variability in SHM, different SHM components namely machine learning, condition parameter, and hypothesis testing (ML-CP-HT), are introduced and reviewed by applications and available methods. Subsequently, the necessary theoretical background for the analyzed procedures is provided. On this basis, the holistic approach for performance evaluation is introduced and formulated theoretically. Further, different technical novelties such as the triangulation-based extraction of modal parameters (TEMP) are given. Automated extraction of modal parameters is shown for a long-span suspension bridge. Finally, an extensive SHM performance evaluation for a benchmark example on a public database is provided and damage detection was realized for the presented damage scenarios. A localization was also possible through accumulated energies. A next step is taken with the application of the proposed procedure to a small-scale wind turbine structure. Through the introduction of reversible damage, SHM performance can be evaluated as well. Again, damage detection could be achieved and performances be evaluated. Finally, the work closes with a real-life monitoring example: A 5 MW offshore wind turbine is investigated with respect to changes in dynamic characteristics due to different operational states. Influences of different ML-instances on CP variability is also analyzed. Subsequently, identification of deviate system states is carried out to illustrate the ability to detect changes in dynamics and the usefulness of a holistic evaluation concept. It is shown that the proposed concept is capable of providing a common basis for the performance evaluation and comparison for a variety of different SHM approaches.

6.2 Conclusions

The following paragraphs will outline conclusions which can be taken from the different analysis presented in Chapters 3 through 5.

Automated Operational Modal Analysis Since modal parameters play a key role as linkage to numerical models and as a possible condition parameter with physical meaning, many monitoring approaches do and will aim for their extraction. To facilitate the analysis of vast amounts of data, a new method to extract modal parameters from parametric system identification procedures, e.g. stabilization diagrams, is presented with the triangulation-based extraction of modal parameters (TEMP). The procedure was applied successfully to data sets from the New Carquinez Bridge (NCB), the three-story benchmark data set (LANL-4DoF), the small-scale wind turbine (LANL-WT), and the full scale 5 MW plant (AV07). Table 6.1 gives an overview of different settings for TEMP in combination with SSI-Data. A rule of thump for the estimation is defined by a minimum frequency of interest f_{min} which should be set to e.g. the lowest modal frequency or a lower filter band limit. The number of extracted model order should be 4 to 10 times higher than the expected state space model order (2*number of channels). The minimum path length should then equal a half to a fourht of the extracted model orders in the stability diagram. For ϕ_{crit}, f_{crit}, ζ_{crit}, and MAC_{crit} empirical value ranges of 10-32.5°, 1-5%, 30-100%, and >0.85 should be used, respectively. The stated parameter values can be used as a basis for future research an application. Through less comparisons between solution in a stability diagram, TEMP provides a fast alternative to existing procedures.

Machine Learning, Condition Parameter, and Hypothesis Testing Machine learning was realized through manual classification and affinity propagation (AP). As shown in Figure 3.12 and in agreement with present literature, AP outperforms classical clustering approaches and is recommended if clustering is a desired ML technique. First, the necessity of clustering is shown by manual clustering with known system states at the benchmark 4-DoF system in Chapter 3.5. Performance improvement through automated clustering by AP is presented in Chapter 4. In Chapter 5, one way to evaluate the influence of different ML settings on parameter distributions within clusters was discussed with inter-percentile ranges as the width of a possible confidence interval. To assure a relatively equal number of data sets in each cluster, a moderate number of clusters is suggested. Overall, an indication of the number of clusters can be taken from the number of data sets in each cluster which should not be smaller than 15 to 20, better 50, to allow

Table 6.1: Overview of TEMP parameter for system identification at investigated structures.

Structure	f_s	f_{min}	N_{shifts}	N_{order}	ϕ_{crit}	f_{crit}	ζ_{crit}	MAC_{crit}	$\hat{P}_{crit}$
Recommended:			$f_s/f_{min}*$ 0.7	4 to $10*2*m$	10-32.5°	1-5%	30-100%	>0.85	
NCB	20 Hz	0.18 Hz	80	$100:2:300$	17.5°	1.5%	35%	0.90	50
LANL-4DoF	320 Hz	5.0 Hz	70	$100:2:300$	12.5°	1.5%	35%	0.90	50
LANL-WT	100 Hz	1.4 Hz	60	$2:2:200$	30°	5%	80%	0.88	30
AV07	50 Hz	0.3 Hz	80	$100:2:300$	32.5°	3%	50%	0.95	50

for the assessment of robust parameter distributions.

Different condition parameters have been included within the analysis; still, many others exist and need to be evaluated. Modal parameters always represent important values for the linkage to numerical models and physical phenomena and should be retained but did not have the ability to detect damage reliably. Accumulated energy proved to be a very valuable addition with a robust behavior, cheap computation, and linkage to physical changes. For the benchmark example in Chapter 3.5, a differentiation between linear and non-linear damage and damage localization is possible. In both Chapters 4 and 5 accumulated energy proved to perform very well in the range of the more complex relative CPs. Overall, the energy level between 80 and 90% energy should be used as CP. Further, the possibility of damage localization is a promising factor. VAR residues CP^{R^2}, $CP^{\mathcal{M}}$ behave well in the presented analysis, since performance stabilizes as the model order increases. In this spirit, a 'safe side' can be chosen for the model order p with $p \gtrapprox 0.7 * f_s/f_{min}$. In the benchmark case of Chapter 3.5, a relative quantification of different damage states could be achieved by $CP^{\mathcal{M}}$. Both parameters showed good performance for all three structures investigated and are considered to be of great potential. SSI based residues CP^{ε} and CP^{γ} provide even higher sensitivity to structural changes but also require more initial effort to tune parameters needed for their estimation where no safe side exist. Guidelines for their estimation given with

$$n_{shift} \lessapprox f_s/f_{min} \text{ for } CP^{\gamma} \qquad\qquad n_{shift} \approx f_s/f_{min} \text{ for } CP^{\varepsilon}$$

$$N_b \approx f_s/f_{min} \text{ for } CP^{\gamma} \qquad\qquad n_{is} \approx n_{shift} * m - n_{sig} \text{ for } CP^{\varepsilon}$$

$$n_{sig} \gtrapprox 2 * m \text{ for } CP^{\gamma}$$

proved to work well and can be used for further benchmark studies. Damage quantification was not as good as for $CP^{\mathcal{M}}$. It can be concluded that kurtosis and accumulated energies of each channel are valuable additions for damage interpretation since VAR- and SSI-based CPs only indicate a *severity* of changes and dynamics while kurtosis and accumulated energy give a physical interpretation, e.g. sign or the trend of change.

Relative CPs are formulated as residues between (at least) two data sets. In the presented studies clustering aided sensitivity and robustness of the parameters since inner-cluster uniformity is increased through clustering. Finally, a combination of different CPs in a single vector and evaluation through MSD is a promising attempt to create even more robust parameters which benefit from all included CPs. The right choice of CPs is a critical point here. It is suggested to only include single parameters from statistics or accumulated energies, or to include relative CPs multiple times into the MSD vector, since every instance in the vector is weighted equally.

Without hypothesis testing (HT), no damage identification is possible. It was shown that the variation of confidence intervals reveals important insight into the quality of a test procedure. Especially many wide vonfidence intervals with $1 - \alpha > 0.95$ should be included in the analysis. The wider the confidence interval with good performance the better. The area under the ROC curve (AUC) is concluded to be a key-component during evaluation and testing of any SHM-system. It is, again, emphasized that the optimization according to AUCs leads to an optimum

for the most difficult detection case within the given testing data sets. The assumption of normal distributed parameters within the clusters forms a good assumption for most of the investigated cases. Nevertheless, investigation of percentiles can reveal abnormal behavior and should be included.

It is stated that the modular SHM concept can be used for damage detection and partially damage localization. For the benchmark case, all damage states can be detected and accumulated energies indicate damage location. For the small-scale wind turbine, even unfavorable conditions for SHM lead to good results. For the investigation of the large-scale wind turbine, based on knowledge drawn from the foregoing examples, detection of abnormal states is possible. In future, profound confidence in different CPs, ML techniques, and HT settings will only be gained through performance evaluation of different structures with different damage scenarios.

Holistic evaluation of SHM performance   It was the goal to set up a global concept for a holistic evaluation of SHM performance with respect to the three main blocks (ML, CP, and HT) in any SHM application. A universal performance metric allows for an investigation of the four main points of variability, namely variation in:

1. Type and parameter setting for machine learning.
2. Type and parameter setting for condition parameter(s).
3. Hypothesis testing: Probability density function, control chart, and confidence interval limit.
4. Training data in number and composition of training sets.

Analysis of different realizations is carried out via the comparison of receiver operating-characteristic curves, more precisely, the area under the curve plus the Youden index. These scalar value enable the comparison of many different settings in a clear manner. All four points mentioned above play an important role for the performance. For machine learning, the adopted affinity propagation is used as clustering approach. - For the initial preference it is suggested to work with the median of the point distances, or values in the same size of magnitude. This results in a feasible amount of clusters. Clustering the database improves performance for all investigated parameters compared to the reference of a single cluster.

It is not possible to recommend one single condition parameter (CP) or setting for a perfect SHM system. It is rather recommended to combine different CPs as accumulated energies plus SSI- and VAR-residues. Including supposedly 'simple' parameters such as time-series statistics and modal parameters aids the SHM system under small expenses, giving feedback to physical phenomena in damage cases or sensor faults. Hypotheses testing (HT) is a critical point as based on the presented examples working with receiver operating characteristics and, potentially, multiple distribution types is highly recommended. The introduced performance lines aid a better visual interpretation of these charts. Having found well operating combinations of ML-CP-HT, a variation not only in testing data but also in training data is crucial for the proof of a robust SHM system. The applicability and usefulness of the concept was demonstrated on a public database as well on a more complex small-scale wind turbine with artificial damage. Finally, the Adwen

wind turbine provided a first example of how to apply the concept under circumstances where no damage can be introduced.

Changes in Structural Dynamics of Large OWTs From the long term observation of measurements at the Adwen AD5-116, different conclusions can be drawn: First, TEMP fundamentally aided the analysis of up to 19,135 data sets in an automated manner with feasible computational efforts. Secondly, assuming fixed values for modal properties of OWT is insufficient since distinct changes are documented.

Through the investigation of different states, it is concluded that soil damping can add 1% and aerodynamic damping 1.5% to the overall critical damping to the first mode for different acceleration amplitudes under standstill. The suggested, refined classification of operational states aids a simpler distinction here.

Through investigation of accumulated energies and averaged standard deviations of acceleration signals on different measurement levels, it was shown that decisive characteristics changes between standstill and in-operation from the first to the third bending mode. The shift from a dominating first global to the third global mode from standstill to operation can be explained by an increase of damping for the first (0.5 to 3.0%) and a decrease of damping for the third bending mode (3 to 1%) in combination with close rotor harmonics. Another remarkable outcome of the analysis is the switch in order of the third SS and FA mode from FA 2.2 to 2.4 Hz and SS from 2.5 to 2.2 Hz, respectively. These findings can aid the general understanding of the dynamic bahviour of wind turbines. E.g. extracted damping values, which were shown to vary over one order of magnitude in mean over different states, could improve the estimation design life to be less conservative.

6.3 Outlook

Setting up the described SHM concept and carrying out the foregoing analysis marks only the beginning of data evaluation with respect to SHM performance and structural dynamics. Of course, many other methods can and should be added within each step to challenge best performing ML-CP-HT combinations.

In the block of machine learning, further potential candidates exist with Neural-Networks and Regression analysis, to name only two. The methods may be introduced alternatively or in combination with the presented clustering approach. The formulation of how to define references for relative condition parameters (residues) in combination with supervised machine learning is an interesting point.

Condition parameters hold, probably by far, the largest potential for variation in the given four points of variability. With the derived benchmark example a quick test is possible to evaluate whether a newly derived parameter performs accurately. The investigated global SSI and VAR residues should be extended to a local version, where only a sub-set of channels is included, to reduce computational effort and include the possibility of damage localization. If sensor pairs or subgroups are used, correlations spanning over damage locations could probably differ more than those that do not. In this thesis, the attempt at cross-correlated accumulated energies

points in a similar direction. Further, major cost factors for residues are reference matrices which must be stored for every data set in the analysis. More importantly, these references must also be stored for each parameter setting of the specific relative CP, e.g. the VAR-model-order. A mathematical extension towards references from which one could extract matrices for a variety of parameter settings could improve computational speed, lower hardware requirements, and facilitate parameter studies.

In hypothesis testing, analyzing the trade-off between the usage of multivariate control charts, for instance to capture AR-coefficients from several sensors, and the usage of VAR-residues is an interesting point. In the first case, dimensionality is reduced in the HT step, while in the latter dimensionality is already reduced in the CP step. Also, rational sub-groups are frequently used in statistical quality control and could provide a possible addition.

For structural health monitoring and damage identification in general and the extraction of modal parameters in specific, the reduction of necessary sensor locations is an important goal. In this sense, the given database from *alpha ventus* provides good potential. Damage detection with a minimum sensor number was evaluated at the presented benchmark. Down-sampling is also applied to data sets from the LANL wind turbine, which can now be evaluated within the global performance . Further sensor types such as velocity, strain, and inclination should be considered as well.

Regarding the analyzed data from the test field *alpha ventus*, further data sets should be added to the database to get a larger base line for modal parameter evaluation and long-term trends. The more estimates under changing environmental and operational conditions exist for damping and frequency; the more profound models can be developed. Also, strain amplitudes should be correlated to the described behavior between standstill and revolving rotor. Recently, different planned maintenance works on both wind turbine types in *alpha ventus* provide possible verification scenarios with a variety of abnormal system states to be identified.

The presented thesis is based on a package of different Matlab functions implemented by a civil, not a software engineer, hence, implementation can be improved to speed up the analysis. Also the user-friendly integration of additional blocks for machine learning, condition parameters, and hypothesis testing should be further realized. If desired, an easy to use package could be developed to allow novice researchers to evaluate self implemented methods on different SHM levels. An adoption or fusion with the Matlab-based SHM system existing at LANL would be a good possibility to start. A transfer to LabView or SimuLink is also a desirable step towards the end user.

With the goal of an objective comparison of performances, a public benchmark database with different structures and damage types, defined by standards, would be a logical next step. Obviously, data from other structures will have to be included, as some CP might perform better for other specific damage scenarios. The database could be used to evaluate many different available condition parameters, machine learning techniques and hypothesis testing schemes on a common basis. Ultimately, only accepted benchmarks will lead to a legitimate comparison of the multitude of present methods, techniques and concepts. This could provide an important step towards the applicability and acceptance of SHM in industry and society.
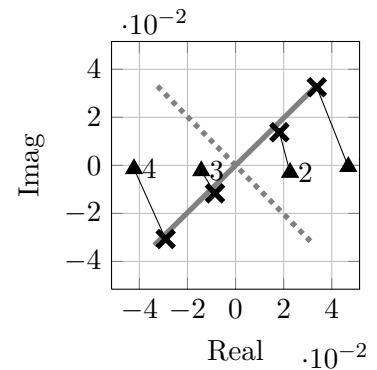
A LANL Three-Story Building Structure
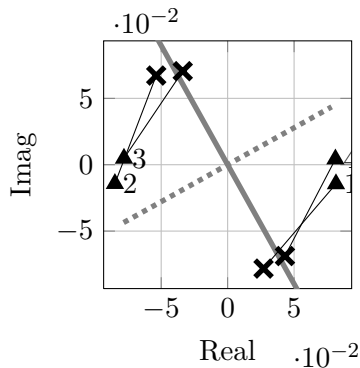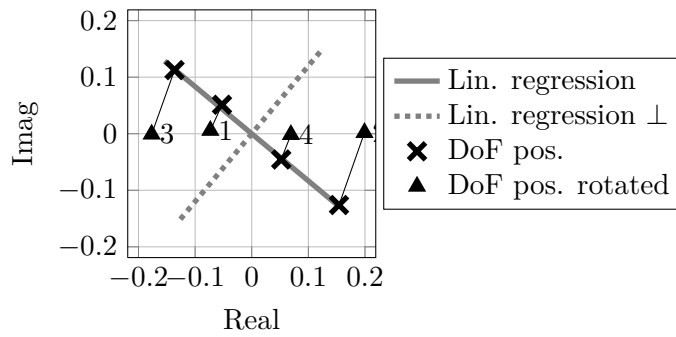
A.1 Mode Shapes
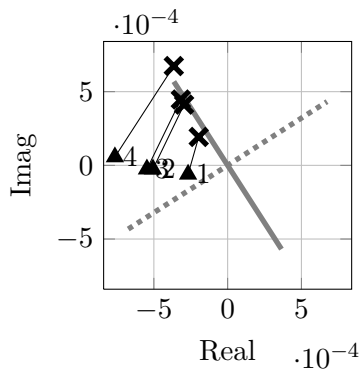
(a) 9.1 Hz in s-plane
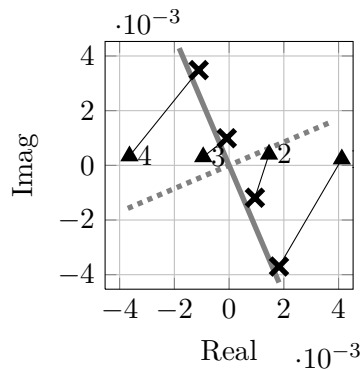
(b) 19.8 Hz in s-plane

**(c)** 29.7 Hz in s-plane

(d) 53.9 Hz in s-plane

(e) 71.5 Hz in s-plane

Figure A.1: S-plane plot for identified global bending modes 1 to 6 at LANL 4-DoF system from data set 'state01_05'. Nodes in Eigenvectors from TEMP plotted before and after rotation by mean phase-angle in complex plane (linear regression). Phase orientation for display of the mode shapes can be derived form the orthogonal dashed line.

A.2 SHM-Performance
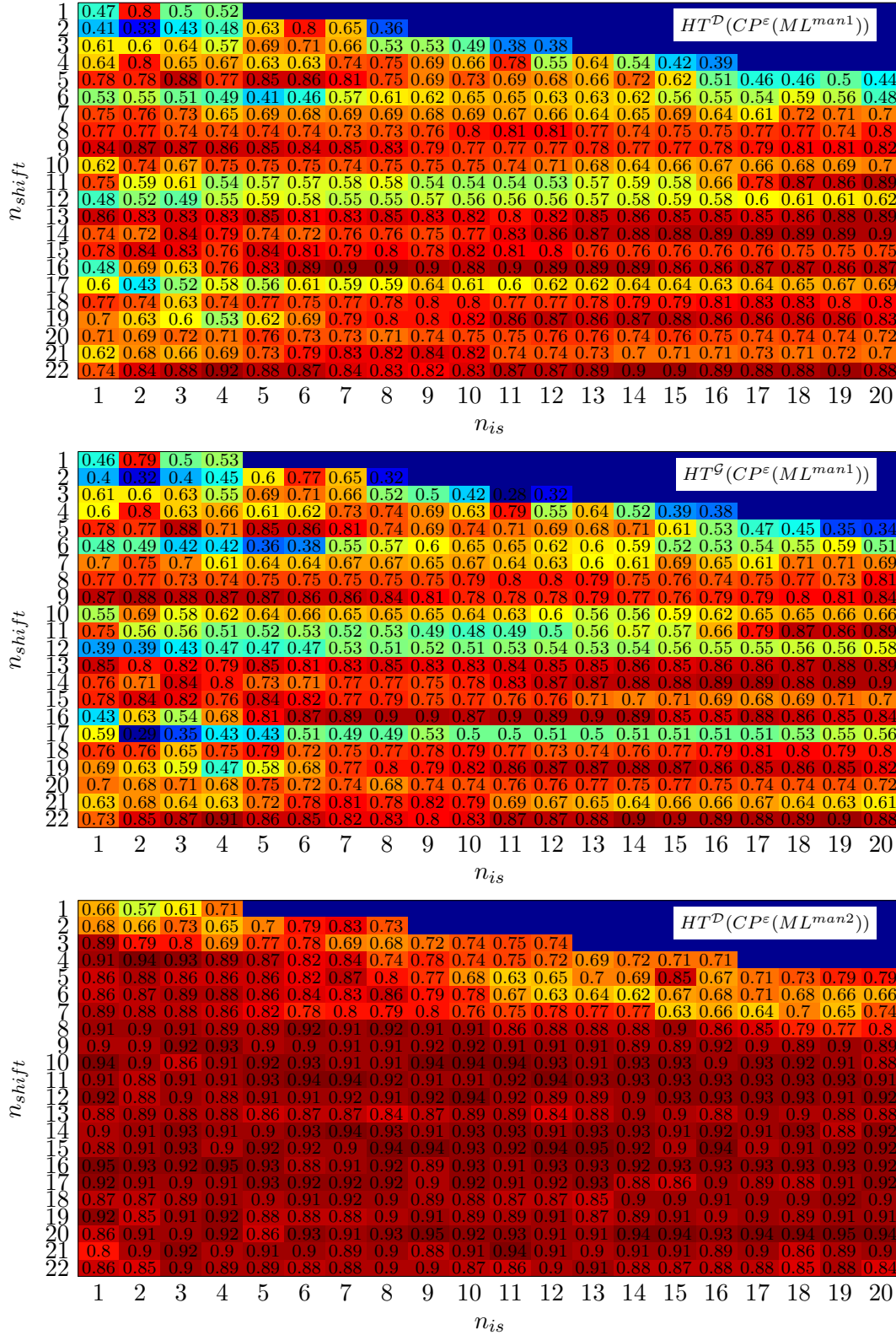
Figure A.2: Parameter study for CP^{ε} at 4-DoF system. AUCs are state for different model orders p and number of insignificant columns n_{is}. Performance values given for CP^{ε} in combination with ML^{Man_1} (1st and 2nd plot) and ML^{Man_2} (3rd plot).
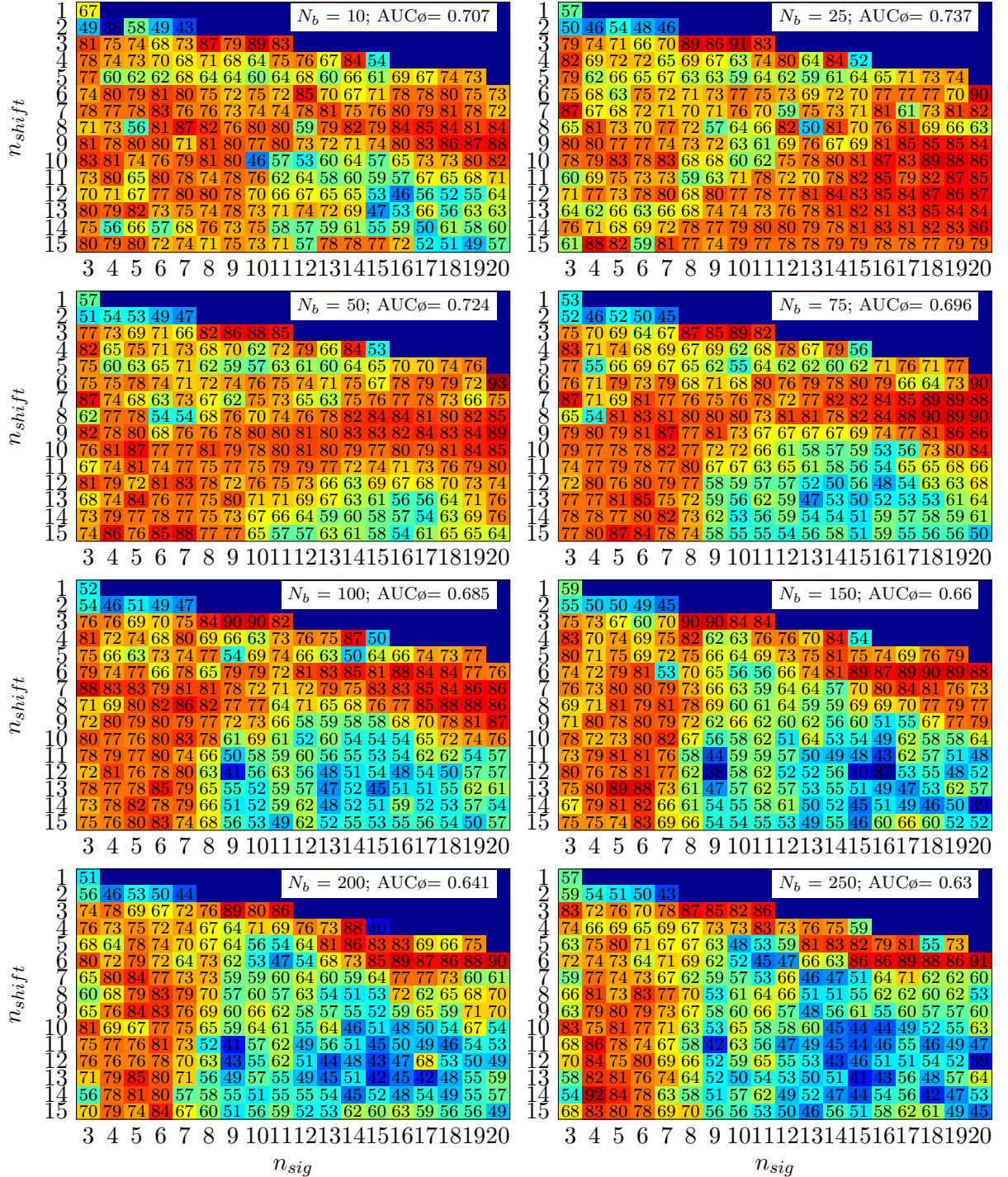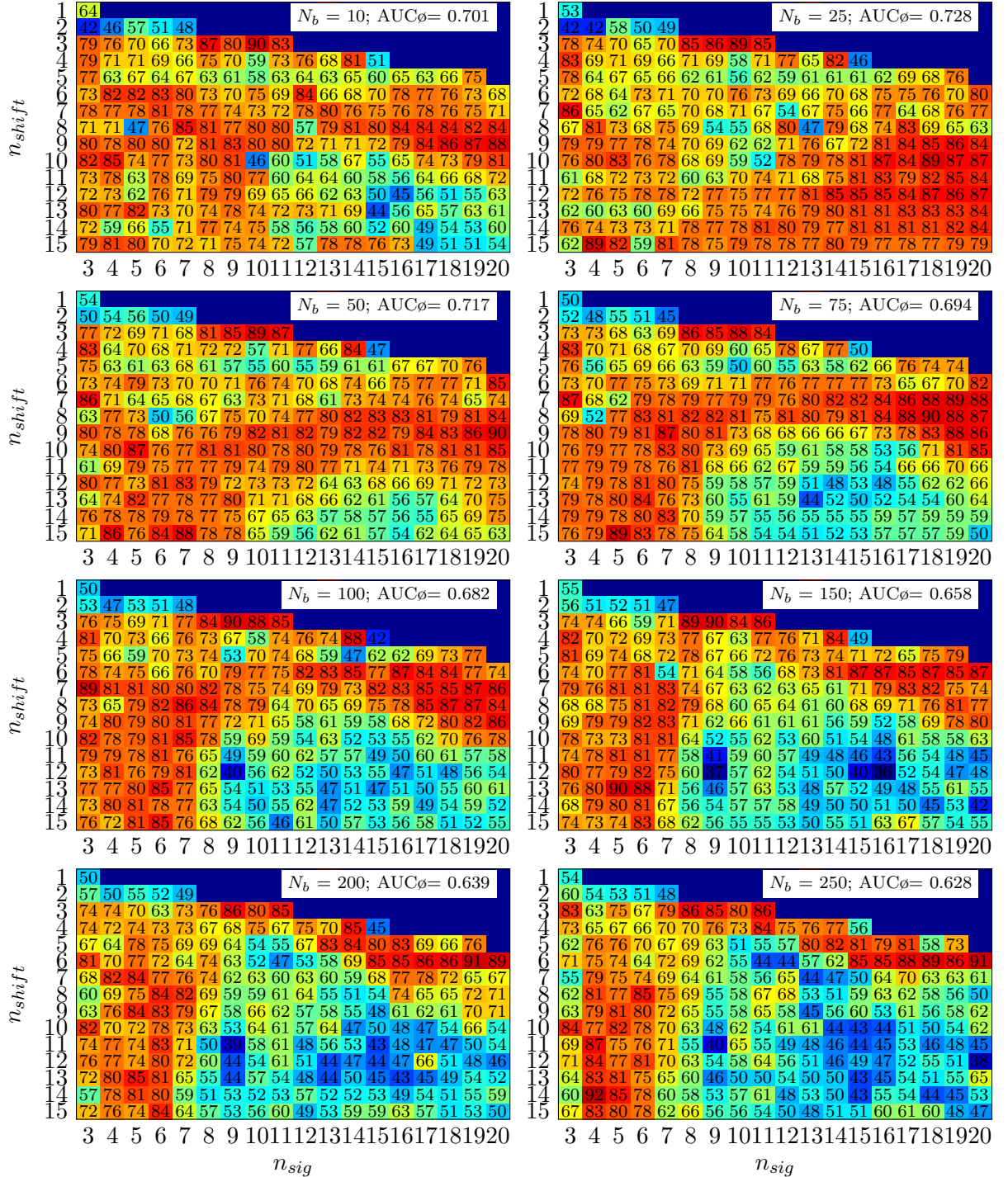
Figure A.3: Parameter study for $HT^{\mathcal{D}}(CP^{\gamma}(ML^{Man_1}))$ over different model orders p (Block size of Hankel-matrix), number of significant columns (n_{sig}), and number of samples per block (N_b). Note, that for the sake of displayability the AUC is ranging form 0 to 100 instead og 0 to 1.
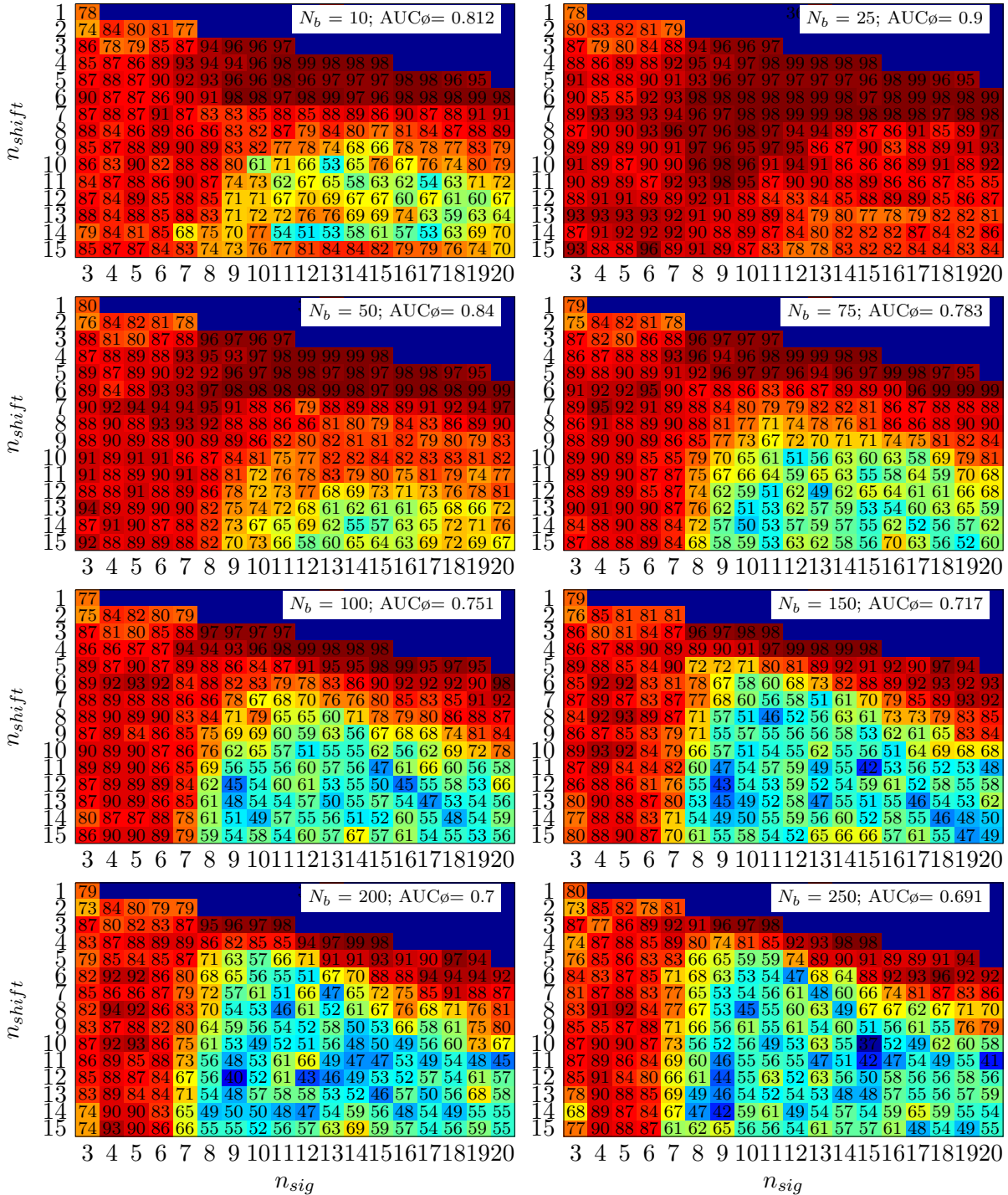
Figure A.4: Parameter study for $HT^{\mathcal{D}}(CP^{\gamma}(ML^{Man_2}))$ over different model orders p (Block size of Hankel-matrix), number of significant columns (n_{sig}), and number of samples per block (N_b). Note, that for the sake of displayability the AUC is ranging form 0 to 100 instead og 0 to 1.

Figure A.5: Parameter study for $HT^{\mathcal{G}}(CP^{\gamma}(ML^{Man_1}))$ over different model orders p (Block size of Hankel-matrix), number of significant columns (n_{sig}), and number of samples per block (N_b). Note, that for the sake of displayability the AUC is ranging form 0 to 100 instead og 0 to 1.
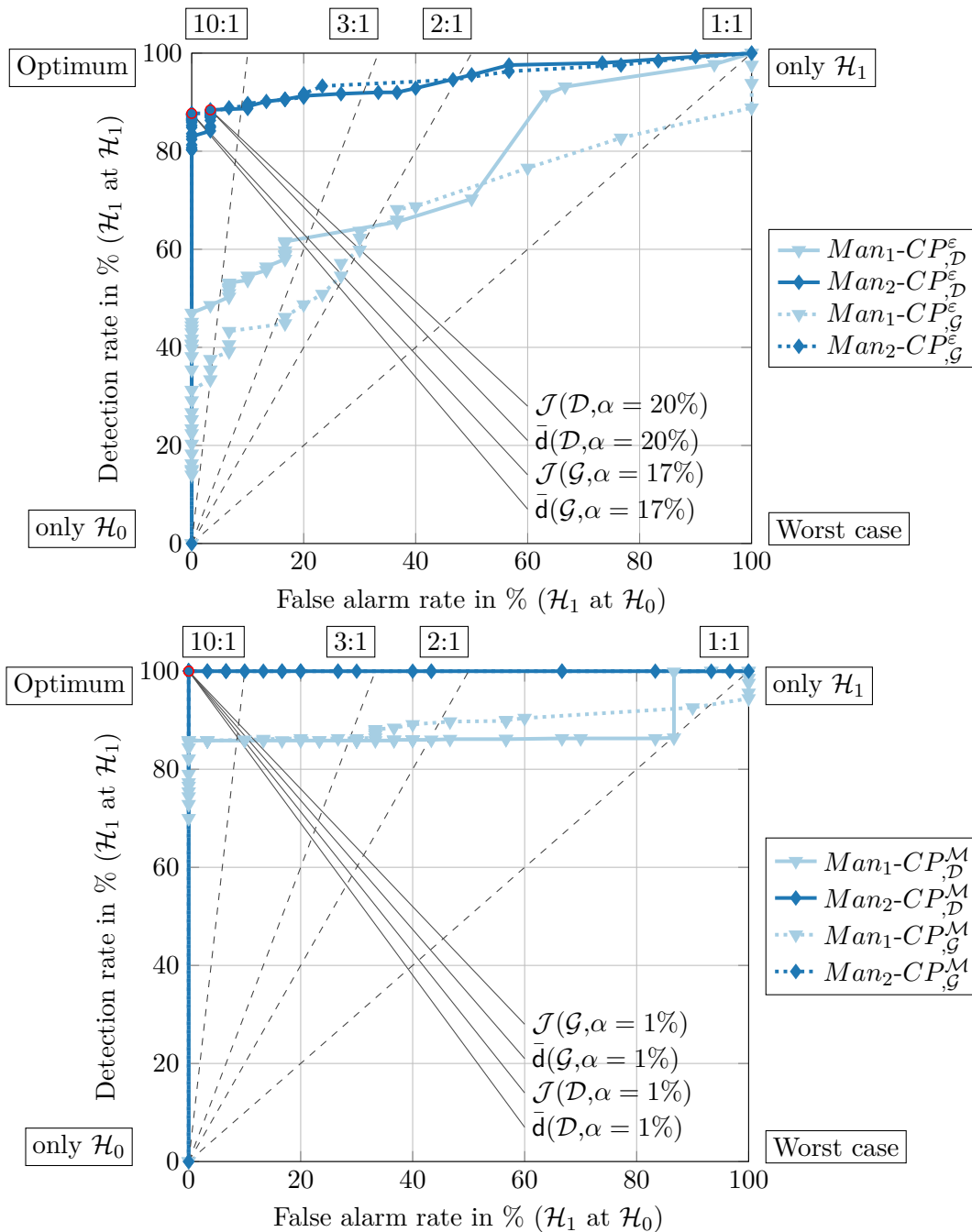
Figure A.6: ROCs for CP^ε (upper plot) and $CP^\mathcal{M}$ (lower plot). Classification "Man1" is indicated by light blue, "Man2" by dark blue, an underlying Gaussian distribution ($\mathcal{G}$) is indicated by dotted a discrete by solid lines ($\mathcal{D}$).

Table A.1: ROC metrics for different CPs. Values >0.7 are underlined whereas values >0.9 are written within a box. Further, maxima per CP (line) are set bold.

	Man_1-$\mathcal{D}$	Man_2-$\mathcal{D}$	Man_1-$\mathcal{G}$	Man_2-$\mathcal{G}$	$\bar{\text{d}}$	α	$\mathcal{J}$	α
$CP_{(1)}^{Max}$	0.398	0.451	0.392	**0.459**	38.4/43.3	0.34	19.4/16.7	0.17
$CP_{(2)}^{Max}$	0.493	**0.596**	0.485	0.593	60.6/46.7	0.5	25.6/**0**	0.17
$CP_{(3)}^{Max}$	0.609	0.575	**0.628**	0.62	51/26.7	0.36	51/26.7	0.36
$CP_{(4)}^{Max}$	0.704	0.708	**0.715**	0.703	63.6/30	0.4	40.6/**3.3**	0.15
$CP_{(1)}^{\sigma}$	0.346	0.725	0.243	**0.731**	69.1/30	0.38	69.1/30	0.38
$CP_{(2)}^{\sigma}$	0.555	**0.74**	0.526	0.733	65.9/20	0.28	59.6/**10**	0.2
$CP_{(3)}^{\sigma}$	0.712	0.76	0.706	**0.772**	65.4/16.7	0.22	63.9/13.3	0.2
$CP_{(4)}^{\sigma}$	0.648	0.705	0.643	**0.709**	56.4/23.3	0.24	41/**6.7**	0.09
$CP_{(1)}^{\gamma_1}$	0.608	**0.651**	0.615	0.63	66.6/43.3	0.6	66.6/43.3	0.6
$CP_{(2)}^{\gamma_1}$	**0.646**	0.604	0.645	0.636	59.1/36.7	0.5	41.7/13.3	0.28
$CP_{(3)}^{\gamma_1}$	0.862	0.824	**0.865**	0.828	**80.3**/16.7	0.4	71.6/**6.7**	0.24
$CP_{(4)}^{\gamma_1}$	0.769	**0.78**	0.772	0.778	59.9/**6.7**	0.16	59.9/**6.7**	0.16
$CP_{(1)}^{\gamma_2}$	0.52	0.518	**0.524**	0.513	71.1/60	0.7	71.1/60	0.7
$CP_{(2)}^{\gamma_2}$	0.499	**0.506**	0.5	0.492	58/53.3	0.6	34/26.7	0.34
$CP_{(3)}^{\gamma_2}$	0.561	**0.563**	0.563	0.525	49.6/36.7	0.5	30.6/16.7	0.26
$CP_{(4)}^{\gamma_2}$	0.701	0.672	**0.71**	0.694	57.1/26.7	0.3	39.7/**3.3**	0.07
$CP_{1,9}^{E_{yy}}$	0.669	**0.675**	0.67	0.65	55.4/26.7	0.32	41.9/**3.3**	0.19
$CP_{2,9}^{E_{yy}}$	0.68	0.919	0.652	0.922	**85.7**/10	0.1	78.9/**0**	0.03
$CP_{3,9}^{E_{yy}}$	0.735	0.887	0.651	0.918	**86.1/3.3**	0.09	**86.1/3.3**	0.09
$CP_{4,9}^{E_{yy}}$	0.718	0.718	0.705	**0.726**	60.6/20	0.2	41.7/**0**	0.04
$CP_{1,9}^{E_{xy}}$	0.728	0.888	0.715	0.905	**82.6/6.7**	0.24	**81.1/3.3**	0.19
$CP_{2,9}^{E_{xy}}$	0.71	0.939	0.659	0.941	**85.3/3.3**	0.18	**84.6/0**	0.16
$CP_{3,9}^{E_{xy}}$	0.74	0.945	0.646	0.943	**87/3.3**	0.14	**87/3.3**	0.14
$CP_{4,9}^{E_{xy}}$	0.776	0.865	0.781	**0.867**	74/**10**	0.12	68/**0**	0.03
$CP_{1,10}^{E_{yy}}$	**0.663**	0.637	0.66	0.586	57.6/30	0.4	57.6/30	0.4
$CP_{2,10}^{E_{yy}}$	0.713	**0.847**	0.718	0.847	77.7/16.7	0.13	72.3/**6.7**	0.05
$CP_{3,10}^{E_{yy}}$	0.758	**0.898**	0.773	0.893	**83.9/10**	0.06	**81.1/3.3**	0.03
$CP_{4,10}^{E_{yy}}$	0.825	0.896	0.796	**0.898**	**80.7/3.3**	0.06	78.7/**0**	0.02
$CP_{1,10}^{E_{xy}}$	0.779	0.917	0.788	0.918	**82.3/3.3**	0.14	**80.3/0**	0.06
$CP_{2,10}^{E_{xy}}$	0.739	0.877	0.746	0.902	**81.9/10**	0.11	76/**0**	0.01
$CP_{3,10}^{E_{xy}}$	0.784	0.873	0.817	**0.899**	**81.3/6.7**	0.06	79.4/**0**	0.01
$CP_{4,10}^{E_{xy}}$	0.802	0.903	0.812	0.916	**82.3/3.3**	0.16	**80/0**	0.04
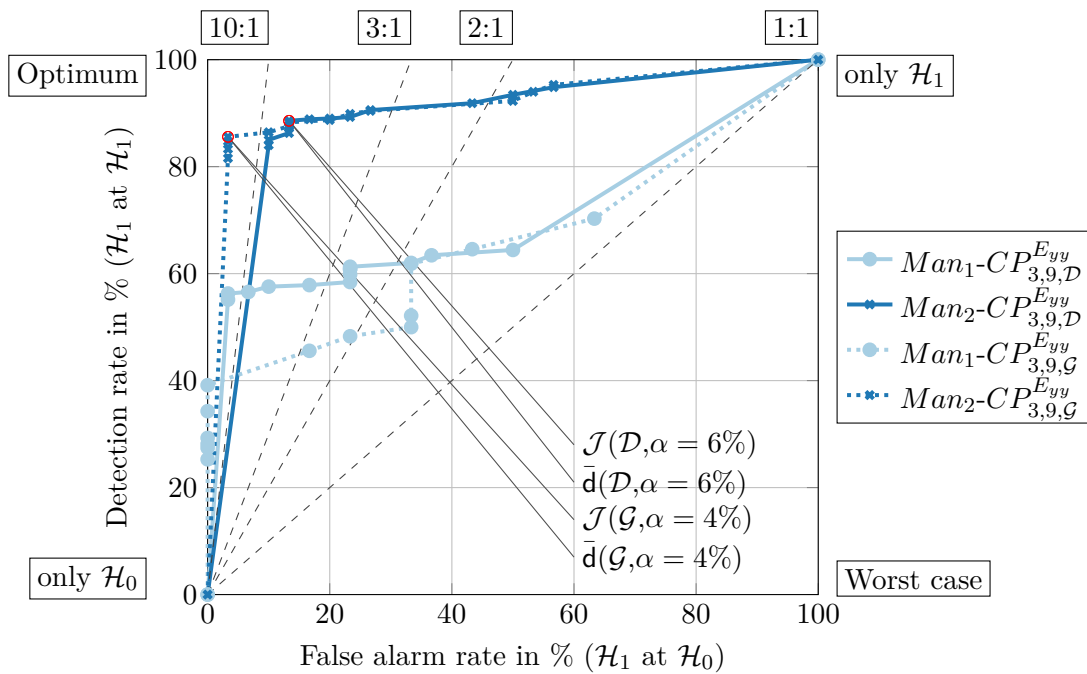
Figure A.7: ROCs for $CP_{3,9}^{E_{yy}}$, classification "Man1" is indicated by light blue, "Man2" by dark blue, an underlying Gaussian distribution ($\mathcal{G}$) is indicated by dotted a discrete by solid lines ($\mathcal{D}$).

B LANL Experimental Wind Turbine

B.1 Data Structure

Table B.1: Description of stored variable for each data set in database in Matlab format.

Dat

| Field names	Description
.Time	[2013 6 21 16 9 37]
	A datevec type vector - Vector holding start time in Matlab time format.
.Data	[12000x10 double] Acceleration time series (e.g. 24 s at 500 Hz) - channels stacked column wise.
.Fs	[double] Sampling rate in Hz
.ChannelNames	10x1 cell / Cell array with channel names
.ChannelUnits	10x1 cell / Cell array with channel units
.ChannelPos	[10x6 double]
	Matrix with channel positions and orientations: (1-3) x-;y-;z-position in m; (4-6) x-;y-;z-measurement direction (1 -> positive in xyz-direction). Global coordinate system has origin in the tower base with z-axis facing upwards and x-axis pointing away from the wire crank.
.Comm	Commentary notes as string (if available)
.EOCdat	[1x36 double]
	Row vector with environmental and operational conditions (EOCs), belonging to data set. Values are closest 15min mean values accessible on-line at LANL "The Weather Machine" . A link to a PDF that describes the weather stations is provided on-line.
.EOCinf	2x36 cell
	Cell array with EOC description (names from LANL weather machine).

B.2 Mode Shapes

Figure B.3 shows plots for mode shape 1 to 7 in the complex plane, twelve nodes (one per sensor) each. The solid lines represent the linear regression of best fit through the origin, the dotted lines an orthogonal. The orthogonal is a very important decision boundary for in- and out-of-phase movement of each node. If the complex numbers of one mode are rotated by the angle of the linear regression, and defining a reference node, phase angles for the whole mode can easily be assigned. These plots can also directly be linked to the MPD, where the deviation from a straight line in the complex plane is measured. Here, only the first mode appears as almost purely real-valued,

mode four at 7.8 Hz has the largest complex parts. In general, the modes behave well, aligning almost on straight lines giving clear decisions for the phase orientation. In general, as well as for this example, decisions about phase orientation are more critical for low amplitude nodes.
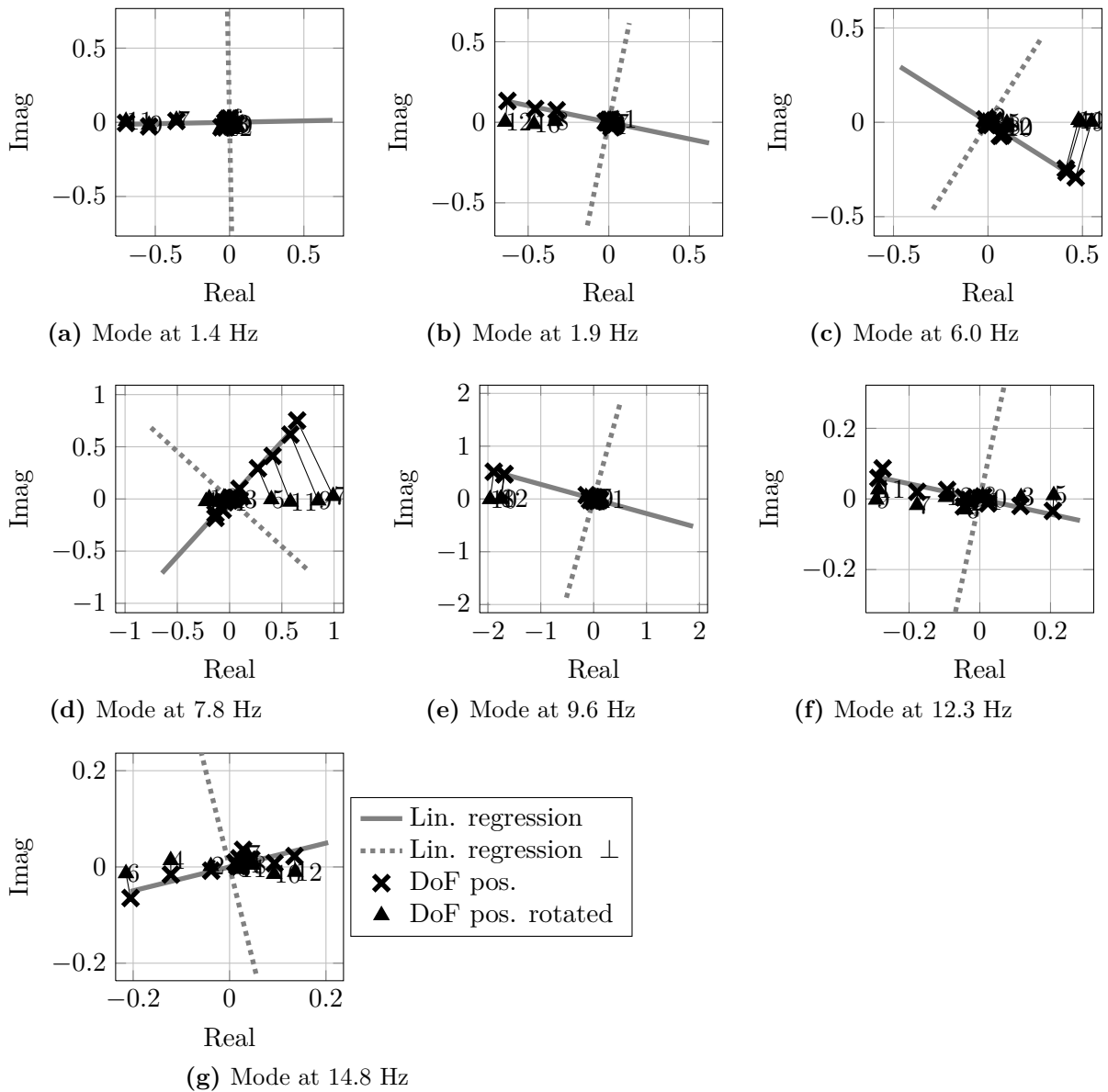

(a)

(b)
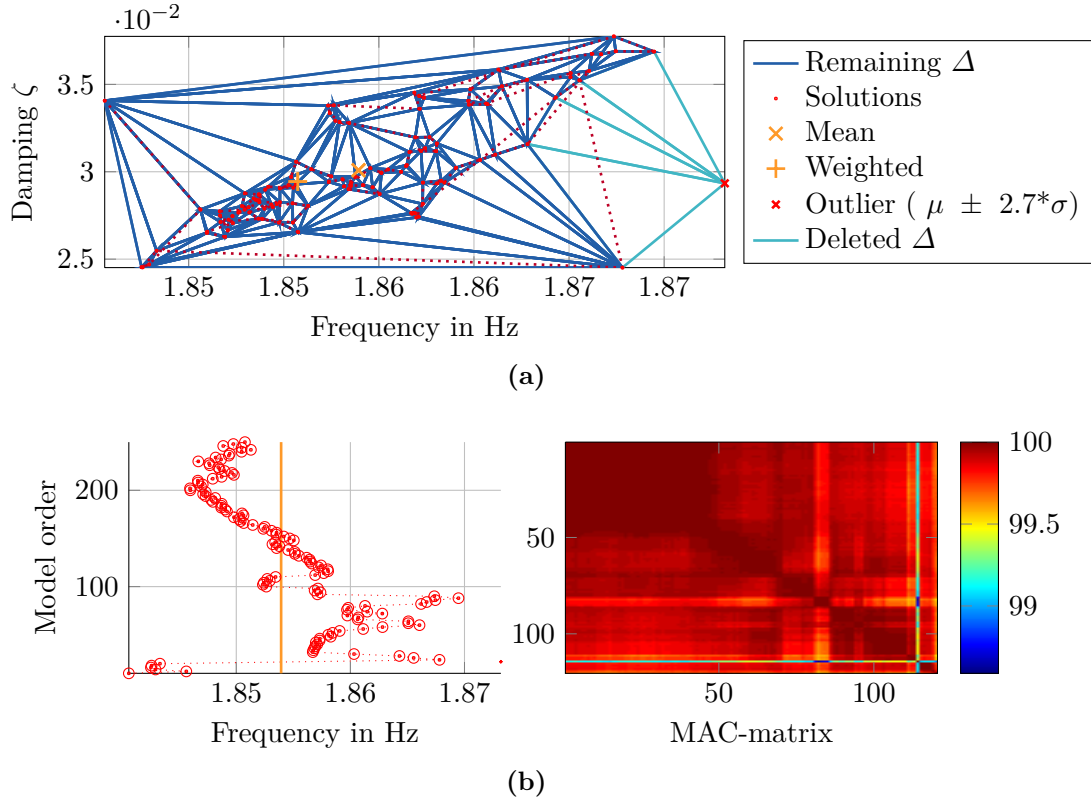
Figure B.1: Path details for second extracted mode: Close up for path in stabilization diagram (B.1b, left) and MAC matrix for all solutions within path (B.1b, right). Extracted path in frequency-damping-plane with outlier, and initial and final set of triangles(B.1a)
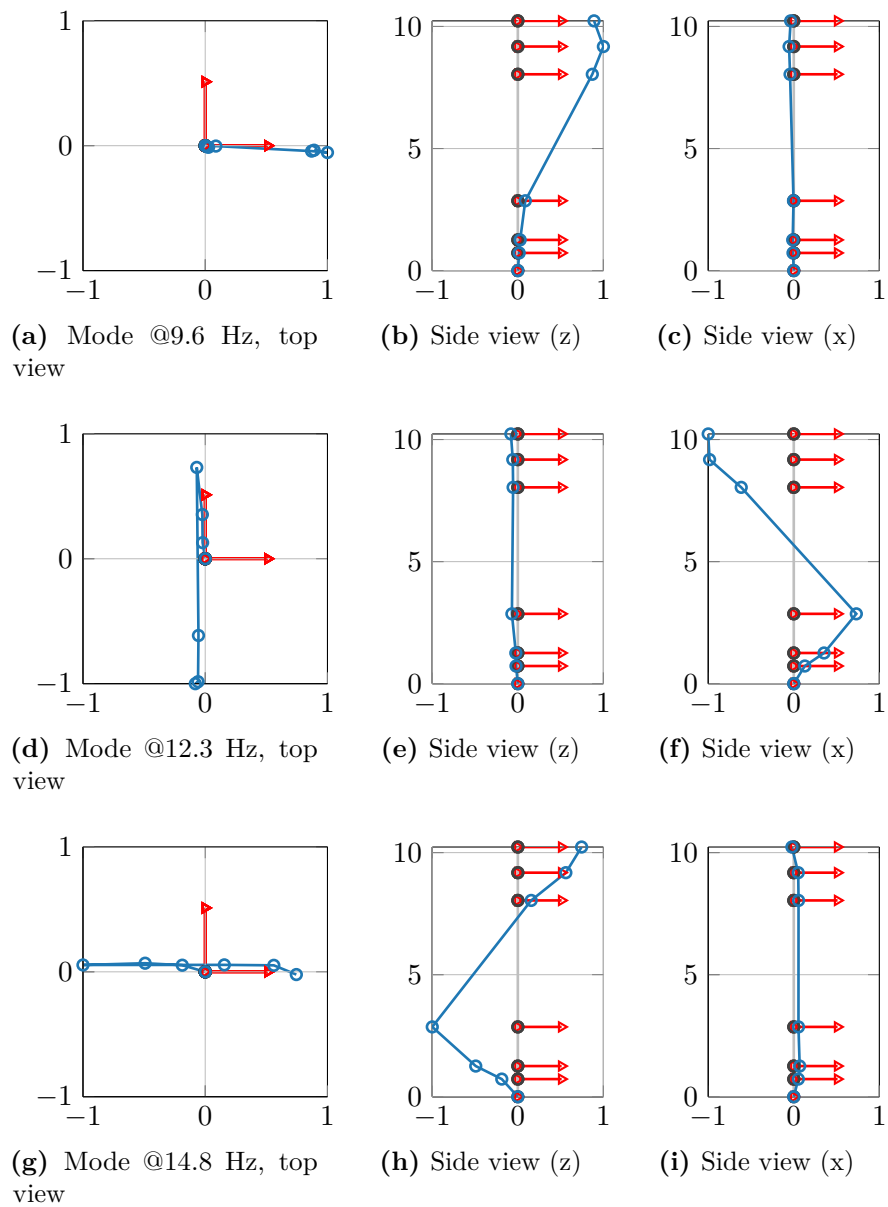
Figure B.2: Identified global bending modes for LANL wind turbine at 9.6, 12.3, and 14.8 Hz

(a) Mode at 1.4 Hz

(b) Mode at 1.9 Hz

(c) Mode at 6.0 Hz

(d) Mode at 7.8 Hz

(e) Mode at 9.6 Hz

(f) Mode at 12.3 Hz

(g) Mode at 14.8 Hz

Figure B.3: S-plane plot for identified global bending modes 1 to 7 at LANL WT system. Nodes in Eigenvectors from TEMP plotted before and after rotation by mean phase-angle in complex plane (linear regression). Phase orientation for display of the mode shapes can be derived form the orthogonal dashed line.

Table B.2: Performance overview for LANL wind turbine. Area under curve values for from receiver operating characteristic curves for different combinations of ML-CP-HT (columns 2 to 13). One CP is displayed per line. Optimal values, estimated through Youden-index and closest point to optimum are given as well (columns 14 to 17).

	$ML_D^{Man_1}$	$ML_D^{Man_2}$	$ML_D^{AP_1}$	$ML_D^{AP_2}$	$ML_D^{AP_3}$	$ML_D^{AP_4}$	$ML_G^{Man_1}$	$ML_G^{Man_2}$	$ML_G^{AP_1}$	$ML_G^{AP_2}$	$ML_G^{AP_3}$	$ML_G^{AP_4}$	$\bar{d}$	α	$\mathcal{J}$	α
$CP_{1,9}^{E_{yy}}$	0.569	<u>0.717</u>	0.632	<u>0.729</u>	<u>0.713</u>	<u>0.711</u>	0.526	<u>0.825</u>	<u>0.746</u>	<u>0.845</u>	**0.849**	<u>0.799</u>	**81**/21	0.36	38/19	0.4
$CP_{2,9}^{E_{yy}}$	0.489	<u>0.795</u>	<u>0.711</u>	<u>0.764</u>	<u>0.726</u>	<u>0.729</u>	0.433	<u>0.798</u>	<u>0.837</u>	**0.852**	<u>0.837</u>	<u>0.796</u>	78/18	0.3	41/26	0.38
$CP_{3,9}^{E_{yy}}$	0.589	0.605	0.698	0.555	0.628	0.623	0.561	<u>0.788</u>	<u>0.794</u>	<u>0.792</u>	**0.808**	<u>0.732</u>	**92**/27	0.5	46/18	0.4
$CP_{4,9}^{E_{yy}}$	0.56	0.452	0.5	0.448	0.451	0.445	0.43	0.492	**0.705**	0.61	0.669	0.598	**81**/38	0.7	22/15	0.26
$CP_{5,9}^{E_{yy}}$	0.645	0.61	0.665	0.612	0.658	0.663	0.606	0.626	<u>0.754</u>	0.686	**0.76**	0.685	78/32	0.5	65/38	0.5
$CP_{6,9}^{E_{yy}}$	0.548	0.428	0.479	0.437	0.49	0.495	0.472	0.47	**0.68**	0.568	0.672	0.607	73/39	0.7	27/21	0.4
$CP_{7,9}^{E_{yy}}$	0.541	0.59	0.579	0.577	0.631	0.619	0.524	0.64	<u>0.71</u>	0.662	**0.737**	0.686	76/26	0.5	35/14	0.4
$CP_{8,9}^{E_{yy}}$	0.529	0.545	0.637	0.544	0.604	0.6	0.488	0.627	<u>0.752</u>	<u>0.702</u>	**0.794**	<u>0.735</u>	**84**/32	0.6	35/18	0.36
$CP_{9,9}^{E_{yy}}$	0.587	0.579	0.688	0.563	0.626	0.615	0.574	0.54	**0.772**	0.616	0.699	0.638	**89**/32	0.6	41/15	0.38
$CP_{10,9}^{E_{yy}}$	0.604	0.62	<u>0.729</u>	0.575	0.674	0.682	0.604	<u>0.718</u>	**0.808**	<u>0.746</u>	<u>0.804</u>	<u>0.77</u>	73/15	0.26	57/21	0.38
$CP_{11,9}^{E_{yy}}$	0.455	0.469	0.611	0.409	0.437	0.446	0.467	0.417	**0.693**	0.547	0.626	0.56	73/27	0.5	30/23	0.38
$CP_{12,9}^{E_{yy}}$	0.663	0.507	0.577	0.522	0.469	0.479	0.573	0.548	**0.677**	0.621	0.606	0.572	62/29	0.6	32/16	0.4
CP^{ε}	0.372	<u>0.742</u>	0.575	<u>0.745</u>	0.655	0.654	0.469	<u>0.771</u>	0.513	**0.805**	<u>0.781</u>	0.668	76/14	0.5	8/4	0.7
CP^{γ}	0.448	0.164	0.336	**0.744**	0.613	0.645	0.522	0.099	0.346	0.694	0.576	0.617	76/25	0.22	89/93	0.9
$CP^{\mathcal{M}}$	<u>0.711</u>	0.355	<u>0.731</u>	<u>0.77</u>	0.677	0.694	0.697	0.607	<u>0.768</u>	**0.791**	<u>0.753</u>	<u>0.716</u>	**84**/24	0.38	65/24	0.32
CP^{R^2}	0.404	0.527	0.64	<u>0.766</u>	0.694	0.609	0.428	0.661	0.685	**0.851**	<u>0.843</u>	<u>0.793</u>	**81**/13	0.22	27/10	0.24
CP^{MSD}	<u>0.788</u>	0.569	<u>0.747</u>	0.903	<u>0.755</u>	<u>0.759</u>	0.65	0.537	<u>0.746</u>	**0.908**	<u>0.798</u>	<u>0.76</u>	**89**/14	0.001	81/68	0.11

C AV07

C.1 Mode Shapes

(a) $f = 0.933$ Hz

(b) $f = 1.19$ Hz

(c) $f = 0.933$ Hz

(d) $f = 1.19$ Hz
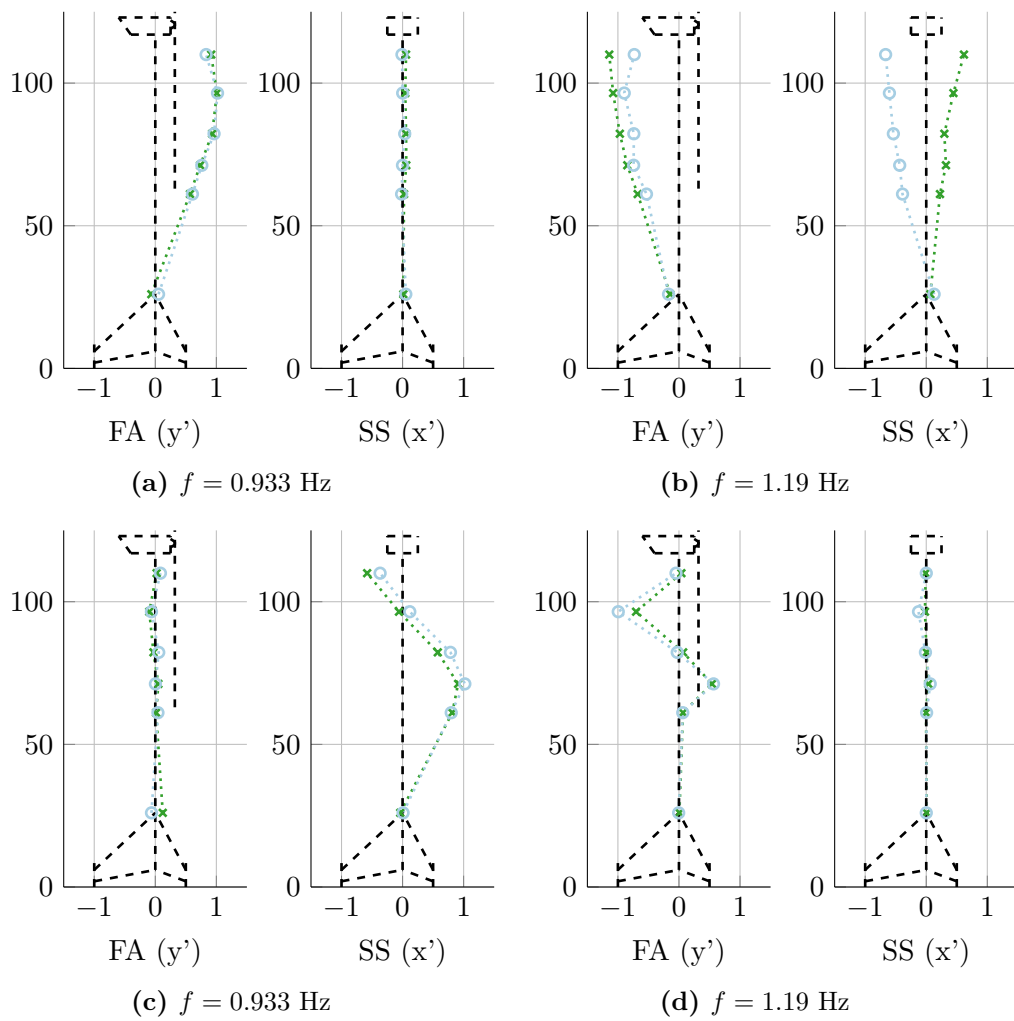
Figure C.1: Additional modes in FA- and SS-plane for AV07.
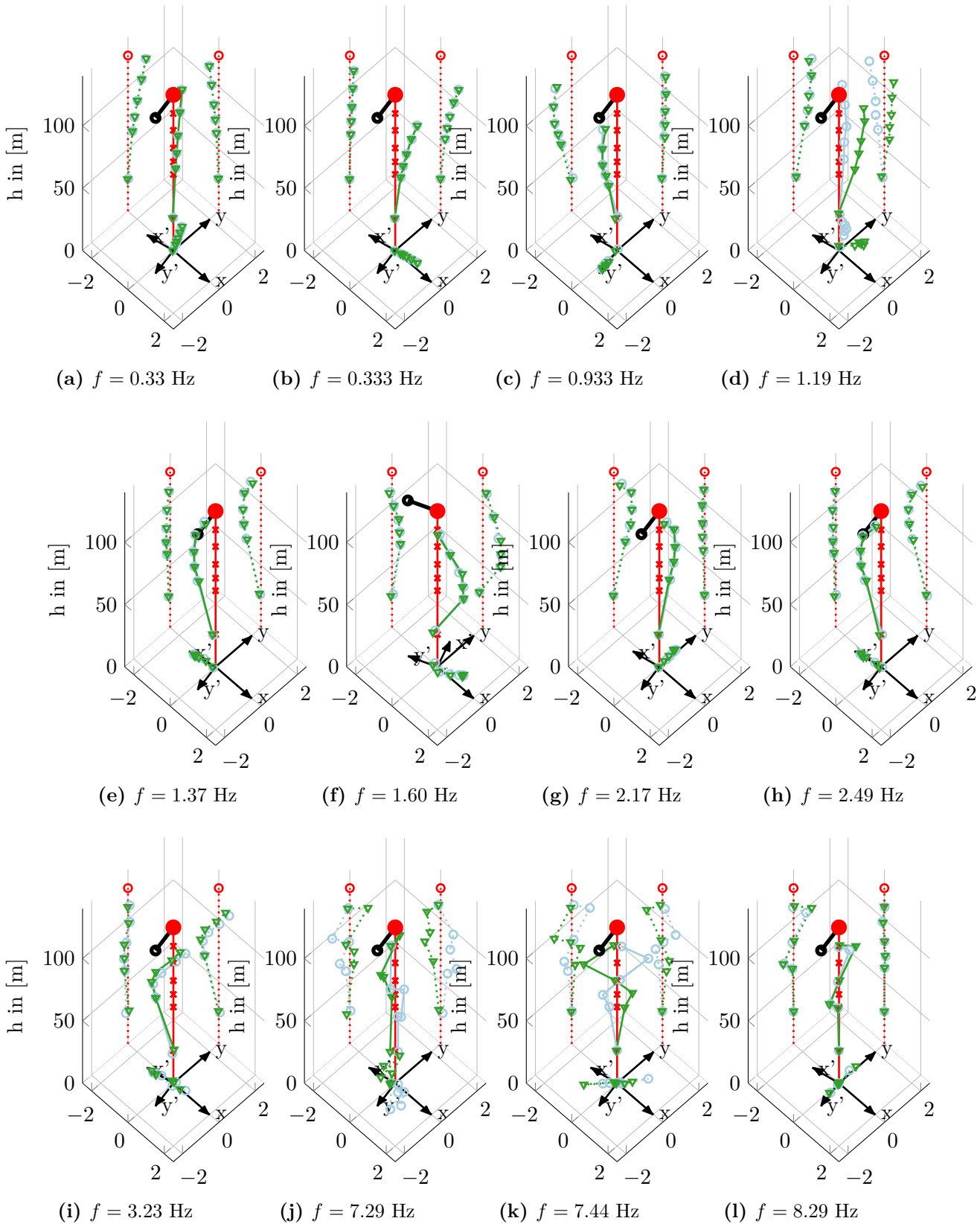
Figure C.2: Three-dimensional, global Eigenvectors of offshore wind energy converter below 10 Hz including projections in global xz- and yz-plane. Rotated coordinate system indicates nacelle position, blue and turquoise the southern and northern sensors within the tower, respectively. Note that the mode for f=1.60 Hz was taken from a different data set and hence nacelle orientation.
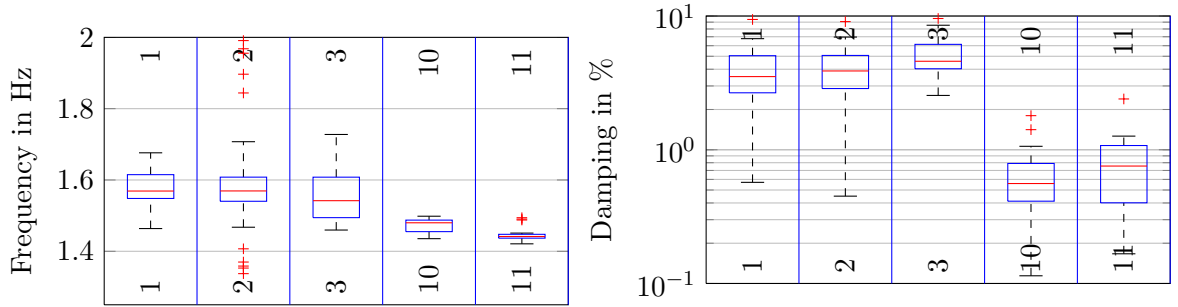
(a) Frequency and damping distributions for FA-2 at $f = 3.23$ Hz
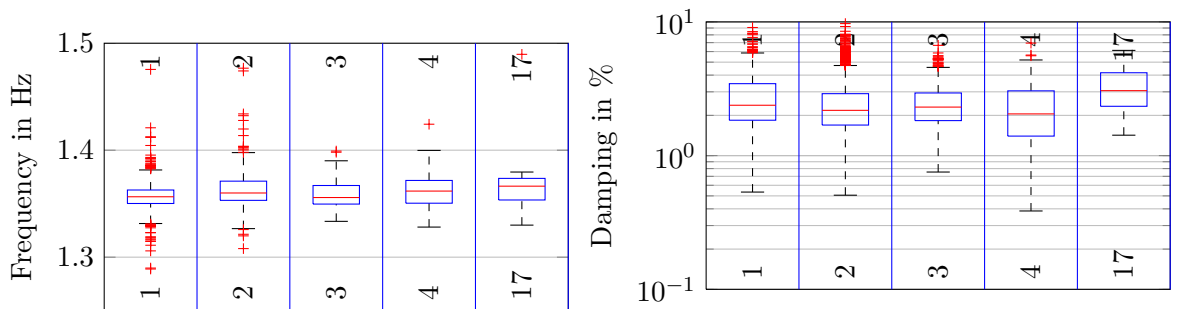
(b) Frequency and damping distributions for SS-2 at $f = 8.29$ Hz
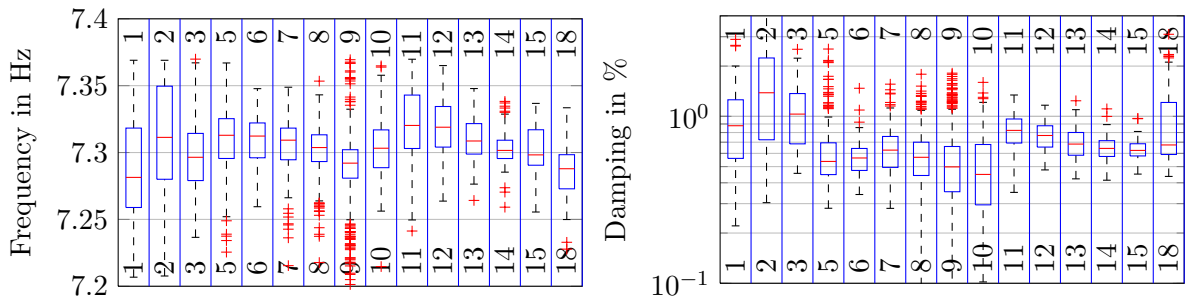
(c) Frequency and damping distributions for T-1 at $f = 7.29$ Hz
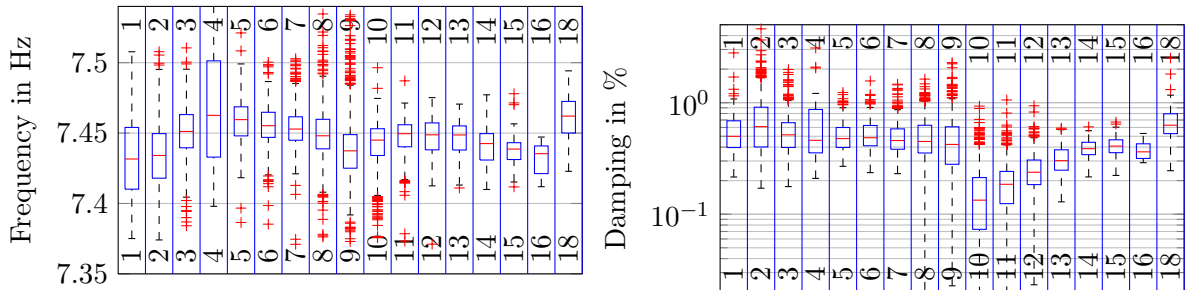
(d) Frequency and damping distributions for T-2 at $f = 7.44$ Hz

Figure C.3: EOC influences on second bending mode of AV07 offshore wind energy converter below 2.5 Hz. Boxplots show mean (red line), 25% and 50% percentiles (blue box), 5% and 95% percentiles (whiskers), and outliers (red crosses, outside $\mu \pm 2.7\sigma$)

C.2 SHM Performance
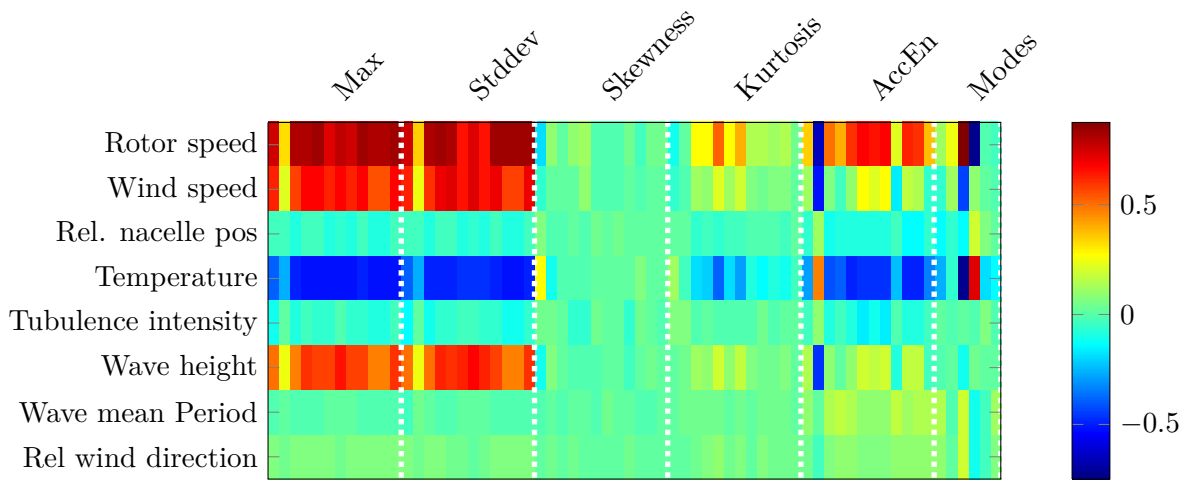
Figure C.4: Correlation coefficients between investigated EOCs and absolute CP for the complete AV07 database. Vertical lines in white separate CP-groups of 12 columns, one for each data channel. For modal parameter FA-1, SS-1, FA-2, SS-2, T-1, and T-2 are displayed (last six columns).
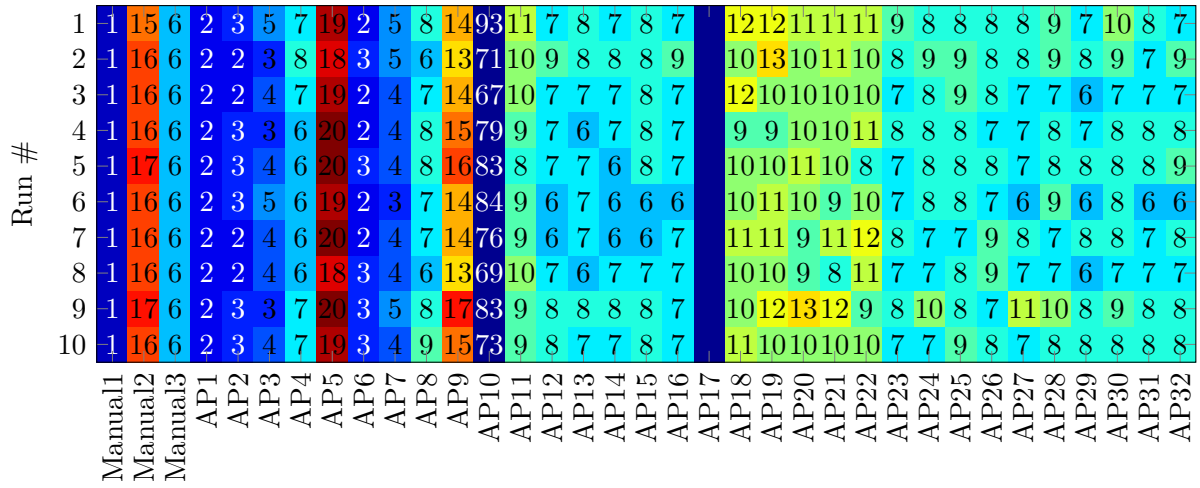
Figure C.5: Number of clusters for different machine learning settings over ten runs with randomly chosen training data for AV07. 250 training sets each.
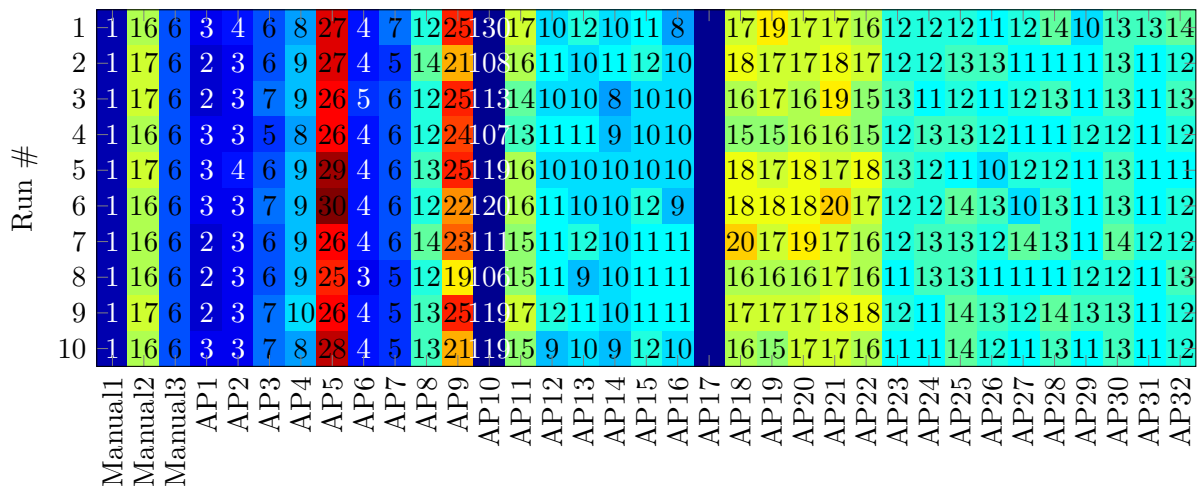
Figure C.6: Number of clusters for different machine learning settings over ten runs with randomly chosen training data for AV07. 500 training sets each.
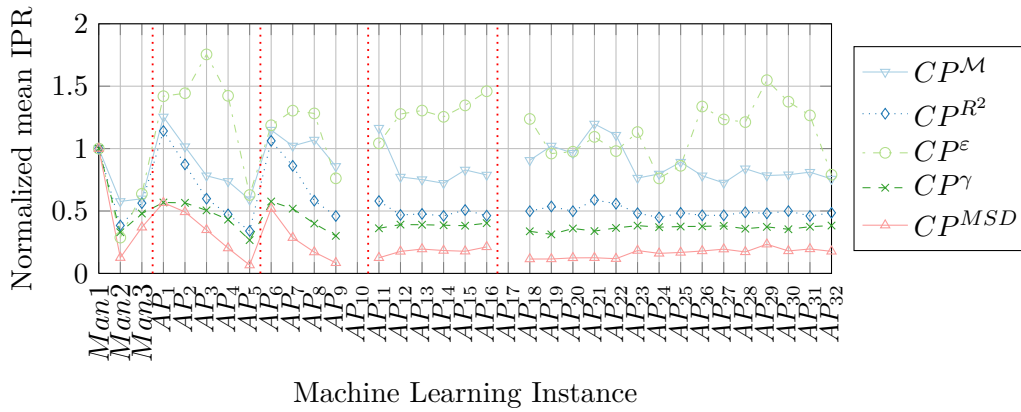
Figure C.7: CP variation for different ML instances at $AV07$: Averaged inter-percentile-ranges (IPRs) for relative CPs from SSI and VAR, 250 training sets used. All values are normalized with respect to the reference ML instance Manual1.
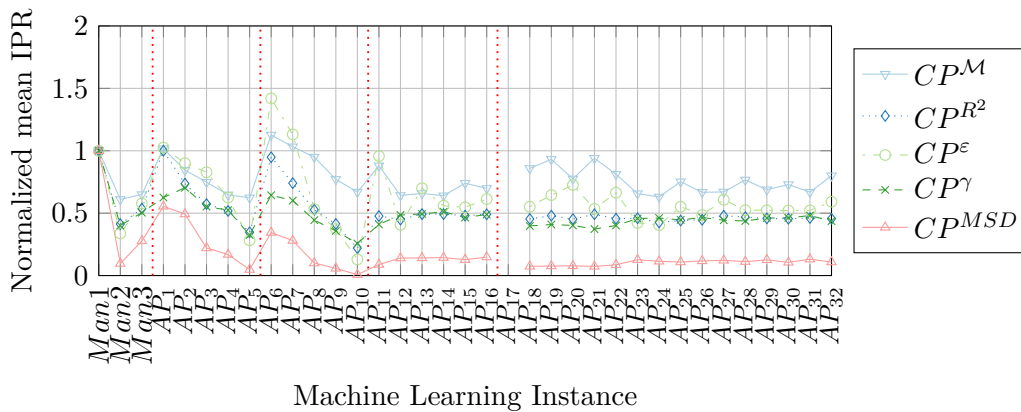
Figure C.8: CP variation for different ML instances at $AV07$: Averaged inter-percentile-ranges (IPRs) for relative CPs from SSI and VAR, 5000 training sets used. All values are normalized with respect to the reference ML instance Manual1.

Figure C.9

Figure C.10: SHM perfromance overview for AV07: AUC values for 1.925 ML-CP-HT combinations. ML-CP combinations for the evaluation of a discrete distribution within each cluster. Only every 2nd y-label is set for $CP^{E}_{i,10}$ and $CP^{E}_{i,p}$ for readability.

Bibliography

[1] D. Adams, J. White, M. Rumsey, and C. Farrar. Structural health monitoring of wind turbines: method and application to a HAWT. *Wind Energy*, 14(4):603–623, May 2011. ISSN 10954244. doi: 10.1002/we.437. URL `http://doi.wiley.com/10.1002/we.437`.

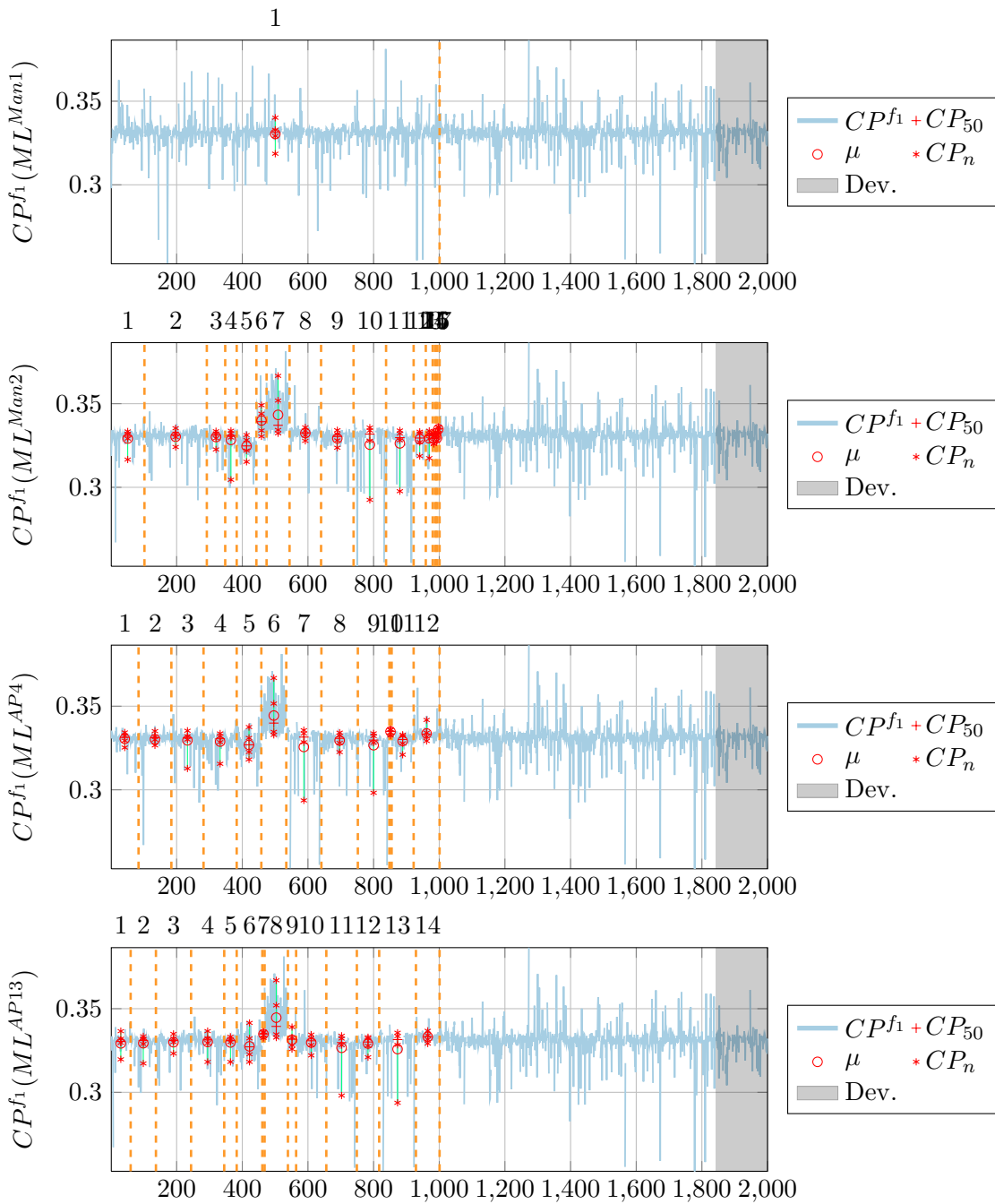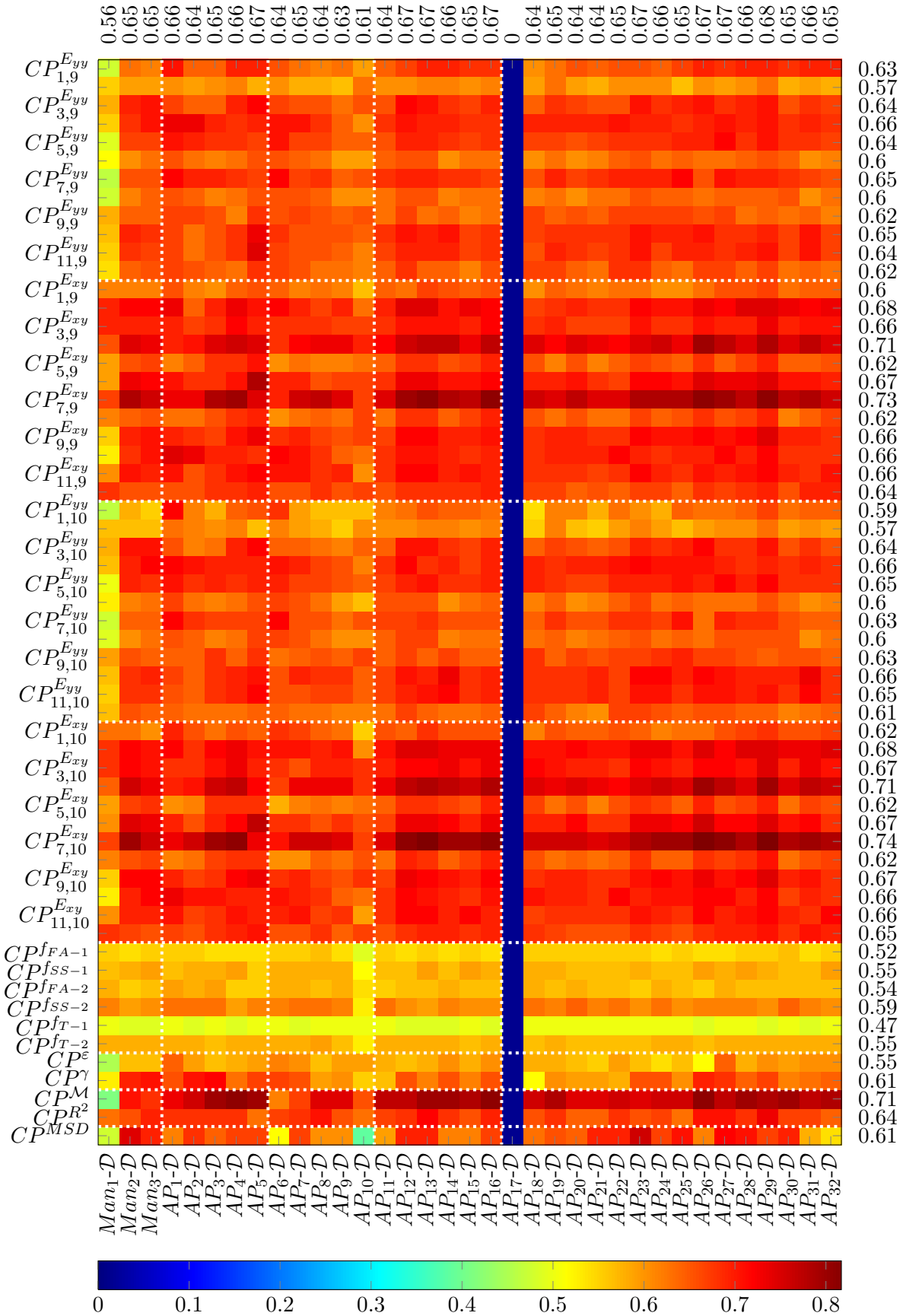[2] A. K. Akobeng. Understanding diagnostic tests 3: receiver operating characteristic curves. *Acta Paediatrica*, 96(5):644–647, May 2007. ISSN 0803-5253, 1651-2227. doi: 10.1111/j.1651-2227.2006.00178.x. URL `http://doi.wiley.com/10.1111/j.1651-2227.2006.00178.x`.

[3] R. Allemang, D. Brown, and A. Phillips. Survey of Modal Techniques Applicable to Autonomous/Semi-Autonomous Parameter Identification. In *Proceedings, International Conference on Noise and Vibration Engineering (ISMA)*, pages 3331–3373, 2010.

[4] R. Allemang, A. Phillips, and D. Brown. Autonomous Modal Parameter Estimation: Statisical Considerations. In *Modal Analysis Topics, Volume 3*, pages 385–401. Springer, 2011.

[5] R. J. Allemang. The modal assurance criterion–twenty years of use and abuse. *Sound and Vibration*, 37(8):14–23, 2003.

[6] R. J. Allemang and D. L. Brown. A correlation coefficient for modal vector analysis. In *Proceedings of the 1st International Modal Analysis*, volume 1, pages 110–116. Union Coll, Schenectady, NY, USA, 1982. URL `http://www.scopus.com/inward/record.url?eid=2-s2.0-0020220627&partnerID=40&md5=7ec86b8729d44a046fd688dda77af23e`.

[7] P. Andersen. *Identification of Civil Engineering Structures using Vector ARMA Models*. PhD thesis, Aalborg University, Department of Building Technology and Structural Engineering, 1997. URL `http://vbn.aau.dk/files/98944/p_andersen01.pdf`.

[8] P. Andersen and P. H. Kirkegaard. Statistical damage detection of civil engineering structures using ARMAV models. In *Proceedings of the 16th International Modal Analysis Conference*, volume 3243 (1), pages 356–362, Bethel Conn. USA, 1998. Society for Experimental Mechanics. ISBN 978-0-912053-59-2.

[9] P. Andersen, R. Brincker, M. Goursat, and L. Mevel. Automated modal parameter estimation for operational modal analysis of large systems. In *Proceedings of the 2 nd International Operational Modal Analysis Conference*, pages 299–308, Copenhagen, Denmark, 2007.

[10] L. D. Avendaño-Valencia, M. D. Spiridonakos, and S. D. Fassois. In-Operation Identification of a Wind Turbine Structure via Non-Stationary Parametric Models. In *Proceedings of the 8th International Workshop on Structural Health Monitoring*, pages 2611–2618, Stanford, CA, USA, 2011. Chang, F.-K. (Ed.), DEStech Publications Inc.

[11] J. Bas, J. Smith, R. Carriveau, S. Cheng, D. S.-K. Ting, and T. Newson. Structural Response of a Commercial Wind Turbine to Various Stopping Events. *Wind Engineering*, 36(5):553–570, Oct. 2012. ISSN 0309-524X. doi: 10.1260/0309-524X.36.5.553. URL `http://multi-science.metapress.com/openurl.asp?genre=article&id=doi:10.1260/0309-524X.36.5.553`.

[12] K. Bassett. *Vibration Based Structural Health Monitoring for Utility Scale Wind Turbines*. Thesis (M.A.Sc.), University of Windsor, Windsor, Canada, 2010.

[13] M. Basseville, L. Mevel, and M. Goursat. Statistical model-based damage detection and localization: subspace-based residuals and damage-to-noise sensitivity ratios. *Journal of Sound and Vibration*, 275(3-5):769–794, Aug. 2004. ISSN 0022460X. doi: 10.1016/j.jsv.2003.07.016. URL `http://linkinghub.elsevier.com/retrieve/pii/S0022460X03009556`.

[14] J. Bendat. *Random Data : Analysis and Measurement Procedures*. Wiley, New York, 1971. ISBN 978-0-471-06470-1.

[15] M. Benedetti, V. Fontanari, and D. Zonta. Structural health monitoring of wind towers: remote damage detection using strain sensors. *Smart Materials and Structures*, 20(5):055009, May 2011. ISSN 0964-1726, 1361-665X. doi: 10.1088/0964-1726/20/5/055009. URL `http://stacks.iop.org/0964-1726/20/i=5/a=055009?key=crossref.4bd46348aaa3b5b4fb91e17674044f76`.

[16] M. Benedetti, V. Fontanari, and L. Battisti. Structural health monitoring of wind towers: residual fatigue life estimation. *Smart Materials and Structures*, 22(4):045017, Apr. 2013. ISSN 0964-1726, 1361-665X. doi: 10.1088/0964-1726/22/4/045017. URL `http://stacks.iop.org/0964-1726/22/i=4/a=045017?key=crossref.70d40dc662e2028cba548ecaa7cb35c0`.

[17] J. C. Bezdek. *Pattern Recognition with Fuzzy Objective Function Algorithms*. Kluwer Academic Publishers, Norwell, MA, USA, 1981. ISBN 0-306-40671-3.

[18] C. Bishop. *Neural networks for pattern recognition*. Oxford Univ. Press, Oxford, repr. edition, 1999. ISBN 978-0-19-853864-6.

[19] J. B. Bodeux and J. C. Golinval. Application of ARMAV models to the identification and damage detection of mechanical and civil engineering structures. *Smart Materials and Structures*, 2001(10):479–489, 2000.

[20] A. W. Bowman. An alternative method of cross-validation for the smoothing of density estimates. *Biometrika*, 71(2):353–360, 1984.

[21] G. Box. A general distribution theory for a class of likelihood criteria. *Biometrika*, 36(3/4): 317–346, 1949.

[22] G. E. P. Box, G. M. Jenkins, and G. C. Reinsel. *Time Series Analysis: Forecasting and Control*. Holden-Day series in time series analysis and digital processing. Holden-Day, ISBN 0-8162-1104-3, 1976. ISBN 0-8162-1104-3.

[23] R. Brincker and P. Andersen. {ARMA} models in modal space. In *Proceedings of the 17th International Modal Analysis Conference (IMAC)*, volume 3727 (2), pages 330–334, Bethel Conn., Feb. 1999. Society for Experimental Mechanics. ISBN 0-912053-64-X.

[24] R. Brincker and P. Andersen. Understanding Stochastic Subspace Identification. In *Proceedings of the 24th International Modal Analysis Conference (IMAC)*, St. Louis, Missouri, 2006.

[25] R. Brincker, L. Zhang, and P. Andersen. Output only modal analysis by frequency domain decomposition. In *Proceedings of the 25th International Seminar on Modal Analysis (ISMA)*, volume 2, pages 717–723, Leuven, Belgium, 2000.

[26] R. Brincker, L. Zhang, and P. Andersen. Modal identification of output-only systems using frequency domain decomposition. *Smart Materials and Structures*, 10:441–445, June 2001. ISSN 0964-1726, 1361-665X. doi: 10.1088/0964-1726/10/3/303. URL `http://stacks.iop.org/0964-1726/10/i=3/a=303?key=crossref.b39fbefdd1466d5de601c6b088f9bc63`.

[27] R. Brincker, P. Andersen, and C. E. Ventura. Why Output-Only Modal Testing is a Desirable Tool for a Wide Range of Practical Applications. In *Proceedings of the 13 th International Modal Analysis Conference (IMAC XIII)*, pages 668–674, Nashville, Tennessee, USA, 2003. URL `http://scholar.googleusercontent.com/scholar?q=cache:II4fsf9PvUIJ:scholar.google.com/+%22why+output-only+modal%22&hl=en&as_sdt=0,5`.

[28] R. Brincker, P. Andersen, and N. Jacobsen. Automated frequency domain decomposition for operational modal analysis. In *Proceedings of The 25th International Modal Analysis Conference (IMAC), Orlando, Florida*, 2007.

[29] D. Brown, R. Allemang, and A. Phillips. Autonomous Modal Parameter Estimation: Application Examples. In *Modal Analysis Topics, Volume 3*, pages 403–428. Springer, 2011.

[30] T. Burton, D. Sharpe, N. Jenkins, and E. Bossanyi. *Wind energy handbook*. Wiley, Chichester, 2011. ISBN 978-0-470-69975-1 0-470-69975-2.

[31] S. Butterfield, S. Sheng, and F. Oyague. Wind Energy's New Role in Supplying the World's Energy_what Role will Structural Health Monitoring Play. In *Proceedings of the 8th International Workshop on Structural Health Monitoring*, Stanford, CA, USA, 2009. Chang, F.-K. (Ed.), DEStech Publications Inc.

[32] E. P. Carden and J. M. W. Brownjohn. Fuzzy Clustering of Stability Diagrams for Vibration-Based Structural Health Monitoring. *Computer-Aided Civil and Infrastructure Engineering*, 23(5):360–372, July 2008. ISSN 1093-9687, 1467-8667. doi: 10.1111/j.1467-8667.2008.00543.x. URL `http://doi.wiley.com/10.1111/j.1467-8667.2008.00543.x`.

[33] C. C. Chang and Z. Sun. Structural damage localization using spatial wavelet packet signature. *Smart Structures and Systems*, 1(1):29–46, 2005. URL `http://technopress.kaist.ac.kr/download.php?journal=sss&volume=1&num=1&ordernum=3`.

[34] J. Chipka, A. Lisicki, C. Nguyen, S. Taylor, G. Park, C. Ammerman, and C. Farrar. Experimental Characterization and Predictive Modeling of a Residential-Scale Wind Turbine. In F. N. Catbas, S. Pakzad, V. Racic, A. Pavic, and P. Reynolds, editors, *Topics in Dynamics of Civil Structures, Volume 4*, Conference Proceedings of the Society for Experimental Mechanics Series, pages 521–533. Springer New York, 2013. ISBN 978-1-4614-6554-6. URL `http://dx.doi.org/10.1007/978-1-4614-6555-3_56`.

[35] A. Clement and S. Laurens. Vibration-based damage detection in a concrete beam under temperature variations using AR models and state-space approaches. *Journal of Physics: Conference Series*, 305:012040, July 2011. ISSN 1742-6596. doi: 10.1088/1742-6596/305/1/012040. URL `http://stacks.iop.org/1742-6596/305/i=1/a=012040?key=crossref.b987c8009ae6b9cb5beb6c537785b7c7`.

[36] N. Cottin. Dynamic Model Updating - A Multiparameter Eigenvalue Problem. *Mechanical Systems and Signal Processing*, 15(4):649–665, July 2001. ISSN 08883270. doi: 10.1006/mssp.2000.1362. URL `http://linkinghub.elsevier.com/retrieve/pii/S0888327000913621`.

[37] N. Cottin and J. Reetz. Accuracy of multiparameter eigenvalues used for dynamic model updating with measured natural frequencies only. *Mechanical Systems and Signal Processing*, 20(1):65–77, Jan. 2006. ISSN 08883270. doi: 10.1016/j.ymssp.2004.10.005. URL `http://linkinghub.elsevier.com/retrieve/pii/S0888327004001682`.

[38] C. J. Crabtree. *Condition monitoring techniques for wind turbines*. PhD thesis, Durham University, 2011.

[39] C. J. Crabtree, P. J. Tavner, W. Yang, C. Booth, and S. Watson. Survey of Commercially Available Condition Monitoring Systems for Wind Turbines. Survey 05, Durham University of Engineering and Computing Science for UK EPSRC Supergen Wind Energy Technologies Consortium, 2010.

[40] E. J. Cross, K. Y. Koo, J. M. W. Brownjohn, and K. Worden. Long-term monitoring and data analysis of the Tamar Bridge. *Mechanical Systems and Signal Processing*, 35(1–2): 16 – 34, 2013. ISSN 0888-3270. doi: http://dx.doi.org/10.1016/j.ymssp.2012.08.026. URL `http://www.sciencedirect.com/science/article/pii/S0888327012003573`.

[41] L. d. F. Da Costa and R. M. Cesar. *Shape analysis and classification: theory and practice*. Image processing series. CRC Press, Boca Raton, FL, 2001. ISBN 0-8493-3493-4.

[42] M. Damgaard, L. Ibsen, L. Andersen, and J. Andersen. Cross-wind modal properties of offshore wind turbines identified by full scale testing. *Journal of Wind Engineering and Industrial Aerodynamics*, 116:94–108, May 2013. ISSN 01676105. doi: 10.1016/j.jweia.2013. 03.003. URL `http://linkinghub.elsevier.com/retrieve/pii/S0167610513000603`.

[43] M. de Berg, O. Cheong, M. van Kreveld, and M. Overmars. *Computational geometry. Algorithms and applications. 3rd ed.* Springer., Berlin, 3 edition, 2008.

[44] E. R. DeLong, D. M. DeLong, and D. L. Clarke-Pearson. Comparing the Areas under Two or More Correlated Receiver Operating Characteristic Curves: A Nonparametric Approach. *Biometrics*, 44(3):837, Sept. 1988. ISSN 0006341X. doi: 10.2307/2531595. URL `http://www.jstor.org/stable/2531595?origin=crossref`.

[45] A. Deraemaeker and K. Worden. *New trends in vibration based structural health monitoring.* Number no. 520 in Courses and lectures / International Centre for Mechanical Sciences. Springer, Wien New York, 2010. ISBN 978-3-7091-0398-2.

[46] A. Deraemaeker, E. Reynders, G. De Roeck, and J. Kullaa. Vibration-based structural health monitoring using output-only measurements under changing environment. *Mechanical Systems and Signal Processing*, 22(1):34–56, Jan. 2008. ISSN 08883270. doi: 10.1016/j.ymssp.2007.07.004. URL `http://linkinghub.elsevier.com/retrieve/pii/S0888327007001148`.

[47] C. Devriendt, F. Magalhaes, W. Weijtjens, G. De Sitter, A. Cunha, and P. Guillaume. Structural health monitoring of offshore wind turbines using automated operational modal analysis. *Structural Health Monitoring*, 13(6):644–659, Nov. 2014. ISSN 1475-9217, 1741-3168. doi: 10.1177/1475921714556568. URL `http://shm.sagepub.com/cgi/doi/10.1177/1475921714556568`.

[48] C. W. Doebling, C. R. Farrar, and M. B. Prime. A summary review of vibration-based damage identification methods. *The Shock and Vibration Digest*, 30(2):91–105, 1998.

[49] S. Doebling, C. Farrar, M. Prime, and D. Shevitz. Damage identification and health monitoring of structural and mechanical systems from changes in their vibration characteristics: A literature review. Technical Report LA–13070-MS, 249299, Los Alamos National Lab., NM (United States), May 1996. URL `http://www.osti.gov/servlets/purl/249299-n4r7Vr/webviewable/`.

[50] M. Döhler, L. Mevel, and F. Hille. Subspace-based damage detection under changes in the ambient excitation statistics. *Mechanical Systems and Signal Processing*, 45(1): 207–224, Mar. 2014. ISSN 08883270. doi: 10.1016/j.ymssp.2013.10.023. URL `http://linkinghub.elsevier.com/retrieve/pii/S0888327013005645`.

[51] R. Duda. *Pattern classification.* Wiley, New York, 2nd ed. edition, 2001. ISBN 978-0-471-05669-0.

[52] D. Dueck. *Affinity Propagation: Clustering Data by Passing Messages*. PhD thesis, University of Toronto, Graduate Department of Electrical & Computer Engineering, 2009.

[53] D. Ewins. *Modal testing: theory, practice and application*. Research Studies Press, Baldock, 2. ed. edition, 2000. ISBN 978-0-86380-218-8.

[54] C. R. Farrar and D. A. Jauregui. Comparative study of damage identification algorithms applied to a bridge: II. Numerical study. *Smart Materials and Structures*, 7(5):720–731, Oct. 1998. ISSN 0964-1726. doi: 10.1088/0964-1726/7/5/014. URL `http://stacks.iop.org/0964-1726/7/i=5/a=014?key=crossref.0ff31cadce7abad7455f6e032562d598`.

[55] C. R. Farrar and D. A. Jauregui. Comparative study of damage identification algorithms applied to a bridge: I. Experiment. *Smart Materials and Structures*, 7(5):704–719, Oct. 1998. ISSN 0964-1726. doi: 10.1088/0964-1726/7/5/013. URL `http://stacks.iop.org/0964-1726/7/i=5/a=013?key=crossref.e00660bcd8cbc6062635ae4e82e22a61`.

[56] C. R. Farrar and N. A. J. Lieven. Damage prognosis: the future of structural health monitoring. *Philosophical Transactions of the Royal Society A: Mathematical, Physical and Engineering Sciences*, 365(1851):623–632, Feb. 2007. ISSN 1364-503X, 1471-2962. doi: 10.1098/rsta.2006.1927. URL `http://rsta.royalsocietypublishing.org/cgi/doi/10.1098/rsta.2006.1927`.

[57] C. R. Farrar and K. Worden. *Structural health monitoring: a machine learning perspective*. Wiley, Chichester, West Sussex, U.K. ; Hoboken, N.J, 2013. ISBN 978-1-119-99433-6.

[58] S. D. Fassois and J. S. Sakellariou. Statistical Time Series Methods for SHM. In C. Boller, F.-K. Chang, and Y. Fujino, editors, *Encyclopedia of Structural Health Monitoring*. John Wiley & Sons, Ltd, Chichester, UK, Sept. 2009. ISBN 978-0-470-05822-0 978-0-470-06162-6. URL `http://doi.wiley.com/10.1002/9780470061626.shm044`.

[59] E. Figueiredo, G. Park, J. Figueiras, C. Farrar, and K. Worden. Structural health monitoring algorithm comparisons using standard data sets. Technical Report Los Alamos National Laboratory Report LA-14393, Los Alamos National Laboratory (LANL), Los Alamos, NM (United States), 2009.

[60] E. Figueiredo, G. Park, C. R. Farrar, K. Worden, and J. Figueiras. Machine learning algorithms for damage detection under operational and environmental variability. *Structural Health Monitoring*, 10(6):559–572, Nov. 2010. ISSN 1475-9217, 1741-3168. doi: 10.1177/1475921710388971. URL `http://shm.sagepub.com/cgi/doi/10.1177/1475921710388971`.

[61] E. Figueiredo, M. Todd, C. Farrar, and E. Flynn. Autoregressive modeling with state-space embedding vectors for damage detection under operational variability. *International Journal of Engineering Science*, 48(10):822–834, Oct. 2010. ISSN 00207225. doi: 10.1016/j.ijengsci.2010.05.005. URL `http://linkinghub.elsevier.com/retrieve/pii/S0020722510000996`.

[62] G. Franklin and D. Powell. *Digital control of dynamic systems.* Addison-Wesley Pub. Co., Reading Mass., 1980. ISBN 978-0-201-02891-1.

[63] B. J. Frey and D. Dueck. Clustering by Passing Messages Between Data Points. *Science*, 315(5814):972–976, Feb. 2007. ISSN 0036-8075, 1095-9203. doi: 10.1126/science.1136800. URL http://www.sciencemag.org/cgi/doi/10.1126/science.1136800.

[64] C.-P. Fritzen and P. Kraemer. Automated System Identification and Validation of Numerical Models of Offshore Wind Turbines as Basis for SHM-Analysis. In *Proceedings of the 8th International Workshop on Structural Health Monitoring*, pages 1656–1663, Stanford, CA, USA, 2011. Chang, F.-K. (Ed.), DEStech Publications Inc.

[65] C.-P. Fritzen and P. Kraemer. Vibration Based Damage Detection for Structures of Offshore Wind Energy Plants. In *Proceedings of the 8th International Workshop on Structural Health Monitoring*, pages 1656–1663, Stanford, CA, USA, 2011. Chang, F.-K. (Ed.), DEStech Publications Inc.

[66] M. L. Fugate, H. Sohn, and C. R. Farrar. Vibration-based damage detection using statistical process control. *Mechanical Systems and Signal Processing*, 15(4):707–721, 2001.

[67] F. P. García Márquez, A. M. Tobias, J. M. Pinar Pérez, and M. Papaelias. Condition monitoring of wind turbines: Techniques and methods. *Renewable Energy*, 46:169–178, Oct. 2012. ISSN 09601481. doi: 10.1016/j.renene.2012.03.003. URL http://linkinghub.elsevier.com/retrieve/pii/S0960148112001899.

[68] R. Gasch and J. Twele. *Wind Power Plants Fundamentals, Design, Construction and Operation.* Springer Berlin Heidelberg, Berlin, Heidelberg, 2012. ISBN 978-3-642-22938-1 3-642-22938-7. URL http://proxy.uqtr.ca/login.cgi?action=login&u=uqtr&db=springer-eb&url=http://dx.doi.org/10.1007/978-3-642-22938-1.

[69] I. Gath and A. B. Geva. Unsupervised optimal fuzzy clustering. *Pattern Analysis and Machine Intelligence, IEEE Transactions on*, 11(7):773–780, 1989.

[70] Germanischer Lloyd. Guideline for the Certification of Offshore Wind Turbines. Technical report, Germanischer Lloyd, Hamburg, July 2005.

[71] I. Goethals and B. D. Moor. Model Reduction and Energy Analysis as a Tool to Detect Spurious Modes. In *Proceedings of ISMA 2002 International Conference on Noise and Vibration Engineering*, pages 1307–1314, Leuven, Belgium, 2002.

[72] I. Goethals, B. Vanluyten, and B. De Moor. Reliable spurious mode rejection using self learning algorithms. In *Proceedings of the International Conference on Noise and Vibration Engineering (ISMA 2004), Leuven, Belgium*, pages 991–1003, 2004.

[73] J. Grover. *Strategic Economic Decision-Making*, volume 9 of *SpringerBriefs in Statistics*. Springer New York, New York, NY, 2013. ISBN 978-1-4614-6039-8 978-1-4614-6040-4. URL http://link.springer.com/10.1007/978-1-4614-6040-4.

[74] D. E. Gustafson and W. C. Kessel. Fuzzy clustering with a fuzzy covariance matrix. In *Decision and Control including the 17th Symposium on Adaptive Processes, 1978 IEEE Conference on*, volume 17, pages 761–766, 1978.

[75] G. Haake. *Systemidentifikation mit Autoregressiven Modellen und Validierung numerischer Strukturmodelle bei Offshore-Windenergieanlagen*. Dissertation, Gottfried Wilhelm Leibniz Universität Hannover, Fakultät für Bauingenieurwesen, Institut für Statik und Dynamik, Hannover, 2010.

[76] M. W. Häckell and R. Rolfes. Long-term Monitoring of Modal Parameters for SHM at a 5 MW Offshore Wind Turbine. In *Proceedings of the 9th International Workshop on Structural Health Monitoring*, pages 1310–1317, Stanford, CA, USA, 2013. Chang, F.-K. (Ed.), DEStech Publications Inc.

[77] M. W. Häckell and R. Rolfes. Monitoring a 5mw offshore wind energy converter—Condition parameters and triangulation based extraction of modal parameters. *Mechanical Systems and Signal Processing*, 40(1):322–343, Oct. 2013. ISSN 08883270. doi: 10.1016/j.ymssp.2013. 04.004. URL `http://linkinghub.elsevier.com/retrieve/pii/S0888327013001908`.

[78] J. F. Hair, W. C. Black, B. J. Babin, R. E. Anderson, and R. L. Tatham. *Multivariate data analysis*, volume 7. Prentice Hall Upper Saddle River, NJ, 2010.

[79] Z. Hameed, Y. Hong, Y. Cho, S. Ahn, and C. Song. Condition monitoring and fault detection of wind turbines and related algorithms: A review. *Renewable and Sustainable Energy Reviews*, 13(1):1–39, Jan. 2009. ISSN 13640321. doi: 10.1016/j.rser.2007.05.008. URL `http://linkinghub.elsevier.com/retrieve/pii/S1364032107001098`.

[80] J. A. Hanley and B. J. McNeil. The meaning and use of the area under a receiver operating characteristic (ROC) curve. *Radiology*, 143(1):29–36, Apr. 1982. ISSN 0033-8419, 1527-1315. doi: 10.1148/radiology.143.1.7063747. URL `http://pubs.rsna.org/doi/abs/10.1148/radiology.143.1.7063747`.

[81] R. Harrison, E. Hau, and H. Snel. *Large wind turbines: design and economics*. Wiley, Chichester ; New York, 2000. ISBN 0-471-49456-9.

[82] S. S. Haykin. *Neural networks: a comprehensive foundation*. Macmillan ; Maxwell Macmillan Canada ; Maxwell Macmillan International, New York : Toronto : New York, 1994. ISBN 0-02-352761-7.

[83] X. He, B. Moaveni, J. P. Conte, A. Elgamal, and S. F. Masri. System Identification of Alfred Zampa Memorial Bridge Using Dynamic Field Test Data. *Journal of Structural Engineering*, 135(1):54–66, Jan. 2009. ISSN 0733-9445, 1943-541X. doi: 10.1061/(ASCE) 0733-9445(2009)135:1(54). URL `http://ascelibrary.org/doi/abs/10.1061/%28ASCE%290733-9445%282009%29135%3A1%2854%29`.

[84] F. Hille, M. Döhler, L. Mevel, and W. Rücker. Subspace-based Damage Detection Methods on a Prestressed Concrete Bridge. In *Proceedings of the 8th International Conference on Structural Dynamics, EURODYN 2011*, pages 2304–2310, Leuven, Belgium, 4-6 July 2011, 2011.

[85] R. Höffer, S. Lachmann, and D. Hartmann. Conceptual study on instrumentation for displacement-based service strength checking of wind turbines. In *Proceedings of the 14th International Conference on Computing in Civil and Building Engineering. Moscow, Russia*, 2012.

[86] J. H. Holland. *Adaptation in natural and artificial systems: an introductory analysis with applications to biology, control, and artificial intelligence.* University of Michigan Press, Ann Arbor, 1975. ISBN 0-472-08460-7. URL `http://mirlyn.lib.umich.edu/Record/001496062`. viii, 183 p.

[87] L. H. Holthuijsen. *Waves in oceanic and coastal waters.* Cambridge University Press, Cambridge, 2007. ISBN 978-0-521-86028-4.

[88] W.-H. Hu. *Operational modal analysis and continuous dynamic monitoring of footbridges.* PhD thesis, Ph. D. Thesis, University of Porto, FEUP, 2011.

[89] W.-H. Hu, C. Mountinho, F. Magalhães, E. Caetano, and A. Cunha. Analysis and extraction of temperature effect on natural frequencies of a footbridge based on continuous dynamic monitoring. In *Proceedings of the 3rd International Operational Modal Analysis Conference. Portonovo, Italy*, pages 55–62, 2009.

[90] I. International Electrotechnical Commission. IEC 61400-1 3rd edn 2005-08 Wind turbines - Part 1: Design requirements, 2005.

[91] N. J. Jacobsen, P. Andersen, and R. Brincker. Using enhanced frequency domain decomposition as a robust technique to harmonic excitation in operational modal analysis. In *Proceedings of ISMA2006: International Conference on Noise & Vibration Engineering*, pages 18–20, 2006. URL `ftp://ftp.svibs.com/Download/Literature/Papers/2006/2006_6.pdf`.

[92] J.-N. Juang. *Applied system identification.* Prentice Hall, Englewood Cliffs N.J., 1994. ISBN 978-0-13-079211-2.

[93] M. Kane, D. Zhu, M. Hirose, X. Dong, B. Winter, M. W. Häckell, J. P. Lynch, Y. Wang, and A. Swartz. Development of an Extensible Dual-Core Wireless Sensing Node for Cyber-Physical Systems. In J. P. Lynch, K.-W. Wang, and H. Sohn, editors, *SPIE Smart Structures and Materials+ Nondestructive Evaluation and Health Monitoring*, pages 90611U–90611U. International Society for Optics and Photonics, Apr. 2014. doi: 10.1117/12.2045325. URL `http://proceedings.spiedigitallibrary.org/proceeding.aspx?doi=10.1117/12.2045325`.

[94] M. B. Kane. *Wirelessly Enabled Control of Cyber-Physical Infrastructure Systems*. PhD thesis, University of Michigan, Department of Civil and Environmental Engineering Department of Electrical Engineering and Computer Science, Ann Arbor, MI, 2014.

[95] J.-T. Kim, Y.-S. Ryu, H.-M. Cho, and N. Stubbs. Damage identification in beam-type structures: frequency-based method vs mode-shape-based method. *Engineering Structures*, 25(1):57–67, Jan. 2003. ISSN 01410296. doi: 10.1016/S0141-0296(02)00118-9. URL `http://linkinghub.elsevier.com/retrieve/pii/S0141029602001189`.

[96] J. Ko and Y. Ni. Technology developments in structural health monitoring of large-scale bridges. *Engineering Structures*, 27(12):1715–1725, Oct. 2005. ISSN 01410296. doi: 10.1016/j.engstruct.2005.02.021. URL `http://linkinghub.elsevier.com/retrieve/pii/S014102960500218X`.

[97] P. Kraemer. *Schadensdiagnoseverfahren für die Zustandsüberwachung von Offshore-Windenergieanlagen*. Dissertation, Universität Siegen, Fakultät IV: Natur- und Ingenieurwissenschaftliche Fakultät, Institut für Mechanik und Regelungstechnik - Mechatronik, Schriftenreihe der Arbeitsgruppe für Technische Mechanik, Siegen, 2011. URL `http://dokumentix.ub.uni-siegen.de/opus/volltexte/2011/532/`.

[98] P. Kraemer and C.-P. Fritzen. Aspects of Operational Modal Analysis for Structures of Offshore Wind Energy Plants. In T. Proulx, editor, *Structural Dynamics and Renewable Energy, Volume 1*, pages 145–152. Springer New York, New York, NY, 2011. ISBN 978-1-4419-9715-9 978-1-4419-9716-6. URL `http://www.springerlink.com/index/10.1007/978-1-4419-9716-6_14`.

[99] J. Kullaa. Vibration-Based Structural Health Monitoring Under Variable Environmental or Operational Conditions. In *NEW TRENDS IN VIBRATION BASED STRUCTURAL HEALTH MONITORING*, Courses and lectures / International Centre for Mechanical Sciences, page 75. Springer, Wien New York, 2010. ISBN 978-3-7091-0398-2.

[100] J. Kullaa. Distinguishing between sensor fault, structural damage, and environmental or operational effects in structural health monitoring. *Mechanical Systems and Signal Processing*, 25(8):2976–2989, Nov. 2011. ISSN 08883270. doi: 10.1016/j.ymssp.2011.05.017. URL `http://linkinghub.elsevier.com/retrieve/pii/S0888327011002196`.

[101] M. Kurata, J. Kim, Y. Zhang, J. P. Lynch, G. W. van der Linden, V. Jacob, E. Thometz, P. Hipley, and L.-H. Sheng. Long-term assessment of an autonomous wireless structural health monitoring system at the new Carquinez Suspension. In H. F. Wu, editor, *SPIE Proceedings*, volume 7983, pages 798312–798312–9, Mar. 2011. doi: 10.1117/12.880145. URL `http://proceedings.spiedigitallibrary.org/proceeding.aspx?articleid=828081`.

[102] M. Kurata, J. Kim, J. P. Lynch, G. W. van der Linden, H. Sedarat, E. Thometz, P. Hipley, and L.-H. Sheng. Internet-Enabled Wireless Structural Monitoring Systems: Development and Permanent Deployment at the New Carquinez Suspension Bridge. *Journal*

of Structural Engineering, 139(10):1688–1702, Oct. 2013. ISSN 0733-9445, 1943-541X. doi: 10.1061/(ASCE)ST.1943-541X.0000609. URL `http://ascelibrary.org/doi/abs/10.1061/%28ASCE%29ST.1943-541X.0000609`.

[103] S. Lachmann, X. Liu, K.-R. Leimbach, R. Höffer, and D. Hartmann. Monitoring und Kontinuierliche Systemidentifikation der Tragstrukturen einer Windenergieanlage zur Schädigungsverfolgung. pages 237–248, Hannover, Germany, Sept. 2011.

[104] J. Lanslots, B. Rodiers, and B. Peeters. Automated pole-selection: Proof-of-concept and validation. In *Proceedings, International Conference on Noise and Vibration Engineering (ISMA)*, 2004.

[105] J. Lau, J. Lanslots, B. Peeters, and H. Van der Auweraer. Automatic modal analysis. Reality or myth? *VDI BERICHTE*, 1982:103, 2007.

[106] K. R. Leimbach, X. Liu, D. Hartmann, and R. Höffer. Model generation, verification, validation and updating for solving problems in structural health monitoring as well as residual lifetime estimation of wind turbines. In *Proc. of the 14th International Conference on Computing in Civil and Building Engineering. Moscow, Russia*, 2012.

[107] T. W. Lim, R. Cabell, and R. Silcox. On-line identification of modal parameters using artificial neural networks. *Journal of vibration and acoustics*, 118(4):649–656, 1996.

[108] C. Liu and J. T. DeWolf. Effect of Temperature on Modal Variability of a Curved Concrete Bridge under Ambient Loads. *Journal of Structural Engineering*, 133(12):1742–1751, Dec. 2007. ISSN 0733-9445, 1943-541X. doi: 10.1061/(ASCE)0733-9445(2007)133:12(1742). URL `http://ascelibrary.org/doi/abs/10.1061/%28ASCE%290733-9445%282007%29133%3A12%281742%29`.

[109] W. Liu, B. Tang, and Y. Jiang. Status and problems of wind turbine structural health monitoring techniques in China. *Renewable Energy*, 35(7):1414–1418, 2010. ISSN 09601481. doi: 10.1016/j.renene.2010.01.006. URL `http://linkinghub.elsevier.com/retrieve/pii/S0960148110000108`.

[110] X. Liu, K. R. Leimbach, D. Hartmann, and R. Höffer. Signal analysis using wavelets for structural damage detection applied to wind energy converters. In *Proc. of the 14th International Conference on Computing in Civil and Building Engineering. Moscow, Russia*, 2012.

[111] H. Lütkepohl. *New introduction to multiple time series analysis.* Springer, Berlin, 2005. ISBN 3-540-26239-3 978-3-540-26239-8.

[112] H. Lütkepohl. *New introduction to multiple time series analysis. Corrected 2nd printing.* Berlin: Springer., 2006. ISBN 3-540-26239-3 978-3-540-26239-8.

[113] J. P. Lynch. An overview of wireless structural health monitoring for civil structures. *Philosophical Transactions of the Royal Society A: Mathematical, Physical and Engineering Sciences*, 365(1851):345–372, Feb. 2007. ISSN 1364-503X, 1471-2962. doi: 10.1098/rsta.2006. 1932. URL `http://rsta.royalsocietypublishing.org/cgi/doi/10.1098/rsta.2006. 1932`.

[114] J. MacQueen et al. Some methods for classification and analysis of multivariate observations. In *Proceedings of the fifth Berkeley symposium on mathematical statistics and probability*, volume 1, page 14, 1967.

[115] F. Magalhães. *Operational Modal Analysis for Testing and Monitoring of Bridges and Special Structures.* Ph.D. Thesis, Faculty of Engineering of the University of Porto, Porto, 2010. URL `http://repositorio-aberto.up.pt/bitstream/10216/59924/1/000143271.pdf`.

[116] F. Magalhães, Á. Cunha, and E. Caetano. Online automatic identification of the modal parameters of a long span arch bridge. *Mechanical Systems and Signal Processing*, 23 (2):316–329, Feb. 2009. ISSN 08883270. doi: 10.1016/j.ymssp.2008.05.003. URL `http: //linkinghub.elsevier.com/retrieve/pii/S0888327008001301`.

[117] F. Magalhães, Á. Cunha, and E. Caetano. Structural Health Monitoring Based on Automated Operational Modal Analysis: Application to an Arch Bridge. In M. Garevski, editor, *Earthquakes and Health Monitoring of Civil Structures*, Springer Environmental Science and Engineering, pages 241–268. Springer Netherlands, 2013. ISBN 978-94-007-5181-1. URL `http://dx.doi.org/10.1007/978-94-007-5182-8_10`.

[118] M. Mahmoud, M. Abe, and Y. Fujino. Analysis of suspension bridge by ambient vibration measurement using time domain method and its application to health monitoring. In *Proceedings of 19th International Modal Analysis Conference*, volume 4359, pages 504–510, Kissimee, FL, 2001.

[119] N. Maia, J. Silva, and J. He. *Theoretical and experimental modal analysis.* Research Studies Press ;;Wiley, Taunton Somerset England ;New York, 1997. ISBN 978-0-86380-208-9.

[120] D. Malcolm and A. Hansen. WindPACT turbine rotor design study. Technical Report 5, National Renewable Energy Laboratory, Golden, CO, 2002.

[121] C. E. Metz. Basic principles of ROC analysis. *Seminars in Nuclear Medicine*, 8(4): 283–298, Oct. 1978. ISSN 00012998. doi: 10.1016/S0001-2998(78)80014-2. URL `http: //linkinghub.elsevier.com/retrieve/pii/S0001299878800142`.

[122] L. Mevel and M. Goursat. A complete scilab toolbox for output only identification. In *Proceedings of the 22st International Modal Analysis Conference*, Detroit, 2004.

[123] L. Mevel, M. Basseville, and M. Goursat. Stochastic Subspace-Based Structural Identification and Damage Detection - Application to the Steel-Quake Benchmark. *Mechanical Systems*

and Signal Processing, 17(1):91–101, Jan. 2003. ISSN 08883270. doi: 10.1006/mssp.2002.1544. URL `http://linkinghub.elsevier.com/retrieve/pii/S088832700291544X`.

[124] L. Mevel, M. Goursat, and M. Basseville. Stochastic Subspace-Based Structural Identification and Damage Detection - Application to the Z24 Bridge Benchmark. *Mechanical Systems and Signal Processing*, 17(1):143–151, Jan. 2003. ISSN 08883270. doi: 10.1006/mssp.2002.1552. URL `http://linkinghub.elsevier.com/retrieve/pii/S0888327002915529`.

[125] L. Mevel, A. Sam, and M. Goursat. Blind Modal Identification for Large Aircrafts. In *Proceedings of the 22st International Modal Analysis Conference*, Detroit, 2004.

[126] P. Mohanty, P. Reynolds, and A. Pavic. Automated interpretation of stability plots for analysis of a non-stationary structure. In *25th International Modal Analysis Conference (IMAC XXV)*, 2007.

[127] M. Molinari, M. Pozzi, D. Zonta, and L. Battisti. In-field testing of a steel wind turbine tower. In *Structural Dynamics and Renewable Energy, Volume 1*, pages 103–112. Springer, 2011.

[128] D. C. Montgomery. *Introduction to statistical quality control.* Wiley, Hoboken, 5 edition, 2005. ISBN 0-471-66122-8.

[129] P. Moser and B. Moaveni. Environmental effects on the identified natural frequencies of the Dowling Hall Footbridge. *Mechanical Systems and Signal Processing*, 25(7):2336–2357, Oct. 2011. ISSN 08883270. doi: 10.1016/j.ymssp.2011.03.005. URL `http://linkinghub.elsevier.com/retrieve/pii/S0888327011001233`.

[130] L. E. Mujica, M. Ruiz, F. Pozo, J. Rodellar, and A. Güemes. A structural damage detection indicator based on principal component analysis and statistical hypothesis testing. *Smart Materials and Structures*, 23(2):025014, Feb. 2014. ISSN 0964-1726, 1361-665X. doi: 10.1088/0964-1726/23/2/025014. URL `http://stacks.iop.org/0964-1726/23/i=2/a=025014?key=crossref.736dd3b30e828ff467efb3487d04236a`.

[131] O. Nelles. *Nonlinear system identification : from classical approaches to neural networks and fuzzy models.* Springer, Berlin ;;New York, 2001. ISBN 978-3-540-67369-9.

[132] J. Neter, W. Wasserman, M. H. Kutner, et al. *Applied linear statistical models*, volume 4. Irwin Chicago, 1996.

[133] A. Neumaier and T. Schneider. Estimation of parameters and eigenmodes of multivariate autoregressive models. *ACM Transactions on Mathematical Software (TOMS)*, 27(1):27–57, 2001.

[134] V. V. Nguyen, D. Hartmann, M. Baitsch, and M. König. A Distributed Agent-based Approach for Robust Optimization. In *Proceedings of the 2nd International Conference*

on Engineering Optimization, page 16, Lisbon, Portugal, 2010. ISBN 978-989-96264-3-0. URL `http://www1.dem.ist.utl.pt/engopt2010/Book_and_CD/Papers_CD_Final_Version/pdf/01/01273-01.pdf`.

[135] N. W. T. C. (NWTC). Computer-aided engineering tools - FAST: An aeroelastic computer-aided engineering (CAE) tool for horizontal axis wind turbines, 2013. URL `https://nwtc.nrel.gov/FAST`.

[136] T. Pahn, M. Kohlmeier, and R. Rolfes. System identification of a jacket support structure for a 5 MW offshore wind turbine due to artificial and ambient excitation. In *TORQUE 2010: The Science of Making Torque from Wind*, pages 769–780, Heraklion, Crete, Greece, 2010.

[137] A. K. Pandey, M. Biswas, and M. M. Samman. Damage Detection From Changes In Curvature Mode Shapes. *Sound and Vibration*, 145(2):321–332, 1991.

[138] R. Pappa, G. James, D. Zimmerman, and L. R. Center. Autonomous modal identification of the space shuttle tail rudder. *Journal of spacecraft and rockets*, 35(2):163–169, 1998.

[139] R. S. Pappa, K. Elliott, and A. Schenk. Consistent-mode indicator for the eigensystem realization algorithm. *Journal of Guidance, Control, and Dynamics*, 16(5):852–858, Sept. 1993. ISSN 0731-5090. doi: 10.2514/3.21092. URL `http://dx.doi.org/10.2514/3.21092`.

[140] R. S. Pappa, S. E. Woodard, and J.-N. Juang. *A benchmark problem for development of autonomous structural modal identification*. Number 110291 in NASA Technical Memorandum. Citeseer, 1996.

[141] J. Park, K. Smarsly, K. H. Law, and D. Hartmann. Multivariate Analysis and Prediction of Wind Turbine Response to Varying Wind Field Characteristics Based on Machine Learning. In *Proceedings of the ASCE International Workshop on Computing in Civil Engineering*, pages 113–120. American Society of Civil Engineers, June 2013. ISBN 978-0-7844-1302-9. doi: 10.1061/9780784413029.015. URL `http://ascelibrary.org/doi/abs/10.1061/9780784413029.015`.

[142] B. Peeters and G. De Roeck. Reference-Based Stochastic Subspace Identification for Output-Only Modal Analysis. *Mechanical Systems and Signal Processing*, 13:855–878, Nov. 1999. ISSN 08883270. doi: 10.1006/mssp.1999.1249. URL `http://linkinghub.elsevier.com/retrieve/pii/S0888327099912499`.

[143] B. Peeters and G. De Roeck. One year monitoring of the Z24 bridge: environmental influences versus damage effects. In *Proceedings of 18th International Modal Analysis Conference*, pages 1570–1576, Kissimee, FL, 2000.

[144] B. Peeters and G. De Roeck. Stochastic System Identification for Operational Modal Analysis: A Review. *Journal of Dynamic Systems, Measurement, and Control*, 123:659, 2001. ISSN 00220434. doi: 10.1115/1.1410370.

[145] B. Peeters and H. Van der Auweraer. PolyMAX: a revolution in operational modal analysis. In *1st International Operational Modal Analysis Conference*, 2005.

[146] B. Peeters, J. Maeck, and G. D. Roeck. Vibration-based damage detection in civil engineering: excitation sources and temperature effects. *Smart Materials and Structures*, 10(3):518–527, June 2001. ISSN 0964-1726. doi: 10.1088/0964-1726/10/3/314. URL `http://stacks.iop.org/0964-1726/10/i=3/a=314?key=crossref.77a38ff0c03ca35b064e86c535876c42`.

[147] B. Peeters, H. Van der Auweraer, P. Guillaume, and J. Leuridan. The PolyMAX frequency-domain method: a new standard for modal parameter estimation? *Shock and Vibration*, 11 (3-4):395–410, 2004.

[148] C. Petersen. *Dynamik der Baukonstruktionen.* Vieweg, Wiesbaden, 1996. ISBN 978-3-528-08123-2.

[149] A. Phillips, R. Allemang, and D. Brown. Autonomous modal parameter estimation: methodology. In *Modal Analysis Topics, Volume 3*, pages 363–384. Springer, 2011.

[150] A. W. Phillips, R. J. Allemang, and W. A. Fladung. The Complex Mode Indicator Function (CMIF) as a parameter estimation method. In *PROCEEDINGS-SPIE THE INTERNATIONAL SOCIETY FOR OPTICAL ENGINEERING*, volume 1, pages 705–710, 1998.

[151] A. Poulimenos and S. Fassois. Parametric time-domain methods for non-stationary random vibration modelling and analysis — A critical survey and comparison. *Mechanical Systems and Signal Processing*, 20(4):763–816, May 2006. ISSN 08883270. doi: 10.1016/j.ymssp.2005.10.003. URL `http://linkinghub.elsevier.com/retrieve/pii/S0888327005001688`.

[152] C. Rainieri and G. Fabbrocino. Automated output-only dynamic identification of civil engineering structures. *Mechanical Systems and Signal Processing*, 24(3):678–695, Apr. 2010. ISSN 08883270. doi: 10.1016/j.ymssp.2009.10.003. URL `http://linkinghub.elsevier.com/retrieve/pii/S088832700900315X`.

[153] C. Rainieri, G. Fabbrocino, and E. Cosenza. Automated Operational Modal Analysis as Structural Health Monitoring Tool: Theoretical and Applicative Aspects. *Key Engineering Materials*, 347:479–484, 2007. ISSN 1662-9795. doi: 10.4028/www.scientific.net/KEM.347.479. URL `http://www.scientific.net/KEM.347.479`.

[154] C. Rainieri, G. Fabbrocino, and E. Cosenza. Fully automated OMA: an opportunity for smart SHM systems. In *Proceedings of the 27th International Modal Analysis Conference (IMAC)*, 2009.

[155] E. Reynders and G. D. Roeck. Reference-based combined deterministic–stochastic subspace identification for experimental and operational modal analysis. *Mechanical Systems and Signal Processing*, 22(3):617–637, Apr. 2008. ISSN 08883270. doi: 10.1016/j.ymssp.2007.09.004. URL `http://linkinghub.elsevier.com/retrieve/pii/S0888327007001823`.

[156] E. Reynders, J. Houbrechts, and G. De Roeck. Automated interpretation of stabilization diagrams. In *Modal analysis topics. proceedings of the 29th IMAC, a conference on structural dynamics, 2011 Volume 3*, New York, 2011. Springer. ISBN 978-1-4419-9299-4 1-4419-9299-5. URL `http://dx.doi.org/10.1007/978-1-4419-9299-4`.

[157] E. Reynders, J. Houbrechts, and G. De Roeck. Fully automated (operational) modal analysis. *Mechanical Systems and Signal Processing*, 29:228–250, May 2012. ISSN 08883270. doi: 10.1016/j.ymssp.2012.01.007. URL `http://linkinghub.elsevier.com/retrieve/pii/S0888327012000088`.

[158] J. A. Rice. *Mathematical statistics and data analysis*. Duxbury advanced series. Thomson/Brooks/Cole, Belmont, CA, 3rd ed edition, 2007. ISBN 0-534-39942-8.

[159] R. G. Rohrmann, S. Thöns, and W. Rücker. Integrated monitoring of offshore wind turbines – requirements, concepts and experiences. *Structure and Infrastructure Engineering*, 6(5): 575–591, Oct. 2010. ISSN 1573-2479, 1744-8980. doi: 10.1080/15732470903068706. URL `http://www.tandfonline.com/doi/abs/10.1080/15732470903068706`.

[160] R. Rolfes, W.-J. Gerasch, G. Haake, J. Reetz, and S. Zerbst. Early Damage Detection System for Tower and Rotor Blades of Offshore Wind Turbines. In *Proceedings of the Third European Workshop on Structural Health Monitoring 2006*, pages 455–462, Granada, 2006. ISBN 1-932078-63-0.

[161] R. Rolfes, J. P. Lynch, W.-J. Gerasch, G. Haake, J. Reetz, and S. Zerbst. Integral SHM-system for offshore wind turbines using smart wireless sensors. In *Proceedings of the 6th International Workshop on Structural Health Monitoring*, Stanford, CA, USA, 2007. Chang, F.-K. (Ed.), DEStech Publications Inc.

[162] R. Rolfes, H. Huhn, P. Schaumann, T. Schlurmann, L. Lohaus, and M. Achmus. Ganzheitliches Dimensionierungskonzept für OWEA-Tragstrukturen anhand von Messungen im Offshore-Testfeld alpha ventus Jahresbericht 2009. Jahresbericht 2, Leibniz Universität Hannover, Hannover, Apr. 2010. URL `http://www.gigawind.de/fileadmin/jahresberichte/GIGAWINDav_J2009.pdf`.

[163] R. Rolfes, M. W. Häckell, and G. Haake. Automated System Identification and Validation of Numerical Models of Offshore Wind Turbines as Basis for SHM-Analysis. In *Proceedings of the 8th International Workshop on Structural Health Monitoring*, pages 2149–2156, Stanford, CA, USA, 2011. Chang, F.-K. (Ed.), DEStech Publications Inc.

[164] S. M. Ross. *Introduction to Probability and Statistics for Engineers and Scientists*. Elsevier Science, Burlington, 2009. ISBN 978-0-08-091937-9 0-08-091937-5. URL `http://public.eblib.com/choice/publicfullrecord.aspx?p=802457`.

[165] R. Ruotolo and C. Surace. Using SVD to Detect Damage in Structures With Different Operational Conditions. *Journal of Sound and Vibration*, 226(3):425 – 439, 1999. ISSN 0022-

460X. doi: http://dx.doi.org/10.1006/jsvi.1999.2305. URL `http://www.sciencedirect.com/science/article/pii/S0022460X99923052`.

[166] A. Rytter. *Vibration based inspection of civil engineering structures*. PhD thesis, Aalborg University, Denmark, 1993.

[167] D. Salzmann and J. Van der Tempel. Aerodynamic damping in the design of support structures for offshore wind turbines. In *Paper of the Copenhagen Offshore Conference*, 2005.

[168] M. Scionti and J. Lanslots. Stabilisation diagrams: Pole identification using fuzzy clustering techniques. *Advances in Engineering Software*, 36(11-12):768–779, Nov. 2005. ISSN 09659978. doi: 10.1016/j.advengsoft.2005.03.029. URL `http://linkinghub.elsevier.com/retrieve/pii/S0965997805001250`.

[169] M. Scionti, J. Lanslots, I. Goethals, A. Vecchio, H. Van der Auweraer, B. Peeters, and B. De Moor. Tools to improve detection of structural changes from in-flight flutter data. In *Proceedings of the Eighth International Conference on Recent Advances in Structural Dynamics*, 2003.

[170] R. Shirzadeh, C. Devriendt, M. Bidakhvidi, and P. Guillaume. Experimental and computational damping estimation of an offshore wind turbine on a monopile foundation. *Journal of Wind Engineering and Industrial Aerodynamics*, 120:96–106, Sept. 2013. ISSN 01676105. doi: 10.1016/j.jweia.2013.07.004. URL `http://linkinghub.elsevier.com/retrieve/pii/S0167610513001359`.

[171] B. W. Silverman. *Density estimation for statistics and data analysis*, volume 26. Chapman & Hall/CRC, 1986.

[172] K. Smarsly, K. H. Law, and D. Hartmann. Implementing a Multiagent-Based Self-Managing Structural Health Monitoring System on a Wind Turbine. In *NSF Engineering Research and Innovation Conference*, 2011.

[173] K. Smarsly, D. Hartmann, and K. H. Law. Integration of structural health and condition monitoring into the life-cycle management of wind turbines. In *Proceedings of the Civil Structural Health Monitoring Workshop*, Berlin, 2012.

[174] K. Smarsly, K. H. Law, and D. Hartmann. Multiagent-Based Collaborative Framework for a Self-Managing Structural Health Monitoring System. *Journal of Computing in Civil Engineering*, 26(1):76–89, 2012.

[175] K. Smarsly, D. Hartmann, and K. H. Law. An integrated monitoring system for life-cycle management of wind turbines. *International Journal of Smart Structures and Systems*, 2013.

[176] H. Sohn. Effects of environmental and operational variability on structural health monitoring. *Philosophical Transactions of the Royal Society A: Mathematical, Physical and Engineering Sciences*, 365:539–560, Feb. 2007. ISSN 1364-503X, 1471-2962. doi: 10.1098/rsta.2006.1935. URL `http://rsta.royalsocietypublishing.org/cgi/doi/10.1098/rsta.2006.1935`.

[177] H. Sohn and C. R. Farrar. Damage diagnosis using time series analysis of vibration signals. *Smart materials and structures*, 10(3):446, 2001. URL `http://iopscience.iop.org/0964-1726/10/3/304`.

[178] H. Sohn, M. Dzwonczyk, E. G. Straser, A. S. Kiremidjian, K. H. Law, and T. Meng. An Experimental Study of Temperature Effect on Modal Parameters of the Alamosa Canyon Bridge. In *of the Alamosa Canyon Bridge.” Earthquake Eng. and Structural Dynamics*, pages 879–897. John Wiley & Sons, 1999.

[179] H. Sohn, J. A. Czarnecki, and C. R. Farrar. Structural health monitoring using statistical process control. *Journal of Structural Engineering*, 126(11):1356–1363, 2000.

[180] H. Sohn, C. R. Farrar, N. F. Hunter, and K. Worden. Structural Health Monitoring Using Statistical Pattern Recognition Techniques. *Journal of Dynamic Systems, Measurement, and Control*, 123(4):706, 2001. ISSN 00220434. doi: 10.1115/1.1410933. URL `http://DynamicSystems.asmedigitalcollection.asme.org/article.aspx?articleid=1409264`.

[181] H. Sohn, K. Worden, and C. R. Farrar. Novelty detection under changing environmental conditions. In S.-C. Liu, editor, *Smart Structures and Materials 2001: Smart Systems for Bridges, Structures, and Highways*, pages 108–118, July 2001. doi: 10.1117/12.434110. URL `http://proceedings.spiedigitallibrary.org/proceeding.aspx?articleid=907873`.

[182] H. Sohn, K. Worden, and C. R. Farrar. Novelty Detection Using Auto-Associative Neural Networks. In *Proceedings of 2001 ASME International Mechanical Engineering Congress and Exposition*, New York, NY, May 2001. URL `http://www.osti.gov/scitech/servlets/purl/782786`.

[183] H. Sohn, K. Worden, and C. R. Farrar. Statistical Damage Classification Under Changing Environmental and Operational Conditions. *Journal of Intelligent Material Systems and Structures*, 13(9):561–574, Sept. 2002. ISSN 1045-389X. doi: 10.1106/104538902030904. URL `http://jim.sagepub.com/cgi/doi/10.1106/104538902030904`.

[184] H. Sohn, C. R. Farrar, F. M. Hemez, D. D. Shunk, D. W. Stinemates, B. R. Nadler, and J. J. Czarnecki. *A review of structural health monitoring literature: 1996-2001*. Los Alamos National Laboratory Los Alamos, NM, 2004.

[185] S. Soyoz and M. Q. Feng. Long-Term Monitoring and Identification of Bridge Structural Parameters. *Computer-Aided Civil and Infrastructure Engineering*, 24(2):82–92, Feb. 2009. ISSN 10939687, 14678667. doi: 10.1111/j.1467-8667.2008.00572.x. URL `http://doi.wiley.com/10.1111/j.1467-8667.2008.00572.x`.

[186] M. Spiridonakos, A. Poulimenos, and S. Fassois. Output-only identification and dynamic analysis of time-varying mechanical structures under random excitation: A comparative assessment of parametric methods. *Journal of Sound and Vibration*, 329(7):768–785, 2010.

[187] J. Stevens. *Applied Multivariate Statistics for the Social Sciences, Fifth Edition*. Taylor and Francis, Hoboken, 2012. ISBN 978-1-136-91070-8 1-136-91070-0.

[188] C. Surace and K. Worden. Novelty detection in a changing environment: A negative selection approach. *Mechanical Systems and Signal Processing*, 24(4):1114–1128, May 2010. ISSN 08883270. doi: 10.1016/j.ymssp.2009.09.009. URL http://linkinghub.elsevier.com/retrieve/pii/S0888327009003069.

[189] J. A. Suykens, J. De Brabanter, L. Lukas, and J. Vandewalle. Weighted least squares support vector machines: robustness and sparse approximation. *Neurocomputing*, 48(1):85–105, 2002.

[190] R. A. Swartz, D. Jung, J. P. Lynch, Y. Wang, D. Shi, and M. P. Flynn. Design of a wireless sensor for scalable distributed in-network computation in a structural health monitoring system. In *5th international workshop on structural health monitoring*, pages 1570–1577, 2005.

[191] R. A. Swartz, J. P. Lynch, S. Zerbst, B. Sweetman, and R. Rolfes. Structural monitoring of wind turbines using wireless sensor networks. *SMART STRUCTURES AND SYSTEMS*, 6(3, SI):183–196, Apr. 2010. ISSN 1738-1584. Workshop on Sensor Networks for Civil Infrastructure Systems, Cambridge, ENGLAND, APR 27-29, 2008.

[192] H. Takizawa and P. C. Jennings. Collapse of a model for ductile reinforced concrete frames under extreme earthquake motions. *Earthquake Engineering & Structural Dynamics*, 8 (2):117–144, 1980. ISSN 00988847, 10969845. doi: 10.1002/eqe.4290080204. URL http://doi.wiley.com/10.1002/eqe.4290080204.

[193] N. N. Taleb. *The black swan: the impact of the highly improbable*. Random House, New York, 1st ed edition, 2007. ISBN 978-1-4000-6351-2.

[194] W. Tong. *Wind power generation and wind turbine design*. WIT Press, Southampton; Boston, 2010. ISBN 978-1-84564-205-1 1-84564-205-8.

[195] V. Valamanesh and A. T. Myers. Aerodynamic Damping and Seismic Response of Horizontal Axis Wind Turbine Towers. *Journal of Structural Engineering*, 140(11):04014090, Nov. 2014. ISSN 0733-9445, 1943-541X. doi: 10.1061/(ASCE)ST.1943-541X.0001018. URL http://ascelibrary.org/doi/abs/10.1061/%28ASCE%29ST.1943-541X.0001018.

[196] C. F. Van Loan. Generalizing the Singular Value Decomposition. *SIAM Journal on Numerical Analysis*, 13(1):pp. 76–83, 1976. ISSN 00361429. URL http://www.jstor.org/stable/2156468.

[197] P. Van Overschee and B. De Moor. Subspace algorithms for the stochastic identification problem. In *Proceedings of the 30th IEEE Conference on Decision and Control*, pages 1321–1326, Brighton, 1991. IEEE. ISBN 978-0-7803-0450-5. doi: 10.1109/CDC.1991.261604. URL `http://ieeexplore.ieee.org/lpdocs/epic03/wrapper.htm?arnumber=261604`.

[198] P. Van Overschee and B. De Moor. *Subspace Identification for Linear Systems: Theory, Implementation, Applications*. Kluwer Academic Publishers, Dordrecht, Netherlands, May 1996. ISBN 0-7923-9717-7.

[199] S. Vanlanduit, P. Verboven, P. Guillaume, and J. Schoukens. An automatic frequency domain modal parameter estimation algorithm. *Journal of Sound and Vibration*, 265 (3):647–661, Aug. 2003. ISSN 0022460X. doi: 10.1016/S0022-460X(02)01461-X. URL `http://linkinghub.elsevier.com/retrieve/pii/S0022460X0201461X`.

[200] P. Verboven, E. Parloo, P. Guillaume, and M. Van Overmeire. Autonomous modal parameter estimation based on a statistical frequency domain maximum likelihood approach. In *Proceedings of the 19th International Modal Analysis Conference*, 2001.

[201] P. Verboven, E. Parloo, P. Guillaume, and M. Van Overmeire. Autonomous structural health monitoring—part I: modal parameter estimation and tracking. *Mechanical Systems and Signal Processing*, 16(4):637–657, 2002.

[202] P. Verboven, B. Cauberghe, E. Parloo, S. Vanlanduit, and P. Guillaume. User-assisting tools for a fast frequency-domain modal parameter estimation method. *Mechanical Systems and Signal Processing*, 18(4):759–780, July 2004. ISSN 08883270. doi: 10.1016/S0888-3270(03) 00053-0. URL `http://linkinghub.elsevier.com/retrieve/pii/S0888327003000530`.

[203] V. Vrabie, P. Granjon, and C. Serviere. Spectral kurtosis: from definition to application. In *Proceedings of the 6th IEEE International Workshop on Nonlinear Signal and Image Processing (NSIP 2003)*, Grado-Trieste, Italy, 2003. URL `http://hal.archives-ouvertes.fr/docs/00/06/31/63/PDF/nsip03.pdf`.

[204] M. M. A. Wahab and G. D. Roeck. Damage detection in bridges using modal curvatures: application to a real damage scenario. *Journal of Sound and Vibration*, 226(2):217 – 235, 1999. ISSN 0022-460X. doi: DOI:10.1006/jsvi.1999.2295. URL `http://www.sciencedirect.com/science/article/pii/S0022460X99922952`.

[205] Z. Wang and K. Ong. Autoregressive coefficients based Hotellings T2 control chart for structural health monitoring. *Computers & Structures*, 86(19-20):1918–1935, Oct. 2008. ISSN 00457949. doi: 10.1016/j.compstruc.2008.02.007.

[206] W. Weijtjens, R. Shirzadeh, G. De Sitter, and C. Devriendt. Classifying resonant frequencies and damping values of an offshore wind turbine on a monopile foundation. *Proceedings of EWEA, Barcelona*, 2014.

[207] W. Weijtjens, T. Verbelen, G. De Sitter, C. Devriendt, and others. Data Normalization for Foundation SHM of an Offshore Wind Turbine: A Real-Life Case Study. In *EWSHM-7th European Workshop on Structural Health Monitoring*, 2014.

[208] H. Wenzel. Industrial Safety and Life Cycle Engineering. Technical report, VCE Vienna Consulting Engineers ZT GmbH, Vienna, Austria, 2013.

[209] K. Worden and G. Manson. The application of machine learning to structural health monitoring. *Philosophical Transactions of the Royal Society A: Mathematical, Physical and Engineering Sciences*, 365(1851):515–537, Feb. 2007. ISSN 1364-503X, 1471-2962. doi: 10.1098/rsta.2006.1938. URL http://rsta.royalsocietypublishing.org/cgi/doi/10.1098/rsta.2006.1938.

[210] K. Worden, H. Sohn, and C. Farrar. Novelty Detection in a Changing Environment: Regression and Interpolation Approaches. *Journal of Sound and Vibration*, 258(4):741–761, Dec. 2002. ISSN 0022460X. doi: 10.1006/jsvi.2002.5148. URL http://linkinghub.elsevier.com/retrieve/pii/S0022460X02951485.

[211] K. Worden, C. R. Farrar, G. Manson, and G. Park. The fundamental axioms of structural health monitoring. *Proceedings of the Royal Society A: Mathematical, Physical and Engineering Science*, 463(2082):1639 –1664, June 2007. doi: 10.1098/rspa.2007.1834. URL http://rspa.royalsocietypublishing.org/content/463/2082/1639.abstract.

[212] N. Yampikulsakul, E. Byon, S. Huang, S. Sheng, and M. You. Condition Monitoring of Wind Power System With Nonparametric Regression Analysis. *IEEE Transactions on Energy Conversion*, 29(2):288–299, June 2014. ISSN 0885-8969, 1558-0059. doi: 10.1109/TEC.2013.2295301. URL http://ieeexplore.ieee.org/lpdocs/epic03/wrapper.htm?arnumber=6714433.

[213] A.-M. Yan, G. Kerschen, P. De Boe, and J.-C. Golinval. Structural damage diagnosis under varying environmental conditions—Part I: A linear analysis. *Mechanical Systems and Signal Processing*, 19(4):847–864, July 2005. ISSN 08883270. doi: 10.1016/j.ymssp.2004.12.002. URL http://linkinghub.elsevier.com/retrieve/pii/S0888327004001785.

[214] A.-M. Yan, G. Kerschen, P. De Boe, and J.-C. Golinval. Structural damage diagnosis under varying environmental conditions—part II: local PCA for non-linear cases. *Mechanical Systems and Signal Processing*, 19(4):865–880, July 2005. ISSN 08883270. doi: 10.1016/j.ymssp.2004.12.003. URL http://linkinghub.elsevier.com/retrieve/pii/S0888327004001797.

[215] W. Yang, P. J. Tavner, C. J. Crabtree, Y. Feng, and Y. Qiu. Wind turbine condition monitoring: technical and commercial challenges. *Wind Energy*, pages n/a–n/a, July 2012. ISSN 10954244. doi: 10.1002/we.1508. URL http://dx.doi.org/10.1002/we.1508.

[216] W. Y. Yang. *Signals and Systems with MATLAB.* Springer Berlin Heidelberg, Berlin, Heidelberg, 2009. ISBN 978-3-540-92953-6 978-3-540-92954-3. URL `http://link.springer.com/10.1007/978-3-540-92954-3`.

[217] W. J. Youden. Index for rating diagnostic tests. *Cancer*, 3(1):32–35, 1950. ISSN 0008-543X, 1097-0142. doi: 10.1002/1097-0142(1950)3:1<32::AID-CNCR2820030106> 3.0.CO;2-3. URL `http://doi.wiley.com/10.1002/1097-0142%281950%293%3A1%3C32% 3A%3AAID-CNCR2820030106%3E3.0.CO%3B2-3`.

[218] C. Zhan, D. Li, and H. Li. A local damage detection approach based on restoring force method. *Journal of Sound and Vibration*, 333(20):4942–4959, Sept. 2014. ISSN 0022460X. doi: 10.1016/j.jsv.2014.05.027. URL `http://linkinghub.elsevier.com/retrieve/pii/S0022460X14004179`.

[219] Q. Zhang and M. Basseville. Advanced numerical computation of chi2–tests for fault detection and isolation. In *Proceedings of the 5th Symposium on Fault Detection, Supervision and Safety for Technical Processes (SAFEPROCESS)*, pages 211–216, Washington, US, June 2003.

[220] Q. W. Zhang, L. C. Fan, and W. C. Yuan. Traffic-induced variability in dynamic properties of cable-stayed bridge. *Earthquake Engineering & Structural Dynamics*, 31(11):2015–2021, Nov. 2002. ISSN 0098-8847, 1096-9845. doi: 10.1002/eqe.204. URL `http://doi.wiley.com/10.1002/eqe.204`.

[221] Y. Zhang and J. Lynch. Long-Term Modal Analysis of the New Carquinez Long-Span Suspension Bridge. In A. Cunha, editor, *Topics in Dynamics of Bridges, Volume 3*, Conference Proceedings of the Society for Experimental Mechanics Series, pages 73–82. Springer New York, 2013. ISBN 978-1-4614-6518-8. URL `http://dx.doi.org/10.1007/978-1-4614-6519-5_8`.

[222] Y. Zhang, M. W. Häckell, J. P. Lynch, and R. Rolfes. Automated Modal Parameter Extraction and Statistical Analysis of the New Carquinez Bridge Response to Ambient Excitations. In *Proceedings of the 32nd International Modal Analysis Conference (IMAC)*, Orlando, Florida, USA, 2014. URL `http://www.sem.org/APP-CONF-List2-Abstract.asp?PaperNo=340`.

[223] W. Zhou, L. Mevel, M. Basseville, M. Goursat, and H. Nasser. Statistical model-based damage localization: implementation within the Scilab toolbox COSMAD. In *Proceedings of the Asia-Pacific Workshop on Structural Health Monitoring*, Yokohama, JP, Dec. 2006.

[224] M. H. Zweig, G. Receiver-operating characteristic (ROC) plots: a fundamental evaluation tool in clinical medicine. *Clinical Chemistry*, 39(4):561–77, 1993. ISSN 0009-9147.

Lebenslauf

Persönliche Daten

Name:	Moritz Werther Häckell
Geburtstag:	10.02.1985
Geburtsort:	Bremen
Eltern:	Ursula Erna Häckell, geb. Metzendorf
	und Jörg-Werther Häckell
Staatsangehörigkeit:	deutsch

Schulbildung

1991-1995:	Grundschule Admiralstraße; Bremen
1995-1997:	Orientierungsstufe Augsburgerstraße; Bremen
1997-2001:	Gymnasiale Mittelstufe am Schulzentrum Findorff; Bremen
2001-2004:	Altes Gymnasiums; Bremen
2004:	Allgemeine Hochschulreife

Hochschulbildung

2005-2010:	Studium des Bauingenieurwesens an der Leibniz Universität Hannover
2010:	Abschluss als Diplom-Ingenieur

Wissenschaftlicher Werdegang

2010-2015:	Wissenschaftlicher Mitarbeiter am Institut für Statik und Dynamik an der Fakultät für Bauingenieurwesen und Geodäsie der Leibniz Universität Hannover